AD

USAAMRDL TECHNICAL REPORT 71-24

AN ANALYTICAL AND EXPERIMENTAL INVESTIGATION OF HELICOPTER ROTOR HOVER PERFORMANCE AND WAKE GEOMETRY CHARACTERISTICS

By

Anton J. Landgrebe

June 1971

EUSTIS DIRECTORATE
U. S. ARMY AIR MOBILITY RESEARCH AND DEVELOPMENT LABORATORY
FORT EUSTIS, VIRGINIA

CONTRACT DAAJ02-69-C-0056
UNITED AIRCRAFT CORPORATION
RESEARCH LABORATORIES
EAST HARTFORD, CONNECTICUT

UNCLASSIFIED

Security Classification

DOCUMENT CONTROL DATA - R & D

(Security classification of title, body of abstract and indexing annotation must be entered when the overall report is classified)

1. ORIGINATING ACTIVITY (Corporate author) United Aircraft Corporation Research Laboratories	2a. REPORT SECURITY CLASSIFICATION Unclassified 2b. GROUP

3. REPORT TITLE

AN ANALYTICAL AND EXPERIMENTAL INVESTIGATION OF HELICOPTER ROTOR HOVER PERFORMANCE AND WAKE GEOMETRY CHARACTERISTICS

4. DESCRIPTIVE NOTES (Type of report and inclusive dates)

Final Report

5. AUTHOR(S) (First name, middle initial, last name)

Anton J. Landgrebe

6. REPORT DATE	7a. TOTAL NO. OF PAGES	7b. NO. OF REFS
June 1971	227	25

8a. CONTRACT OR GRANT NO. DAAJ02-69-C-0056 b. PROJECT NO. Task 1F162203A13903 c. d.	9a. ORIGINATOR'S REPORT NUMBER(S) USAAMRDL Technical Report 71-24 9b. OTHER REPORT NO(S) (Any other numbers that may be assigned this report) UARL K910828-31

10. DISTRIBUTION STATEMENT

Approved for public release; distribution unlimited.

11. SUPPLEMENTARY NOTES	12. SPONSORING MILITARY ACTIVITY
	Eustis Directorate U. S. Army Air Mobility R&D Laboratory Fort Eustis, Virginia

13. ABSTRACT

An analytical and experimental investigation was conducted to acquire systematic model rotor performance and wake geometry data and to evaluate the accuracy of various analytical methods in predicting the effects on performance of changes in helicopter rotor design and operating parameters. Both classical hover performance analyses and analytical methods recently developed at the United Aircraft Research Laboratories were evaluated. Of primary concern in the study was the assessment of assumptions in the analyses regarding the geometry of the rotor wake. It was found that analyses based on a contracted wake geometry generally provided significantly improved predictions of performance for those rotor operating conditions where the more classical uncontracted wake analyses exhibited major shortcomings. Attempts to develop a theoretical method for predicting contracted wake geometries were only partially successful although the method yielded good qualitative results. Of particular interest was the prediction by the analysis of an instability of the tip vortex helix at moderate distances from the rotor which appeared to be substantiated by available experimental results. In lieu of an accurate theoretical wake method, it was recommended that the experimental wake data measured in this study provide the contracted wake geometries needed in performance calculations. Analysis of the wake data for that portion of the wake which was stable (i.e., near the rotor) indicated that the data could be expressed in relatively simple generalized equations which facilitate the rapid estimation of contracted wake geometries for a wide range of rotor designs and operating conditions. Finally, it was demonstrated that rotor performance is sensitive to small changes in the position of the tip vortex relative to the following blade, and it was recommended that additional full scale correlation studies be made to provide further information on the adequacy of the generalized model rotor wake geometry charts provided herein.

DD FORM 1 NOV 65 1473 REPLACES DD FORM 1473, 1 JAN 64, WHICH IS OBSOLETE FOR ARMY USE.

UNCLASSIFIED

Security Classification

DISCLAIMERS

The findings in this report are not to be construed as an official Department of the Army position unless so designated by other authorized documents.

When Government drawings, specifications, or other data are used for any purpose other than in connection with a definitely related Government procurement operation, the U.S. Government thereby incurs no responsibility nor any obligation whatsoever; and the fact that the Government may have formulated, furnished, or in any way supplied the said drawings, specifications, or other data is not to be regarded by implication or otherwise as in any manner licensing the holder or any other person or corporation, or conveying any rights or permission, to manufacture, use, or sell any patented invention that may in any way be related thereto.

DISPOSITION INSTRUCTIONS

Destroy this report when no longer needed. Do not return it to the originator.

14. KEY WORDS	LINK A		LINK B		LINK C	
	ROLE	WT	ROLE	WT	ROLE	WT
Helicopter Rotors						
Helicopter Rotor Hover Performance						
Helicopter Rotor Wake						
Wake Geometry						
Vortices						
Hovering						
Helicopter Rotor Aerodynamics						
Helicopter Rotor Airloads						
Flow Visualization						
Distorted Wake						
Model Tests						
Model Helicopter Rotor Tests						

DEPARTMENT OF THE ARMY
U. S. ARMY AIR MOBILITY RESEARCH & DEVELOPMENT LABORATORY
EUSTIS DIRECTORATE
FORT EUSTIS, VIRGINIA 23604

This report has been reviewed by the U. S. Army Air Mobility Research and Development Laboratory and is considered to be technically sound. The purpose of the research was: (1) to examine model rotor hover performance and wake geometry characteristics as influenced by variations in rotor configuration parameters, (2) to evaluate the accuracy of various hover performance theories, and (3) to modify the distorted wake program to permit the prediction of hover wake geometry characteristics.

The report is published for the exchange of information and the stimulation of ideas. The program was conducted under the technical management of Mr. John L. Shipley and Mr. G. Thomas White of the Aeromechanics Division of this Directorate.

Task 1F162203A13903
Contract DAAJ02-69-C-0056
USAAMRDL Technical Report 71-24
June 1971

AN ANALYTICAL AND EXPERIMENTAL INVESTIGATION OF HELICOPTER ROTOR HOVER PERFORMANCE AND WAKE GEOMETRY CHARACTERISTICS

UARL K910828-31

by

Anton J. Landgrebe

Prepared by

United Aircraft Corporation
Research Laboratories
East Hartford, Connecticut

for

EUSTIS DIRECTORATE
U. S. ARMY AIR MOBILITY RESEARCH AND DEVELOPMENT LABORATORY
FORT EUSTIS, VIRGINIA

SUMMARY

An analytical and experimental investigation was conducted to acquire systematic model rotor performance and wake geometry data and to evaluate the accuracy of various analytical methods in predicting the effects on performance of changes in helicopter rotor design and operating parameters. Both classical hover performance analyses and analytical methods recently developed at the United Aircraft Research Laboratories were evaluated. Of primary concern in the study was the assessment of assumptions in the analyses regarding the geometry of the rotor wake. It was found that analyses based on a contracted wake geometry generally provided significantly improved predictions of performance for those rotor operating conditions where the more classical uncontracted wake analyses exhibited major shortcomings. Attempts to develop a theoretical method for predicting contracted wake geometries were only partially successful although the method yielded good qualitative results. Of particular interest was the prediction by the analysis of an instability of the tip vortex helix at moderate distances from the rotor which appeared to be substantiated by available experimental results. In lieu of an accurate theoretical wake method, it was recommended that the experimental wake data measured in this study provide the contracted wake geometries needed in performance calculations. Analysis of the wake data for that portion of the wake which was stable (i.e., near the rotor) indicated that the data could be expressed in relatively simple generalized equations which facilitate the rapid estimation of contracted wake geometries for a wide range of rotor designs and operating conditions. Finally, it was demonstrated that rotor performance is sensitive to small changes in the position of the tip vortex relative to the following blade, and it was recommended that additional full scale correlation studies be made to provide further information on the adequacy of the generalized wake geometry charts provided herein.

FOREWORD

This investigation was sponsored by the U. S. Army Aviation Materiel Laboratories (now the Eustis Directorate, U. S. Army Air Mobility Research and Development Laboratory) under Contract DAAJ02-69-C-0056, Task 1F162203A13903. Efforts under this contract were initiated in April 1969 and completed in February 1971. The experimental program reported herein was conducted during the period July to October 1969.

The guidance and assistance provided to this investigation by Mr. Peter J. Arcidiacono, Chief, Aerodynamics (UARL), is gratefully acknowledged. In addition to general management, Mr. Arcidiacono provided invaluable assistance with (1) the evaluation of the Wake Geometry Program and (2) preparation of the final report. Also acknowledged is the assistance provided by Mr. M. C. Cheney, Supervisor, Rotary Wing Technology (UARL), E. Dean Bellinger, Research Engineer, and Charles B. Pike, Computer Analyst. The Technical Representatives of the Contracting Officer for this contract were John L. Shipley and G. Thomas White.

TABLE OF CONTENTS

LIST OF ILLUSTRATIONS

Figure		Page

Figure		Page

Figure		Page

Figure		Page

LIST OF TABLES

LIST OF SYMBOLS

A,B	denote end points of straight vortex element in wake (Figure 77 and Appendix I only); otherwise, A represents the diameter of far wake nondimensionalized by radius
$\bar{A}$	typical intersection of smoke filament with vortex sheet (see Figure 10)
AP,BP	distances from vortex end points, A & B, to point P in wake at which induced velocities are computed, ft
AR	blade aspect ratio, chord divided by rotor radius
b	number of blades
$\bar{B}$	typical intersection of vortex sheet extension with tip vortex boundary (see Figure 10)
c	blade chord, ft
c_d	section drag coefficient
c_l	section lift coefficient
C	constant of proportionality relating to k_2 and $\sqrt{C_T/2}$
$\bar{C}$	typical intersection of inboard smoke filament with blade span axis (see Figure 10)
C_T	rotor thrust coefficient: rotor thrust divided by $\rho\pi R^2(\Omega R)^2$
C_Q	rotor torque coefficient: rotor torque divided by $\rho\pi R^3(\Omega R)^2$
d	axial spacing of far wake (see Figure 76)
D_f	diameter of far wake, equal to twice the radial coordinate of the last point in near wake (see Figure 76)

$\bar{D}$	radial location at which blade circulation is a maximum
I,J,K	functions of wake geometry defined in Appendix I
IGE	abbreviation denoting In-Ground-Effect
k_1	average axial velocity of a tip vortex element from the time at which it was shed by a given blade until it passes the following blade, nondimensionalized by ΩR
k_2	average axial velocity of a tip vortex element generated by a given blade after it passes the following blade, nondimensionalized by ΩR
$K_{1 \text{ and } 2, \bar{r}=1}$	parameters defining the axial position of an imaginary extension of the inboard sheet to $\bar{r} = 1.0$; see Equations (4) and (5)
$K_{1 \text{ and } 2, \bar{r}=0}$	parameters defining the axial position of an imaginary extension of the inboard sheet to $\bar{r} = 0$; see Equations (4) and (5)
K	function of wake geometry defined in Appendix I
M	local blade section Mach number
M_T	Mach number of blade tip
N_F	number of far wake revolutions (see Figure 76)
OGE	abbreviation denoting Out-of-Ground-Effect
P	denotes representative point in wake at which wake-induced velocities are to be computed (see Figure 77)
$\bar{r}$	distance from rotor axis of rotation to blade section or wake vortex element, measured parallel to plane of rotation and nondimensionalized by R
R	rotor radius, ft
T	rotor thrust, lb

v	velocity of vortex element, fps
v_z	induced velocity at blade in axial direction, fps
$v_{z_{MOM}}$	momentum value of induced velocity, equals $\Omega R\sqrt{C_T/2}$, fps
WS	abbreviation denoting whirlstand
x,y,z	fixed axis system coordinates, ft
$\bar{x},\bar{y},\bar{z}$	fixed axis system coordinates nondimensionalized by R (see Figure 77)
$\bar{z}_T$	axial coordinate of wake element measured from the tip of the blade, positive in the direction of rotor thrust and nondimensionalized by R
Z_G	distance between the center of the rotor hub and the simulated ground, ft
α	section angle of attack, deg
Γ	local blade circulation (equal to $\Omega R\bar{r}cc_\ell/2$), or strength of vortex element in wake, ft^2/sec
Γ_{max}	maximum value of Γ on blade, also equal to strength of tip vortex, ft^2/sec
$\Delta(C_T/\sigma)$	increment in rotor thrust coefficient/solidity resulting from k_1 and k_2
$\Delta k_1, \Delta k_2$	increments in k_1 and k_2 wake parameters
Δt	time increment used in numerical integration of wake velocities, sec
$\Delta x_p, \Delta y_p, \Delta z_p$	increments in x, y, and z coordinates of wake element end point resulting from an integration of the velocities acting on that point over a time Δt, ft (see Appendix I)
$\Delta\bar{z}_T$	increment in $\bar{z}_T$

$\Delta\psi$	nondimensional time increment, $\Omega\Delta t$, used in numerical integration of wake velocities, equal to rotation of rotor blade during time Δt, rad
$\Delta\psi_w$	increment in wake azimuth angle, deg or rad
θ_1	rate of change of local blade pitch angle due to built-in linear twist with respect to blade spanwise direction, positive when tip section is twisted leading-edge up relative to root section, deg or rad
θ_{75}	blade collective pitch as measured at three-quarter span station, deg or rad
λ	wake parameter representing rate of contraction of the wake (see Equation (3))
ρ	air density, $lb\text{-}sec^2/ft^4$
σ	rotor solidity, ratio of total blade area to disc area, $bc/\pi R$
ϕ_w	local pitch angle of helix, rad
ψ	blade azimuth angle measured from x axis (see Figure 77), deg or rad
ψ_w	wake element azimuth angle measured from blade (see Figure 77), deg or rad
$\psi_{w,F}$	wake element azimuth angle as measured in the fixed coordinate system (see Figure 77), deg or rad
ω	torsional frequency of blade, rad/sec
Ω	rotor rotational frequency, rad/sec

SUBSCRIPTS

deg	denotes units in degrees
IGE	denotes quantity evaluated in-ground-effect
OGE	denotes quantity evaluated out-of-ground-effect

P	denotes point at which velocity is computed
rad	denotes units in radians
x,y,z	denotes direction of velocity

INTRODUCTION

The need for attaining peak lift system performance is greater with rotary-wing VTOL aircraft than with conventional aircraft. This results directly from the generally lower payload to gross weight ratio of such aircraft which, in turn, increases the payload penalty associated with any unexpected deficiencies in performance that might arise as a result of shortcomings in the design analyses employed. For example, since the payload is typically 25% of the gross weight, a performance deficiency of 1% in lift capability can result in a 4% reduction in payload.

As described in Reference 1, commonly used theoretical methods become inaccurate as number of blades, blade solidity, blade loading, and tip Mach number are increased. The discrepancies noted appear to stem from simplifying assumptions made in the analyses regarding the geometric characteristics of the rotor wake. In Reference 1, a method for considering the effects of wake contraction on hover performance was introduced. This computerized method, developed at the United Aircraft Research Laboratories (UARL) and termed the UARL Prescribed Wake Hover Performance Method, requires a prior knowledge of the wake geometry. However, at the time Reference 1 was written (1967), available wake geometry data were extremely limited. Due to the expense involved, systematic wake geometry data on full-scale rotors were almost nonexistent. Available model results, on the other hand, were limited to rotors having three blades or less and operating at low tip Mach numbers. Thus, two methods of approach were initiated under this investigation to obtain the required wake geometry information. In the first an experimental investigation, using model rotors, was conducted in which a systematic, self-consistent set of data on rotor performance and associated wake geometry characteristics was obtained for a wide range of blade designs and operating conditions. In the second, an available analytical method for predicting rotor wake geometry in forward flight, described in Reference 2, was extended to the hover condition. Briefly, the method developed involves the establishment of an initial wake model comprised of finite vortex elements and the repeated application of the Biot-Savart law to compute the velocity induced by each vortex element at the end points of all other vortex elements in the wake. These velocities are then integrated over a small increment of time to determine the new positions of the wake elements, and the entire process is repeated until a converged wake geometry is obtained.

The incorporation of the experimental and analytical wake geometry in the Prescribed Wake Method results in two analyses (the Prescribed Experimental Wake Analysis and the Prescribed Theoretical Wake Analysis) for computing hover performance. The availability of model rotor data permits the evaluation of these analyses by (1) providing experimental wake data both for input to the Prescribed Experimental Wake Analysis and for comparison with predicted wake geometry results of the Prescribed Theoretical Wake Method, and (2) providing consistent experimental performance data for comparison with predicted performance results. Thus, the principal objectives of this investigation were to:

(a) Provide experimental information on the performance and wake geometry characteristics of hovering model rotors as influenced by number of blades, blade twist, blade aspect ratio, rotor tip speed, and blade collective pitch setting

(b) Modify an existing forward-flight distorted wake program to permit the prediction of the wake geometry characteristics in hover

(c) Evaluate the accuracy of various hover performance theories having differing rotor wake geometry assumptions

Included in this report are: (1) a description of the model rotor experimental program, (2) a discussion of the experimental rotor performance and wake geometry results, (3) comparisons of the experimental wake geometry results with other experimental sources, (4) descriptions of the theoretical methods for predicting wake geometry and hover performance, (5) a discussion of the results of the evaluation of the wake geometry analysis, and (6) a discussion of the results of the evaluation of the theoretical methods for predicting hover performance.

MODEL ROTOR HOVER TEST

TEST EQUIPMENT

Model Test Facility

The test program was conducted on a model rotor hover test facility located at the United Aircraft Research Laboratories (UARL). The test facility, shown in Figure 1, consists of a large enclosed area approximately 45 by 55 feet with a ceiling height of 40 feet. The facility is equipped with a rotor test rig, flow visualization equipment, and a movable ground plane which was considered to be in an out-of-ground-effect position when lowered to 3.5 rotor radii below the rotor. A whirl-stand model is also available for the simulation of conditions on the Sikorsky Aircraft full-scale whirl stand. This facility is the same one used for the model tests reported in Reference 1.

A photograph of the model rotor test rig is shown in Figure 2. A 40-horsepower, variable-speed electric motor was used as a power source. The rotor was driven through a 3:1 speed reduction system to allow operation at a tip speed of 700 ft/sec at maximum available power. Average rotor thrust and torque measurements were made by means of strain-gaged load cells mounted above the rotor on a support frame. The motor-balance assembly is shown schematically in Figure 3. Additional instrumentation, used to monitor operation, included a solid-state counter for measuring rpm, vibration meters, and a model power control console.

Flow visualization equipment included the following:

1. Ammonium sulphite "smoke".

2. Variable-position smoke rakes.

3. Two high-intensity, short-duration light sources (microflash units) for stop-action still photographs.

4. High-intensity lights for high frame-speed movies.

5. An electronic time-delay control for cameras and microflash units to permit systematic photographing of the cyclic time history of the rotor wake.

6. Polaroid, 70 mm, and Fastax movie cameras.

Model Rotors

The model rotor system consisted of a multibladed rotor hub and specially designed model blades. The rotor hub, shown in Figure 4, was designed to accommodate any number of blades up to and including eight. Flapping hinges were provided (but no lag hinges), and blade collective pitch was varied manually.

Four sets of model rotor blades were used to conduct the test program. The model blade design consisted of an aluminum spar and a balsa trailing-edge section, as shown in Figure 5. The blades were untapered and designed such that the elastic axis, section center of gravity, and center of pressure were coincident at the quarter-chord position (within 1% of the chord). The mass and stiffness properties of the model blades greatly exceeded those of model blades dynamically scaled to typical full-scale blades. For example, the Lock number of the blades with an aspect ratio of 18.2 operating at a tip speed of 700 fps was approximately 3.0 compared to a typical full-scale Lock number of 10. Hence, model blade coning angles were lower than full-scale coning angles. However, the use of such rotor blades permitted concentration on the aerodynamic, rather than aeroelastic, aspects of rotor hover performance. The blade parameters are summarized in Table I.

TABLE I. MODEL ROTOR BLADE PARAMETERS

Blade Parameter	Design (1)	Design (2)	Design (3)	Design (4)
Linear Twist, θ_1(deg)	0	-8	-16	-8
Aspect Ratio, AR	18.2	18.2	18.2	13.6
Radius, R (in.)	26.75	26.75	26.75	26.75
Chord, c (in.)	1.47	1.47	1.47	1.96
Airfoil Section (NACA)	0012	0012	0012	0012
Root Cutout (%R)	14.8	14.8	14.8	14.8
Flapping Hinge Offset (%R)	6.8	6.8	6.8	6.8
Taper	None	None	None	None

The second set of blades listed in Table I (θ_1 = -8 deg, AR = 18.2) was constructed and performance-tested by United Aircraft prior to this investigation. At the time of this investigation, four of these blades were available in their original form and eight were available in a modified form. The modification consisted of the adaption of a plastic tip section to the outer 12% of the blade. This tip section was nominally identical in shape to the removed aluminum-balsa section. The plastic tip blades were used in this investigation to obtain ground-effect and flow visualization results for the six- and eight-blade configurations of this particular blade design. Other performance results for this design are included from the United Aircraft investigation mentioned above. The blades corresponding to the three other blade designs were fabricated specifically for this investigation.

Each rotor blade design was tested with the following numbers of blades and rotor solidity ratios:

	Number of Blades, b			
	2	4	6	8
Rotor Solidity Ratio, σ(Designs (1)-(3))	0.035	0.070	0.105	0.140
Rotor Solidity Ratio, σ(Design (4))	0.0467	0.0933	0.140	0.1867

TEST PROCEDURES

Calibration

Prior to testing, the thrust and torque instrumentation was calibrated. The thrust load cell was calibrated on the test rig by hanging weights from the rotor shaft. The rig was calibrated in torque by suspending weights through a known moment arm. The thrust and torque calibration derivatives were determined directly in strain gage units per pound (SGUS/lb) and strain gage units per foot-pound (SGUS/ft-lb), respectively.

A dowel pin, mounted perpendicular to an arm extending from the root of the blade along the blade chord (see Figure 4), was used to manually set collective pitch angle relative to a flat on the blade retention fitting (attached to the hub). For each blade, the distance from the pin to the flat, measured by means of a depth micrometer, was calibrated with respect to the collective pitch angle at the three-quarter radius. Blade tracking was checked by observation of the blade tips through a transit, with lighting supplied by a Strobotac triggered at a specified number of flashes per rotor revolution. In this manner, several blades were observed at once, and their tip positions were compared.

To calibrate the flow visualization photographs and to minimize errors due to camera angle and lens distortion, a planar grid indicating 2% increments of the rotor radius (0.475 in.) was placed in the plane of the smoke (reference plane) and photographed prior to the test. Photographs of this grid system (Figure 6) were used in the construction of a grid template overlay for the reduction of the flow visualization photographs to radial and axial wake coordinates. The blade azimuth position was calibrated for each rpm by calculating the delay time between the passage of a reference blade through the reference plane and the passage of a single gear tooth mounted on the rotor shaft.

Test Parameters

Systematic data were obtained to measure the effect of the following parameters on rotor hover performance and associated wake geometry characteristics.

Primary Test Parameter	Nominal Test Values
1. Number of Blades, b	2, 4, 6, 8
2. Blade linear twist, θ_1	0, -8, -16 deg
3. Blade aspect ratio, AR	13.6 and 18.2
4. Rotor tip speed, ΩR	525, 600, 700 fps
5. Collective pitch, θ_{75}	0 to max*

*Determined by operating stall limits

Variations in three of the above primary test parameters were equivalent to independent variations in three related parameters. That is, variations in number of blades were equivalent to variations in rotor solidity, as specified previously. Variations in rotor tip speed of 525, 600, and 700 fps were equivalent to variations in tip Mach number of 0.46, 0.525, and 0.61, respectively. Finally, variations in collective pitch were used to produce variations in rotor thrust level. Nominal collective pitch settings of 0, 6, 8, 10, and 12 deg were used whenever possible. Additional values were tested to provide more extensive data for some test configurations, particularly in the stall region where the maximum collective pitch was limited at the higher tip speeds by an apparent stall flutter.

Data regarding the effect of the parameters listed above were obtained with rotors operating substantially out of ground effect (height above the ground plane equal to 3.5 rotor radii). In addition to the out-of-ground-effect (OGE) conditions, a number of data points were taken in ground effect (IGE) and with a model whirl stand simulating the Sikorsky Aircraft full-scale rotor whirl stand shown in Figure 7.

Test Configurations

The test parameter combinations (test configurations) that were investigated are given in Table II.

TABLE II. TEST PARAMETER COMBINATIONS

Linear Twist (deg)	Aspect Ratio	Rotor Condition	Rotor Height/ Radius	No. of Blades	No. of Tip Speeds	No. of Collective Pitch Values
0	18.2	OGE	3.5	2,4,6,8	3	5*
-8	18.2	OGE	3.5	2,4**,6**,8	3	5*
-16	18.2	OGE	3.5	2,4,6,8	3	5*
-8	13.6	OGE	3.5	2,4,6,8	3	5*
-8	18.2	IGE	1.67	2,4,6,8	3	1
-8	18.2	IGE	0.67, 1.0,1.33, 1.67,2.0	6,8	3	2
-8	18.2	Whirl Stand	1.67	2,4,6,8	3	1

*Minimum number.
**Performance results obtained from previous investigation.

Data Acquisition

The procedure for data acquisition fundamentally consisted of setting the test configuration (collective pitch, ground plane position, and number of blades) and then recording performance and wake geometry data at the required tip speeds. The ambient temperature and pressure in the enclosed area were monitored and recorded during the test. The rotor thrust and torque data were obtained by manually recording the outputs of the thrust and torque load cells on self-balancing potentiometers in strain gage units (SGUS). Oscillations of the potentiometer readings as high as ±10 SGUS (±0.03 lb) for thrust and ±30 SGUS (±0.2 ft-lb) were observed for some test conditions. To obtain representative steady-state values, average readings were recorded. Each test condition was repeated twice within a test run (a test run consisted of data recorded between the starting and stopping of the rotor rotation), and the results were averaged. In addition, most test conditions were repeated in two consecutive runs. Many of the test conditions were also repeated on different dates to check the repeatability of the data.

For most rotor configurations, the maximum collective pitch at which operation was possible was limited by the occurrence of a rapid increase in rotor noise as tip speed was increased beyond a certain level. A strain gage to measure torsional response was placed at the root of the blade and substantial increases in blade torsional response were noted under these conditions, and it was inferred that a stall flutter boundary was being penetrated. Collective pitch (thrust level) at a given tip speed was then limited by what will be described as a stall flutter boundary in the discussion of results.

To obtain flow visualization data, smoke was injected into the flow by movable smoke rakes located above and to both sides of the rotor (Figure 2). Ammonium sulphite smoke was generated by mixing ammonium gas and sulphur dioxide gas from separate ports on each smoke nozzle mounted on the smoke rakes. The smoke rakes were positioned by remote control to insure a clearly defined tip vortex. The wake patterns were recorded on film with remotely operated cameras. Illumination was provided for still photographs by two microflash units (time duration 0.5 microsecond for stop action) and for high frame-speed movies by sixteen 350-watt floodlights. A time-delay system was used to trigger the cameras and microflash units when the rotor was at a desired azimuth position. The delay system used a one/rev signal from the rotor shaft as a reference, and the delay time (manually adjusted) was measured on an electronic counter. For each test condition, 70mm photographs were taken at preselected azimuth positions of a reference blade with respect to the plane of the smoke. For example, for a two-bladed rotor, photographs were generally taken at azimuth angles of 0, 15, 30, 60, 90, 120, and 150 deg. For a six-bladed rotor, azimuth angles were generally 0, 15, 30, and 45 deg. Normally, two or three photographs were taken at each azimuth position. Two cameras were used to obtain photographs of both the complete rotor-wake system and close-up views of the right half of the rotor-wake system. To supplement these still photographs, high frame-speed movies (2000 frames/sec) were taken at selected conditions.

DATA REDUCTION

Performance Data

Thrust and torque measurements (in SGUS) were converted to thrust (lb) and torque (ft-lb), thrust coefficient (C_T) and torque coefficient (C_Q), and thrust coefficient-solidity ratio (C_T/σ) and torque coefficient-solidity ratio (C_Q/σ) values for all test conditions. The air density (ρ) used in nondimensionalizing the data was calculated for each test condition, based on the recorded temperature and pressure readings.

Flow Visualization Data

To introduce the procedures used in reducing the flow visualization data, a brief discussion of the fundamental characteristics of the hovering rotor wake and the interpretation of these characteristics from smoke photographs is presented. A schematic of the wake from one blade, reproduced directly from Gray's interpretation in Reference 3, is shown in Figure 8. The wake contains two primary components. The first, and most prominent, is the strong tip vortex which arises from the rapid rolling up of the portion of the vortex sheet shed from the tip region of the blade. The second feature is the vortex sheet shed from the inboard section of the blade. This sheet does not roll up but generally remains in the form of distributed vorticity. The vertical or axial transport velocity near the outer end of the inboard vortex sheet is much greater than that of the tip vortex. The vertical velocity of the inboard sheet also increases with radial position, resulting in a substantially linear cross section of the inboard sheet at any specific azimuth position as shown in Figures 9 and 10. These characteristics result directly from the velocities induced by the strong tip vortex. Although the radial extent of the vortex sheet is depicted in Figure 8 as ending abruptly, it probably retains some connection with the tip vortex. The exact nature of this connection, however, has been difficult to distinguish in flow visualization studies. In addition to the wake structure shown in

Figure 8 for one blade, similar wake structures for other blades also exist, with the aggregate forming the complete wake representation.

The schematic in Figure 8 is representative of the three-dimensional wake pattern which would be observed if smoke were emitted from the blade (i.e., in the rotating system). To take advantage of the symmetrical nature of the wake of a hovering rotor as well as to facilitate the acquisition of quantitative data, the wake for this investigation was observed by emitting smoke externally from the blades (i.e., in the nonrotating system). Smoke was emitted from smoke rakes in a single plane and the flow patterns were photographed, as shown for the two-bladed rotor in Figure 9. In this manner, a two-dimensional cross section of the wake was recorded. The cross sections of the tip vortices appear as circles in which the central regions are clear of smoke due to the local centrifugal field which forces the smoke particles radially outward. The center of the circular cross sections are interpreted as the centers of the vortex core. The vortex sheet cross sections are indicated by the discontinuities present in the smoke filaments passing through the inner region of the rotor wake.

The photographic wake data were analyzed for selected test conditions to determine the principal wake geometry characteristics. The conditions were selected so as to permit assessment of the effects of the primary test parameters. Radial and axial wake coordinates were determined from the photographs as functions of the wake azimuth angle (ψ_w), which is equivalent to the blade azimuth travel ($\psi = \Omega t$) from the time it generates the vortex cross section. For example, on the right side of Figure 9, the uppermost tip vortex and vortex sheet cross section were shed by blade 2, which has travelled 180 deg from the time it passed through the plane of smoke on the right side (reference side). The following tip vortex and vortex sheet cross section were shed by blade 1 the previous time it passed through the reference side of the smoke plane, and thus the wake azimuth angle for these cross sections is 360 deg. Likewise, the azimuth angle of the third cross section, shed by blade 2, is 540 deg. It should be noted that the cross sections in the visible wake near the rotor remain approximately in the same plane (rotor wake tangential velocities are small). The azimuth angle, ψ_w, was used as the third coordinate in the wake geometry analysis. In Figure 10, a schematic of the wake of Figure 9 and the wake coordinate system is presented. For a stable, hovering rotor wake, the radial and axial coordinates at a given azimuth angle are equivalent for each blade due to symmetry. Thus the complete coordinate system of the wake for a given test condition was determined by the following procedure.

A transparent grid template was constructed from the photograph of the reference grid shown in Figure 6. With the grid template as an overlay, the radial and axial coordinates of the wake from several blades in a single photograph were determined along with the corresponding wake azimuth coordinates. This was repeated for a sequence of photographs taken with the rotor at a series of prescribed rotational positions. A sample sequence is presented in Figure 11, in which the rotor rotational positions are designated by the azimuth position, ψ, of the blade which most recently passed through the reference plane containing the smoke. Considering the known azimuth positions of the reference blade and relating each vortex cross section to the appropriate blade, the radial and axial coordinates were obtained from the photographs in Figure 11 for the following wake azimuth angles:

Reference Blade Azimuth, ψ, deg	Wake Azimuth, ψ_w, deg
0	0,180,360,540
15	15,195,375,555
30	30,210,390,570
60	60,240,420,600
90	90,270,450,630
120	120,300,480,660
150	150,330,510

The coordinate results from the series of photographs were then plotted as functions of ψ_w as shown in Figures 12 and 13. To facilitate the comparison of wake geometries from varying rotors and test conditions, the radial and axial coordinates were nondimensionalized by the rotor radius, and differences in axial coordinates due to blade coning were eliminated by using the blade tip as the reference ($\bar{z}_T$ instead of $\bar{z}$). The range of wake azimuth angles for which data could be acquired was limited by the visibility of the smoke. For example, for two- and four-bladed rotors, generally only 1 to 2 tip vortex revolutions per blade, were visible. For six- and eight-bladed rotors, less than one revolution from each blade was visible. However, it will be shown that rotor performance is mainly sensitive to this near wake geometry and insensitive to reasonable extrapolations of this geometry made to define the far wake. Thus, knowledge of the exact positioning of the far wake elements is not essential to the objectives of the rotor performance portion of this study.

Since the cross sections of the vortex sheet from each blade are essentially lines rather than discrete points, as is the case for the tip vortex cross sections, the following procedure for transforming the photographic data for the vortex sheets to coordinate form was found to be convenient. Assuming the vortex sheet cross sections to be linear, the axial position of a vortex sheet at a given azimuth can be defined by two points. For simplicity, the two points selected were the imaginary extensions of the cross section to $\bar{r} = 0$ at one end and to $\bar{r} = 1.0$ at the other end, as shown in Figures 10 and 13. These two points establish the intercept at the axis of rotation and the slope of the vortex sheet. Using this procedure, it is unnecessary to reduce, for each smoke filament, the coordinates of their intercepts with the vortex sheet cross sections if the following assumption is made. It was assumed that the radial position of such intercepts (e.g., point $\bar{A}$ of Figure 10) is linearly proportional to the radial coordinate of the intersection of the vortex sheet with the vortex sheet boundary (point $\bar{B}$). With the exception of the immediate vicinity of the blade ($\psi_w < 2\pi/b$), the vortex sheet boundary was assumed to be equivalent to the boundary formed by the locus centers of the tip vortex cross sections (equivalently, tip vortex streamline). For ψ_w less than the blade spacing, $2\pi/b$, the boundary was faired from the point of maximum circulation on the blade (point $\bar{D}$ of Figure 10) to the tip vortex boundary. The constant of proportionality was assumed to be the ratio of the radial position of the origination of the smoke filament streamline at the blade (point $\bar{C}$) to the radial position of the vortex sheet boundary at the blade (point $\bar{D}$). That is,

$$\bar{r}_{\bar{A}} = \left(\frac{\bar{r}_{\bar{C}}}{\bar{r}_{\bar{D}}}\right)\bar{r}_{\bar{B}} \tag{1}$$

It was found that this was a reasonable approximation for use in the theoretical wake model for rotor performance calculations to be presented in a later section.

TEST DATA ACCURACY

Static data repeatability for thrust and torque was determined from repeated calibrations of the strain gages made while determining the calibration derivatives discussed in the Test Procedures section. The repeatability values, represented by two standard derivations, are listed below:

	Thrust, lb	Torque, ft-lb
Static Repeatability:	± 0.0087	± 0.1130

The dynamic data repeatability was established by considering the range of C_T/σ and C_Q/σ measurements observed from consecutive test points at a given tip speed for each test configuration. Normally, four test points were available from two consecutive runs between which the rotor was stopped and restarted. The mean range was established and related to the standard deviation using the procedures outlined by Hoel (Reference 4, p. 241). The results obtained are given below.

	Average	b=2, ΩR=525 fps	b=8 ΩR=700 fps
Dynamic Data Repeatability, C_T/σ	± 0.00024	± 0.00044	± 0.00015
C_Q/σ	± 0.000022	± 0.000045	± 0.000012

By choosing consecutive test points in the above analysis, variations due to differences in collective pitch setting were eliminated. These differences were significant, as will be shown in the presentation of the performance data. However, they did not significantly influence the rotor thrust - torque relationship.

The estimated accuracies with which the parameters determining a given test condition could be set are as follows:

Parameter	Accuracy
Collective Pitch, θ_{75}	± 0.2 deg
Tip Speed, ΩR	± 1 fps
Rotor Height, Z_G/R	± 0.03 R

The estimated accuracy and repeatability of the tip vortex coordinates are listed below.

Wake Coordinate	Accuracy	Repeatability
Azimuth, ψ_w	± 3 deg	--
Radial, $\bar{r}$	± 0.005	$\sim \pm 0.01$
Axial, $\bar{z}_T$	± 0.005	$\sim \pm 0.01$

The accuracy of the radial and axial coordinate represents the degree of accuracy to which coordinates of a wake point could be measured from the grid system used. The repeatability represents the normal repeatability of a wake point in a series of photographs taken during a single test condition (e.g., see Figure 12). This repeatability pertains only to the tip vortex in the near wake region of the rotor (to be discussed later). Figure 14 shows the repeatability of the tip vortex coordinates for a test condition as repeated on three different dates.

DISCUSSION OF EXPERIMENTAL ROTOR PERFORMANCE RESULTS

The rotor performance test data were transformed to graphical form for the various combinations of number of blades (solidity), blade twist, aspect ratio, tip speed, and simulated ground height. The resulting graphs were analyzed to assess the separate influence of each of these parameters on model rotor hover performance. The performance characteristics of the model rotors are presented in nondimensional form in Figures 15 through 18 for each combination of blade twist and aspect ratio tested. This series of graphs, which contains data for out-of-ground-effect operation ($Z_G/R = 3.5$), also includes results for various tip speeds.

Thrust (Collective Pitch) Limits

As noted previously, maximum thrust (collective pitch) was limited, for each rotor configuration, by the rapid increase in noise level when a specific tip speed was exceeded. Oscillograph records, displaying a signal produced by torsional strain gages mounted at the root end of a blade, were analyzed to determine the frequency of the blade torsional response. The frequency (ω = approximately 12 cycles per rotor revolution) was found to agree with both the measured acoustic frequency and an estimate of the first natural frequency of the blade in torsion when nondimensionalized by Ω. Thus, it was concluded that the performance boundary had the characteristics of incipient stall flutter. Previous stall flutter investigations (e.g., Reference 5) have shown that the thrust boundary (hereafter referred to as the stall flutter boundary) is lowered with an increase in the following parameter which is the inverse of the reduced frequency parameter:

$$\text{STALL FLUTTER PARAMETER} = \frac{\Omega R}{c\,\omega}$$

The test results indicated that the stall flutter boundaries were lowered with increased tip speed, ΩR, and decreased chord, c, indicating apparent agreement with the above relation. The stall flutter boundaries were also lowered with decreasing blade twist due to the earlier stall of the blade tip section.

Effect of Collective Pitch

The results of Figures 15 to 18 are presented in terms of rotor thrust versus rotor torque to minimize scatter introduced by the accuracy with which collective pitch, θ_{75}, could be set. Nominal values of constant collective pitch are, however, indicated by the dashed lines in each figure. In addition, representative variations of C_T/σ and C_Q/σ with θ_{75} are presented in Figure 19 corresponding to the faired data presented in Figure 17. As anticipated, rotor torque increases rapidly at the higher collective pitch levels due to divergence of the airfoil drag characteristics. However, no corresponding fall-off in thrust, an indication of lift stall, is evident for the range of pitch values tested.

Effect of Solidity and Number of Blades

Rotor solidity was changed, for each blade design, by varying the number of blades from 2 to 8 as indicated in Figures 15 through 18. Since each of these figures represents rotors with fixed blade chord, radius, and tip speed, C_T/σ and C_Q/σ are directly representative of thrust and torque per blade (blade thrust and torque loading). Comparison of the results for varying numbers of blades within each figure demonstrates the improved blade efficiency (thrust/blade (C_T/σ) per torque/blade (C_Q/σ)) with decreasing solidity. The improved blade efficiency occurs for two reasons. First, and most important, at a given blade loading, the fewer the number of blades (or the smaller the solidity), the lower will be the total thrust and disc loading of the rotor. As a result, the average downwash (which is a measure of energy expended) induced by the rotor wake will be lower and hence the blade induced drag will be less. A second smaller effect arises from the reduced local interference caused by the tip vortex shed by one blade on the loading of the following blade. This will be discussed further in a later section of this report.

Although lower solidity at constant aspect ratio implies greater blade efficiency, there is a limit to which it also implies greater rotor efficiency. This is shown in Figure 20, in which the total rotor performance coefficients (C_T and C_Q) are presented for the blade design and tip speed corresponding to Figure 16(a). Since the blade radius and tip speed are fixed in Figure 20, C_T and C_Q are representative of total rotor thrust and torque. Figure 20 shows that the rotor efficiency (rotor thrust per rotor torque) is improved with lower solidity only up to a point which is determined by blade stall considerations.

Effect of Aspect Ratio at Constant Solidity

Of particular interest to the rotor designer is the trade-off in performance between chord and number of blades while maintaining constant rotor solidity (total blade area and disc area held constant). The experimental results comparing the hover performance for eight 18.2-aspect-ratio blades (c = 1.47 in.) and six 13.6-aspect-ratio blades (c = 1.96 in.) at a constant solidity of 0.140 are presented in Figure 21. Over the thrust range tested (i.e., up to the stall flutter boundary), the results are essentially equivalent for the two configurations. The existence of the stall flutter boundary prohibited the investigation of the trade-off of number of blades and chord at conditions associated with deep penetration into stall. The eight narrow chord-blades exhibited stall flutter at lower performance levels than the six wide-chord blades. This implies that the aeroelastic, rather than the aerodynamic, characteristics of the blades may ultimately be the determining factor in selecting blade aspect ratio.

Effect of Blade Twist

The effect of blade linear twist rate on experimental model rotor performance is shown in Figure 22 for two- and six-bladed rotors operating at a tip speed of 700 fps. For clarity, only the faired curves through the experimental data from Figures 15 to 17 are presented. An improvement in performance is noted at the higher thrust levels as blade twist is increased. For the six-bladed rotor most of the improvement is due to the initial 8 degrees of twist. For the two-bladed, -16-degree-twist rotor blades, the higher profile drag at low thrust and the improved performance in the stall region result in a crossover in blade efficiency relative to the blades of lower twist.

Effect of Tip Speed

The effect of variations in tip speed (from 525 to 700 fps) on rotor performance is shown in Figures 23 and 24. As in Figure 22, only the faired experimental curves are presented. Performance results are presented for two- and six-bladed rotors with 0 and -16-degree-twist blades. The influence of compressibility, which results in decreasing performance with increasing tip speed, is evident for all rotors. The influence is less for the -16-degree-twist blades because the high-Mach-number tip sections are operating at lower angles of attack relative to the tip sections of the zero-twist blades.

Ground Effect

The relative position of the rotor with respect to the ground was varied by raising or lowering the ground plane. The rotor configuration and collective pitch setting were held fixed during a series of simulated rotor height variations. The effect of rotor height above ground (ground effect) on rotor performance coefficients is shown in Figure 25 for six- and eight-bladed rotors with a -8-degree twist and an aspect ratio of 18.2. Data are presented for variations in rotor height from 3.5 R, which is essentially out of ground effect (OGE), to 0.67 R, which is well in ground effect (IGE). The OGE data differs slightly from that presented previously because the plastic tip blades were used for this series of data; however, this should have no effect on the relative performance between the IGE and OGE conditions. It is shown in Figure 25 that the variation of thrust with torque is essentially linear as rotor height is varied. Thrust augmentation, which is defined as the increase in rotor thrust at constant torque for IGE operation over that for OGE operation, was obtained using the following relation:

$$\frac{T_{IGE}}{T_{OGE}} = \left[\frac{(C_T/\sigma)_{IGE}}{(C_T/\sigma)_{OGE}}\right]_{\text{CONSTANT } C_Q/\sigma}$$

The thrust augmentation results are presented in Figure 26, where it is shown that the effect of rotor height is virtually independent of both variations in solidity corresponding to six and eight blades and variations in OGE thrust level. The thrust at the minimum rotor height tested was increased by approximately 18% over the thrust for OGE operation. It should be noted that the results presented are for -8-degree linear twist blades. The detailed investigation of ground effect was not a primary objective of this study and thus was not investigated for all rotor configurations. Results of recent tests at UARL and Sikorsky Aircraft indicate a variation in thrust augmentation with blade twist.

In addition to the variation in rotor height discussed above, the -8-degree-twist blades (AR = 18.2) were tested IGE in a manner to simulate typical full-scale whirl-stand operation. For these conditions, the rotor was 1.67 R above the ground plane and was tested with and without the presence of a model whirl stand (IGE and IGE/WS). The following tabulation consists of representative averages of the thrust augmentation results.

Tip Speed (fps)	No. of Blades	Thrust Augmentation Ratio, T_{IGE}/T_{OGE} IGE	IGE/WS
700	2, 6, 8	1.03	1.035
525	2, 6, 8	1.02	1.025

Although the scatter in the individual T_{IGE}/T_{OGE} results used in determining the above averages was approximately ±1%, taken in aggregate, the data indicated a slight increase in thrust augmentation due to the presence of the whirl stand.

DISCUSSION OF EXPERIMENTAL ROTOR WAKE GEOMETRY RESULTS

Sample Photographs

In addition to the sequence of photographs previously presented in Figure 11 for a two-bladed rotor, similar sequences for four, six, and eight blades are presented in Figures 27 through 29. These photographs, for the zero twist rotor operating at a tip speed of 700 fps and a collective pitch setting of 8 degrees, show the time history of the wake as the reference blade rotates to various azimuth positions. The tip vortex cross sections in the "near wake" (portion of wake within one or two wake revolutions beneath the rotor) are clearly evident, as are the discontinuities in the inboard smoke filaments which identify the inboard vortex sheet locations. Also evident are the rapid contraction of the wake and the decreased axial wake spacing with increasing number of blades.

A characteristic of all the photographs taken during this investigation is the absence of the tip vortex cross sections beyond those corresponding to approximately three to four blade passages. That is, no more than four vortex cross sections normally appear clearly on any given photograph. Thus, the limiting azimuth for visualization of the tip vortex varied with number of blades according to the following:

No. of Blades	Azimuth Spacing Between Blades (deg)	Approximate Azimuth Limit (Azimuth Spacing x 4) (deg)
2	180	720
4	90	360
6	60	240
8	45	180

At first it was believed that the tip vortex cross sections became indistinguishable due to diffusion of the smoke by turbulent mixing as mentioned by Gilmore in Reference 6. However, close scrutiny of the photographs and high-frame-speed movies resulted in the conclusion that the far-wake region of a hovering rotor is unstable or, at best, neutrally stable. Whether the tip vortex undergoes a form of viscous dissipation (decay) or vortex breakdown (bursting) as characterized by certain fixed wing tip vortices (Reference 7) is conjecture at this time. However, the results of this investigation indicate a definite departure from the classical concept of a smoothly contracting wake below the rotor. Evidence of this is shown in Figure 11, in which the fourth vortex cross section proceeds to travel radially outward (note particularly the photographs for $\psi = 90$ and 120 deg) until it is no longer visible at $\psi = 150$ deg. Perhaps a more dramatic example of the instability is presented in the series of Figure 30, in which the fourth vortex cross section moves radially out and eventually to the side of the third. Although it is recognized that a small perturbation such as a small amount of ambient wind or a slight blade-out-of-track may be necessary to precipitate the instability, this is believed to be an academic consideration since full-scale rotor operation is certainly subject to greater disturbances than those present under the laboratory conditions of this investigation. More photographic examples and a more complete discussion of the unstable nature of the far wake will be presented in a later section of this report.

Sample enlarged photographs for combinations of rotor configurations and test conditions representative of variations of the primary test parameters are presented in Figures 31 through 40. Three photographs for IGE and whirl-stand conditions are also included. Single photographs for each configuration and condition are shown with the reference blade at the zero azimuth position. Note that the top tip vortex cross section in each photograph corresponds to the tip vortex shed from the previous blade. A time exposure (Figure 32) of the wake is included to show the streamline patterns of the smoke filaments. Note that this photograph is for the same condition as one of the previous stop-action photographs presented in Figure 31. Sample photographs for the rotor in a simulated whirl-stand environment and IGE are presented in Figures 38 through 40. The radial expansion of the wake as it approaches the ground plane is evident in these latter photographs. One of the observations made during review of these and other photographic data was that the tip vortex never passed above the blades.* Photographic evidence of the location of the tip vortex of a full-scale rotor above the plane of rotation was shown in Reference 1, where it was attributed to a small amount of wind. The absence of this phenomenon in the model tests is ascribed to the controlled laboratory conditions. The wake characteristics observed in the flow visualization photographs are discussed in more detail in the following section.

Tip Vortex Coordinates

Sample results obtained from the reduction of the flow visualization photographs to coordinate form, are presented in Figures 41 through 52 for the tip vortex. Note that in order to present the axial and radial coordinates on the same scale, and since the experimental tip vortices were always located below the rotor tip path plane, the negative of the axial coordinate with respect to the blade tip ($-\bar{Z}_T$) was plotted. The symbols at a specific azimuth represent an average of all the data reduced from multiple photographs for a given rotor operating condition. The repeatability of the radial and axial coordinates was generally within ± 0.01 R in the stable near-wake region. The flight conditions for which data are presented were selected from over 70 analyzed conditions to provide typical results indicating the effect of independent variations of the primary test parameters. Since the data in Figures 41 through 52 correspond to specific test points, it is suggested that they be used only to exemplify trends but not for final wake generalization purposes. Generalized plots based on data from all reduced test conditions will be presented in a later section.

*In some of the photographs showing the time history of the wake (e.g., Figures 27 and 28), a tip vortex cross section appears to be above the blade. This is attributed to the viewing angle of the camera which was placed beneath the rotor plane. Since the blades in these photographs move out of the plane of the smoke, their position is distorted relative to the wake cross sections in that plane.

General Wake Features

Several general features of the tip vortex geometry are evident in Figures 41 through 52. When an element of the tip vortex is shed from a blade, its rate of axial displacement is very low until it passes beneath the following blade (at $\psi_w = 360$ deg/b). At that point, the tip vortex element lies radially inboard of the tip vortex of the following blade and thus experiences a large downward induced velocity from that vortex. The axial transport velocities before and after the passage of the following blade are fairly constant in the near wake, as can be seen from the substantially linear variations of the axial displacement, $\bar{z}_T$, with wake azimuth angle in these regions. The radial displacement, $\bar{r}$, of the tip vortex decays in an apparently exponential manner as the wake azimuth is increased. The fairings of the data in the figures are based on these general wake characteristics.

Effect of Thrust Level (Collective Pitch) for Fixed Number of Blades

The tip vortex coordinates for a two-bladed rotor operating at three thrust levels corresponding to three collective pitch values are shown in Figure 41. Figure 42 shows the coordinates for a six-bladed rotor for a similar variation. The axial displacement and radial contraction of the tip vortex is shown to increase with increasing thrust level. It should be noted that this result differs from the generalized wake model assumed by Rorke and Wells (Reference 8), which was based on limited experimental data.

Effect of Number of Blades at Constant Blade Loading

The effect on tip vortex geometry of varying the number of blades while holding the blade loading (or C_T/σ) constant is shown in Figure 43 for the zero-degree-twist rotor. The rates of axial displacement for the two- and six-bladed rotors are equal up to the azimuth position corresponding to that of the following blade. Beyond this point the tip vortex of the six-bladed rotor, which has a greater total thrust, travels downward at a faster rate. The radial contraction for the six-bladed rotor is also greater than that of the two-bladed rotor. Similar results are shown in Figure 44 for a -8-degree-twist rotor.

Effect of Number of Blades at Constant Disc Loading

The effect on tip vortex geometry of varying the number of blades while holding the rotor disc loading (or C_T) constant is shown in Figure 45. The rate of axial displacement is greater for the two-bladed rotor, which has the greater blade loading, up to the azimuth position corresponding to the following blade. Beyond this point the displacement rates are equivalent. Also, the radial coordinates are equivalent at constant disc loading.

Effect of Blade Twist

To show the independent effect of blade twist rate on tip vortex geometry, the tip vortex coordinates have been plotted in Figure 46 for a two-bladed rotor at a constant thrust level. Although the radial coordinates are independent of twist variations, the axial displacement decreases with increasing twist rate -- particularly between -8 and -16 degrees. Similar results are shown in Figure 47 for a six-bladed rotor.

Effect of Aspect Ratio at Constant Solidity

The effect of aspect ratio on tip vortex geometry is shown in Figure 48, in which the data for six wide-chord blades are compared at a constant thrust level with the data for eight narrow-chord blades having the same solidity ratio. The radial coordinates and the axial displacement rates are approximately equivalent. The axial displacement after the following blade passes is greater for the high-aspect-ratio rotor due to the lesser blade spacing of the eight-bladed rotor.

Effect of Tip Speed

Tip vortex geometry is shown in Figures 49 and 50 to be independent of tip speed. Data for two- and six-bladed rotors are presented for tip speeds of 525, 600, and 700 fps, which, as previously mentioned, correspond to the tip Mach number range of 0.46 to 0.61.

Effect of Ground and Whirl Stand

The effect of the simulated ground and whirl stand on tip vortex geometry is shown in Figures 51 and 52 for two- and six-bladed rotors. For each rotor, the collective pitch setting was held constant, and the ground plane position was changed from the OGE to the IGE position and the whirl-stand model inserted. As shown in these figures, the axial displacement of the tip vortex is not sensitive to the whirl stand and corresponding ground plane position ($Z_G/R = 1.67$). Conflicting results were obtained for the radial coordinates of the two- and six-blade tip vortices. For the two-bladed rotor, the presence of the ground or ground and whirl stand resulted in an expansion of the tip vortex boundary (Figure 51). However, no difference was evident for the six-bladed rotor (Figure 52). It is noted that these IGE results are based on a limited amount of data, and further investigation is recommended. Also, the rotor height above ground for the simulated whirl-stand condition does not correspond to what would be considered a severe ground effect condition (see Figure 26). Investigation of the effect of ground height on wake geometry was beyond the scope of this program.

Generalized Tip Vortex Geometry Results

It has been shown in the preceding section that the tip vortex flow visualization data can be well represented by a series of straight lines for the axial coordinate and by an exponential function for the radial coordinate. The parameters defining these curves were determined for all conditions that were reduced and cross plotted in an attempt to generalize the tip vortex geometry in terms of fundamental rotor parameters. The procedures followed and results obtained are described below. It is recognized that some of the conclusions reached in interpreting these data depend on the manner in which the data are faired. The fairings used represent our interpretation of the data and are believed to be consistent and reasonable, taking into consideration, as they do, all of the data availabe for the different blade designs.

Tip Vortex Axial Coordinate

All axial coordinate data, including those of Figures 41 through 52, have been approximated by the following relations:

$$\bar{z}_T = \begin{cases} k_1 \psi_W & \text{for } 0 \le \psi_W \le \frac{2\pi}{b} \\ (\bar{z}_T)_{\psi_W = \frac{2\pi}{b}} + k_2\left(\psi_W - \frac{2\pi}{b}\right) & \text{for } \psi_W \ge \frac{2\pi}{b} \end{cases} \quad (2)$$

The constants k_1 and k_2 are defined as follows:

$$k_1 \text{ or } k_2 = \frac{\Delta \bar{z}_T}{\Delta \psi_W} = \frac{v_z}{\Omega R} = \tan \phi_W$$

$$\text{for } k_1 : \Delta\psi_W = \frac{2\pi}{b}$$

$$\text{for } k_2 : \Delta\psi_W = \psi_W - \frac{2\pi}{b}$$

k_1 applies prior to the azimuth position of the following blade ($2\pi/b$) and k_2 applies thereafter. It is shown in the above equation that k_1 and k_2 also represent (1) the axial transport velocity of the tip vortex, v_z, nondimensionalized by the rotor tip speed and (2) the tangent of the local pitch angle of the contracted helix (ϕ_W) of the tip vortex. k_1 and k_2 values were determined by linear fairings through the axial coordinate data as previously shown in Figures 41 through 52.

It was indicated in Figures 42 and 43 that for a given blade design, k_1 may be uniquely determined by blade loading (or more precisely, C_T/σ). Thus, the variation of k_1 with the parameter C_T/σ was plotted and is presented in Figure 53. Data for all numbers of blades and tip speeds of the test are included for each of the four blade designs (twist, aspect ratio combinations). The fairings of the data which eliminate differences due to number of blades and tip speed are believed to be justified in light of the experimental accuracy of the flow visualization data. If the repeatability of Δz_T in the k_1 region and for a given test condition is ± 0.015 (see Figure 14), the following accuracy of k_1 results from Equation (2) for rotors of varying numbers of blades:

No. of Blades	Accuracy of k_1
2	± 0.005
4	± 0.010
6	± 0.014
8	± 0.019

Essentially all of the data points in Figure 53 lie within the accuracy range of the faired lines. It is possible that the consistency of the separation of the data for six and eight blades, -8-degree twist, and an aspect ratio of 18.2 from the faired line may be attributable to the use of the plastic tip blades for these rotor configurations. Based on the faired lines, the following is concluded regarding the k_1 wake parameters for the tip vortex:

1. k_1 increases linearly with blade loading (or C_T/σ).
2. At a given C_T/σ, k_1 is independent of tip speed.
3. At a given C_T/σ, k_1 is independent of number of blades - at least within the range of experimental accuracy of this investigation.

4. The rate of k_1 with respect to C_T/σ is independent of blade twist and aspect ratio (slopes of k_1 vs C_T/σ are essentially constant in Figure 53).

5. At a given C_T/σ, k_1 increases with blade twist rate.

6. At a given C_T/σ, k_1 is independent of aspect ratio.

It is noted that conclusions 5 and 6 are qualified by the fact that the variations of the fairings are within the experimental accuracy.

It was indicated in Figure 44 that for a given blade design, k_2 may be uniquely determined by rotor thrust coefficient. Thus, the variation of k_2 with the parameter C_T was determined, and the results are presented in Figures 54 through 57. Data for all numbers of blades and tip speeds of the test are included. Considering the experimental accuracy, it was again possible, for each blade design, to determine a single fairing which eliminates differences due to number of blades and tip speed. It was found that the k_2 data could be faired in direct proportion to the $\sqrt{C_T/2}$. This enables the axial displacement velocity of the tip vortex in the k_2 region to be directly related to the momentum inflow velocity as follows:

$$k_2 = C\sqrt{C_T/2}$$

$$v_z = \Omega R\, k_2 = \Omega R\, C\sqrt{C_T/2} = C v_{z_{MOM.}}$$

The proportionality constant, C, varied from -1.41 to -1.19 with increasing twist (0 to -16 deg), and was not affected by variations in aspect ratio. Based on the faired curves, the following is concluded regarding the k_2 wake parameter for the tip vortex in the stable wake region:

1. k_2 is linearly proportional to $\sqrt{C_T/2}$. This implies that the axial displacement velocity of the tip vortex is linearly proportional to the momentum inflow velocity.

2. For a fixed C_T (or disc loading), k_2 is independent of tip speed and number of blades.

3. The constant of porportionality between k_2 and the $\sqrt{C_T/2}$ (or between v_z and $v_{z_{MOM}}$) decreases with increasing blade twist but is independent of blade aspect ratio, being given by the expression $C = -1.41 - 0.0141\,\theta_1$ (deg).

Tip Vortex Radial Coordinate

It was indicated in Figure 44 that the tip vortex radial coordinate, $\bar{r}$, may be uniquely determined by rotor thrust coefficient. Thus the variation of the radial coordinates with C_T at selected azimuth positions was determined, and the results are presented in Figures 58 through 61. The data symbols in these figures represent the mean of all available data points reduced at a given azimuth for a specific rotor configuration and test condition. Data for all numbers of blades and tip speeds are included, and, again, it was possible to represent the data with faired lines which eliminate differences due to number of blades and tip speed. The faired lines shown for a given azimuth are identical for each blade design, indicating that the radial coordinates are also insensitive to twist and aspect ratio variations at a constant C_T. For a given azimuth, the radial coordinate decreases linearly with increasing C_T. Further analysis of the faired lines shown in Figures 58 through 61 indicated that they could be accurately represented by the following equation:

$$\bar{r} = A + (1-A)e^{-\lambda\psi_w} \qquad (3)$$

provided that the constant A was selected as 0.78 and that the constant λ was determined from the function of rotor thrust coefficient given in Figure 62. The values of A and λ were selected to fit the near wake radial coordinates.

In summary, then, the following is concluded regarding the radial coordinates of the tip vortex in the stable wake region:

1. For a given azimuth, the radial coordinates are linearly proportional to disc loading (or C_T) and decrease with increasing disc loading.

2. For a fixed disc loading (or C_T), the radial coordinates are independent of tip speed, number of blades, blade twist, and aspect ratio.

3. The radial coordinates (near wake) are accurately represented by the equation

   $$\bar{r} = 0.78 + 0.22\,e^{-\lambda\psi_w}$$

   where λ is a function of C_T alone and is given in Figure 62.

Vortex Sheet Axial Coordinates

As discussed in the subsection entitled Flow Visualiation Data, it was convenient to approximate the cross sections of the vortex sheet shed by the inboard portions of the blades as varying linearly with $\bar{r}$. These linear approximations are extended (as in Figure 10) at both ends until they intercept the axis of rotation ($\bar{r}$ = 0) or an imaginary cylinder of radius $\bar{r}$ = 1. The axial coordinates of the intercepts were found to be approximated well by the following equations:

$$(\bar{z}_T)_{\bar{r}=1} = \begin{cases} \left(K_{1_{\bar{r}=1}}\right)\psi_W & \text{for } 0 \leq \psi_W \leq \frac{2\pi}{b} \\ \left(K_{1_{\bar{r}=1}}\right)\frac{2\pi}{b} + \left(K_{2_{\bar{r}=1}}\right)\left(\psi_W - \frac{2\pi}{b}\right) & \text{for } \psi_W \geq \frac{2\pi}{b} \end{cases} \tag{4}$$

$$\bar{z}_{\bar{r}=0} = \begin{cases} 0 & \text{for } 0 \leq \psi_W \leq \frac{\pi}{2} \\ \left(K_{2_{\bar{r}=0}}\right)\left(\psi_W - \frac{\pi}{2}\right) & \text{for } \psi_W \geq \frac{\pi}{2} \end{cases} \tag{5}$$

The fairings through the data shown in Figure 13 are based on these equations. Although better fits to the data for $\bar{r}$ = 0 could be obtained for individual conditions, the parameters used in Equation (5) above appeared to give the best overall fit to the $\bar{r}$ = 0 data for the conditions analyzed. Further refinements were not considered valid in view of the scatter present.

An attempt was made to express the constants appearing in Equations (4) and (5) in terms of more fundamental rotor parameters, as was done for the tip vortex coordinates. Analysis of the results indicated that reasonable correlation of the data with rotor thrust coefficient existed, as shown in Figures 63 through 65. There appeared to be little measurable effect of twist, aspect ratio, tip speed, or numbers of blades on the outboard axial coordinate parameters, $K_{1_{\bar{r}=1.0}}$ and $K_{2_{\bar{r}=1.0}}$ (Figures 63 and 64). However, some effect of twist was noted on the inboard axial coordinate parameter, $K_{2_{\bar{r}=0}}$, as shown in Figure 65. Although scatter is present, the data of Figure 65 show a reasonably consistent trend of increasing $K_{2_{\bar{r}=0}}$ with increasing twist. This means that the axial velocities of the air through the inner portion of the rotor increase with twist. This appears to be reasonable since twist is used to increase the loading and, hence, the circulation of the inboard blade sections.

With the axial locations of the inboard sheet cross sections established (from Figures 63 through 65) together with the radial coordinates of the tip vortex (from Figures 58 through 62 or Equation (3)), the radial coordinates of the inboard vortex filaments can be computed using Equation (1). This equation essentially assumes that the contraction of the inboard vortex filaments (as measured along the sheet cross section) is determined by the degree of contraction of the tip vortex at the axial location where the inboard sheet extension intersects the tip vortex trajectory.

Generalized Wake Equations

The generalized wake equations (applicable in the stable wake region) are summarized below.

1. Tip Vortex Axial Coordinates:

$$\bar{z}_T = \begin{cases} k_1 \psi_W & \text{for } 0 \le \psi_W \le \frac{2\pi}{b} \\ (\bar{z}_T)_{\psi_W = \frac{2\pi}{b}} + k_2 \left(\psi_W - \frac{2\pi}{b}\right) & \text{for } \psi_W \ge \frac{2\pi}{b} \end{cases}$$

$$k_1 = -0.25 \left(C_T/\sigma + 0.001\, \theta_{1_{deg}}\right)$$

$$k_2 = -\left(1.41 + 0.0141\, \theta_{1_{deg}}\right) \sqrt{C_T/2}$$

$$\sim -\left(1 + 0.01\, \theta_{1_{deg}}\right) \sqrt{C_T}$$

2. Tip Vortex Radial Coordinates:

$$\bar{r} = A + (1 - A) e^{-\lambda \psi_W}$$

$$A = 0.78 \quad \text{(near wake)}$$

$$\lambda = 0.145 + 27\, C_T$$

3. Vortex Sheet Axial Coordinates:

$$(\bar{z}_T)_{\bar{r}=1} = \begin{cases} K_{1_{\bar{r}=1}} \psi_W & \text{for } 0 \le \psi_W \le \frac{2\pi}{b} \\ \left(K_{1_{\bar{r}=1}}\right) \frac{2\pi}{b} + \left(K_{2_{\bar{r}=1}}\right)\left(\psi_W - \frac{2\pi}{b}\right) & \text{for } \psi_W \ge \frac{2\pi}{b} \end{cases}$$

$$K_{1_{\bar{r}=1}} = -2.2 \sqrt{C_T/2}$$

$$K_{2_{\bar{r}=1}} = -2.7 \sqrt{C_T/2}$$

$$\bar{z}_{\bar{r}=0} = \begin{cases} 0 & \text{for } 0 \le \psi_W \le \frac{\pi}{2} \\ \left(K_{2_{\bar{r}=0}}\right)\left(\psi_W - \frac{\pi}{2}\right) & \text{for } \psi_W \ge \frac{\pi}{2} \end{cases}$$

$$K_{2_{\bar{r}=0}} = \left[\frac{\theta_{1_{deg}}}{128}\left(0.45\,\theta_{1_{deg}} + 18\right)\right]\sqrt{C_T/2}$$

4. Vortex Sheet Radial Coordinates:

(see Equation (1))

It is recognized that some of the above equations and constants for the wake parameters depend on the manner in which the data is faired. The fairings used represent our interpretation of the data and are believed to be consistent and reasonable, taking into consideration, as they do, all of the data available for the different blade designs. However, it will be shown that the analytical rotor performance results are very sensitive to wake geometry. In view of this sensitivity, small systematic refinements to the fairings and thus the above wake constants may be required if consistently accurate performance predictions are to be achieved.

COMPARISONS OF TIP VORTEX GEOMETRY WITH OTHER SOURCES

The model rotor tip vortex geometry was compared with available data from other sources to investigate the consistency between data obtained on different rotors, on different test stands, and by different personnel. The available data was found to be quite limited in that no one had previously conducted a test program such as the one described herein, in which wake geometry was obtained from systematic variations of the blade design and operating parameters.

One of the most important considerations concerning model rotor wake geometry is whether it agrees with that of full-scale rotors. Tip vortex geometry obtained from the model rotor test was compared with limited full-scale CH-53A data measured on the Sikorsky whirl stand as presented by Clark and Leiper in Reference 9. A comparison of the model and full-scale tip vortex coordinates is shown in Figure 66. The model coordinates were obtained by extrapolating the generalized model rotor wake to a thrust coefficient of 0.01. These coordinates are in good agreement with the full-scale tip vortex coordinates. If this correlation is representative, it may be concluded that the generalized wake determined from model testing is applicable to full-scale rotors. However, since it will

THEORETICAL METHODS FOR PREDICTING HOVER PERFORMANCE

A principal objective of this investigation was to evaluate the accuracy of certain theoretical methods, including several developed at UARL, for predicting rotor hover performance -- particularly as affected by assumptions made regarding rotor wake geometry. The methods considered in this study are listed below.

1. Blade Element - Momentum Analysis
2. Goldstein-Lock Analysis
3. Prescribed Classical Wake Analysis
4. Prescribed Experimental Wake Analysis
5. Prescribed Theoretical Wake Analysis

Each method is described below with emphasis placed on the last three, inasmuch as the first two methods have been in widespread use for many years.

BLADE ELEMENT - MOMENTUM ANALYSIS

As described briefly in Reference 1, this analysis is based on the assumption that the lift acting on an annulus of the rotor disc is equal to the change in momentum of the air passing through that annulus. Each annulus or, equivalently, each blade section is assumed to operate independently of all other sections. The relations developed can be shown (Heyson, Reference 15) to be equivalent to those obtained using vortex theory in which the rotor is modeled by an infinite number of blades and the vorticity deposited in the wake of the rotor forms a continuous cylindrical vortex sheet having a diameter equal to the rotor diameter. The equations relating local blade thrust and local induced velocity at the disc are solved iteratively on a digital computer using appropriate two-dimensional airfoil data to account for any stall or compressibility effects that may be present. Losses due to flow around the tips of the blades are accounted for by specifying a "tip loss factor", which assumes complete loss of lift over a small, arbitrary percentage of the blade tip region. As used herein, the parameters specified as input to the analysis were rotor radius, solidity, tip speed, blade twist, collective pitch, blade coning angle, air density, speed of sound, airfoil c_ℓ and c_d data, and tip loss factor (0.97).

THEORETICAL METHODS FOR PREDICTING HOVER PERFORMANCE

A principal objective of this investigation was to evaluate the accuracy of certain theoretical methods, including several developed at UARL, for predicting rotor hover performance -- particularly as affected by assumptions made regarding rotor wake geometry. The methods considered in this study are listed below.

1. Blade Element - Momentum Analysis
2. Goldstein-Lock Analysis
3. Prescribed Classical Wake Analysis
4. Prescribed Experimental Wake Analysis
5. Prescribed Theoretical Wake Analysis

Each method is described below with emphasis placed on the last three, inasmuch as the first two methods have been in widespread use for many years.

BLADE ELEMENT - MOMENTUM ANALYSIS

As described briefly in Reference 1, this analysis is based on the assumption that the lift acting on an annulus of the rotor disc is equal to the change in momentum of the air passing through that annulus. Each annulus or, equivalently, each blade section is assumed to operate independently of all other sections. The relations developed can be shown (Heyson, Reference 15) to be equivalent to those obtained using vortex theory in which the rotor is modeled by an infinite number of blades and the vorticity deposited in the wake of the rotor forms a continuous cylindrical vortex sheet having a diameter equal to the rotor diameter. The equations relating local blade thrust and local induced velocity at the disc are solved iteratively on a digital computer using appropriate two-dimensional airfoil data to account for any stall or compressibility effects that may be present. Losses due to flow around the tips of the blades are accounted for by specifying a "tip loss factor", which assumes complete loss of lift over a small, arbitrary percentage of the blade tip region. As used herein, the parameters specified as input to the analysis were rotor radius, solidity, tip speed, blade twist, collective pitch, blade coning angle, air density, speed of sound, airfoil c_l and c_d data, and tip loss factor (0.97).

In summary, the Blade Element - Momentum Analysis neglects effects due to the finite number of blades as well as those related to wake contraction.

GOLDSTEIN-LOCK ANALYSIS

This analysis is effectively the rotary-wing equivalent of the classical lifting-line analysis used successfully for fixed wings. The analysis is based principally on the work of Goldstein (Reference 16), who obtained a solution for the velocity potential for the flow about an axially translating, doubly-infinite, rigid helicoidal surface. This surface was shown by Betz (Reference 17) to represent the minimum energy wake of a propeller (or rotor) having a finite number of blades. By satisfying the flow boundary conditions on the helical surfaces representing the wake, the optimum (or Goldstein) distribution of circulation in the wake was obtained. Goldstein's results were applied by Lock (Reference 18), who showed how the results could be used to design a propeller. This was accomplished by assuming the propeller to be lightly loaded so that the wake was essentially uncontracted, in which case the circulation distribution in the wake can be related directly to the circulation distribution on the blade. Through this assumption and the use of the Goldstein velocity potential to define the induced velocities at the plane of the propeller, the blade twist and chord distributions necessary to produce the Goldstein (optimum) circulation can be determined. Lock also postulated techniques for handling the inverse problem, wherein the blade geometry is defined and the circulation distribution and the associated propeller performance are required. This situation arises, for example, when one designs an optimum propeller for operation at a specified design condition and then wishes to know the performance of this propeller at off-design operating conditions. In his approach, Lock assumed that the circulation at each blade section was part of a Goldstein optimum circulation distribution but allowed the optimum distribution associated with each section to be different. This implies a different wake pitch angle variation with radius than would be the case for a blade whose local circulation values formed part of the <u>same</u> optimum distribution. The resulting wake structure is, therefore, technically inconsistent with the optimum wake assumptions made by Goldstein; however, reasonable answers are expected for conditions where large departures from the Goldstein optimum circulation distribution are not involved. Numerical implementation of the Goldstein-Lock method, which involves an iteration at each blade section between the local circulation and local wake pitch angle, was accomplished using an existing computer program provided by the Sikorsky Division.

In summary, the Goldstein-Lock Analysis accounts for the finite number of blades on a rotor (thereby eliminating the need for fictitious tip loss factors) but still retains the assumptions that the blades are lifting lines and that the wake is uncontracted (light loading).

UARL PRESCRIBED WAKE HOVER PERFORMANCE PROGRAM

The next three analyses to be discussed all employ the UARL Prescribed Wake Hover Performance Program (or briefly, the Prescribed Wake Program) for the solution of the blade circulation and inflow distribution and the corresponding integrated rotor performance. Complete generality (within the framework of the assumptions to be mentioned) regarding the specification of the geometry of the wake was maintained in the computer program. This generality permits the evaluation of a wide variety of wake geometries such as a classical uncontracted wake geometry (hereafter referred to as the classical wake), a realistic model of the experimental wake, and a theoretically defined wake. The incorporation of these three wake models in the Prescribed Wake Program results in the analyses listed below:

1. Prescribed Classical Wake Analysis
2. Prescribed Experimental Wake Analysis
3. Prescribed Theoretical Wake Analysis

These analyses are identical except for the representation of the wake. A description of the wake model used in each will be presented in the following sections. Other than assumptions regarding wake shape, the following are the major assumptions that currently exist in the Prescribed Wake Program:

1. Each blade is represented by a lifting line (bound vortex) divided into a finite number of segments (blade segments), each having a different circulation strength. The aerodynamic characteristics determined at the centers of each segment are assumed to be representative of the entire segment.

2. The wake is represented by a finite number of vortex filaments trailing from the blade segment boundaries. Each filament is divided into straight segments, the lengths of which are determined by a specified wake azimuth interval, $\Delta\psi_w$. The circulation strength of each trailing vortex filament is constant along its length and is equivalent to the difference

between the circulation values of its adjacent bound vortex segments in accordance with Helmholtz laws of conservation of vorticity.

3. The blade and wake characteristics are assumed to be independent of azimuth position.

4. The airflow at the blades is assumed to be two-dimensional (radial induced velocity components are neglected). For the rotor performance calculations, tabulated two-dimensional airfoil data (c_ℓ, c_d, α) are provided which include compressibility effects (Mach number variations). For the circulation calculations, a set of lift curve slopes and stall angles of attack are provided which vary with Mach number.

5. Tangential induced velocity components are neglected.

6. Small-angle assumptions are included for the inflow angles in the circulation solution.

7. Following the blade circulation and inflow solution, conventional strip theory is assumed applicable to compute the rotor performance characteristics.

The method differs from that developed by Rorke and Wells (Reference 8) in that the blade inflow distribution is determined completely by the induced effects of the wake (by application of the Biot-Savart law) as opposed to introducing approximate momentum considerations. A flow diagram showing the required input, sequence of major operations, and output of the program is presented in Figure 71. As indicated in this figure, the program is divided into three independent parts. The first transforms the wake geometry input to wake coordinates. The second contains the computation of the wake influence coefficients at the blade, as defined by the Biot-Savart law, and the numerical procedures for solving the circulation matrix and associated induced velocity distribution. In the third part, performance characteristics are computed. A provision for automatic plotting of the wake filaments is included. Sample computer plots are shown in Figure 72 for a typical experimental wake and a classical wake model. In the Prescribed Theoretical Wake Analysis, the theoretical wake geomety is determined from a seperate program (Wake Geometry Program) and is used as input to the Prescribed Wake Program. The computer time required by the Prescribed Wake Program normally varies from approximately 15 seconds to 2 minutes (UNIVAC 1108 computer) depending on the number of blades, number of wake elements, and number of internal iterations required.

For all applications reported herein, the blade-wake model in the Prescribed Wake Program was represented as follows:

Number of blade segments	15
Number of wake filaments per blade	16
Number of wake revolutions	11
Wake azimuth increment	30 deg

The 15 blade segments were distributed such that 10 were spaced at 0.02 R intervals over the outer 20% of the blade span. Wake revolutions beyond the eleventh were found to have a negligible effect on rotor performance.

PRESCRIBED CLASSICAL WAKE ANALYSIS

This analysis is, in many respects, similar to the Goldstein-Lock Analysis described above in that a finite number of blades is assumed, each blade is represented by a lifting line, and an uncontracted wake geometry is prescribed. The primary differences in the analyses are as follows:

1. The helical sheets of vorticity representing the blade wakes are approximated by a finite number of discrete trailing vortex filaments to facilitate numerical solution (on a computer) of basically the same equations which, for the optimum case, Goldstein solved analytically. The availability of a numerical solution also permits a more direct solution of the inverse problem wherein the geometry of the rotor is specified as opposed to the circulation distribution.

2. The wake geometry assumed in this version of the analysis differs from that for the Goldstein optimum wake in that the axial transport velocity of each vortex element in the wake is constant with radius and is equal to the momentum value. Tangential transport velocities are assumed to be zero. For the low helical wake pitch angles associated with helicopter rotor disc loadings, the outer portion of the wake used approximates the Goldstein wake.

A sample plot of the classical wake trajectory was presented in Figure 72.

The operating conditions for which rotor performance was computed using the Prescribed Classical Wake Analysis are listed in Table III.

TABLE III. PRESCRIBED CLASSICAL WAKE CONDITIONS

Rotor	Twist (deg)	Aspect Ratio	No. of Blades	Tip Speed (fps)	Collective Pitch (deg)
Model	-8	18.2	2	700	6,8,10
Model	-8	18.2	4	700	6,8,10
Model	-8	18.2	6	700	6,8,10
Model	-8	18.2	8	700	8,10
Model	-8	18.2	2	525	6,8,10
Model	-8	18.2	6	525	6,8,10
Model	0	18.2	2	700	6,8,10
Model	0	18.2	4	700	6,8,10
Model	0	18.2	6	700	6,8,10,11
Model	0	18.2	8	700	8,10
Model	-16	18.2	2	700	6,8,10
Model	-16	18.2	6	700	6,8,10
Model	-8	13.6	2	700	6,8,10
Model	-8	13.6	6	700	6,8,10
[illegible]-1A	-1[illegible]	17.[illegible]	2	713	7,9,11
CH-53A	-6	16.7	6	698	8,10,12

All conditions investigated correspond to OGE operation.

PRESCRIBED EXPERIMENTAL WAKE ANALYSIS

This analysis differs from the previous analyses in that a more realistic, contracted wake geometry based on experimental flow visualization data is used as input to the Prescribed Wake Program. Rather than input coordinates for each vortex element in the wake, Equations (1) through (5) are used to define the wake and the individual coordinates are computed in the program. In this manner it is only necessary to input the following wake constants and certain wake azimuth angles:

$$A, \lambda, k_1, k_2, K_{1_{\bar{r}=0}}, K_{2_{\bar{r}=0}}, K_{1_{\bar{r}=1}}, K_{2_{\bar{r}=1}}$$

The required wake azimuth angles are simply the junction angles that bound the k_1 and k_2 regions. Use of the wake equations and the above constants greatly simplifies the input requirements while retaining sufficient accuracy for the computation of induced velocities at the rotor blades.

Figure 72 indicates how the computer transforms the input wake constants to coordinate form and plots the resulting wake pattern. On the left side of this figure are the top and side views of the computer representation of a typical experimental wake. For clarity, only the wakes from 1 blade and 12 vortex filaments are shown. For this test condition, 5 of the 16 vortex filaments over the outer 8% of the blade were used to represent the tip vortex. The spanwise division between the vortex sheet and tip vortex regions is determined by the requirement that the vortex filaments grouped in the tip vortex have the same circulation sense and one which is consistent with a negative derivative of the final computed bound circulation distribution ($-d\Gamma/d\bar{r}$) over the tip region of the blade. This results in the radial location of the peak bound circulation as the dividing point between the inboard sheet and tip vortex portions of the wake. An iteration is built into the computer program to insure this consistency. A program refinement, included under this contract, was an improvement of the wake geometry representation through incorporation of a provision for approximating the roll-up of the tip vortex filaments into a single filament. This was accomplished by truncating the inner tip vortex filaments at an input azimuth (30 degrees was used in this investigation) and assigning the experimental tip vortex geometry and the combined circulation strength to the remaining filament (Figure 72). In addition, an improved representation of the vortex sheet was included which allows the vortex sheet to extend to the tip vortex boundary. Finally, a provision was included for inputting tip vortex coordinates rather than using the curve fit equations, if such a mode of operation is desired. The far wake model was assumed to be a smoothly contracting extension of the near wake as shown in Figure 72. The inclusion of provisions accounting for the instability of the far wake observed in this investigation was beyond the scope of this study. The exact nature of this instability, and whether the unstable region is sufficiently removed from the rotor so as not to affect rotor performance remains to be investigated.

The operating conditions for which rotor performance was computed using the Prescribed Experimental Wake Analysis are listed below.

TABLE IV. PRESCRIBED EXPERIMENTAL WAKE CONDITIONS

Rotor	Twist (deg)	Aspect Ratio	No. of Blades	Tip Speed (fps)	Collective Pitch (deg)
Model	-8	18.2	2	700	6,8,10
Model	-8	18.2	6	700	6,8,10
Model	-8	18.2	2	525	6,8,10
Model	-8	18.2	6	525	6,8,10
Model	0	18.2	2	700	8,10
Model	0	18.2	6	700	8,10
Model	-8	13.6	2	700	8,10
HU-1A	-12	17.3	2	713	7,9,11
CH-53A	-6	16.7	6	698	8,10,12

All conditions investigated correspond to OGE operation.

PRESCRIBED THEORETICAL WAKE ANALYSIS

General Approach

The final performance method evaluated was the so-called Prescribed Theoretical Wake Analysis. In this method the wake is again prescribed as input to the Prescribed Wake Program in order to compute the blade and wake circulation distributions and the associated integrated rotor performance. In this instance, however, the input wake geometry is determined principally from theoretical considerations rather than from experiment. Conceptually, the computation of the theoretical wake geometry can be accomplished by the following steps:

1. Estimate the vorticity (circulation strength) in the wake from a previous solution of the bound circulation distribution on the blade.

2. Specify an initial wake geometry.

3. Apply the classical Biot-Savart relation to compute the velocities induced in the wake by the wake vorticity.

4. Integrate these velocities over a small increment in time to define a new wake geometry.

5. Repeat Steps 3 and 4, alternately, until a converged wake geometry corresponding to the initial estimate of blade bound circulation is obtained.

6. Compute a new estimate of the blade bound circulation distribution using the Prescribed Wake Program and the wake geometry from Step 5.

7. Repeat Steps 2 through 6, iterating until a compatible geometry-circulation solution is obtained.

The process just described is illustrated schematically in Figure 73. In the top half of this figure, the fundamental iteration between the blade circulation and wake geometry is indicated, while the lower half of the figure indicates the second iteration required to obtain a geometry consistent with the current estimate of the blade circulations. A computer program termed the Wake Geometry Program has been developed to perform this second iteration. Iterations of the type described are necessary because the complexity of the rotor wake geometry precludes a closed-form solution to the problem.

Although the process described above is conceptually straightforward, its actual numerical implementation represents a formidable task, even with modern computers, because of the great number of vortex elements that conceivably could be used to represent the wake. Approximations are, therefore, necessary to limit computing time requirements. The following sections describe the procedures and approximations employed in this study.

Before proceeding to the detailed discussion of the procedures and approximations used, a few general remarks are in order regarding the computer program developed. The core program available for this study was basically one which was capable of computing wake geometries for forward flight conditions (see Reference 2). As a result, the program is not optimized for the hover condition and thus, for example, the symmetry features of the hover flight condition are not included. Incorporation of such features could significantly reduce computing time. Also, initial attempts to apply the program in hover disclosed an apparent instability of the wake at moderate distances from the rotor. This instability appeared to conflict with the more or less classical conception of the hovering rotor wake as being a stable, smoothly contracting wake. Considerable effort was expended in investigating the possibility that the apparent instability was a result of the numerical procedures used; in the process, several modes of operation of the program were developed before a conclusion was reached that the physical wake is apparently unstable. The different operating modes allow the user to check various assumptions made in the computation of the wake geometry. The resulting computer program should, therefore, be considered a research program rather than one which is optimized for maximum efficiency in production use.

Numerical Procedures and Approximations

The procedures and approximations employed in developing a numerical method for computing rotor wake geometries for hovering flight are described below. The reader is also referred to Reference 2 for more background material.

Discrete Vortex Representation

The continuous helical sheets of vorticity trailed by the various blades of the rotor are represented by a finite number of discrete trailing vortex filaments. This approach is fairly standard, being used by Westwater in Reference 19, for example, to compute the geometry of fixed-wing wakes. Figure 74 shows a schematic representation of a continuous sheet wake from one blade and the approximation to this sheet made using discrete filaments. Because of the nature of rotor blade bound circulation distributions, the discrete vortices naturally group into two parts: a strong, rolled-up tip vortex filament and several weaker filaments representing the inboard portion of the vortex sheet. In addition, it is evident from Figure 74 that the discrete vortices are each represented by a series of straight-line segments rather than by continuous curves. The length of the segments is determined by the time increment used in the integration of the distorting velocities acting on the filaments and the magnitude of the distorting velocities themselves. Each discrete vortex was assumed to have a finite core radius equal to 0.005 R. Velocities within the core were arbitrarily set to zero. More elaborate representation of the velocities within the core are available (e.g., Reference 20) but were not used herein in view of other, more important assumptions made in this analysis.

Far Wake Representation

Theoretically, the helical wake under the rotor extends downstream to infinity. As indicated previously, the basic computer program available for this study was a forward-flight program. In this program the wake is truncated after a specified number of revolutions as indicated in Figure 75 (for a hover condition). Initial attempts to compute the distortions of such a truncated wake in hover showed that it quickly tended to roll up as shown in Figure 75. In Figure 75(a), the truncated wake at the start of the computation is shown; while in Figure 75(b), the early stages of roll-up are evident after 12 time steps. This phenomenon is similar to that observed in Reference 21, where distortions of a wake represented by a finite number of vortex rings were computed. The roll-up observed is reasonable inasmuch as symmetry considerations dictate that the self-induced radial velocities acting on the truncated helical vortex must be antisymmetric about the midpoint of the helix. In an attempt to avoid this problem (which was considered to be a fictitious problem caused only by the wake truncation feature) and at the same time keep computing times low, a modification to the basic program was made wherein the overall wake was divided into near- and far-wake regions as shown in Figure 76. The near wake is allowed to distort freely under the influence of the wake-induced velocities. The far wake, however, was artifically constrained so that its diameter D_F, was at each time step set equal to twice the radius of the last vortex element in the immediately preceding near wake. The axial spacing was set equal to the last revolution of the initial wake (which for these calculations was based on experimental data). As will be discussed below, the partially constrained far wake moves away from the rotor as the computation proceeds, so that its influence continuously diminishes.

Numerical Integration

The numerical computation of the distorted wake geometry involves two basic steps: (1) the use of the Biot-Savart Law to compute the wake distortion velocities (v_{x_P}, v_{y_P}, v_{z_P}) produced by a given wake geometry and vorticity at any point (P) joining the straight-line vortex elements (see Figure 77), and (2) the integration of these velocities over a small time increment (or time step) to establish a new wake geometry. These basic steps are successively repeated until there is no change in the computed wake geometry. The expressions used to compute and integrate these velocities are given in Appendix I. As the wake distorts during the time increment, the blades are allowed to rotate to new positions. This rotation leads to the generation of new near-wake elements. As a result, the number of near-wake elements continually builds up while the partially constrained far wake moves axially away from the rotor. The process will be illustrated by a specific example in a later section. Other modes of operation are possible with the program but were not evaluated in this contract. These will be described in the report documenting the program itself.

Further Inboard Wake Approximations

As noted above, the inboard sheet has been approximated by a series of discrete, segmented vortex filaments. If one were to consider computing the contribution of each vortex element in the wake to the velocities acting on all other elements in the wake, one would find that the computing time quickly gets out of hand. Significant reductions in computing time can be accomplished by (1) eliminating elements in the wake, (2) avoiding the computation of the distorting velocities induced by certain elements at each and every time step, or (3) avoiding altogether the computation of the distorting velocities induced by certain elements on other elements. A combination of all three approaches was used in this study (although it should be noted that the program has optional modes of operation which will allow a complete interaction computation if one so desires). Thus, the far wake was truncated after N_F revolutions. Also, advantage was taken of the fact that the circulation strength of each inboard vortex filament is significantly less than that of the tip vortex. The distorting velocities induced by the inboard elements on the tip vortex are, therefore, generally small compared to those induced by the tip vortex itself. Rather than neglect the inboard wake completely in the wake geometry computation as was done in Reference 2, it was decided to (1) specify a representative inboard wake-tip vortex geometry, (2) compute the velocities induced along the tip vortex by the inboard wake for this geometry at the initial time step, and (3) keep these velocities constant for all succeeding time steps during which the tip vortex distorts under both its own variable influence, which varies with time, and that of the inboard wake, which is constant with time. The representative wake geometry used to compute the inboard wake effect on the tip vortex was estimated for each operating condition from the experimental wake data given in Figures 53 through 65. A typical geometry is shown in Figure 78. As shown in this figure, the outer boundary of the inboard wake was terminated at a distance about 0.04 R from the tip vortex trajectory, except in the immediate vicinity of the blade, where, of course, the radial location was determined from the nature of the bound circulation distribution. The resulting boundary appeared reasonable when compared with smoke picture observations and considering that the local trajectory of a vortex element should be dominated by the rotational velocity induced by the nearest element of the tip vortex. Finally, specification of the inboard sheet geometry eliminated the necessity of computing the effect of the tip vortex on the inboard sheet. By incorporating these approximations, the computing times required were reduced by about an order of magnitude to about $\frac{1}{2}$ minute per time step for a typical two-bladed rotor case and $2\frac{1}{2}$ minutes per time step for a typical six-bladed rotor case (UNIVAC 1108 Computer).

Bound Vortex Effect

The velocities induced on the tip vortex by the blade bound vorticity were neglected. This eliminated an artificial numerical problem resulting from the representation of the blade as a lifting line and from the computation of velocities at discrete points in the wake. As a result, unrealistically large fluctuations in induced velocity occurred as the bound vortex passed over points on the tip vortex generated by the previous blade. Removal of these basic restrictions to the program was beyond the scope of this study. Because the generally antisymmetric nature of the velocities induced by the bound vortex and their rapid decay with increasing distance from the bound vortex, it is believed that the neglect of these velocities should have little effect on the computed average position of the tip vortex.

Operating Conditions and Program Parameters Selected

The operating conditions for which rotor wake geometries and associated performance characteristics were computed using the Prescribed Theoretical Wake Analysis are given below.

TABLE V. PRESCRIBED THEORETICAL WAKE CONDITIONS

Rotor	Aspect Ratio	Twist (deg)	No. of Blades	Tip Speed (fps)	Collective Pitch (deg)
Model	18.2	-8	2	700	6,8,10
Model	18.2	-8	2	525	8,10
Model	18.2	0	2	700	8,10
Model	13.6	-8	2	700	8,10
Model	18.2	-8	6	700	8
HU-1A	17.3	-12	2	713	9
CH-53A	16.7	-6	6	698	10

All conditions investigated correspond to OGE operation.

In computing the wake geometries and rotor performance for the conditions described above, the following parameters were selected as input to the Wake Geometry Program (input to the Prescribed Wake Program was the same as that described in the section entitled "UARL PRESCRIBED WAKE HOVER PERFORMANCE PROGRAM").

1.	Number of inboard wake filaments	4 to 5 (as required)
2.	Initial number of near wake revolutions (tip vortex)	3/blade for b = 2 2/blade for b = 6
3.	Far-wake revolutions (tip vortex)	8/blade for b = 2, 3/blade for b = 6
4.	Number of time steps used in integration	49 for b = 2, 29 for b = 6,
5.	Nondimensional time interval used in integration, $\Delta\psi = \Omega\Delta t$	0.524 (30 deg) for b = 2, 0.349 (20 deg) for b = 6
6.	Number of inboard wake revolutions	4 for b = 2, 3 for b = 6
7.	Initial wake geometry	estimated from Figures 53 through 65.

Although the number of filaments per blade in the initial wake was less for the six-bladed rotor because of program storage limitations, the total number of filaments in the wake for the two- and six-bladed rotors were comparable.

Wake Stability Characteristics

Evidence of Wake Instability

Initial results for the two-bladed model rotor obtained from the Wake Geometry Program (as modified for this study) disclosed an apparent instability of the helical tip vortex. This instability, which occurred at axial distances from the rotor plane as low as 0.15 R, is illustrated in Figure 79. Here the computed axial and radial coordinates of the tip vortex for several different time steps in the calculation are presented. At the start of the computation (extreme left-hand panel of Figure 79), the wake is assumed to smoothly contract and to be composed of the near- and far-wake regions described previously. That portion of the near wake in the immediate vicinity of the rotor plane was obtained from the generalized experimental results of Figures 53 through 65. The remainder of the initial wake was obtained through extrapolation in a manner consistent with the classical conception of a smoothly contracting rotor wake in hover. As the calculation of the geometry proceeds (i.e., as the number of time steps increases), the rotor rotates, new near-wake vortex elements are created, the far wake moves downstream, and the near wake distorts under both its own influence and that of the far wake. The remaining panels of Figure 79 illustrate the process by showing the wake as computed after 6, 12, 18, and 24 time steps. (For the nondimensional time used in this computation, 0.524, 12 time steps correspond to one revolution of the rotor.) The circles shown on the wake boundary represent the intercepts of the helical tip vortices of both blades with the $\bar{r}$ - $\bar{z}$ plane containing one of the blades as a reference. These circles would mark the positions of the vortices that would be observed in photographs taken in a flow visualization experiment (such as conducted under this contract) where smoke was introduced into the rotor flow field in the nonrotating system. It is evident from Figure 79 that the wake becomes unstable at some distance below the rotor.

In view of the importance of the conclusion regarding the stability of the rotor wake, additional checks on the numerical procedures being used were made. In addition, available literature and data were reviewed in an attempt to obtain supporting evidence. The numerical checks included the use of different nondimensional time intervals and other numerical integration techniques such as the Runge-Kutta method. All results obtained were qualitatively the same.

The review of the literature disclosed an analysis by Levy and Forsdyke (Reference 22) which indicated that a doubly-infinite, constant-diameter, helical vortex can be unstable when the pitch angle of the helix is less than 0.3 radian. Helix pitch angles for helicopter hover conditions lie in this critical range. Although the actual rotor wake in hover is a contracting wake, it is believed that the results from Reference 22 imply the possibility of a potential stability problem. Comparison of the unstable wake results obtained herein with results of other analyses in which attempts were made to compute the geometry of rotor wakes in hover was generally inconclusive because of differing assumptions and numerical techniques employed. For example, interpretation of the results of Reference 21 (where vortex rings are used and the equations are integrated as in this study) are complicated by the general roll-up problem of a truncated wake noted earlier. However, a lack of convergence of certain areas of the wake was noted. In Reference 9, an analysis employing helical vortex filaments but a fundamentally different numerical computation scheme is described. Also, only two fully distorting revolutions of the wake are considered together with a partially constrained far wake. Qualitative convergence tests are employed, and no mention of any observed wake instability is made in connection with the limited results presented. In spite of apparent differences regarding wake stability, results of Reference 9 appear to agree well with results obtained in this study for the region of the wake near the rotor plane. This will be discussed further in a subsequent section.

Experimental flow visualization data reviewed included that from References 1, 10, and 12, as well as data obtained under this contract. The review led to the following observations:

1. The critical area of the wake where the instability was predicted was generally poorly defined.

2. In a large number of cases, evidence of a rolling of successive coils of the helical tip vortexes around one another (local roll-up) could be found. In those experiments where smoke was injected into the nonrotating system, such as the present study, this roll-up was inferred from an uneven axial spacing of the tip vortexes and, more importantly, from the fact that downstream vortexes had radial coordinates greater than those for upstream vortexes.

3. Shortly after evidence of roll-up of the experimental wake was noted, further tracking or observation of the tip vortexes became exceedingly difficult. Thus, the roll-up may be the cause of the poorly defined wake noted in Item 1 above.

4. In no case was a smoothly contracting tip vortex observed over large enough axial distances below the rotor as to definitely preclude the possibility of an instability.

These observations are substantiated by the sample photographs presented previously (Figure 30) and the additional photographs presented in Figures 80 through 82. A schematic interpretation of these photographs showing local roll-up of the tip vortex is shown in Figure 83. In summary, then, the prediction of an unstable wake does not appear to be inconsistent with available evidence; further work should, however, be undertaken to define the characteristics of experimental wakes in more detail in the critical areas. Standard flow visualization techniques appear to be of marginal usefulness of this purpose, and hot-wire and/or holographic approaches should be considered.

Implications of Instability on Procedures Employed

The existence of a wake instability obviously complicates both the computation of wake geometries and the use of these geometries in the subsequent computation of rotor performance. Some modification of anticipated procedures was necessitated and those procedures that were used are described in the following paragraphs.

Close examination of the geometry results obtained indicated that although the computed wake did become unstable at moderate distances from the rotor, the portion of the wake in the immediate vicinity of the rotor plane (extreme near-wake) did converge to a reasonably stable answer, with the degree of convergence improving with increasing proximity to the rotor. This presumably is due to the fact that one end of the wake is perfectly stable, being tied as it is to the blade itself. The convergence of the extreme near-wake, which was also observed in the study of Reference 21, is illustrated in the sample results presented in Figures 84 and 85. In Figure 84, the time histories of the radial and axial coordinates for two critical points in the wake of a two-bladed rotor are shown. These are the points of the wake lying immediately below the blade (ψ_w = 180 deg and 360 deg). In Figure 85, on the other hand, the computed radial and axial coordinates at two different time steps are presented as a function of wake azimuth position. Experimental results are also shown in Figure 85 for reference purposes. Convergence of the extreme near-wake to a stable solution is apparent. Also, results such as these led to the selection of 49 time steps in the wake geometry integration as being adequate for all two-bladed rotor computations. This corresponds to a computation of the wake for a time period corresponding to four rotor revolutions or eight blade passage cycles. For the six-bladed rotor, only 29 time steps (i.e., 1.61 rotor revolutions, 9.66 blade passage cycles) were used because of machine storage limitations. It was also necessary to reduce the time interval to 0.349 (20 deg) to avoid a mathematical instability. In spite of the lower number of time steps, reasonable near-wake convergence was obtained.

In using the predicted tip vortex geometries to compute new blade circulation distributions by means of the Prescribed Wake Program, the converged near-wake results were in most instances approximated by the same analytic expressions (Equations [illegible] and [illegible]) used in analyzing the experimental wake data; namely,

$$\bar{z}_T = \begin{cases} k_1 \psi_w & \text{for } 0 \le \psi_w \le \frac{2\pi}{b} \\ k_1 \frac{2\pi}{b} + k_2\left(\psi_w - \frac{2\pi}{b}\right) & \text{for } \psi_w \ge \frac{2\pi}{b} \end{cases}$$

$$\bar{r} = A + (1-A)e^{-\lambda\psi_w}$$

Constants in the expressions were determined by emphasizing correct positioning of the vortices in the immediate vicinity of the blade (i.e., at ψ_w = 180 deg and 360 deg for a two-bladed rotor). In an isolated case, where the above analytical expressions did not appear to represent a good fit to the computed geometry, the actual computed $\bar{r}$, $\bar{z}$ values of the extreme near-wake were used and extrapolated in a reasonable manner to obtain the entire wake. By using these procedures, the necessity for employing computed wake coordinates for that portion of the wake which was predicted to be unstable was avoided.

Sample Wake Geometry-Blade Circulation Computation

In view of the relative complexity of the procedures involved in computing the wake geometry and associated rotor performance, a specific example illustrating the various steps of the process is desirable and is presented below.

Rotor and Rotor Operating Condition

Number of Blades	2
Twist	-8 deg
Tip Speed	700 fps
Aspect Ratio	13.6
Nominal C_T/σ	0.095
Radius	2.23 ft
Collective Pitch	10 deg

Procedures

1. Estimate the wake geometry using the experimental results of Figures 53 through 65 (see Figure 86).*

2. Compute the bound circulation distribution using the experimental wake geometry from Step 1 as input to the Prescribed Wake Program. These results are shown in Figure 87.

3. Approximate the continuous bound circulation distribution from Step 2 by five constant-circulation segments as shown in Figure 87. Note that the circulation peak (Γ_{max}) near the tip of the blade has been increased in magnitude and decreased in radial extent in making the approximation. This is done in anticipation of the expected final circulation distribution. The particular changes made were prompted by the observation that the theory generally predicted the vortex from the previous blade to lie closer to the rotor and farther outboard than was observed experimentally. The step changes in circulation, of course, imply the generation of trailing vortex filaments having circulation strengths equal to the changes in bound circulation. The tip vortex is trailed from the $\bar{r} = 1$ location, while the vortexes representing the inboard sheet trail from $\bar{r} = 0.15$, 0.25, 0.4, 0.75, and 0.885 in this example.

4. Using the approximate bound circulation distribution from Step 3 to specify the circulation strengths of the inboard and tip vortex filaments and using the geometry shown in Figure 87 for the initial starting wake, compute the corresponding distortions of the tip vortex using the Wake Geometry Program. Figure 88 shows the resulting distortions computed.

5. Approximate the extreme near-wake using Equations (2) and (3) as shown in Figure 88.

---

*The experimental results provided a realistic starting wake, thereby reducing convergence time; however, the independence of the wake solution to the starting wake model was verified using an uncontracted wake model.

6. Use the wake from Step 5 as input to the Prescribed Wake Program and compute a second estimate of the bound circulation. Compare the new circulation distribution with the approximation used in Step 4 (see Figure 89). If differences are within the tolerances indicated in Appendix II to be acceptable (as is the case in Figure 89), then the wake geometry and circulation distribution solutions are considered compatible; if not, a further iteration is required starting with Step 3.

EVALUATION OF ANALYTICAL TECHNIQUES

MODEL BLADE AIRFOIL DATA

The airfoil data used in the theoretical calculation were based on available two-dimensional, low-Reynolds-number data adjusted, through a synthesization procedure, to provide correlation between the test results for the untwisted two-bladed rotor and the results of the Blade-Element Momentum Analysis. Performance results were first compared on C_T/σ versus C_Q/σ plots for the three tip Mach numbers tested to determine the general quality of correlation between test and this particular theory. More detailed comparisons were then made on C_T/σ versus θ_{75} and C_Q/σ versus θ_{75} plots to estimate the relative magnitude of change required in the airfoil lift curve slope, stall angle, and drag data to improve correlation. Approximately five iterations were required at each tip Mach number condition to achieve acceptable correlation in both the thrust-torque results and the thrust-torque-collective pitch results. The final synthesized airfoil data generated (Figure 90) were then used in all other theoretical calculations. In comparing these data with the original two-dimensional data, only small changes were noted. The synthesized data have generally higher lift curve slopes, higher maximum lift coefficients, and lower profile drag coefficients. The differences are attributed to differences in Reynolds number and surface conditions for the blades tested.

EVALUATION OF WAKE GEOMETRY PROGRAM

Figures 91 through 95 compare the predicted radial and axial coordinates of the tip vortex with those measured experimentally. The experimental curves shown were obtained from the faired curves given in the generalized wake charts of Figures 53 through 62. The basic trends of the experimental data have already been discussed in the section entitled DISCUSSION OF EXPERIMENTAL WAKE GEOMETRY RESULTS, and only the general ability of the theory to predict the observed results is considered here.

Examination of the results in Figures 91 through 95 leads to the following general observations regarding the accuracy of the theory:

1. The theory predicts values of k_1 (the average slope of the $\bar{z}_T$ curve between $0 \leq \psi_w \leq \frac{2\pi}{b}$ or, equivalently, the nondimensional axial velocity) which are significantly lower than those measured. As a

result, the tip vortex from one blade is predicted to pass closer to the following blade than is observed experimentally. This is particularly true for the two-bladed rotor results, where the predicted vortex-following blade distance is generally about one-half of the measured value. For the six-bladed rotor condition shown in Figure 93, the predicted value of k_1 is actually positive, with the result that the vortex passes above the following blade instead of below the blade as is observed. In this case, the predicted and measured vortex-to-following-blade distances are about the same.

2. The predicted rate of contraction of the tip vortex in the immediate vicinity of the rotor is somewhat less than that measured. As a result, the predicted radial position of the tip vortex at the important wake azimuth angle of 360 deg/b (i.e., in the vicinity of the following blade) is approximately 0.02 R farther outboard.

3. The analysis predicted accurately the experimental values of k_2, the average slope of the $\bar{z}_T$ curve for $\psi_w > 360$ deg/b.

4. The analysis appears to be generally capable of predicting the changes observed in the wake geometry when various rotor or flight condition parameters are altered; e.g., the greater k_2 and increased contraction observed with increased thrust (Figures 91 and 93).

The results obtained from the Wake Geometry Program for the full-scale CH-53A rotor were also compared with analytical and experimental results presented by Clark in Reference 9. The comparison is shown in Figure 96, where the tip vortex axial and radial coordinates are presented versus wake azimuth angle. Although some difference exists in the rotor thrust levels, the comparisons can be considered quite favorable, at least until evidence of wake instability is noted in the results of this study at the larger values of ψ_w.

In summary, the wake geometry analysis developed herein predicts many of the qualitative characteristics observed in rotor wakes. The quantitative accuracy of the analysis is limited by one major shortcoming; namely, the inability to predict accurately the average axial transport velocity of a tip vortex element between the time when it is generated and the time when the element passes the next blade. Although the exact reason for this discrepancy is not known at this time, the need for replacement of the discrete filament wake model by a continuous sheet model in the vicinity of the blade is probably implied. Consideration should also be given to reducing the computing time of the current Wake Geometry Program so that a more thorough assessment of some of the other assumptions made in this study can be considered. A significant reduction in time could be achieved by incorporating the symmetry features of the hover mode of operation.

EVALUATION OF PERFORMANCE METHODS

The theoretical performance methods were evaluated by comparing the predicted hover performance results of the model rotors and two full-scale rotors with test results. The full-scale rotors selected were the six-bladed Sikorsky CH-53A and the two-bladed Bell HU-1A. The discussion of the performance results follows.

Model Rotors

Performance Predicted by Uncontracted Wake Methods

The performance results of the Momentum Analysis, Goldstein-Lock Analysis, and the Prescribed Classical Wake Analysis are presented in Figures 97 through 102. These methods do not account for wake contraction and will hereafter be termed uncontracted wake methods. They are considered separately from the contracted wake methods (Prescribed Experimental Wake Analysis and Prescribed Theoretical Wake Analysis) because (1) they represent the state-of-the-art prior to the consideration of contracted wake effects, and (2) due to their operational simplicity and minimal computer cost requirements, they were applied to a greater number of test conditions. The experimental data points in these figures represent the results of the fairings of the collective pitch data presented in Figures 15 through 18. The performance results for varying numbers of blades are shown in Figures 97 and 98 for the -8-degree-twist, 18.2-aspect-ratio rotor. The predicted performance of all methods is in good agreement with the experimental results at low thrust levels but becomes increasingly optimistic with increasing thrust and number of blades. The results of the three undistorted wake methods agree closely for four, six, and eight blades. For two blades, some separation of the predicted results at the high thrust levels is evident. The aforementioned results were found to be generally true for all the rotors tested, and the trends with thrust level and number of blades are the same as have been cited for full-scale rotors in Reference 1. Correlation results for rotors of 0 and -16 degrees of twist are presented in Figures 99 and 100, respectively, for two and six blades. It should be noted that, as discussed previously, the airfoil data used was synthesized by matching the results of the Momentum Analysis to the test results for the two-bladed, zero twist rotor. For six blades, the predicted performance is increasingly optimistic with decreasing blade twist (e.g., compare results from Figures 99 and 100 at $C_T/\sigma = 0.075$). In Figure 101, the results for the low-aspect-ratio blades (AR = 13.6) are presented. Slightly improved correlation between theoretical and experimental results compared to that of the high-aspect-ratio blades (AR = 18.2) of Figure 97 is indicated. Since for the same number of blades and rotor radius, rotor solidity increases with decreasing aspect ratio, this indicates that the correlation improves with increased rotor solidity when such increases result from varying aspect ratio. This is opposite to the correlation trend established when solidity was increased by varying the number of blades. The dependence of the correlation on the manner in which solidity is varied (i.e., number of blades versus aspect ratio) also agrees with the conclusions of Reference 1 based on full-scale rotors. Finally, the small improvement in correlation of the predicted and measured model performance results at a tip speed of 525 fps (Figure 102), noted for the two-bladed rotor, also parallels the full-scale results of Reference 1, in which the correlation is shown to improve with decreasing tip Mach number.

It is thus concluded that the discrepancies between the experimental performance and the performance predicted by the uncontracted wake methods generally exhibit the same trends for the model rotor as they do for full-scale rotors: the deterioration in performance prediction with increasing number of blades, blade loading, and tip Mach number. In addition, a tendency for improved agreement with increased blade twist was noted with the models. These discrepancies are believed to be primarily the result of the assumptions made in these methods regarding the rotor wake geometry and the impact which such assumptions have on the proximity of the operating conditions of the tip sections to stall.

Integrated Performance Predicted by the Contracted Wake Analyses

The performance results from the contracted wake methods (i.e., the Prescribed Experimental Wake Analysis and the Prescribed Theoretical Wake Analysis) are compared with the test results in Figures 103 through 106. Also included for comparison are the results from one of the uncontracted wake analyses (Goldstein-Lock Analysis) presented previously. The Goldstein-Lock Analysis was selected because it is a widely used hover performance analysis. The results for all conditions analyzed using the contracted wake methods are included in these figures. Application of the

Prescribed Theoretical Wake Analysis to a six-bladed model rotor was limited to one condition because of the computing time requirements of the program at this time. For consistency, the generalized experimental wake results of Figures 53 through 65 were used to obtain all Prescribed Experimental Wake method results shown in this set of figures. The sensitivity of predicted performance to variations from the generalized wake coordinates was significant and will be discussed later in this section. The performance predicted by the prescribed contracted wake methods generally correlates well with the experimental model rotor results, particularly for the six-bladed rotors. Reasonable correlation with collective pitch also exists except for the low-aspect-ratio blades (Figure 105), for which all of the theories predict higher thrust and torque than measured for a given pitch. Except in one instance, the thrust based on the theoretical wake is consistently lower than that predicted using the experimental wake. This is due to the previously mentioned prediction of the tip vortex as being nearer the blade than was observed from experiment. The prescribed contracted wake methods appear to have one distinct advantage over the uncontracted wake methods: the ability to predict more accurately the performance trends with increased number of blades and blade loading (C_T/σ). As shown previously in Figures 97 through 102, the Momentum, Goldstein-Lock, and Prescribed Classical Wake methods all predict optimistic performance for high thrust levels and high number of blades. For the six-bladed rotor operating at the high thrust condition, the results of the Prescribed Experimental Wake Analysis based on the generalized wake indicate reduced performance relative to the Goldstein-Lock results and improved correlation with the measured data.

Section Characteristics

Some insight into the reasons for the above-mentioned changes in predicted performance may be gained from Figure 107, where the theoretical spanwise distributions of axial induced velocity, section angle of attack, thrust, and torque are compared. The predicted distributions corresponding to the six-bladed rotor of Figures 97 and 103 operating at a 10-degree collective pitch setting were selected for this comparison. The influence of the experimental tip vortex geometry on the induced velocity distribution and the resulting effects on the angle of attack, thrust, and torque distributions are apparent in Figure 107. For low thrust levels, number of blades, and tip Mach numbers, the distributions of the uncontracted wake methods are generally compensative between the inboard and tip regions of the blades as far as integrated performance is concerned. However, at a condition such as that of this figure, the contracted wake geometry considerations result in a decrease in integrated performance relative to that predicted by the uncontracted wake methods. In the real wake, the tip vortices are positioned much closer to the tip path plane than is assumed in the Goldstein-Lock and Prescribed Classical Wake analyses. As the number of blades increases, due to the reduced separation between blades, each blade is closer to the tip vortex generated by the blade ahead, and increased aerodynamic interference results. The circulation strength of the tip vortex also increases with the increased thrust level associated with high numbers of blades. This, coupled with the close proximity of the preceding blade's tip vortex to the blade, results in increased local angle-of-attack values in the blade tip region due to the upflow generated by the contracted vortex. It should be noted that the predicted performance deterioration is attributable to deterioration in integrated thrust rather than torque. In fact, the predicted torque based on the experimental wake for the subject test condition is slightly less than the torque predicted by the undistorted wake analyses. As shown in Figure 107c, this is caused by the reduction in induced torque.

Performance Sensitivity to Tip Vortex Geometry

As mentioned previously, the performance results were found to be sensitive to certain wake parameters. The sensitivity results are summarized in the following listing, in which the wake parameters and their primary influence on the wake geometry are presented in decreasing order of importance:

k_1 and k_2 (the axial position of the tip vortex)

A and λ (the radial position of the tip vortex)

$K_{1_{\bar{r}=1}}$ and $K_{2_{\bar{r}=1}}$ (the axial position of the outer region of the vortex sheet)

$K_{1_{\bar{r}=0}}$ and $K_{2_{\bar{r}=0}}$ (the axial position of the inner region of the vortex sheet)

The axial position of the tip vortex, defined by k_1 and k_2, was found to have the dominant influence on the performance results. To illustrate the sensitivity to the tip vortex axial position, the effect of variations in k_1 on hover performance is shown in Figure 108. k_1 was varied so as to axially displace the tip vortex from the generalized wake position by

±1% of the rotor radius (±1% R) at and beyond the wake azimuth position equal to the blade spacing*. This effectively moved the tip vortex 1% R closer to or farther from the following blade. The magnitude of the changes approximately represents the accuracy of the tip vortex generalization. The performance results show increasing sensitivity with number of blades (two versus six in Figure 108). To analyze these results in greater detail, distributions of the blade section characteristics were compared. For example, the blade airload distribution and tip vortex positions are shown in Figure 109 for the lettered conditions indicated on Figure 108. (Note that the nominal conditions A-D are the ones for which tip vortex streamlines were presented in Figure 70.) The larger change in loading distribution for the six-bladed rotor conditions (C and C"; D and D") is due to the increased proximity of the tip vortex to the blade. Also evident in this figure is (1) the typical change in the character of the loading in the tip region with varying number of blades and thrust level, and (2) the radially outward movement of the peak loading with increased number of blades which corresponds to the movement in the radial position of the tip vortex.

Predicted performance was fairly insensitive to changes in A and λ providing they were changed in combination rather than independently so as to maintain the radial coordinates of the near-wake portion of the tip vortex within the experimental accuracy -- particularly beneath the following blade. As mentioned previously, A = 0.78 was selected in the wake generalization to curve-fit the near-wake radial coordinates when used in combination with the specific λ values given in Figure 62 as a function of C_T. For a given test condition, there are other combinations of A and λ that would fit the near-wake data within the experimental accuracy. However, the performance was relatively insensitive to such changes even though the far-wake contraction varied considerably (0.78 to 0.72). Least senstivity resulted from variations of the inboard wake (vortex sheet). For example, a 10% change in the axial coordinates of the vortex sheet for a typical condition resulted in less than a 1% change in thrust and torque for a two-bladed rotor and less than a 2% change for

*Results for a 1% R displacement of the tip vortex of the six-bladed rotor toward the rotor disc are not included in Figure 108. This displacement resulted in the vortex passing within 0.5% R of the following blade. Theoretical applications involving passage of the vortex within this distance of the blade are questionable due to the limitations of lifting line theory and limited information on vortex core size.

a six-bladed rotor. In summary, rotor performance becomes more sensitive to wake geometry variations as number of blades and/or thrust level is increased. Performance is particularly sensitive to the axial position of the tip vortices due to their close proximity to the blades. This sensitivity of blade loading to small changes in tip vortex position predicted by the Prescribed Wake Analysis confirms certain phenomena observed on full-scale rotors. This will be discussed in the following section.

Full-Scale Rotors

The theoretical methods were applied to compute the hover performance of the six-bladed, Sikorsky CH-53A rotor. Two-dimensional airfoil data, supplied by Sikorsky, were used in all calculations. In Figure 110, the theoretical performance results are compared with test results from the Sikorsky whirl stand shown in Figure 7. The absolute accuracy of thrust at a given power level measured on this facility is estimated as $\pm 2\%$. The test data presented in Figure 110 have been corrected for ground effect and whirl stand interference. As shown in this figure, the performance predicted by the Momentum, Golstein-Lock, and Prescribed Classical Wake analyses (uncontracted wake methods) is increasingly optimistic with increasing thrust level, which is consistent with the previously recognized trend. On the other hand, the results of the Prescribed Experimental Wake and Prescribed Theoretical Wake analyses (contracted wake methods) are slightly pessimistic relative to the experimental data. The generalized wake coordinates from the model rotor test were used in the Prescribed Experimental Wake Analysis to obtain the full-scale CH-53A performance results. The performance corresponding to small deviations of the tip vortex geometry from the generalized coordinates, within the experimental wake accuracy, is presented in Figure 111. It is shown that the performance variations associated with small changes in wake geometry are significant. In fact, as indicated, it was possible to obtain correlation with the test data by displacing the tip vortex only $\frac{1}{2}\%$ R farther away from the rotor disc.

The section angle of attack distributions predicted by the various theoretical methods for the 12-degree collective pitch condition of Figure 110 are presented in Figure 112. The prescribed experimental wake results again exhibit a large angle-of-attack increase near the tip caused by the strong influence of the contracted tip vortex. The angle-of-attack distribution in the tip region of the blade has been substantiated on the Sikorsky whirl stand in a recent test in which pressure measurements were recorded at three stations over the outer 15% of the blade. It was found that with minor adjustments to the generalized wake coordinates, the angle-of-attack distribution and total rotor performance could be predicted within the experimental limits of the test data. This emphasizes the inadequacy of the uncontracted wake methods for predicting the distributions of the performance characteristics. Also, although this is encouraging insofar as the accuracy of the Prescribed Experimental Wake Analysis is concerned, additional pressure measurement data sufficient in extent to obtain the complete angle-of-attack distribution along the blade for various rotors and operating conditions would obviously be desirable to permit further evaluation of this method and refinement of the generalized wake model. Examination of the theoretical radial loading distributions associated with the operating conditions of Figure 112 revealed that the outer 10% of the blade generates approximately one-third of the blade lift according to this theory, compared to only one-quarter of the lift according to the Goldstein-Lock theory. This comparison implies an extreme sensitivity of rotor thrust to the aerodynamic characteristics over the blade tip region and the need for an accurate simulation of the airfoil characteristics and velocities induced by the wake in this area. The assumption of two-dimensional flow over the blade span has been shown in Reference 24 to be questionable in the blade tip region. The magnitude of three-dimensional corrections and their influence on the results predicted by the prescribed wake analyses remain to be determined.

The theoretical methods were also applied to compute the hover performance of the two-bladed Bell HU-1A rotor. Again, the Blade Element-Momentum, Goldstein-Lock, and Prescribed Wake methods were used. Two-dimensional airfoil data, synthesized by the Bell Helicopter Company, were used for the NACA 0015 airfoil section in all calculations. In Figure 113, the theoretical performance results are compared with test data from a tethered aircraft test reported in Reference 25 (whirl-stand data for isolated rotor performance was not available for two-bladed rotors). For the test data shown, the engine shaft horsepower was reduced by 15% to account for tail rotor, transmission, and accessory power losses. The wake data used in the prescribed experimental wake calculations were obtained by interpolating the generalized rotor wake data to the appropriate twist and thrust levels. The theoretical results, including contracted wake results, are all optimistic relative to the experimental results. It is somewhat uncertain, for this rotor, as to whether the performance discrepancies are attributable to limitations of the theoretical methods, to inaccuracies in the estimation of the power losses, and/or to the synthesis of the airfoil data. It is thus suggested that the results presented in Figure 113 be considered preliminary until other two-bladed rotors are analyzed.

The sensitivity of blade loading to small changes in the tip vortex position tends to confirm vortex interference as the source of certain phenomena observed on full-scale rotors. As explained in Reference 1, the presence of a small amount of ambient wind can produce changes in the tip vortex position which, at certain conditions, are reflected in the rotor characteristics as vibratory flapping and tip stall. Since the publication of that reference, blade tracking problems at high thrust levels (greater than normal operating levels) have been related to vortex interference effects. The Prescribed Wake Program appears to be of potential value for analyzing these phenomena. However, for increasing number of blades, the problem associated with the sensitivity of the predicted results to minor wake geometry variations is recognized. With further experience with the method, and through small, systematically developed adjustments to the generalized wake model presented herein and/or further refinements in the Wake Geometry Program, it may become possible to consistently predict hover performance to a high degree of accuracy with the method in its present form. However, until this is accomplished, further investigation of three-dimensional tip effects and unsteady wake effects associated with both ambient wind variations and the apparent instability of the far wake appears warranted.

RESULTS AND CONCLUSIONS

1. Model rotors of the scale tested can be successfully used to obtain performance and wake geometry data which are both systematic and, more importantly, indicative of those characteristics observed for full-scale rotors. The use of an indoor, small-scale facility greatly reduces the cost of acquiring such information.

2. The model rotor wake geometry for the region directly beneath the rotor (i.e., within approximately one-fourth of the rotor radius) can be represented by simple generalized equations which facilitate the rapid estimation of rotor wake coordinates for a wide range of rotor designs and operating conditions. The generalization was based on the following observations:

   a. The rate of descent of an element of the tip vortex from a blade is substantially constant prior to its passage beneath the following blade. This axial velocity increases approximately linearly with increasing blade loading and decreases slightly with increasing blade twist. Within the experimental accuracy of the data, the axial velocity is insensitive to variations in number of blades.

   b. The axial velocity of a tip vortex element after the passage of the following blade is increased to a new, relatively constant value. This velocity increases with increasing disc loading in a manner proportional to the momentum inflow velocity. The constant of proportionality is approximately 1.4 for rotors with untwisted blades and decreases with increasing twist.

   c. The radial position of a tip vortex element decreases in a decaying exponential manner. The rate of decrease (or contraction) appears to be primarily determined by rotor disc loading and is greater with increasing disc loading.

   d. The inboard vortex sheet from each blade is fairly linear with radial position at a specific wake azimuth location. The axial velocity of the sheet increases with increasing disc loading and, to a lesser extent, with blade twist. The rate of descent of the outer portion of the vortex sheet is approximately twice that observed for the tip vortex following the passage of the next blade.

e. Wake geometry is insensitive to independent variations in aspect ratio and tip speed. The influence of number of blades is limited to the establishment of the wake azimuth angle at which the wake axial descent velocities are observed to increase significantly.

3. The stability of the experimental wake decreases with increasing distance from the rotor, indicating that the classical concept of a smoothly contracting wake may be incorrect.

4. Attempts to develop an analytical method for predicting the contracted tip vortex geometry based upon the interaction of discrete vortex filaments were partially successful. The method predicts the general features of the tip vortex and the qualitative variation of these features with changes in rotor or flight condition parameters. However, the position of the tip vortex shed by one blade relative to the following blade was not accurately predicted by the analysis. Compared to the experimental observations, the predicted vortex was generally closer to the blade and farther outboard. In addition, the contracting tip vortex was predicted to become unstable at moderate distances below the rotor plane, thus complicating the problem of predicting the wake geometry beyond the near-wake region. Available experimental evidence appears to substantiate this prediction.

5. Rotor hover performance methods which assume that the blades are lifting lines and that the rotor wake is uncontracted give generally comparable performance predictions. As was noted for full-scale rotors, the accuracy of these methods in predicting model rotor performance decreased as the number of blades, blade loading, and tip Mach number increased. In addition, the model rotor correlations indicated a decrease in accuracy when the twist of the rotor blades under consideration was reduced. The partial success achieved with these methods in the past results from compensating errors in the blade loading distributions.

6. The elimination of the uncontracted wake assumption through the use of generalized experimental wake data significantly improves the accuracy of performance characteristics predicted for model rotor conditions for which the uncontracted wake methods exhibit major shortcomings (i.e., for conditions with increasing number of blades and thrust levels). Application of the experimental wake method to full-scale rotors, using model rotor wake data, yielded similar improvements for the limited number of conditions examined. In addition, the method predicts blade spanwise angle-of-attack distributions which are greatly different and more realistic than those predicted using uncontracted wake analyses.

7. The use of predicted contracted wake geometries in computing rotor performance led generally to reasonable but more conservative (lower thrust for same power) estimates relative to those obtained using the generalized experimental wake results. This was mainly due to the prediction of a smaller axial distance between the tip vortex and the following blade than was observed experimentally.

8. The performance predicted on the basis of lifting line theory using a realistic contracted wake is very sensitive to small changes in wake geometry, particularly for rotors for which the tip vortex is positioned very close to the following blade. While the generalized wake geometry results presented herein are believed to be based on reasonable fairings of the data available, in view of this sensitivity, small systematic refinements to the fairings may be required if consistently accurate performance predictions are to be achieved.

RECOMMENDATIONS

1. Because of the more accurate definition of the radial distributions of blade section angles of attack which they provide, contracted wake analyses should be used to predict hover performance. They should be particularly useful in evaluating and developing improved blade tip designs.

2. In lieu of an accurate method for predicting the geometry of a contracted wake, the Prescribed Wake Analysis, together with the generalized experimental wake geometry charts, should be employed.

3. Efforts to obtain accurate wake geometry data from full-scale rotors should continue to substantiate further the applicability of generalized model rotor wake geometry data to full-scale rotors.

4. Measurements of blade pressure distributions should be obtained to provide experimental data for detailed comparisons with predicted distributions based on the generalized wake information.

5. An experimental investigation, employing model rotor flow visualization techniques, should be conducted to obtain systematic rotor performance and wake geometry data for blade designs with taper, nonlinear twist, and promising tip shapes.

6. Investigations should be undertaken to examine in detail the stability characteristics of the wake of a hovering rotor.

7. Further work should be undertaken to reduce the computing time required by the analysis developed herein for predicting the geometry of the rotor wake. This will greatly facilitate further studies designed to improve the quantitative accuracy of the analysis.

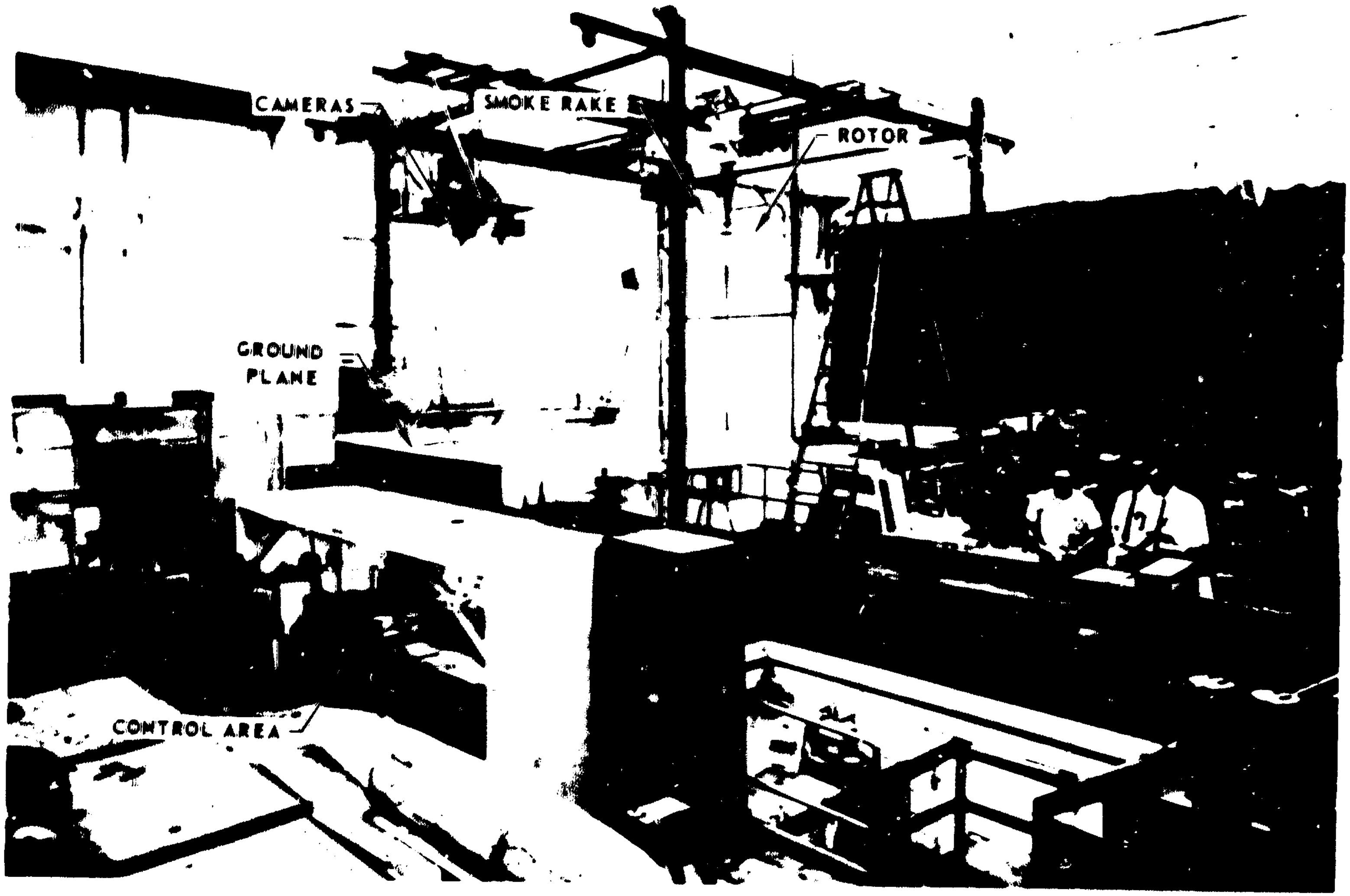

Figure 1. JARL Model Helicopter Rotor Hover Facility.

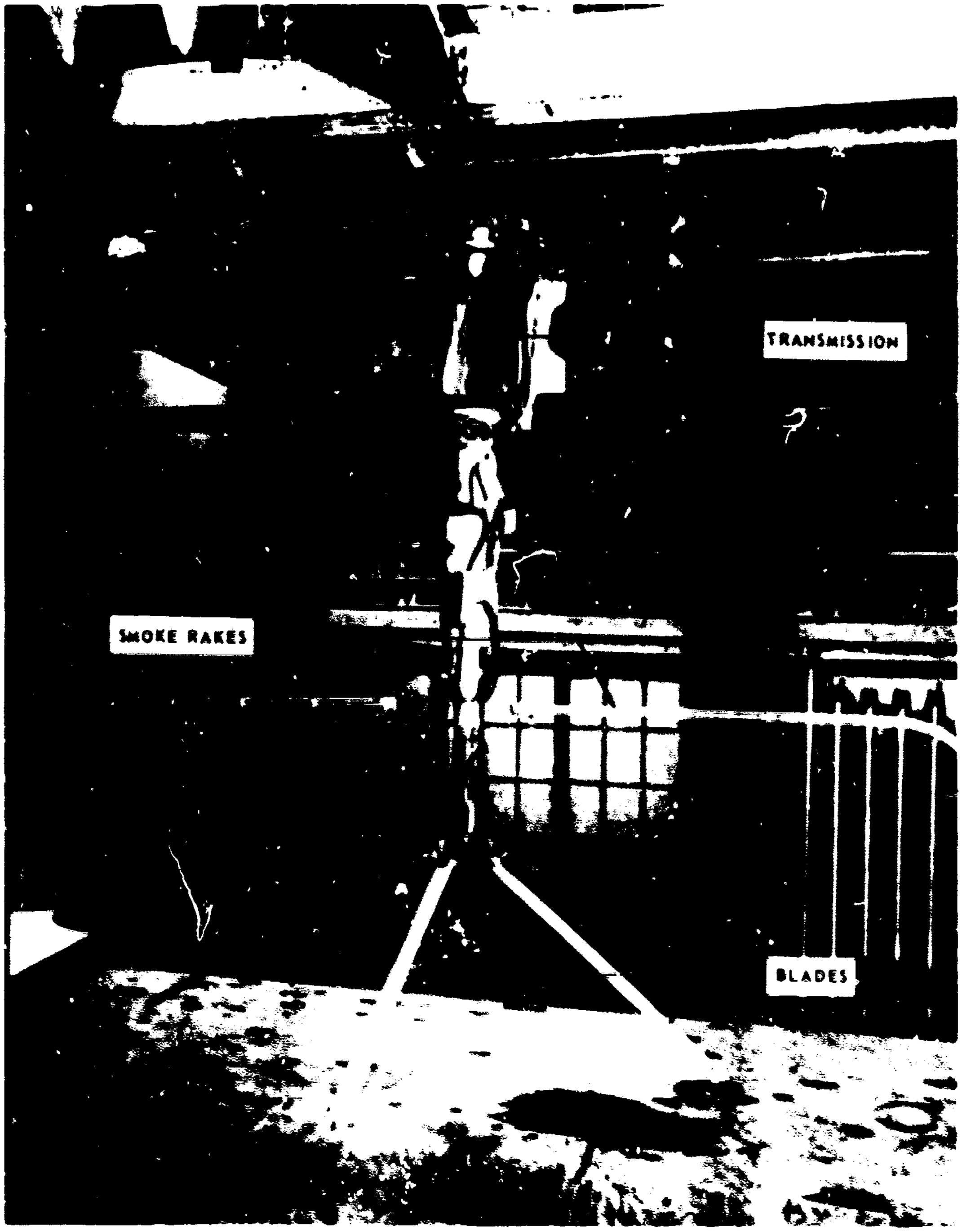

Figure 2. Rotor Test Rig.

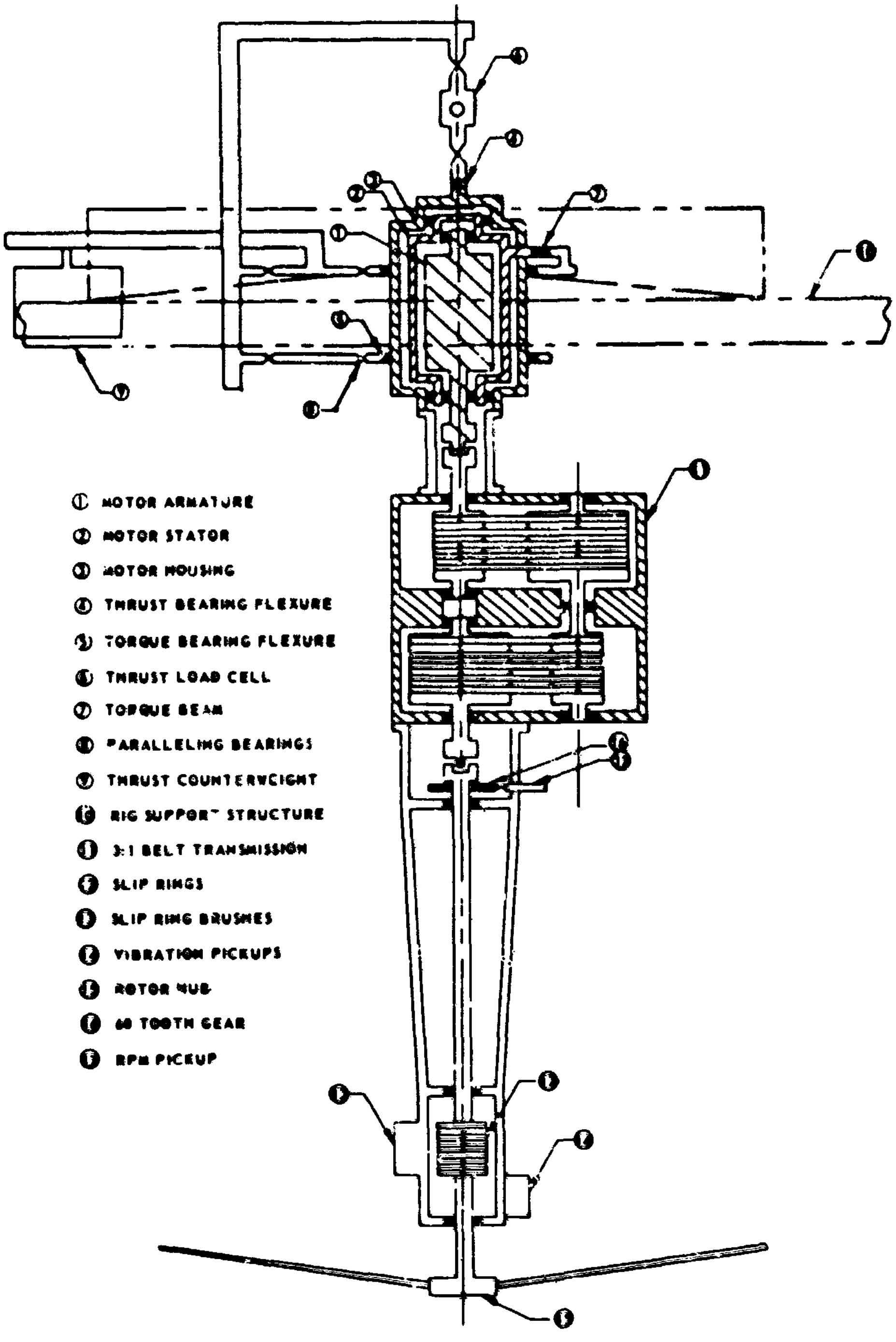

Figure 3. Schematic Cross Section of Motor Test Rig.

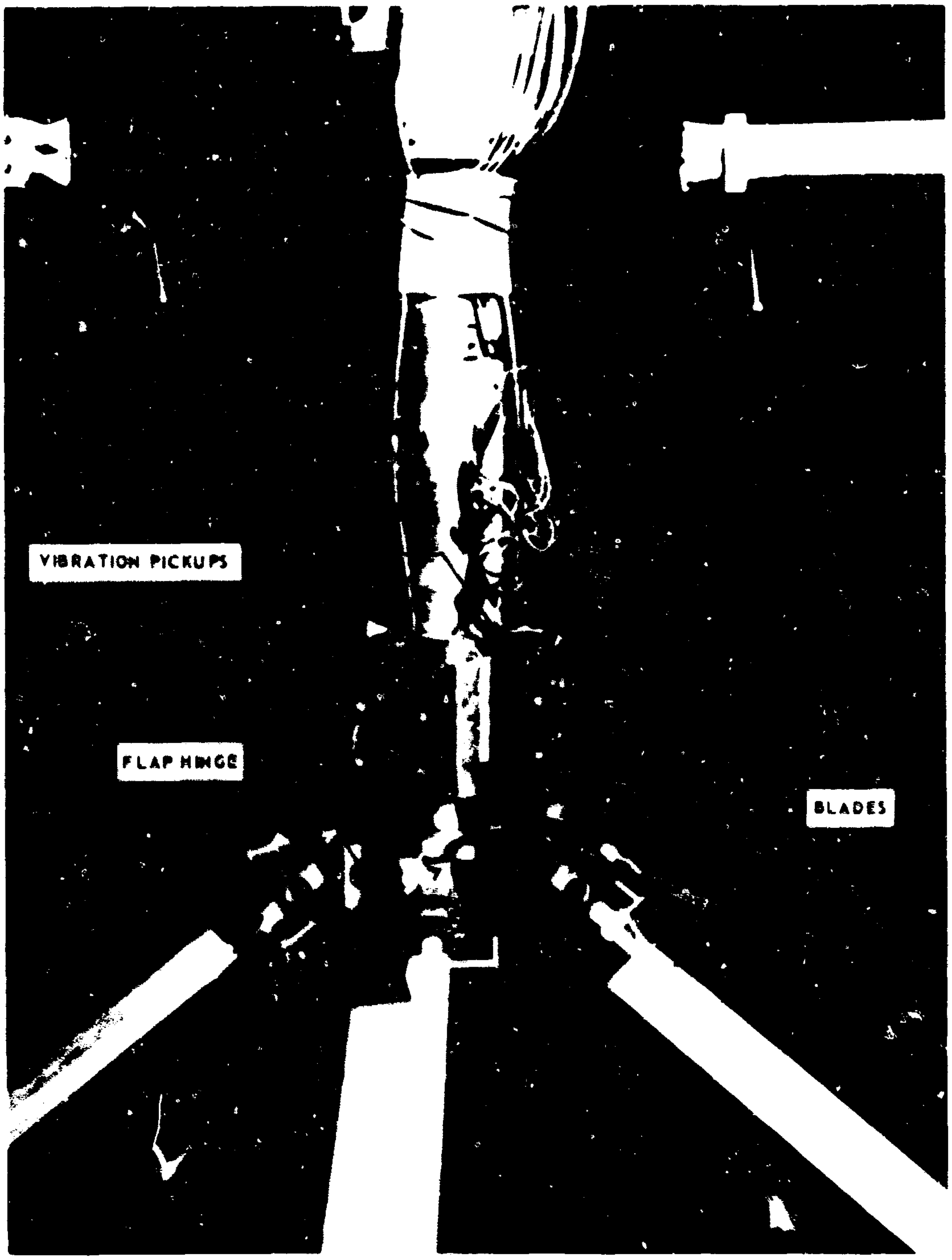

Figure 4. Rotor Hub.

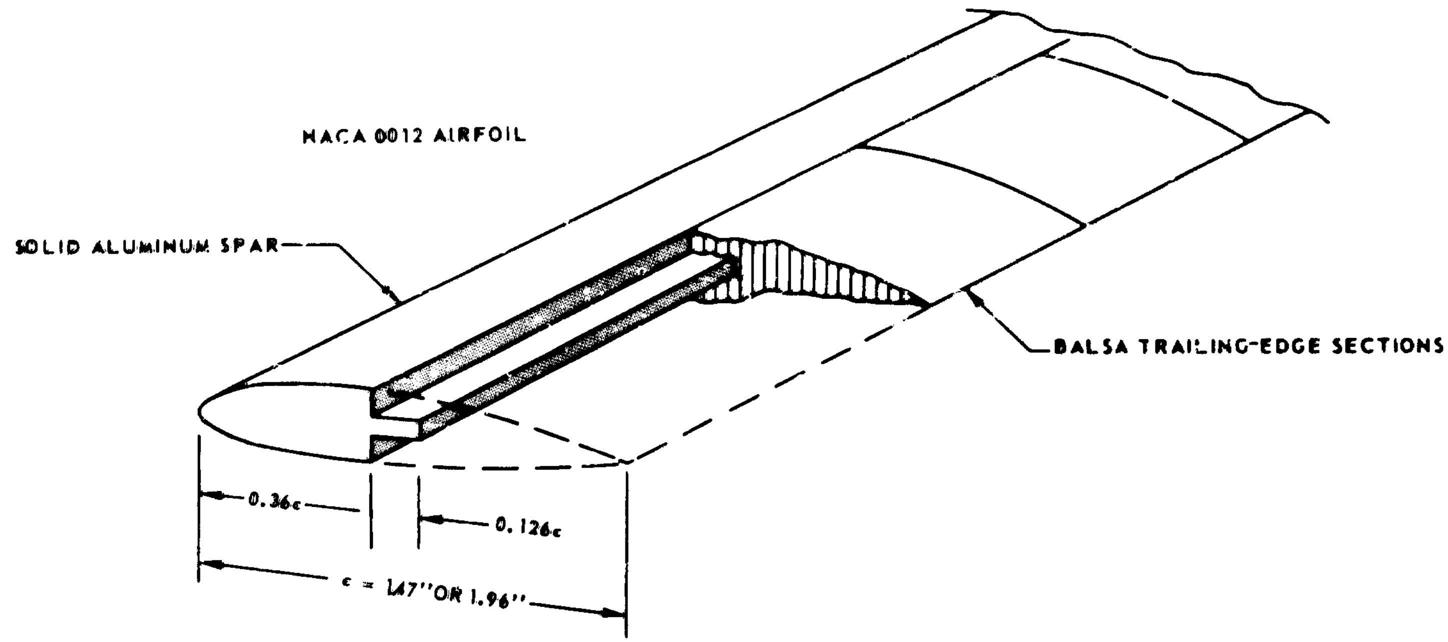

Figure 5. Schematic of Model Rotor Blade Construction.

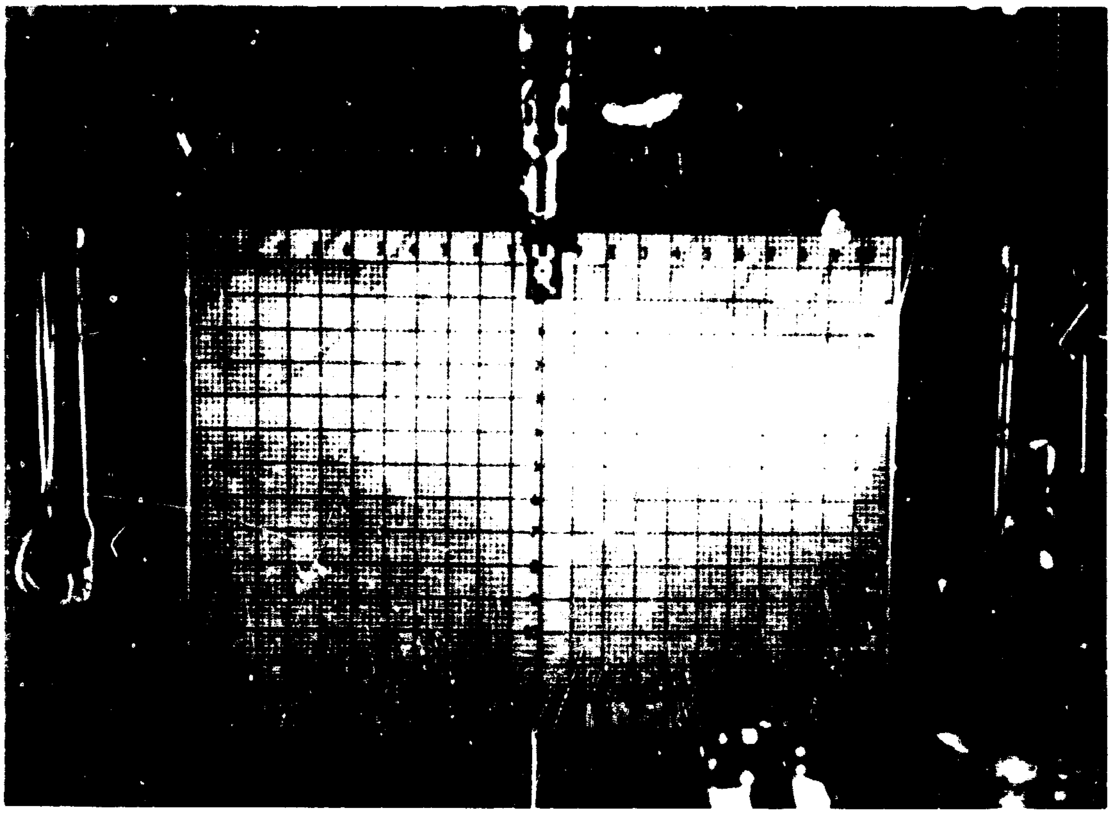

Figure 6. Flow Visualization Grid.

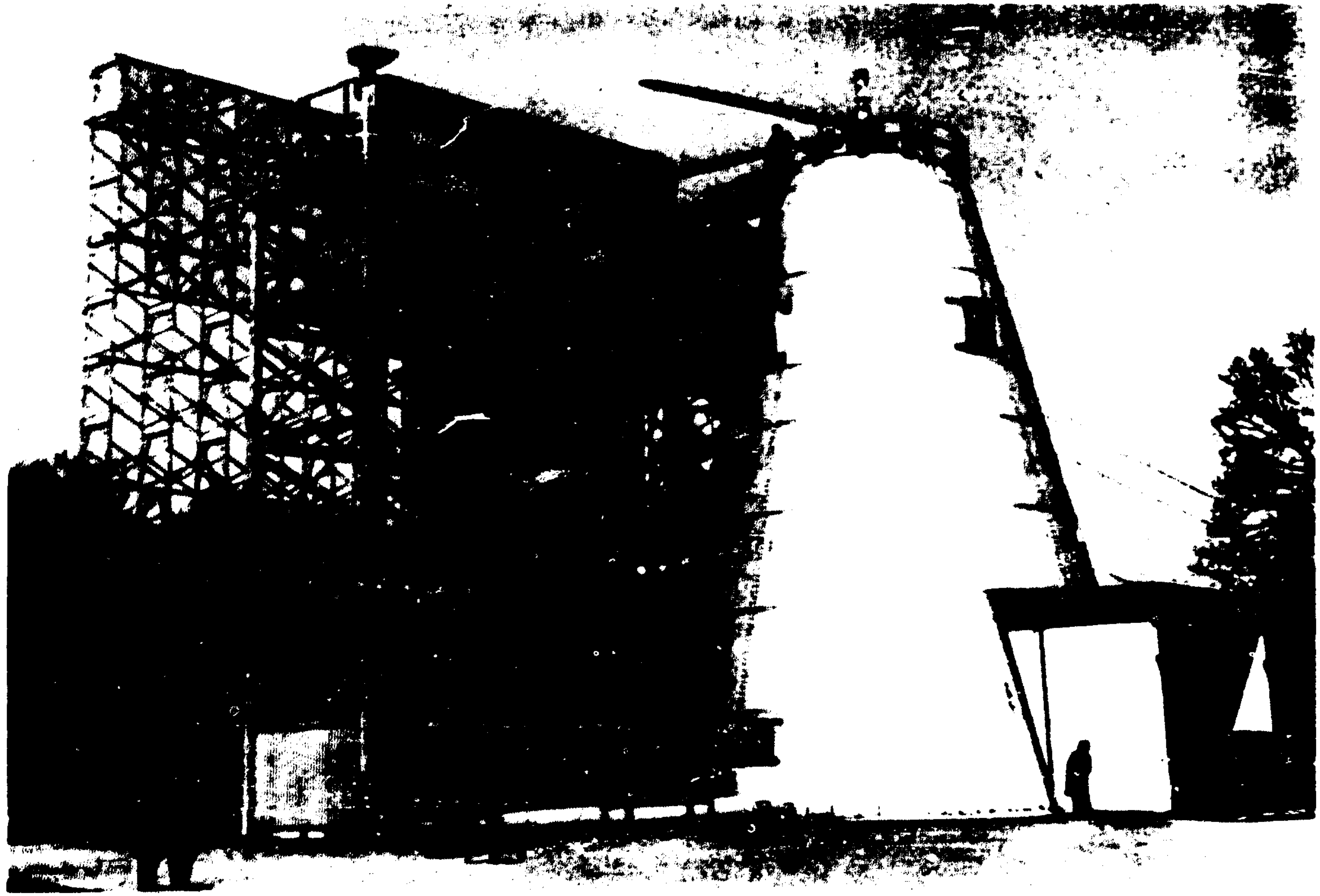

Figure 7. Sikorsky Aircraft Full-Scale Rotor Whirl Stand.

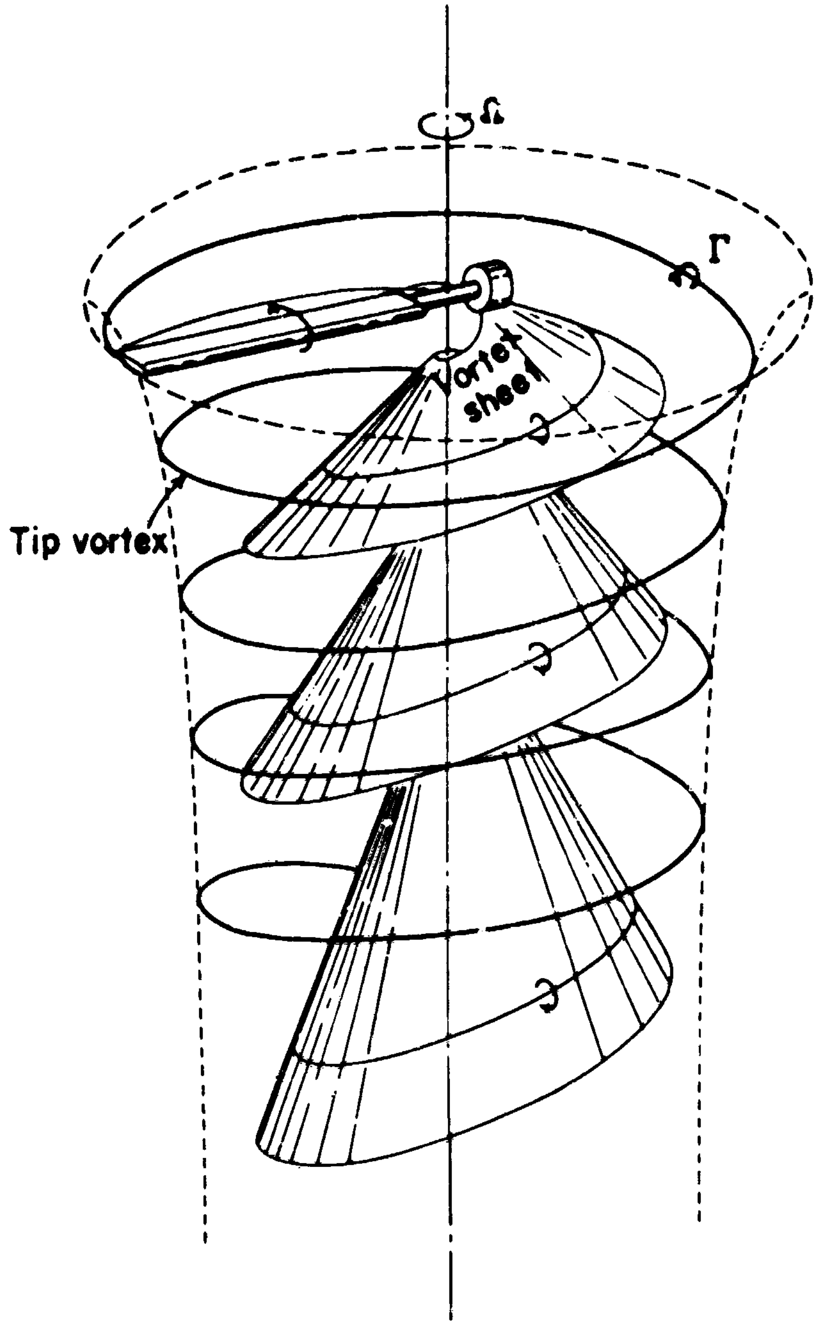

Figure 8. Schematic of Rotor Wake Structure.

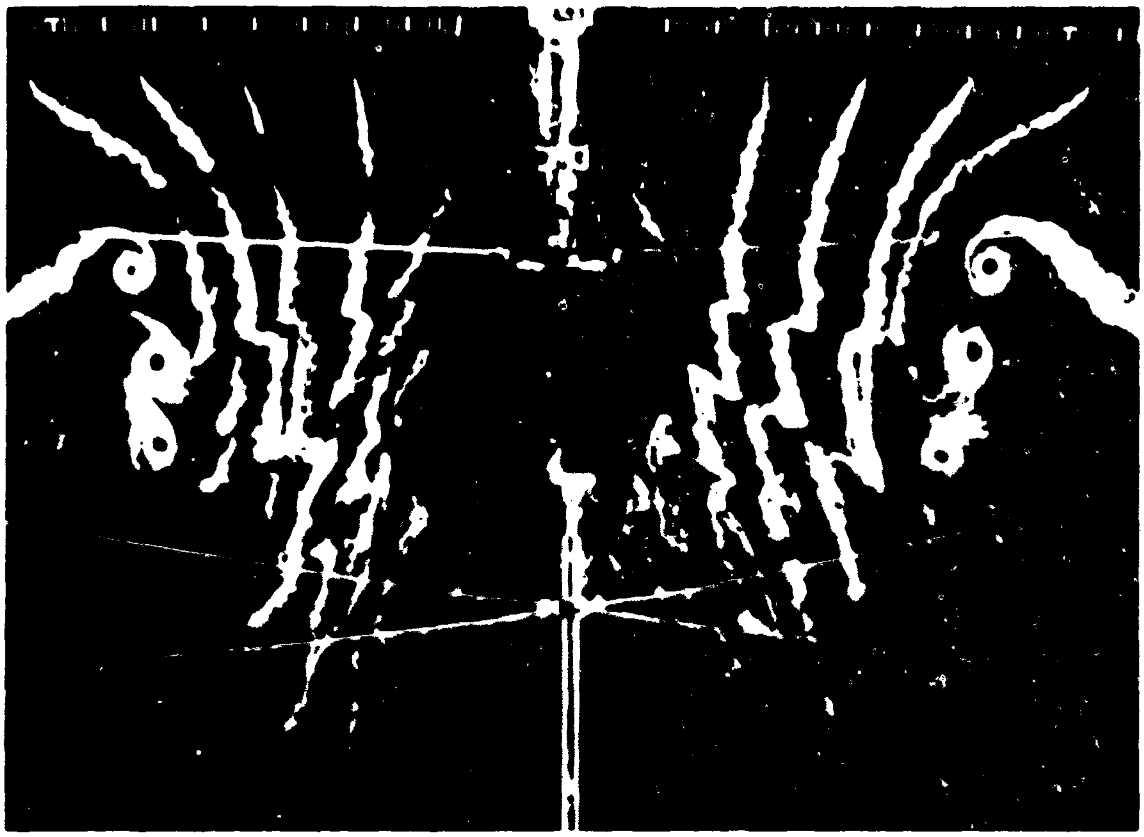

Figure 9. Sample Flow Visualization Photograph.

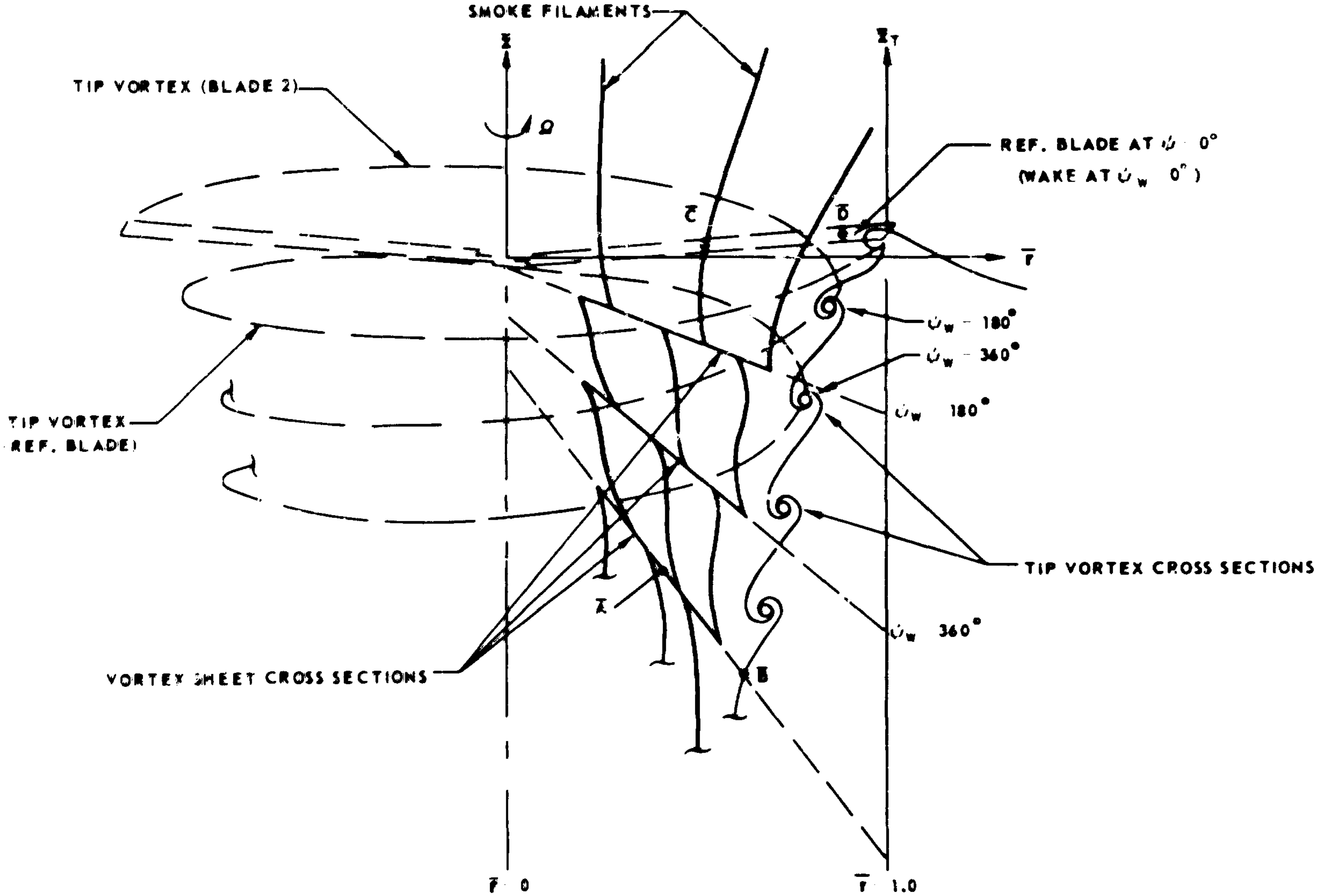

Figure 10. Schematic of Wake Cross Section Showing Wake Coordinate System.

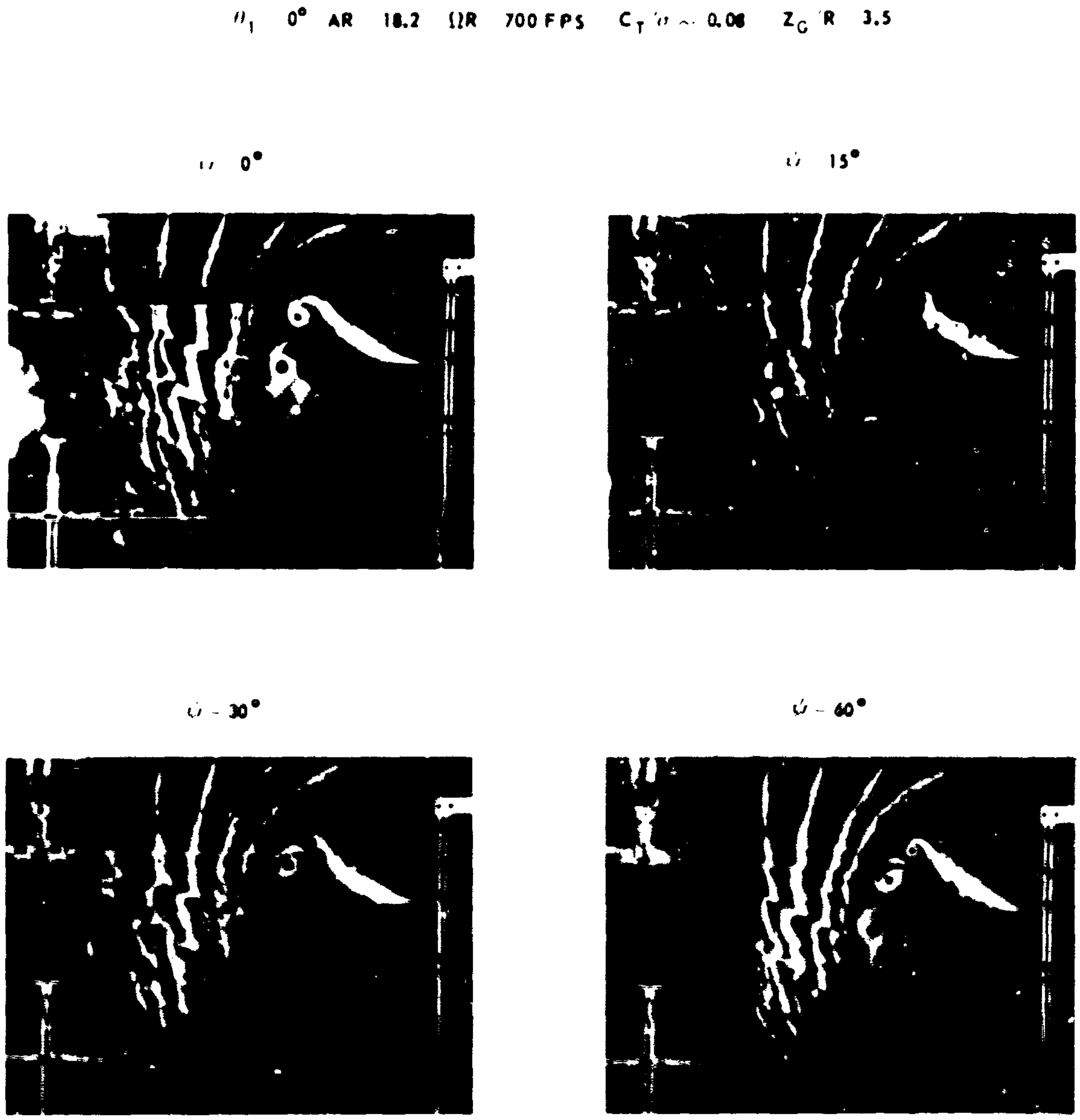

(a) $\psi = 0°$ to $60°$

Figure 11. Sequence of Photographs Showing Time History of Wake -- b = 2.

θ_1 0° AR 18.2 ΩR 700 FPS C_T/σ 0.08 Z_G/R 3.5

ψ 90°

ψ 120°

ψ - 150°

(b) ψ = 90° to 150°

Figure 11. Concluded.

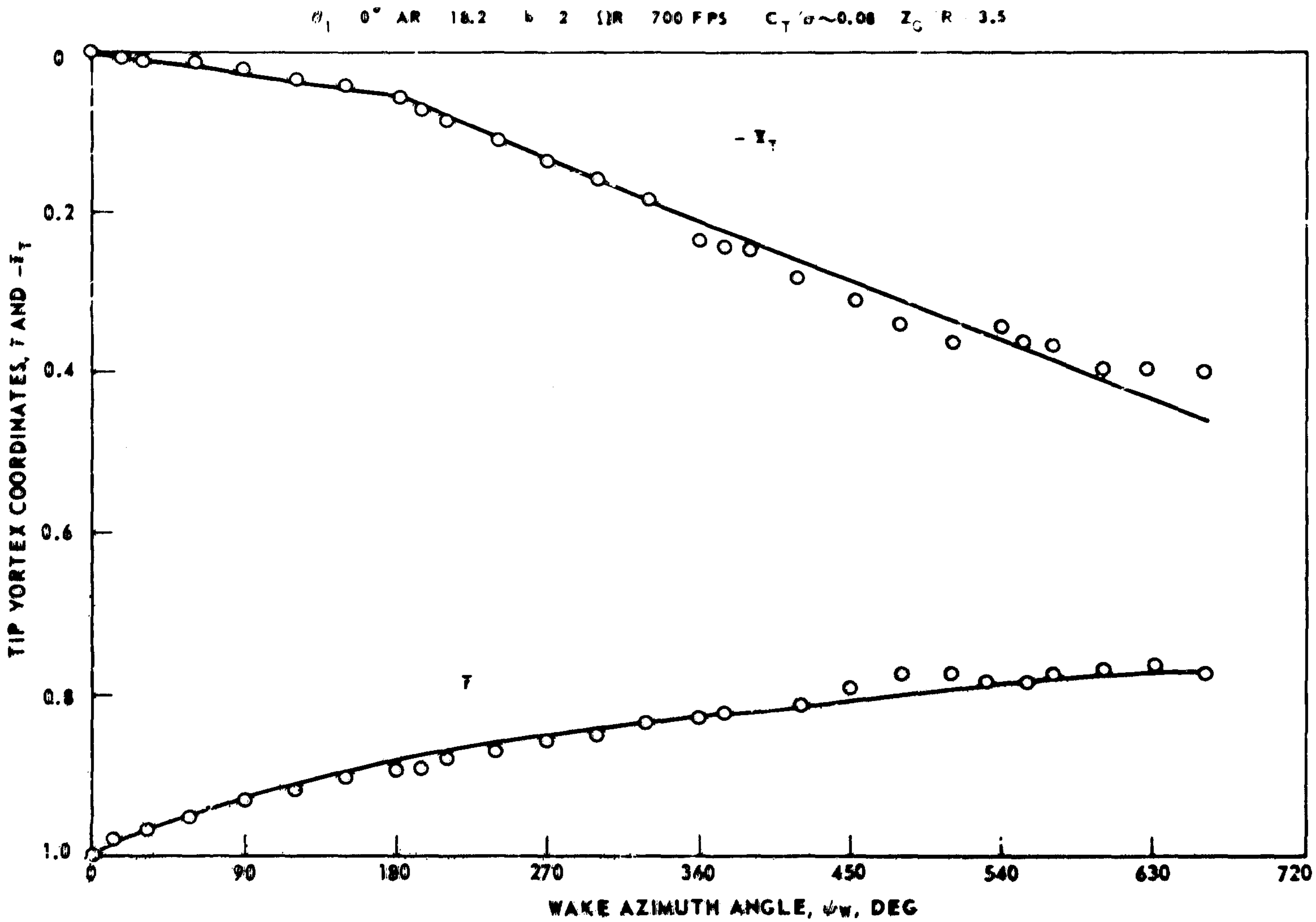

Figure 12. Tip Vortex Coordinates Measured From Photos of Figure 11.

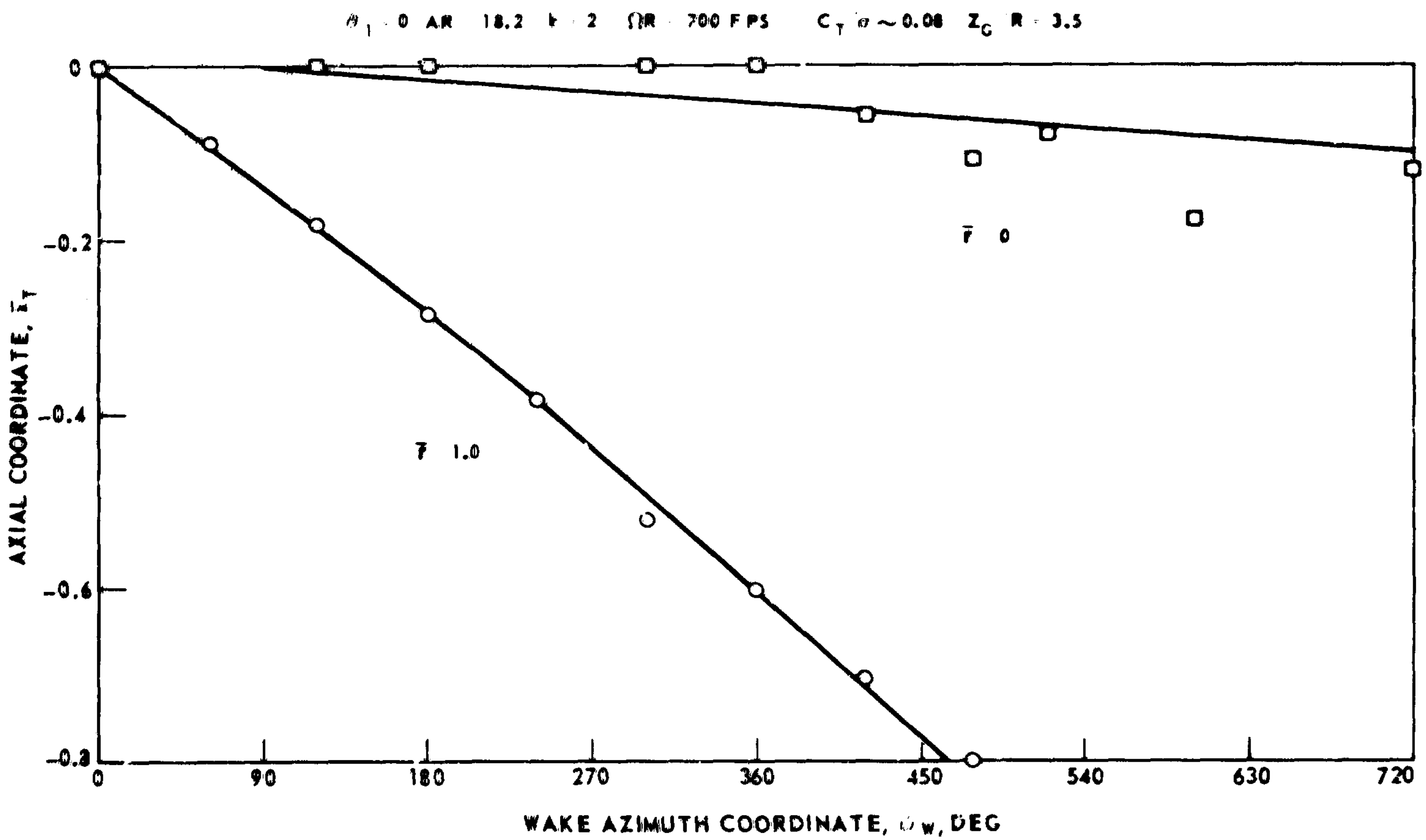

Figure 13. Inboard Vortex Sheet Coordinates Measured From Photos of Figure 11.

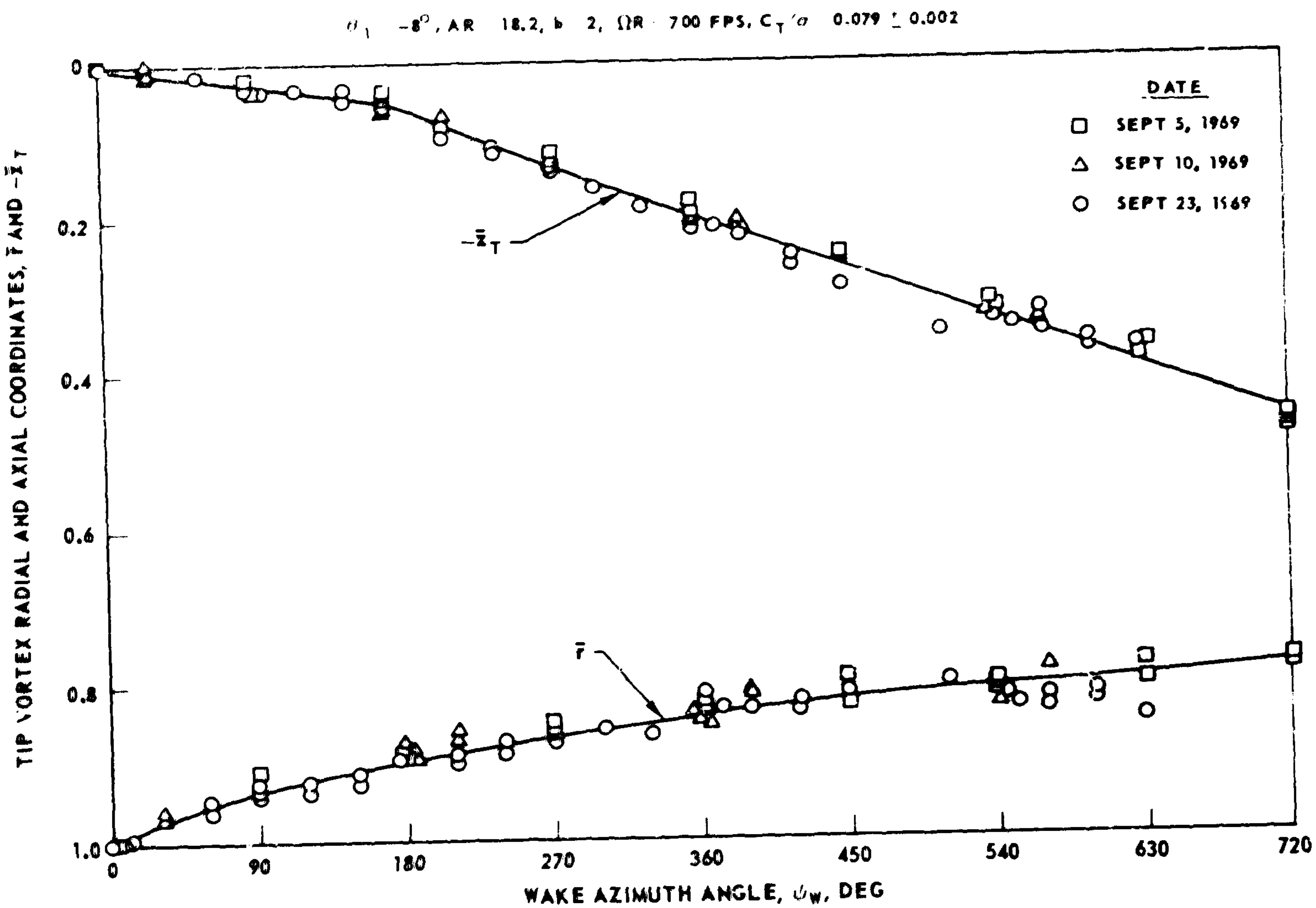

Figure 14. Repeatability of Tip Vortex Coordinates.

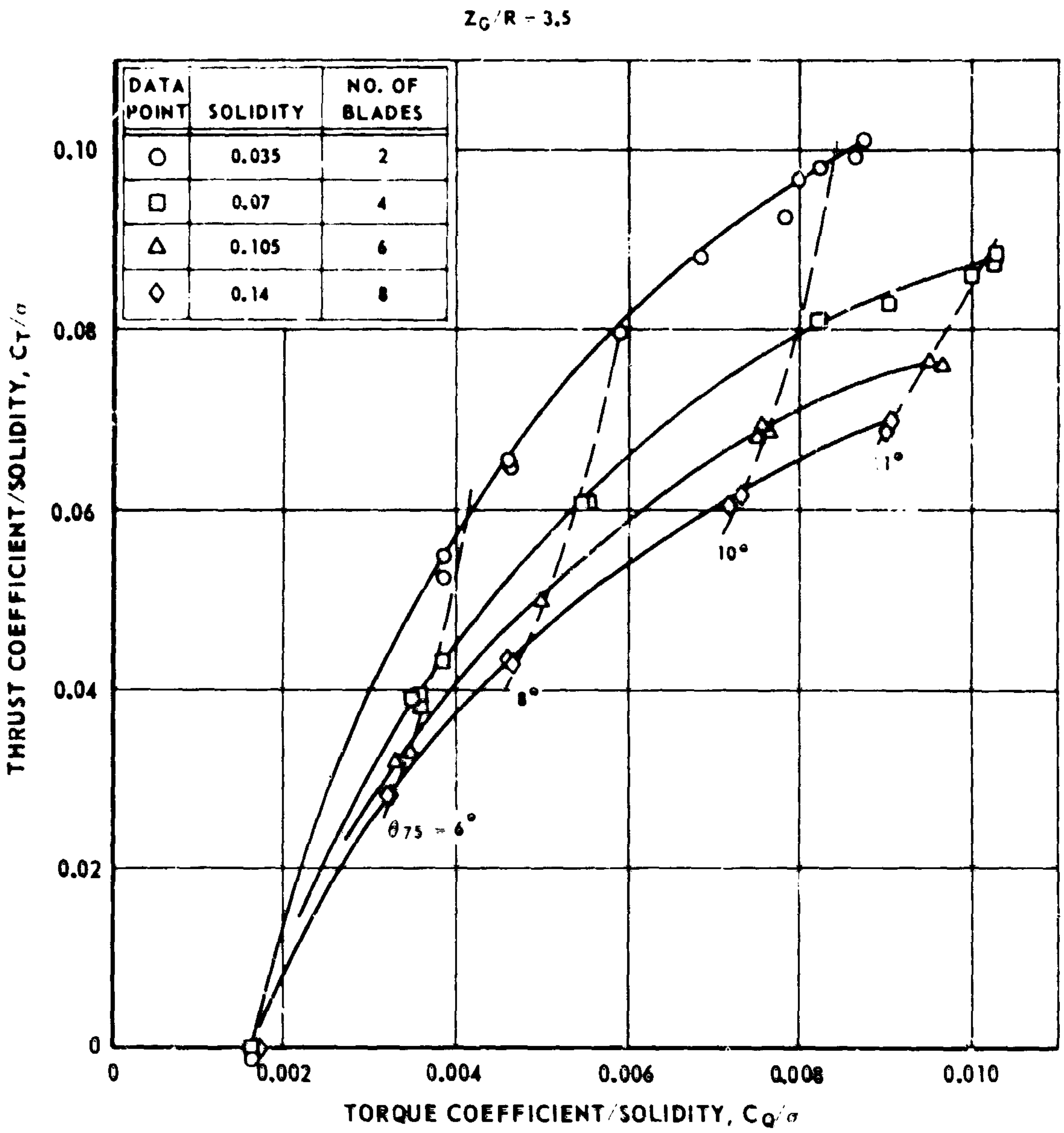

(a) ΩR = 700 FPS

Figure 15. Experimental Model Rotor Performance -- $\theta_1 = 0°$, AR = 18.2.

$Z_G/R = 3.5$

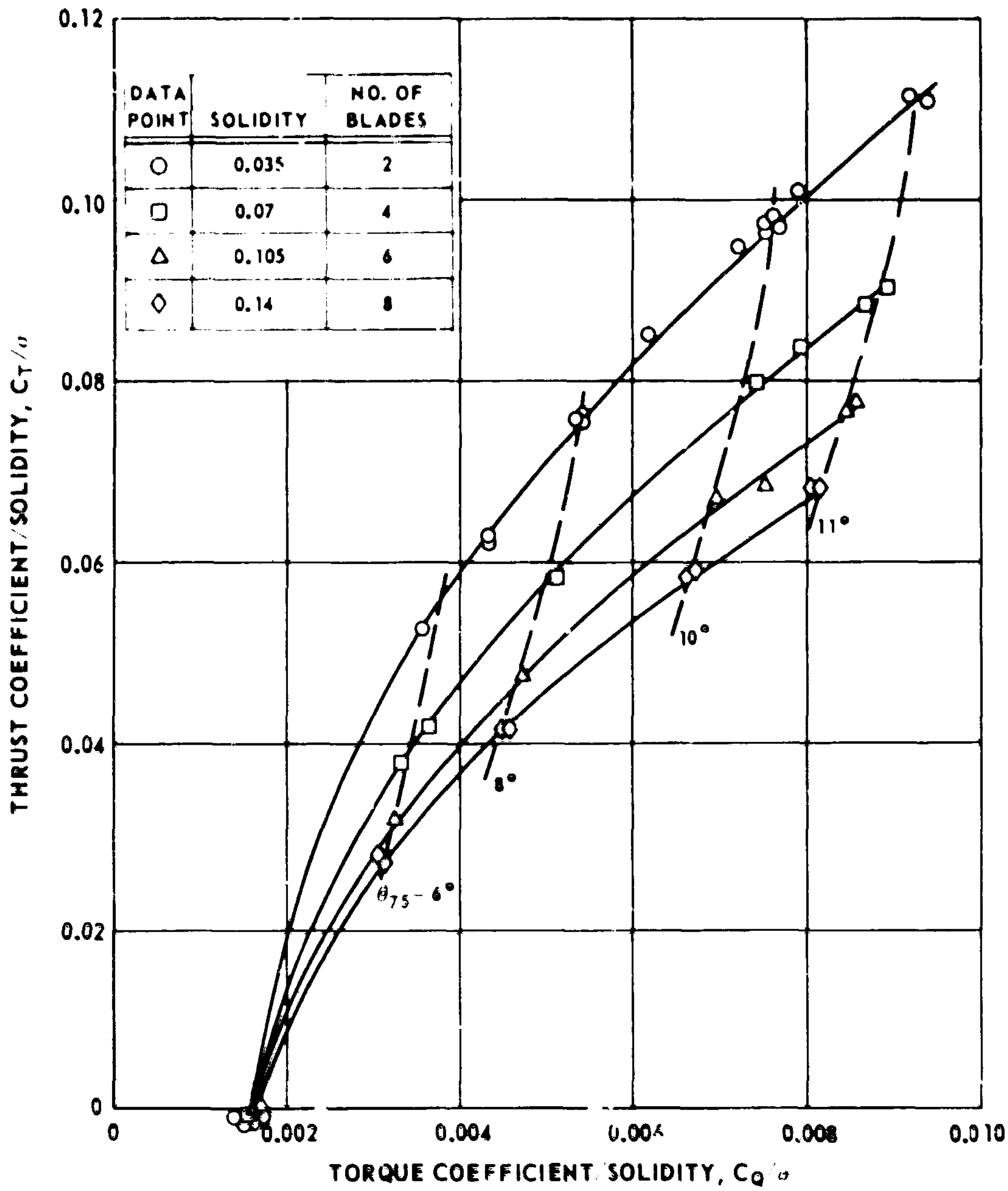

(b) ΩR = 600 FPS

Figure 15. Continued.

Z_G/R 3.5

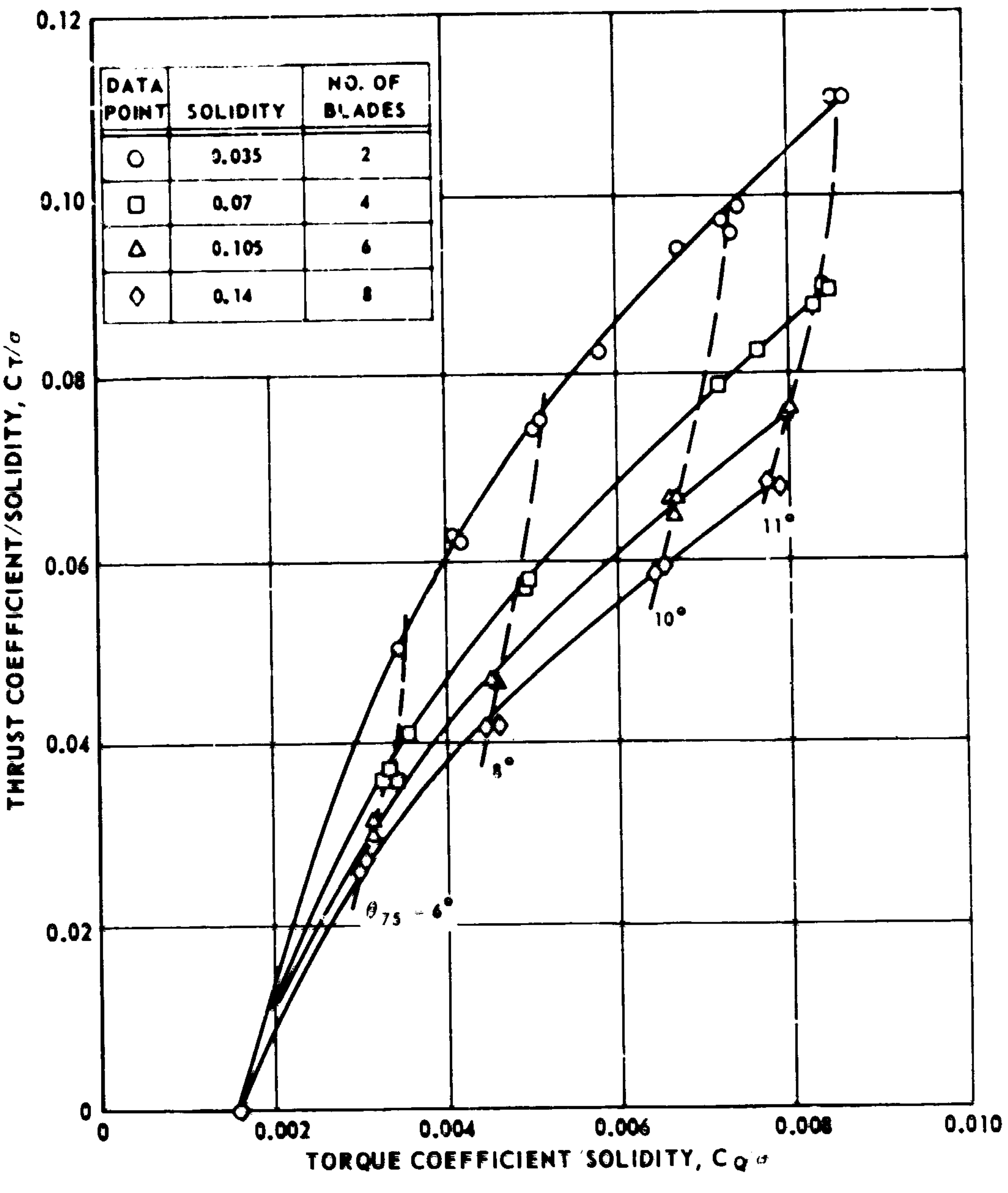

(c) ΩR = 525 FPS

Figure 15. Concluded.

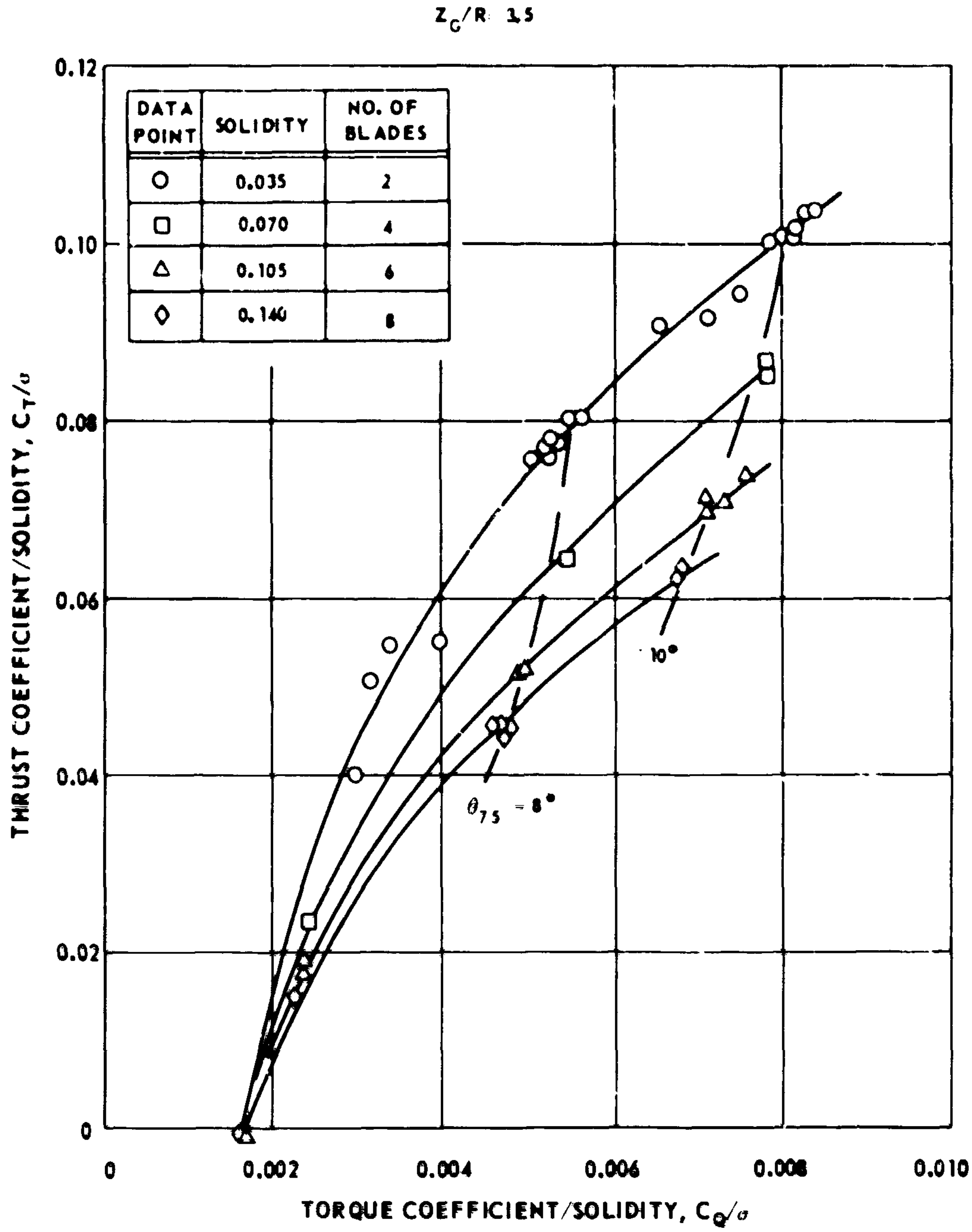

(a) ΩR = 700 FPS

Figure 16. Experimental Model Rotor Performance -- θ_1 = -8°, AR = 18.2.

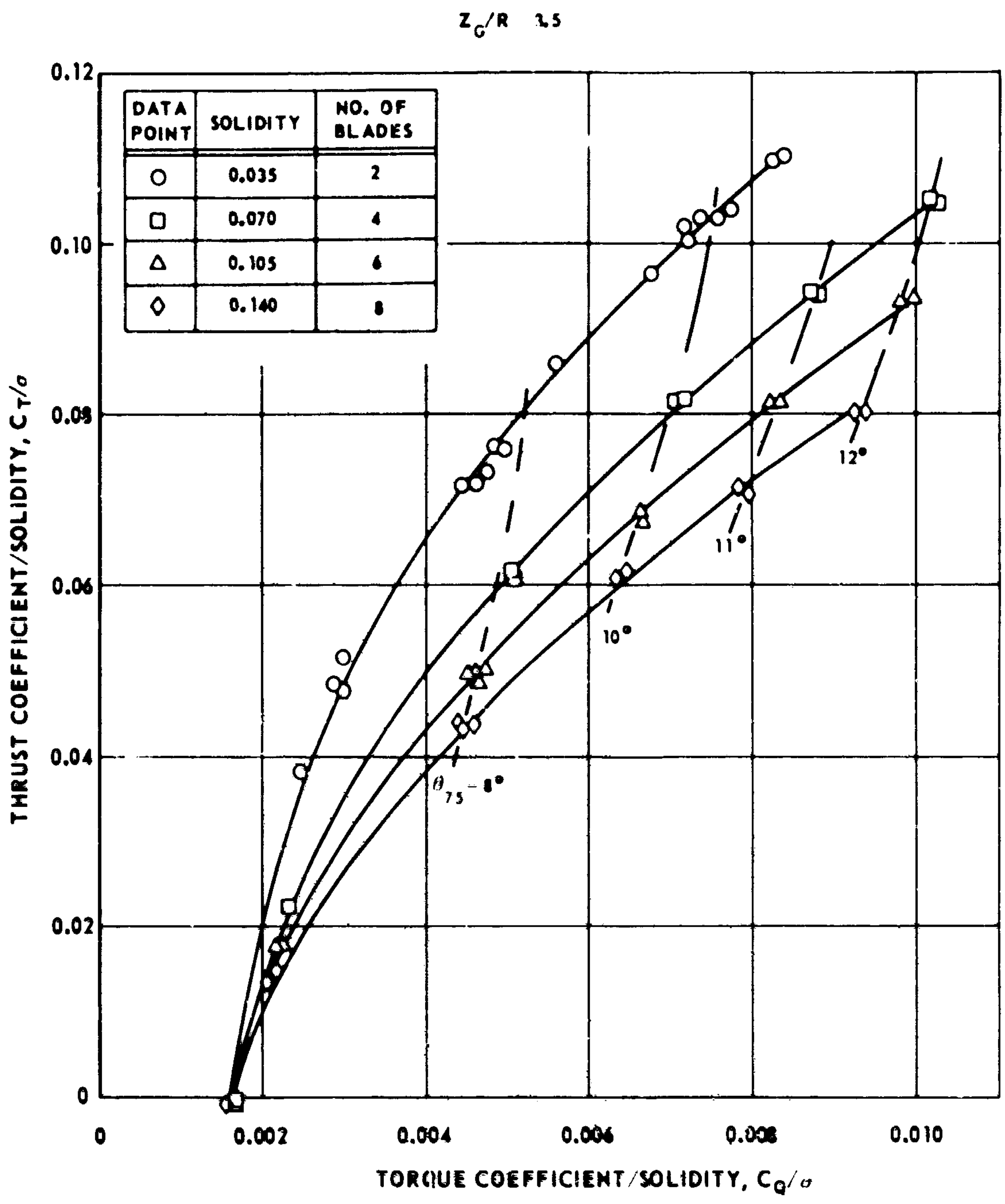

(b) ΩR = 525 FPS

Figure 16. Concluded.

Z_G/R 3.5

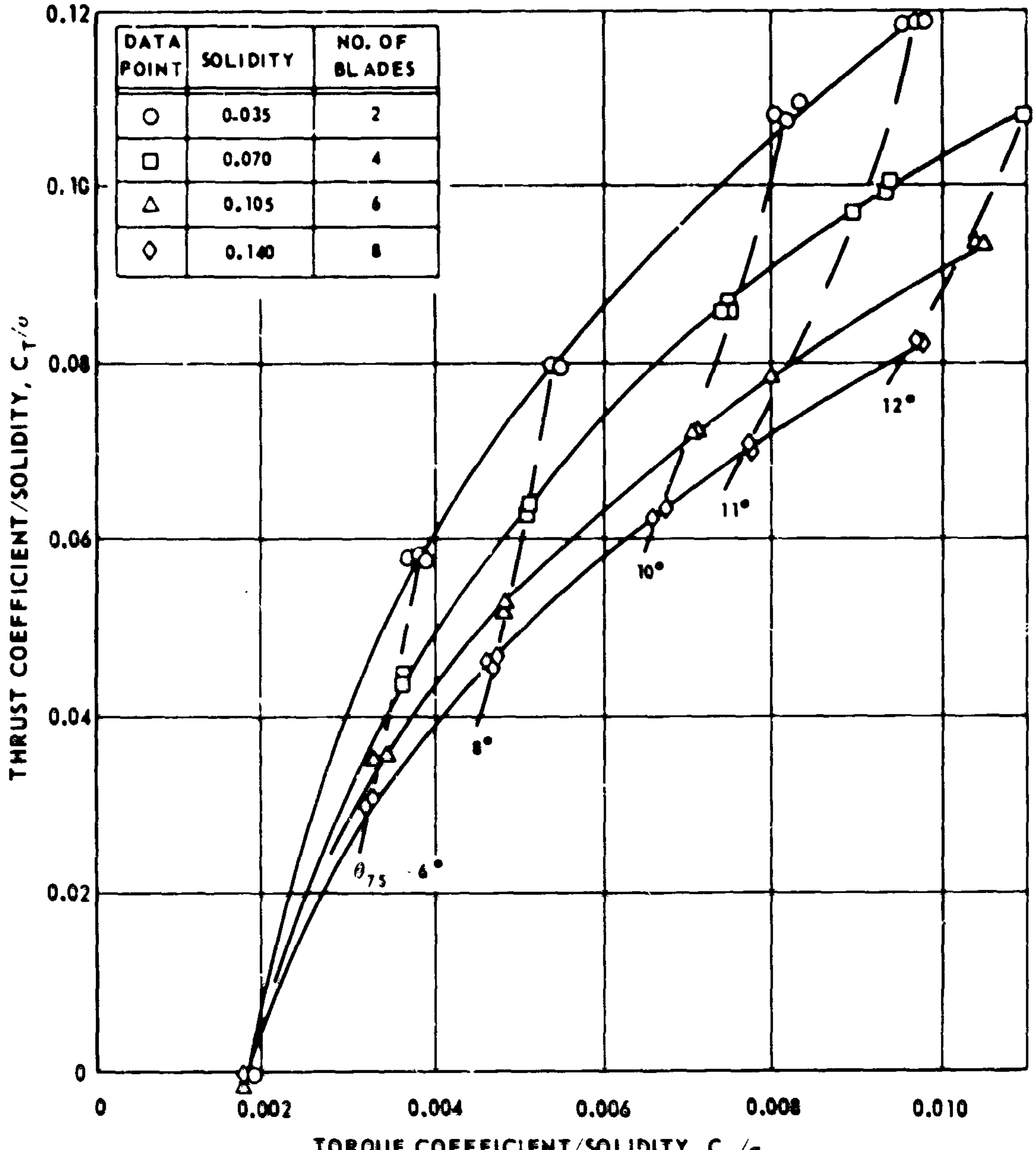

(a) ΩR = 700 FPS

Figure 17. Experimental Model Rotor Performance -- θ_1 = -16°, AR = 18.2

$Z_G/R = 3.5$

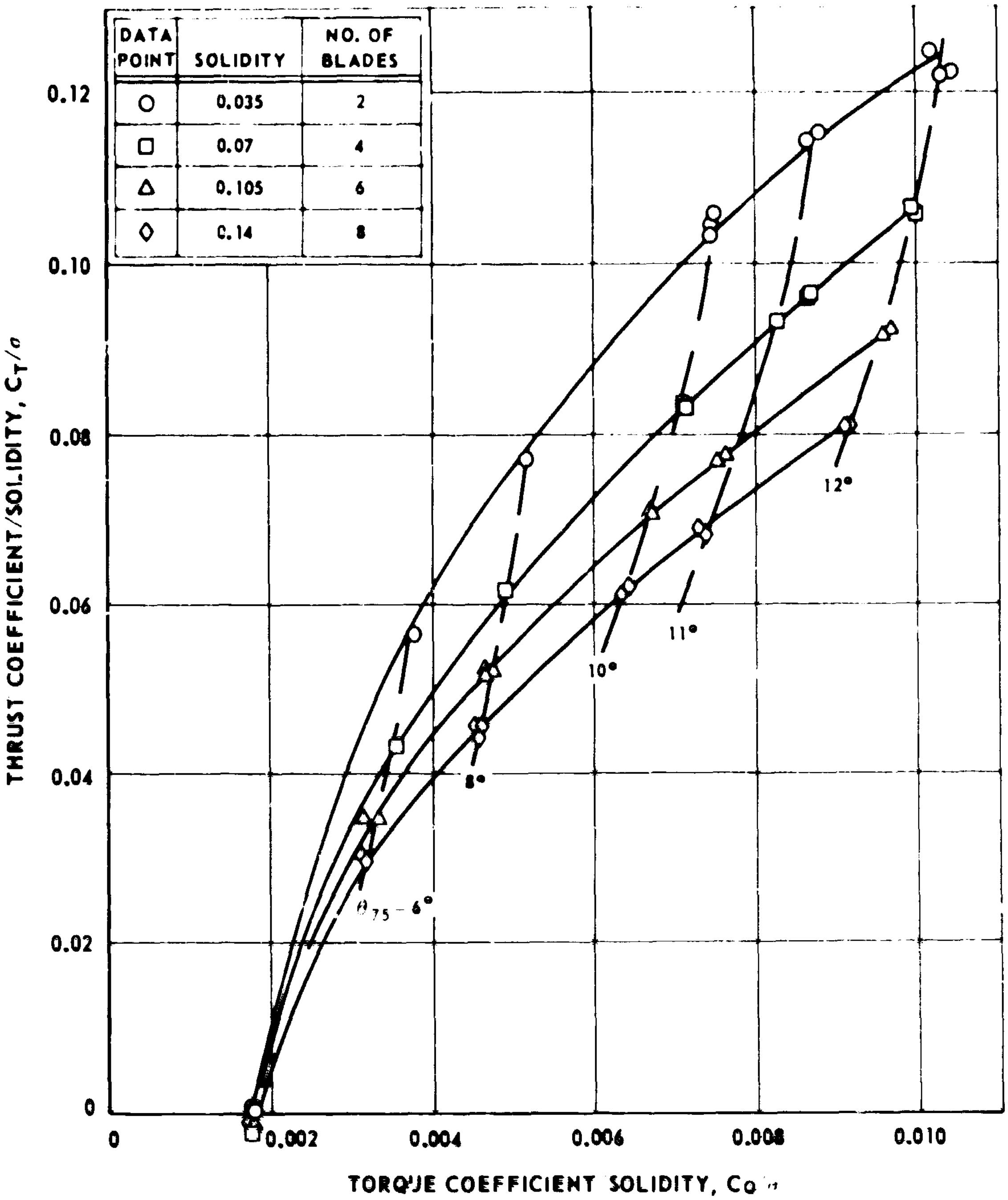

(b) ΩR = 600 FPS

Figure 17. Continued.

Z_G/R 3.5

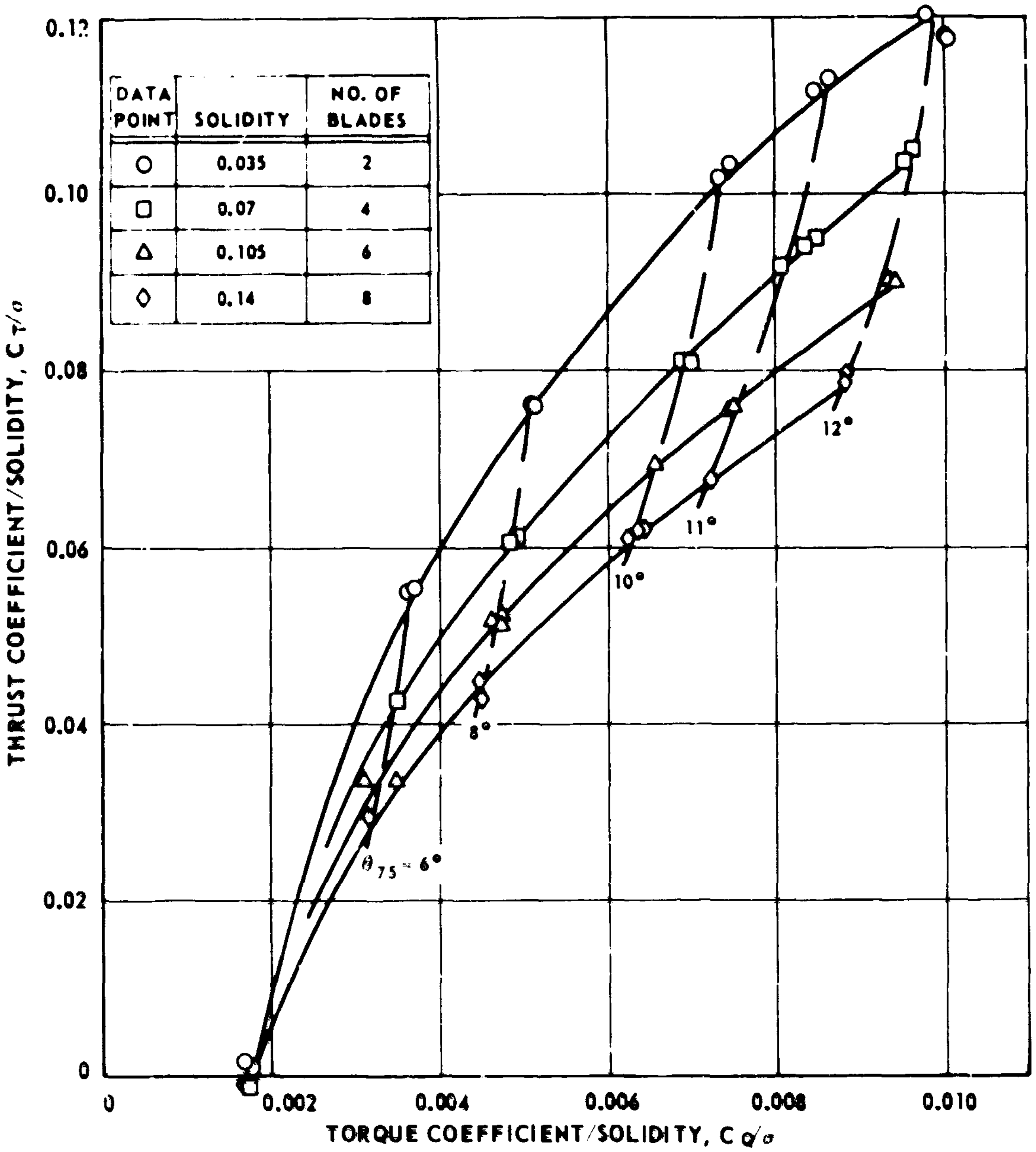

(c) ΩR = 525 FPS

Figure 17. Concluded.

Z_G/R 3.5

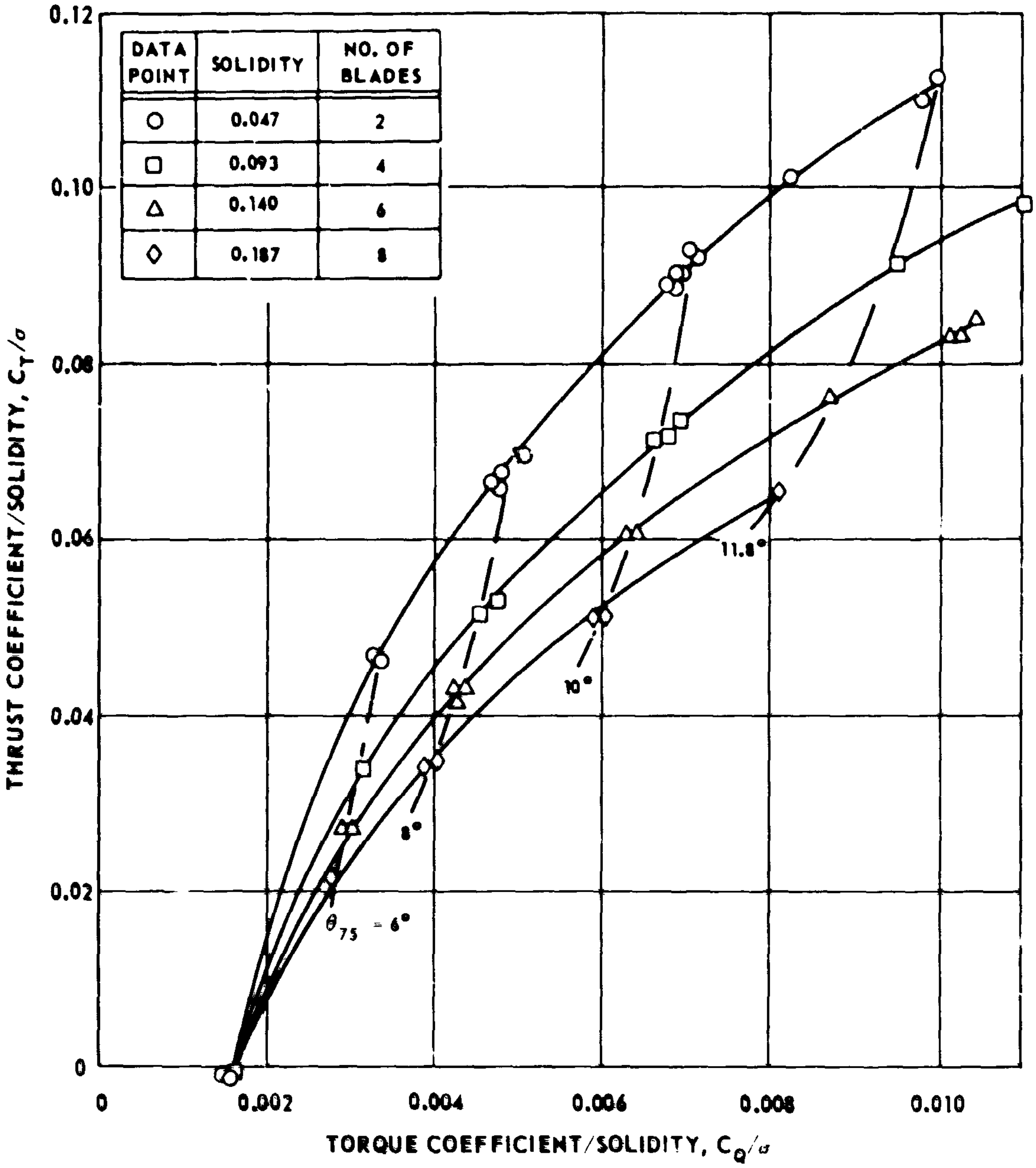

(a) ΩR = 700 FPS

Figure 18. Experimental Model Rotor Performance -- θ_1 = -8°, AR = 13.6.

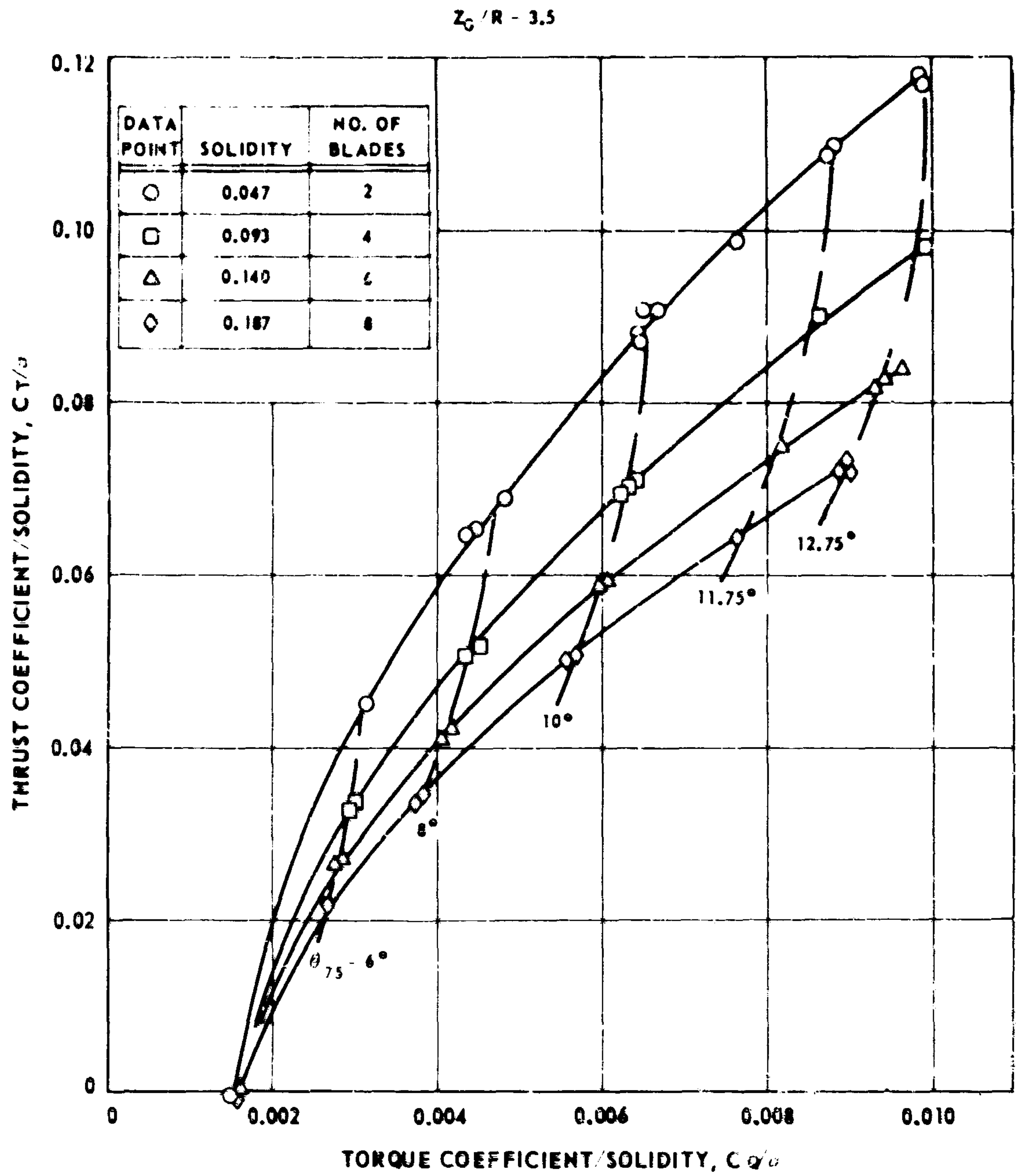

(b) ΩR = 525 FPS

Figure 18. Concluded.

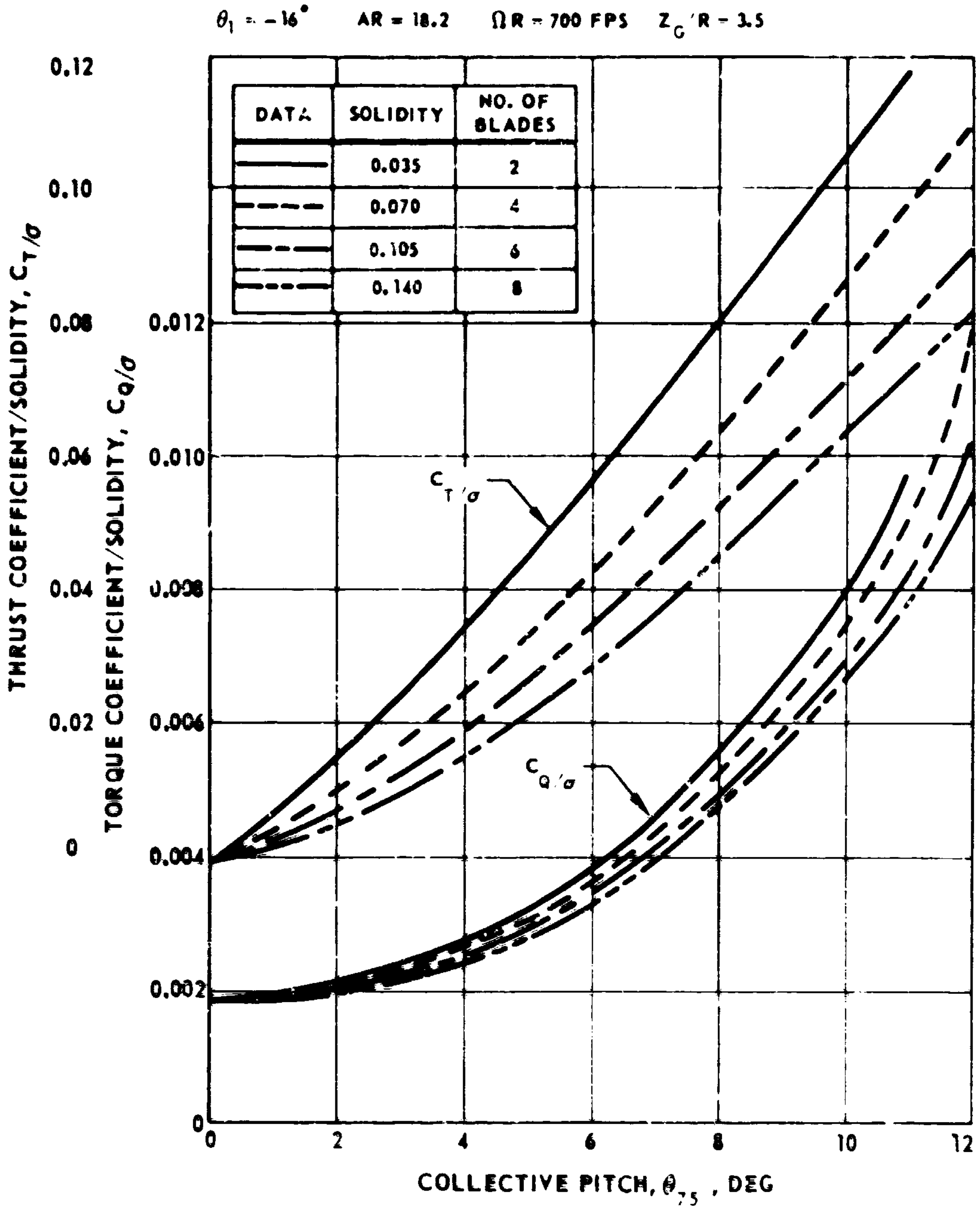

Figure 19. Typical Effect of Collective Pitch on Model Rotor Performance.

$\theta_1 = -8°$ AR = 18.2 ΩR = 700 FPS Z_G/R = 3.5

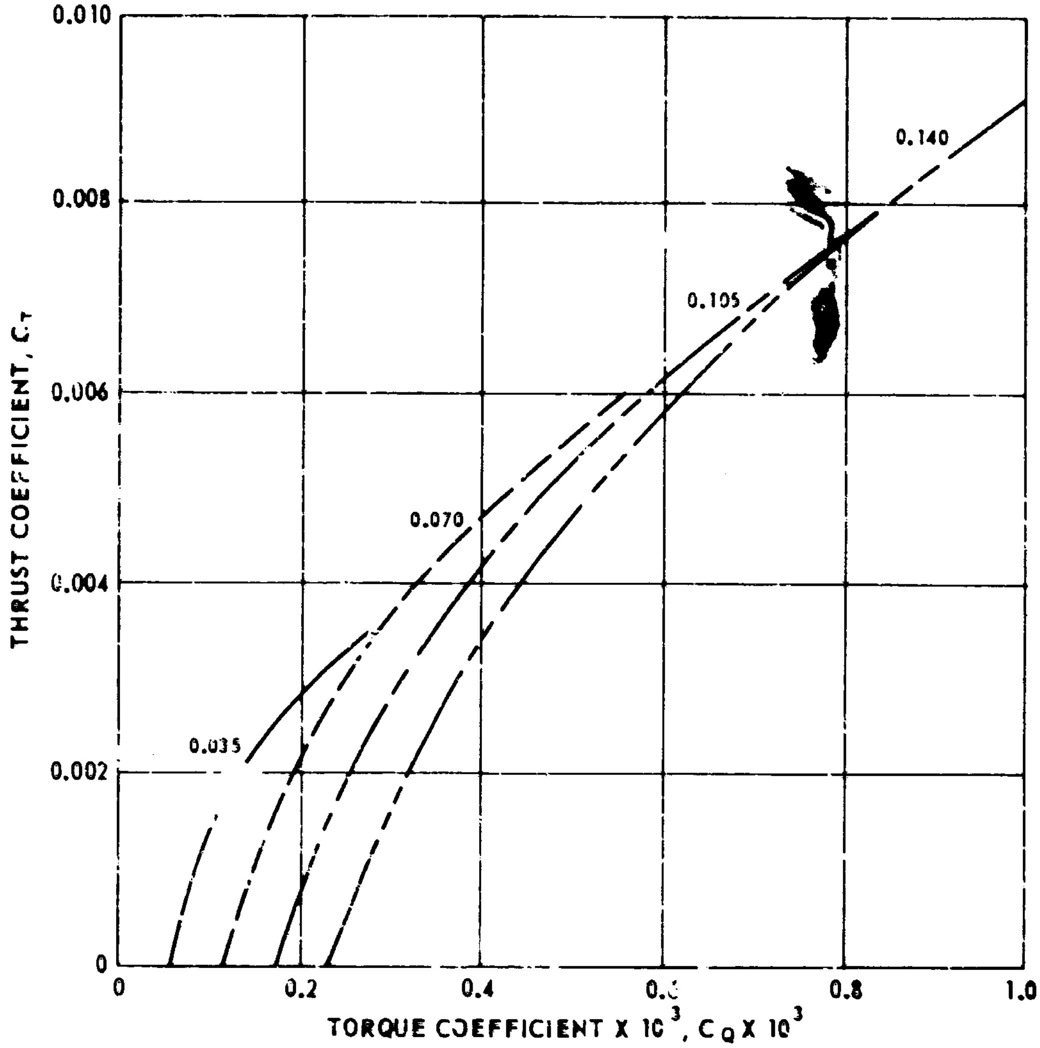

Figure 20. Typical Experimental Model Rotor Performance Expressed in Terms of Thrust and Torque Coefficients.

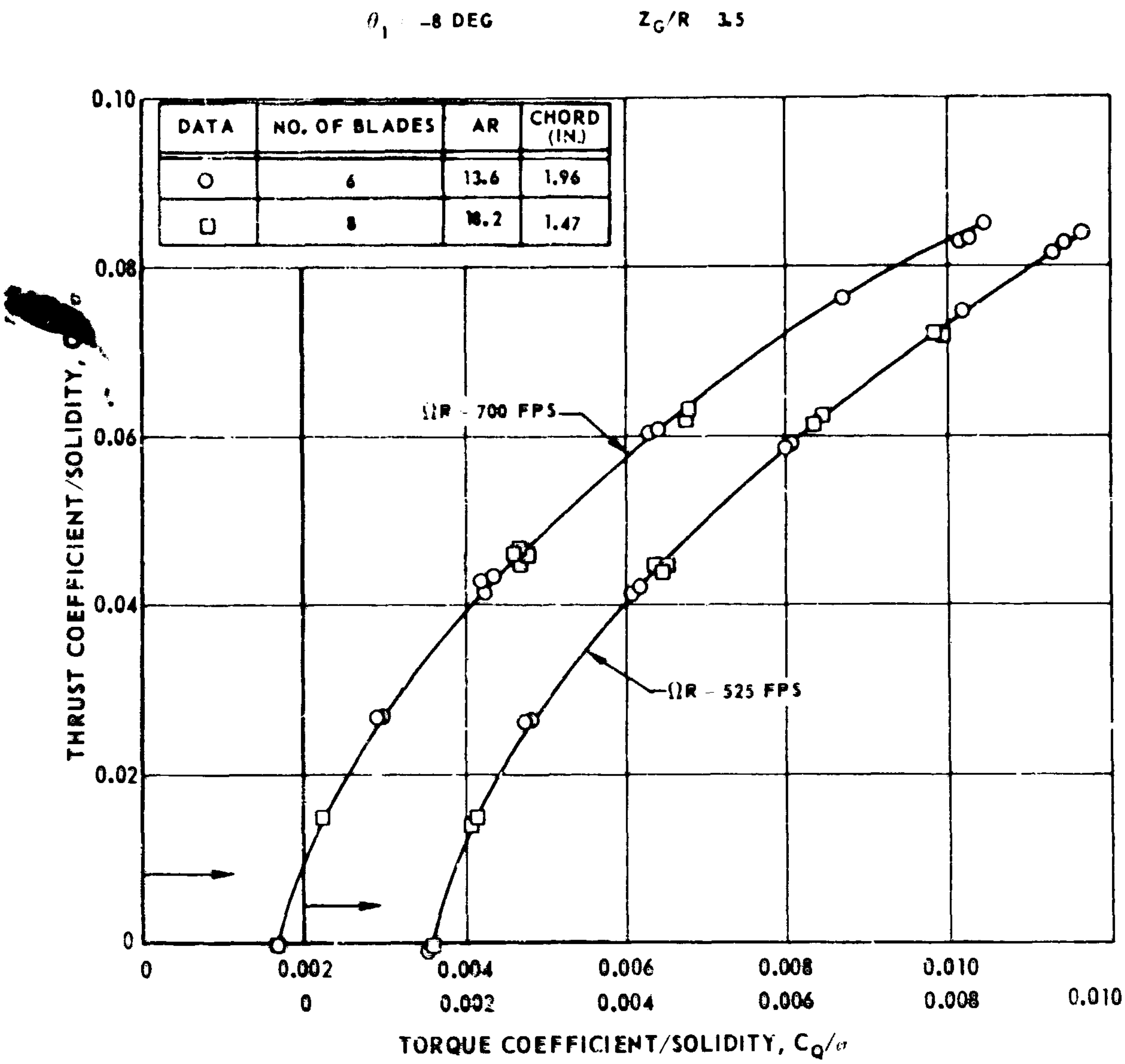

Figure 21. Effect of Aspect Ratio on Experimental Performance of Model Rotors Having a Solidity of 0.140.

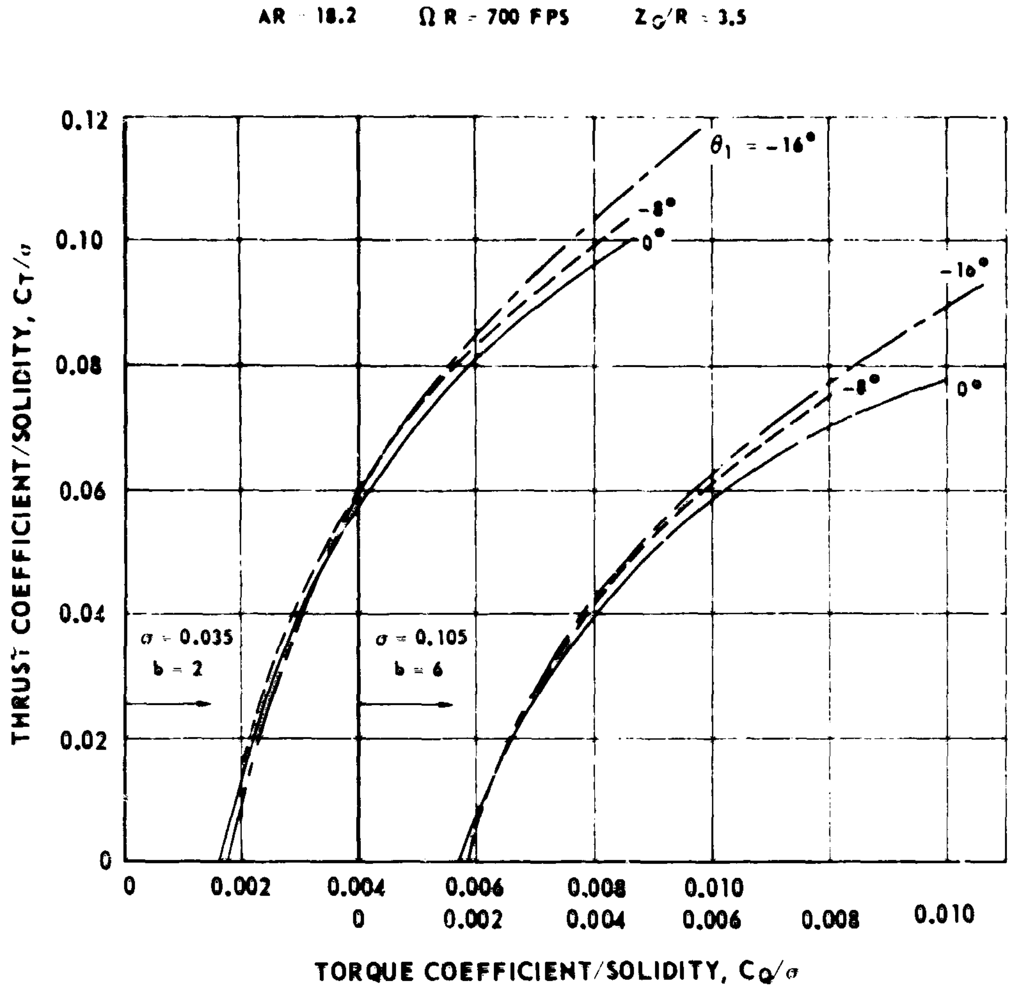

Figure 22. Effect of Blade Twist on Experimental Model Rotor Performance.

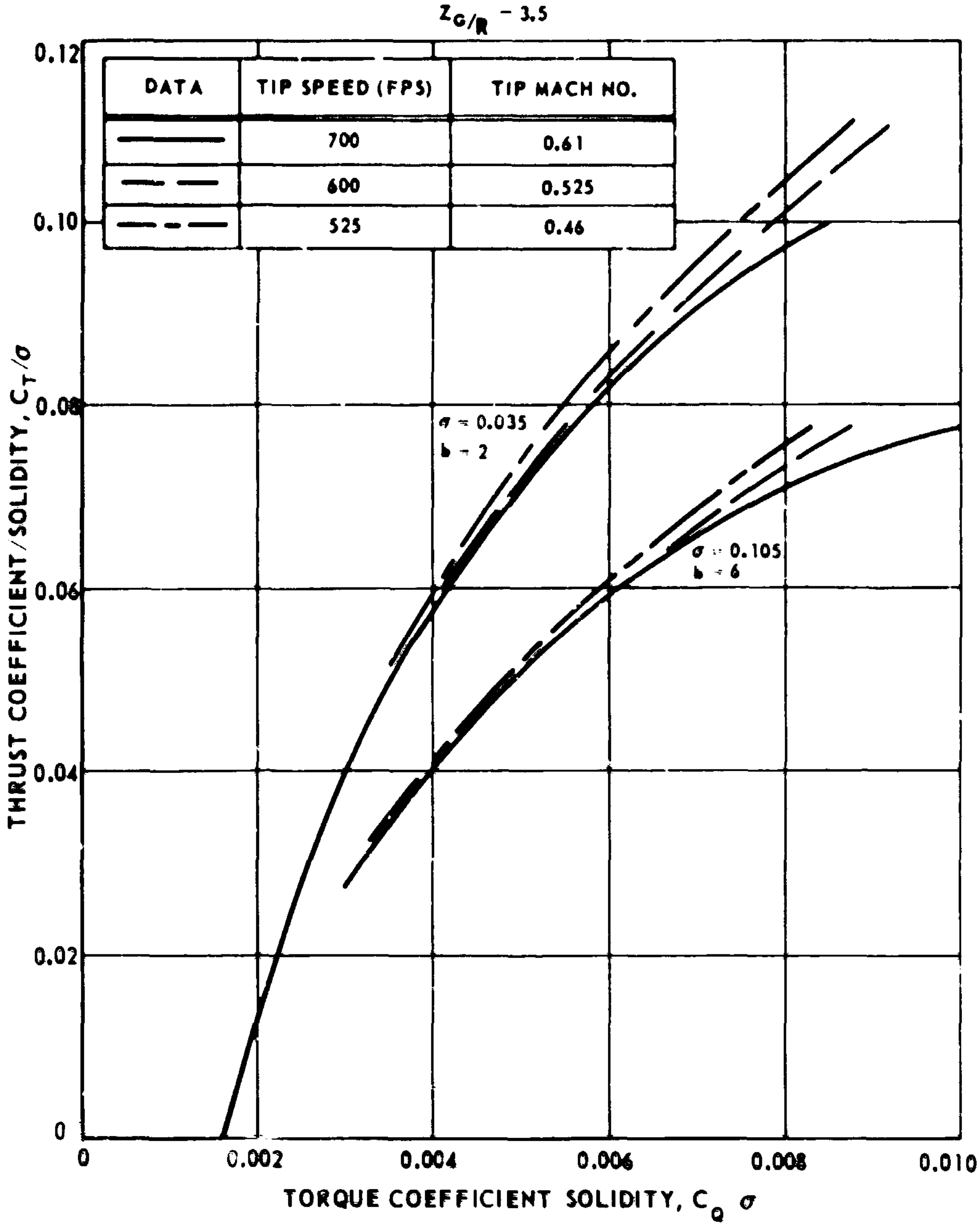

Figure 23. Effect of Tip Speed on Experimental Model Rotor Performance -- $\theta_1 = 0°$, AR = 18.2.

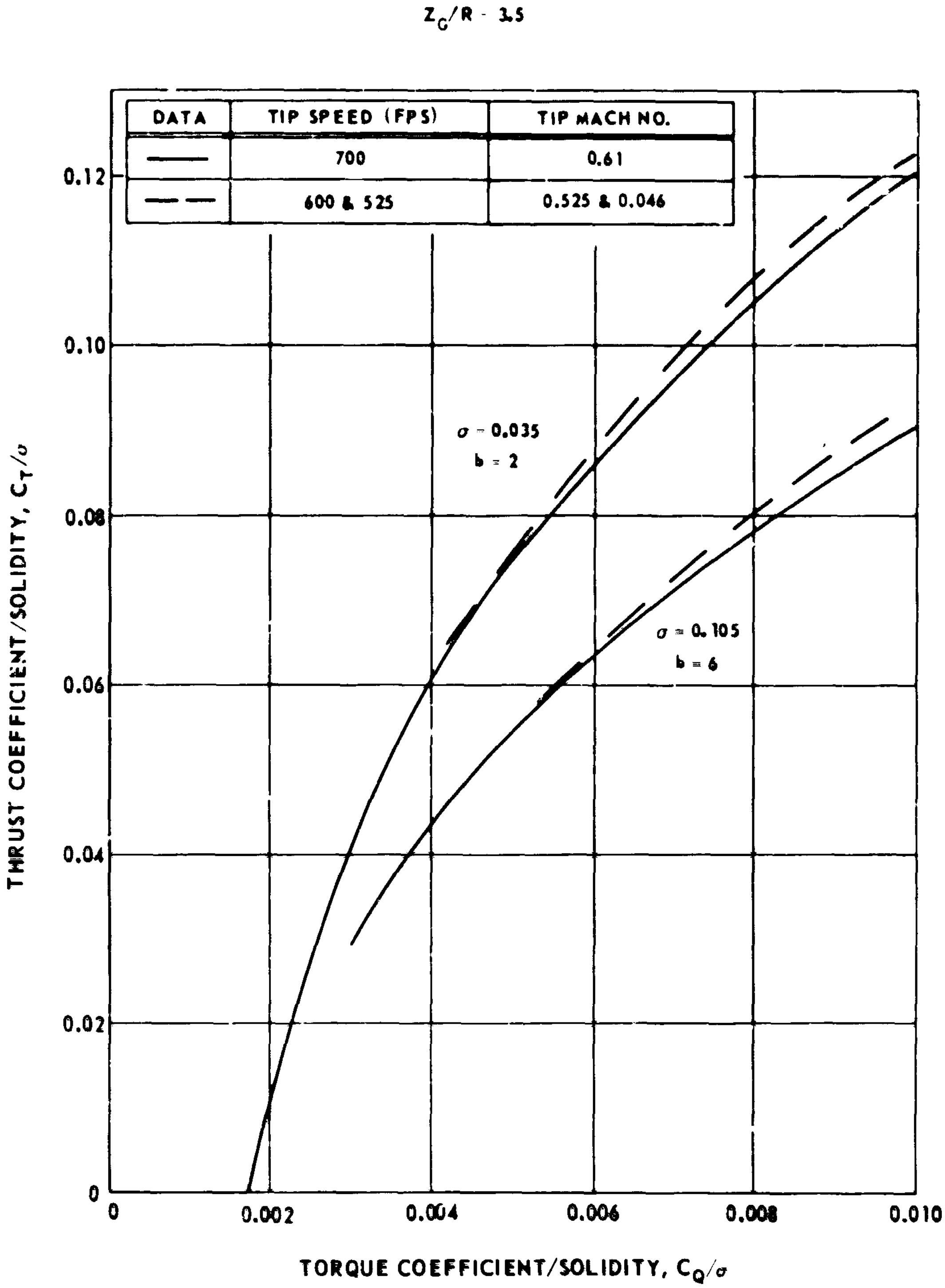

Figure 24. Effect of Tip Speed on Experimental Model Rotor Performance -- θ_1 = -16°, AR = 18.2.

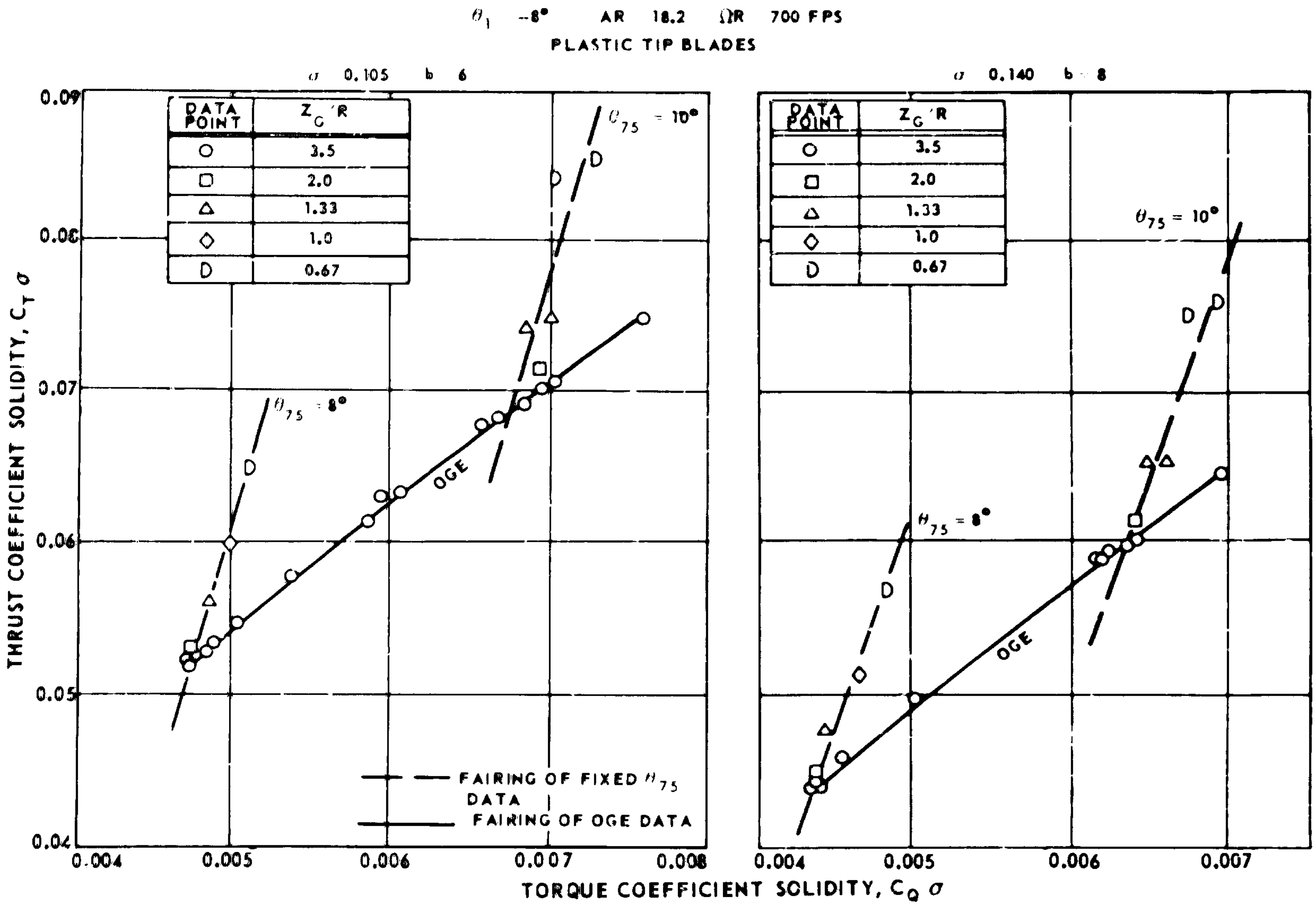

Figure 25. Experimental Model Rotor Performance for Various Rotor Heights Above the Ground.

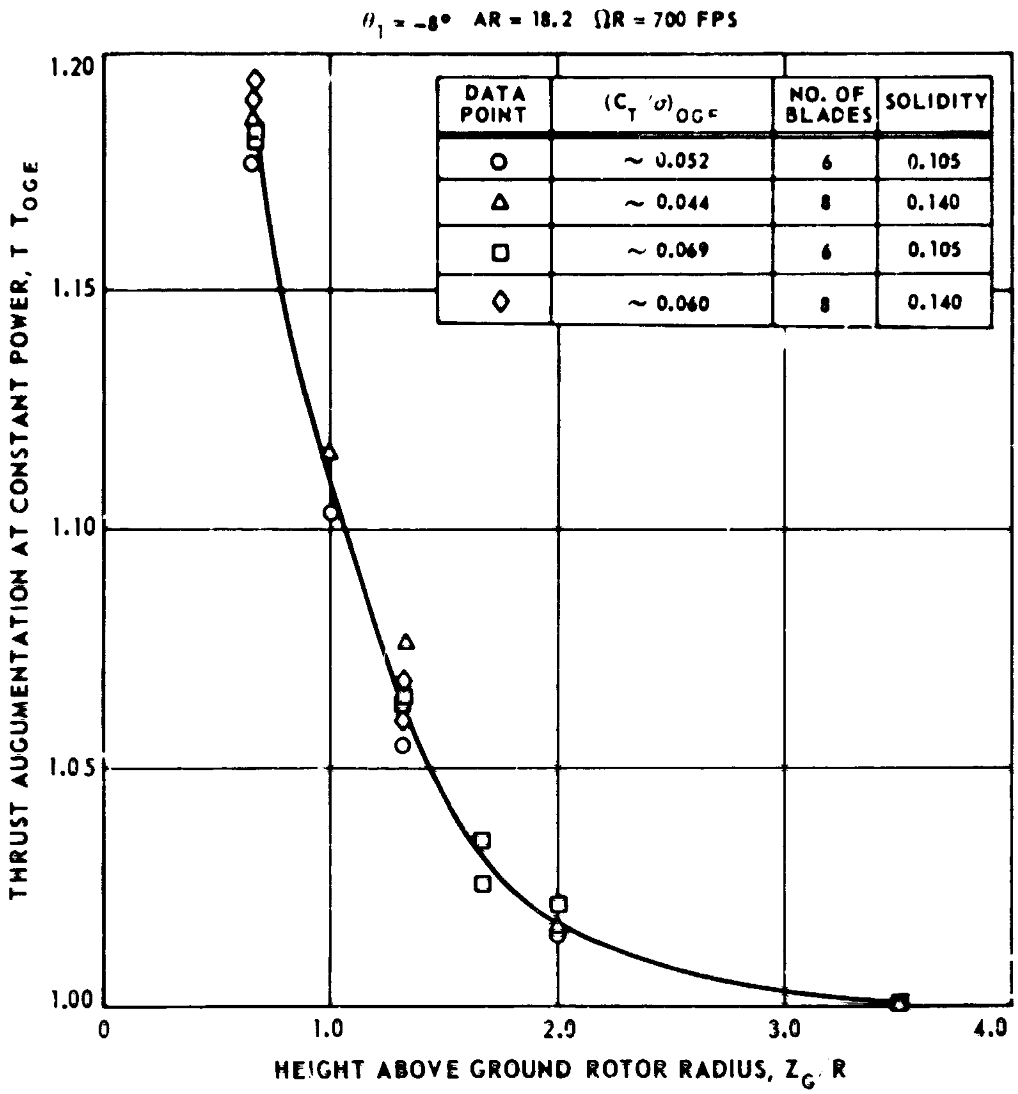

Figure 26. Effect of Rotor Height Above the Ground on Rotor Thrust Augmentation.

θ_1 0° AR 18.2 ΩR 700 FPS θ_{75} 8° $C_T/\sigma \sim 0.06$ Z_G/R 3.5

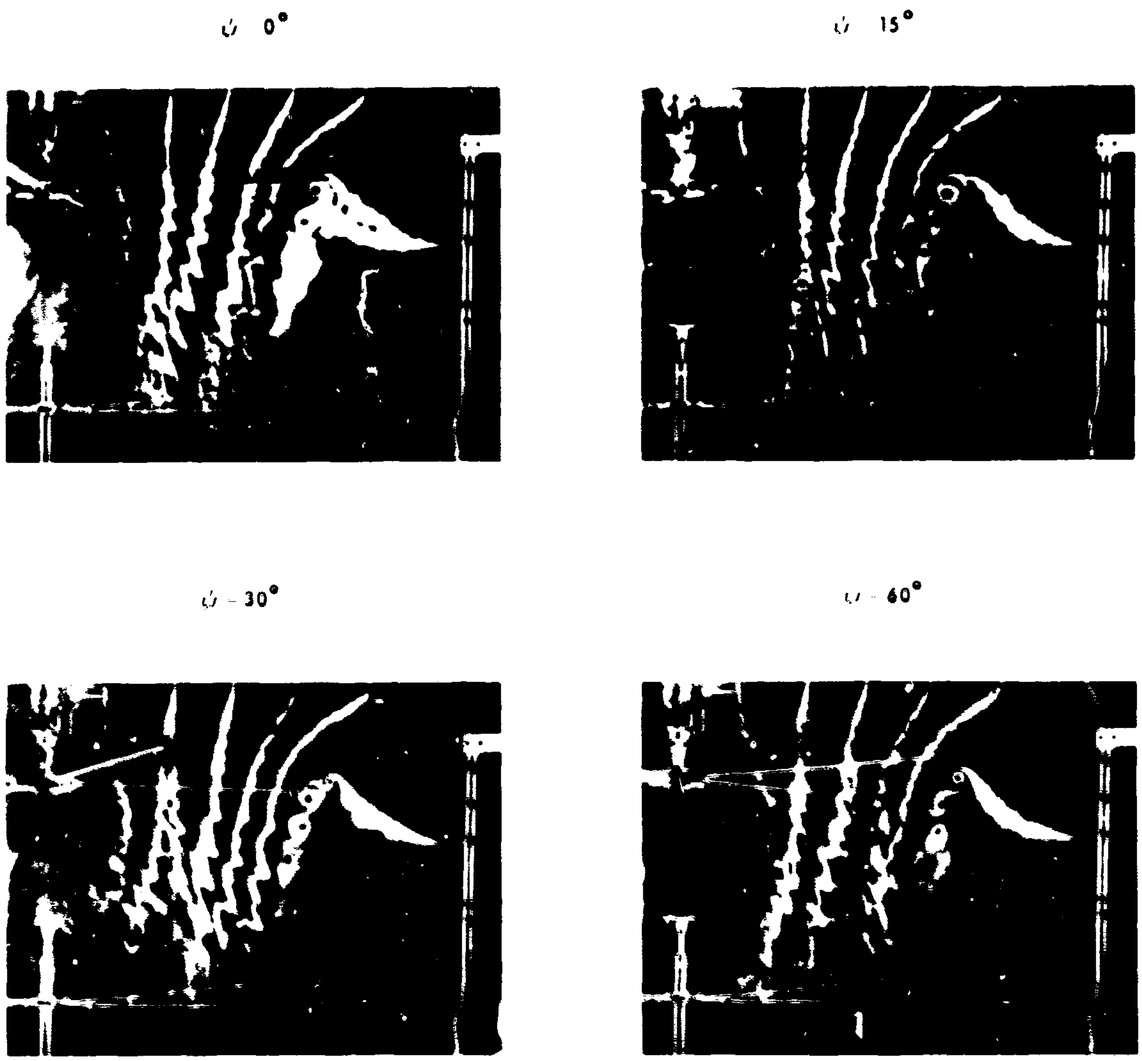

Figure 27. Sequence of Photographs Showing Time History of Wake -- b = 4.

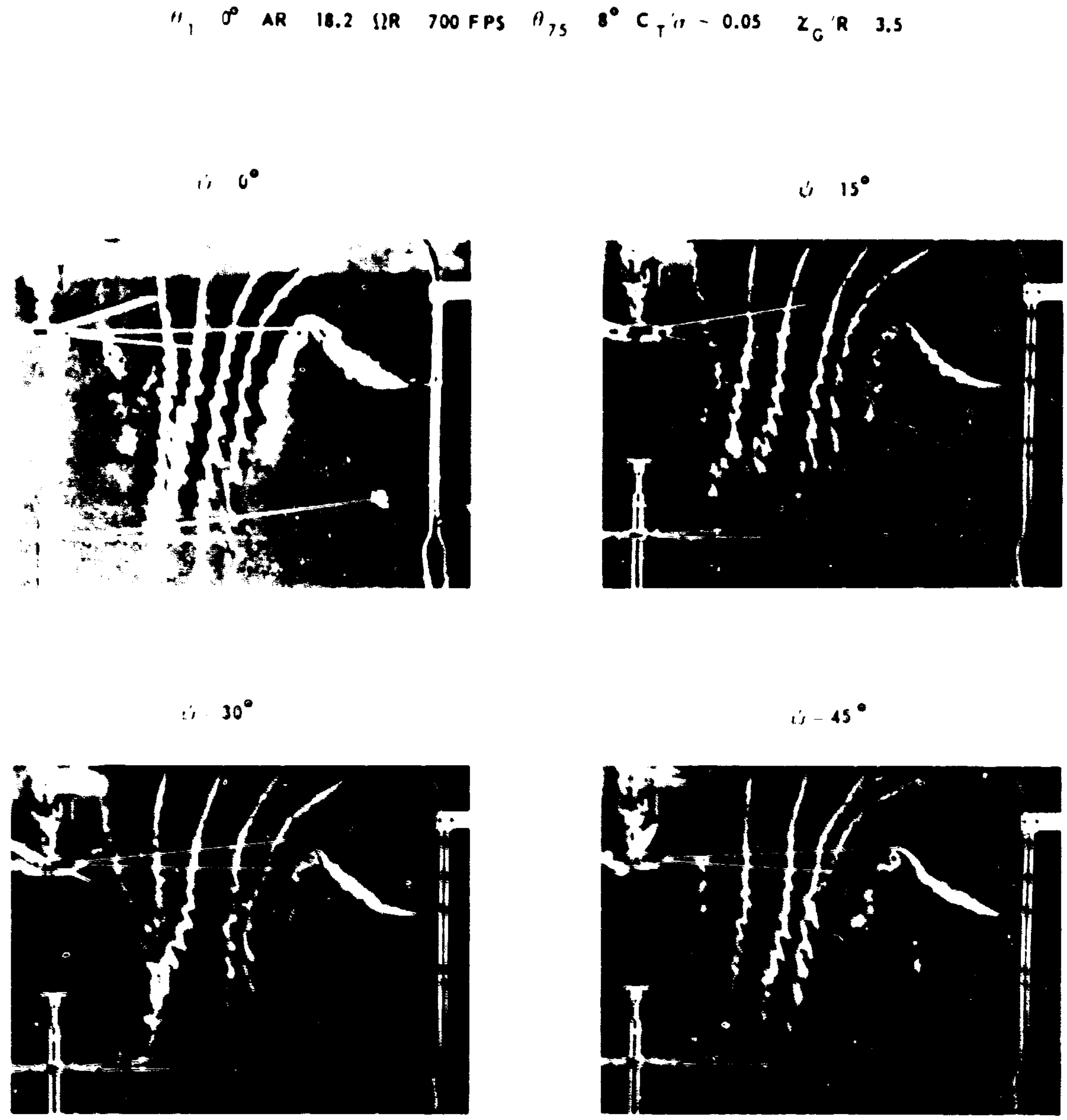

Figure [illegible]. Sequence of Photographs Showing Time History of Wake -- b = [illegible].

$\theta_1 = 0°$ AR = 18.2 ΩR = 700 FPS $\theta_{.75}$ = 8° $C_T/\sigma \sim 0.043$ Z_G/R = 3.5

$\psi = 0°$

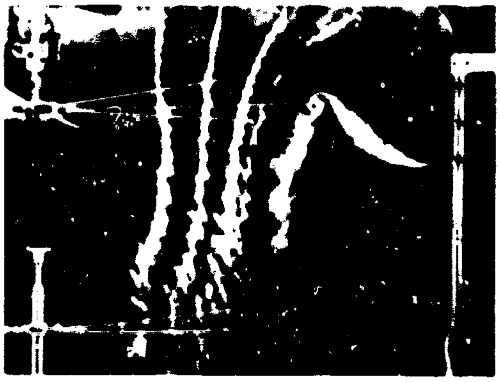

$\psi = 15°$

$\psi = 30°$

Figure 29. Sequence of Photographs Showing Time History of Wake -- b = 3.

$\theta_1 = 0°$ AR = 18.2   b = 2 ΩR = 700 FPS $\theta_{.75} = 9°$ $C_T/\sigma \sim 0.09$ $Z_G/R = 3.5$

$\psi = 0°$ $\psi = 15°$

$\psi = 30°$ $\psi = 60°$

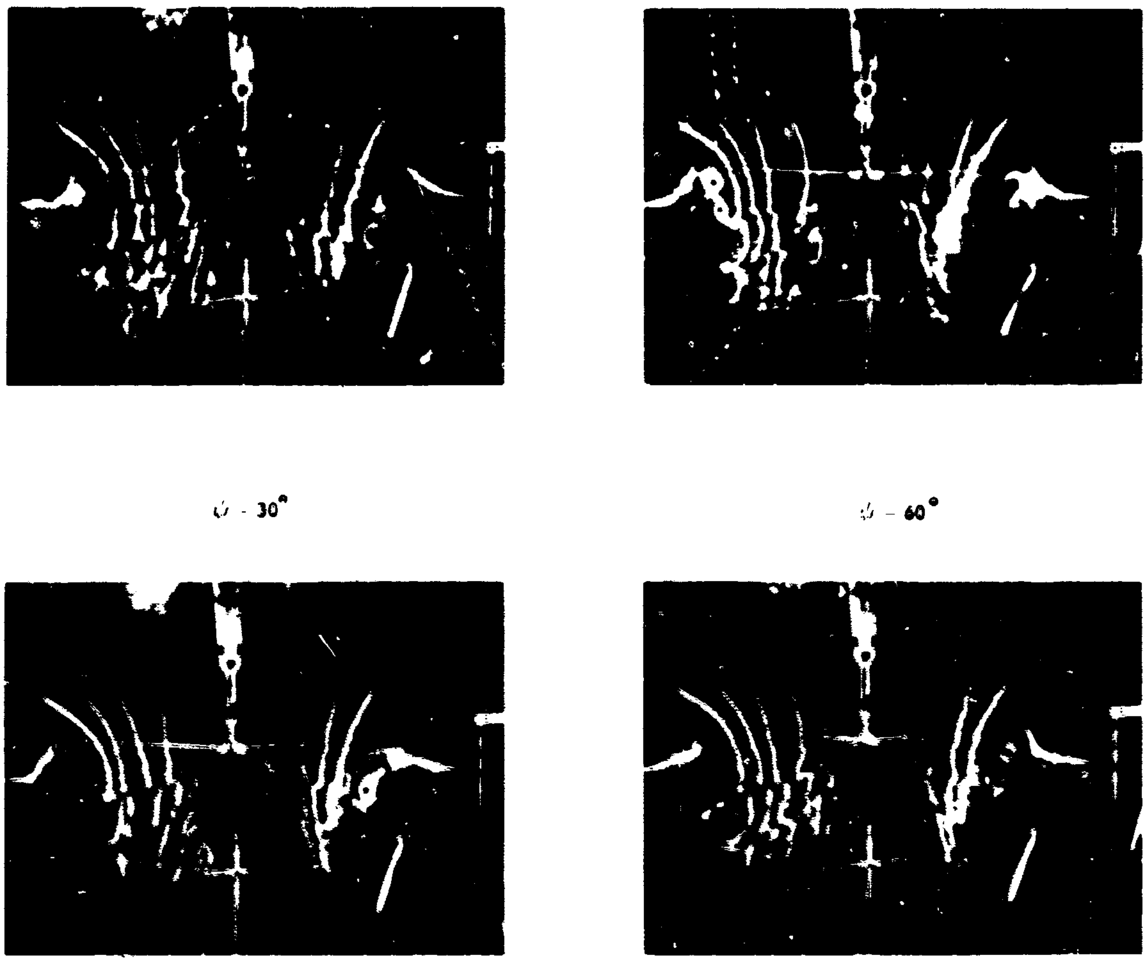

(a) $\psi = 0°$ to $60°$

Figure 30. Sequence of Photographs Showing Wake Instability.

ψ = 90°

ψ = 120°

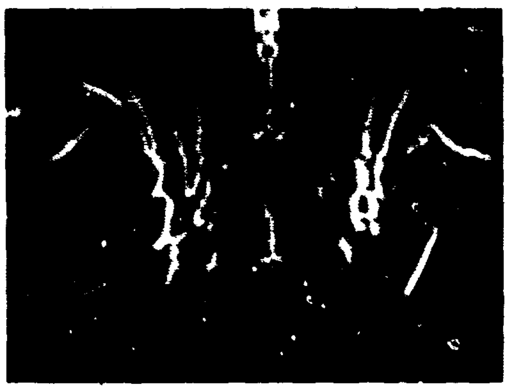

(b) ψ = 90° to 120°

Figure 30. Concluded.

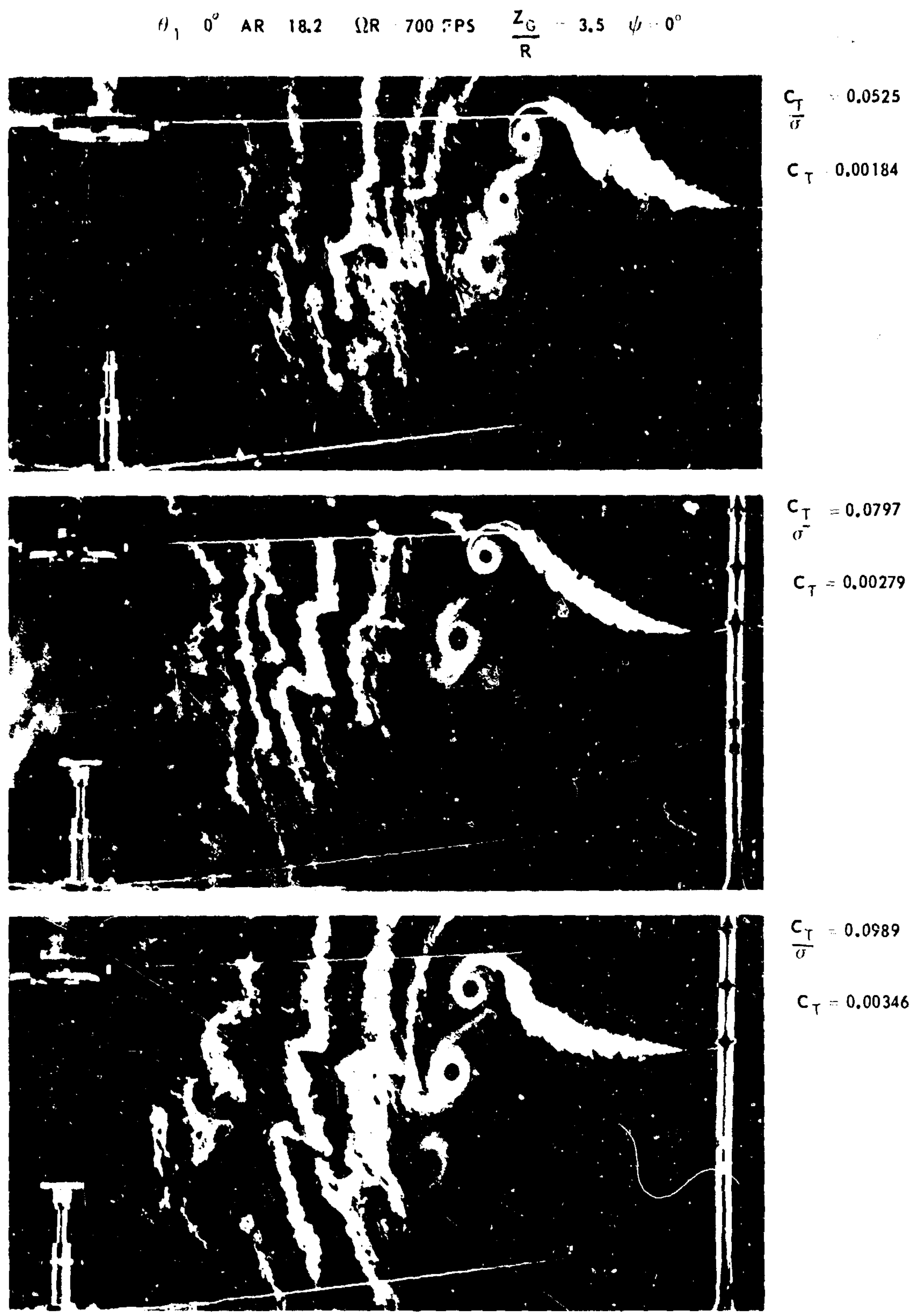

Figure 31. Photographs Showing Effect of Thrust on Wake Geometry -- b = 2.

$\theta_1 = 0°$ AR = 18.2 b = 2 ΩR = 700 FPS $C_T/\sigma \sim 0.0989$ $C_T \sim 0.00346$ Z_G/R 3.5

Figure 32. Typical Wake Flow Time Exposure Photograph.

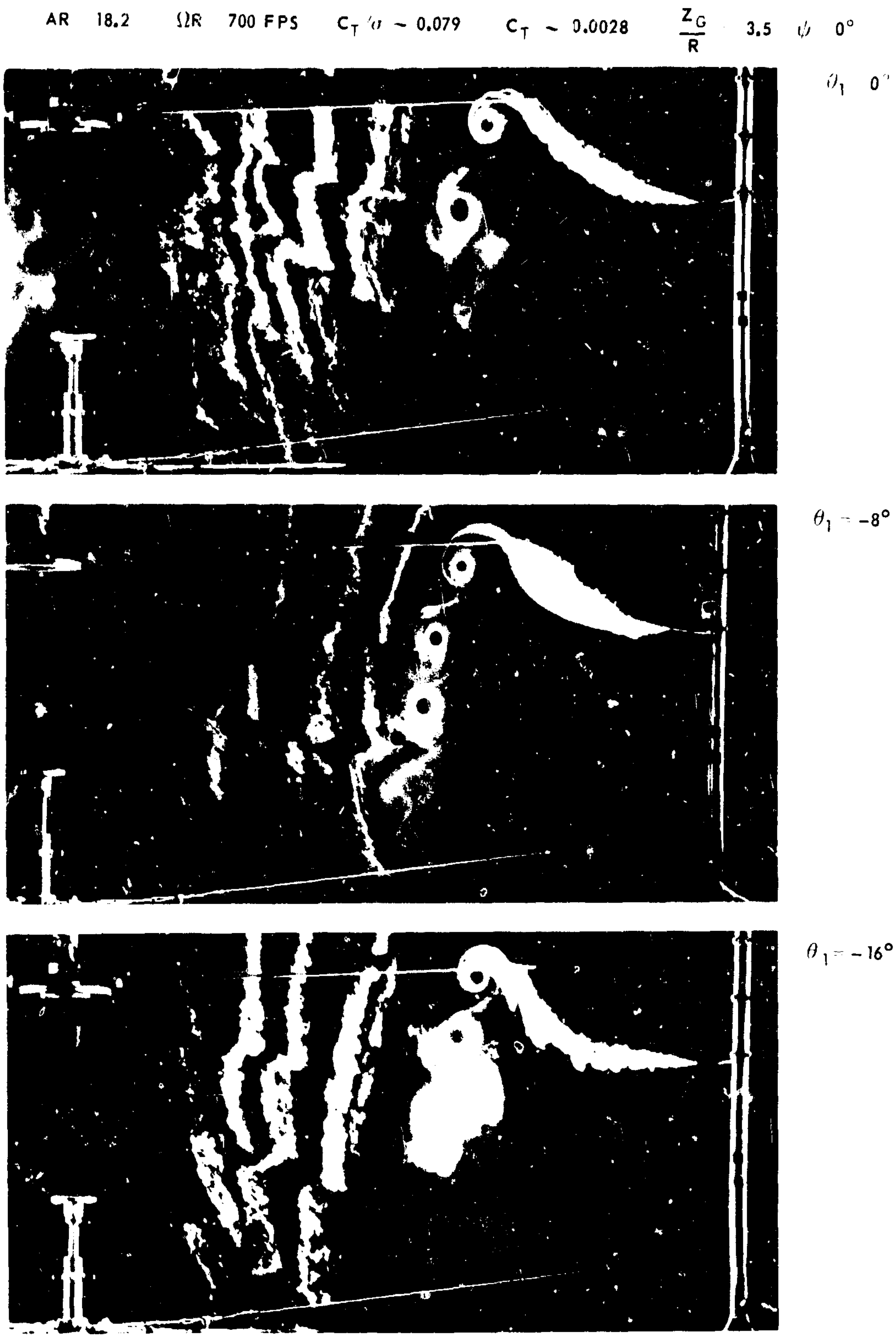

Figure 33. Photographs Showing Effect of Twist on Wake Geometry -- b = 2.

$\theta_1 = -8°$ AR = 18.2 ΩR = 700 FPS Z_G/R = 3.5 ψ = 0°

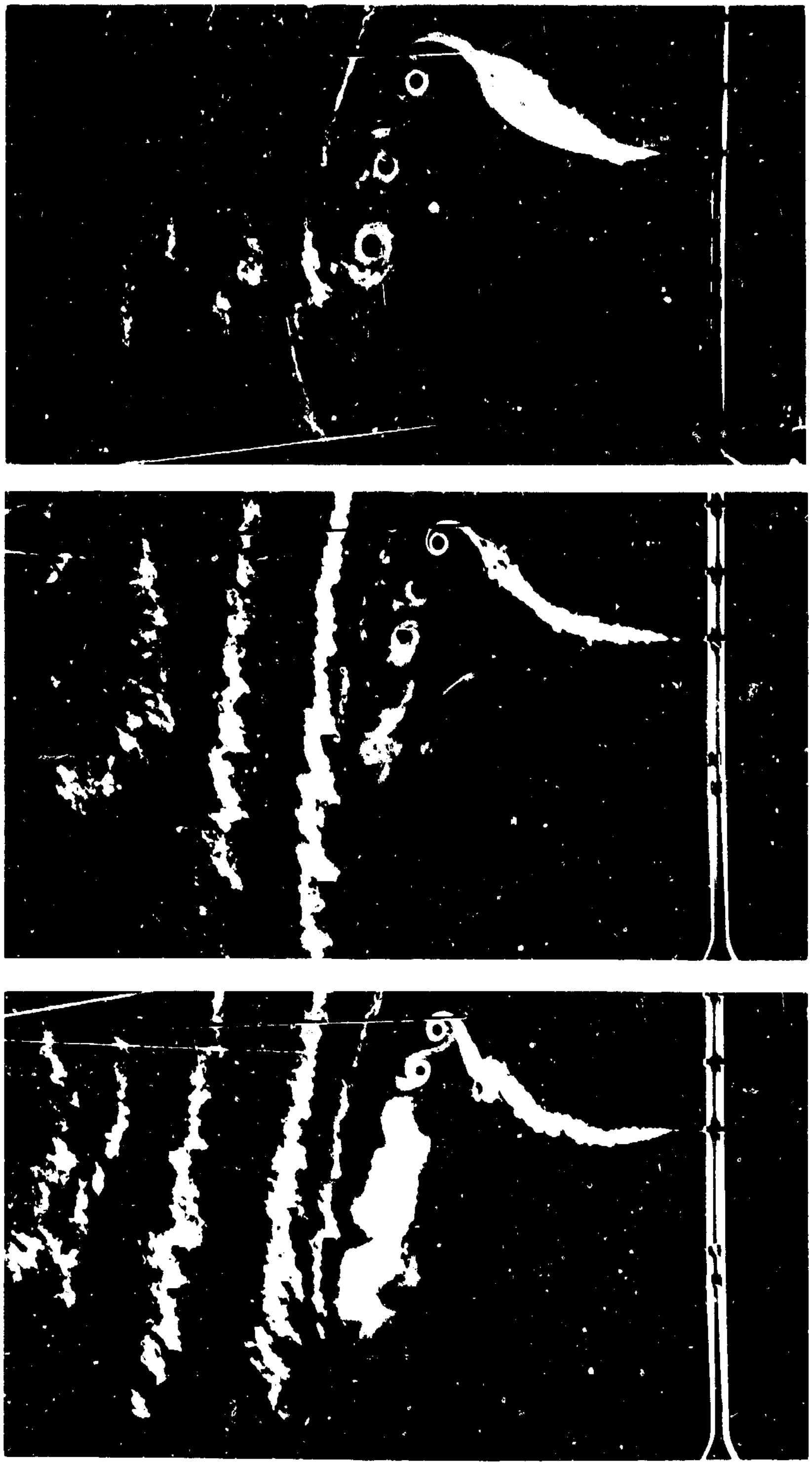

b = 2
$\frac{C_T}{\sigma}$ = 0.0771
C_T = 0.0027

b = 6
$\frac{C_T}{\sigma}$ = 0.0690
C_T = 0.00725

b = 8
$\frac{C_T}{\sigma}$ = 0.0597
C_T = 0.00836

Figure 34. Photographs Showing Effect of Number of Blades and Thrust Level on Wake Geometry.

θ_1 -8° ΩR 700 FPS $C_T \sim 0.0084$ $C_T/\sigma \sim 0.06$ Z_G/R 3.5 ψ 0°

AR 18.2 b = 8

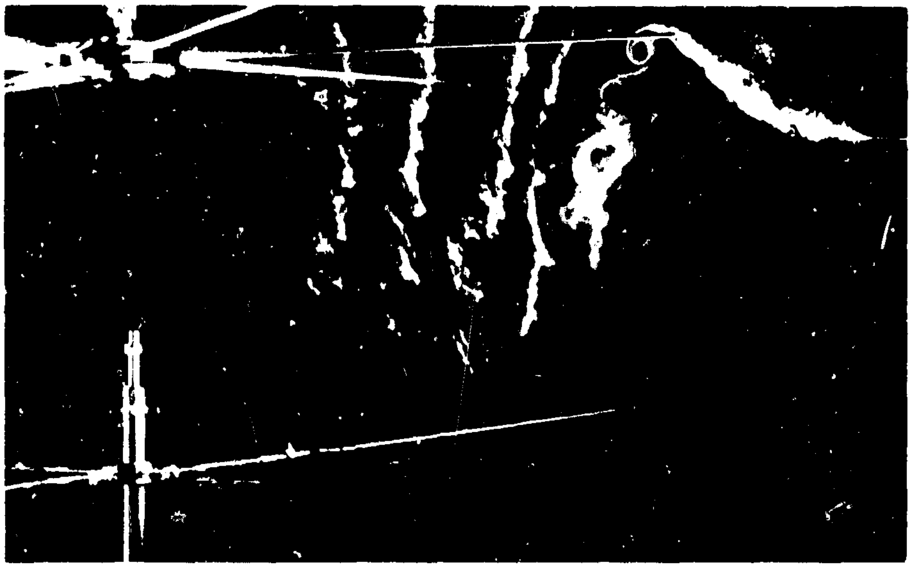

AR = 13.6 b = 6

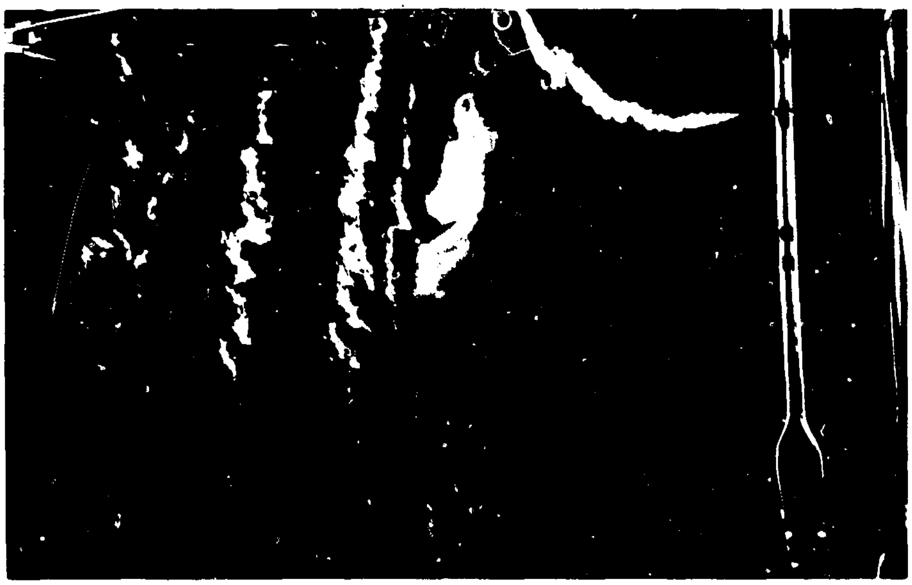

Figure 35. Photographs Showing Effect of Number of Blades on Wake Geometry for Rotor Solidity of 0.140.

θ_1 -8°   AR 13.6 θ_{75} 8° Z_G/R 3.5 ψ 0°

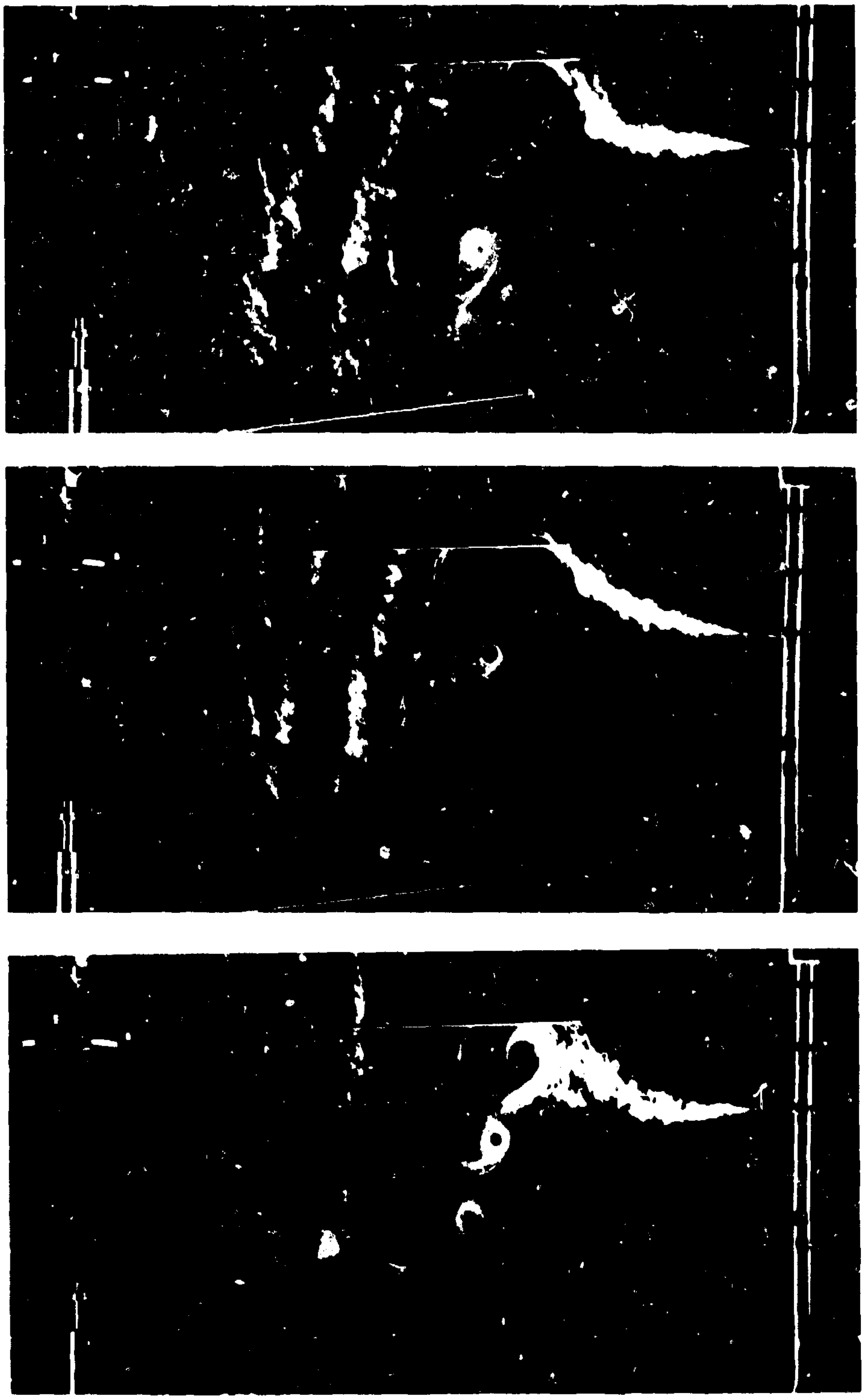

ΩR 525 FPS
C_T/σ 0.0695
C_T 0.00325

ΩR 600 FPS
C_T/σ 0.0681
C_T 0.00318

ΩR 700 FPS
C_T/σ 0.0678
C_T 0.00317

Figure 36. Effect of Tip Speed on Wake Geometry -- b = 2.

$\theta_1 = -8^\circ$ AR = 18.2 $\frac{Z_G}{R} = 3.5$ $\psi = 0^\circ$

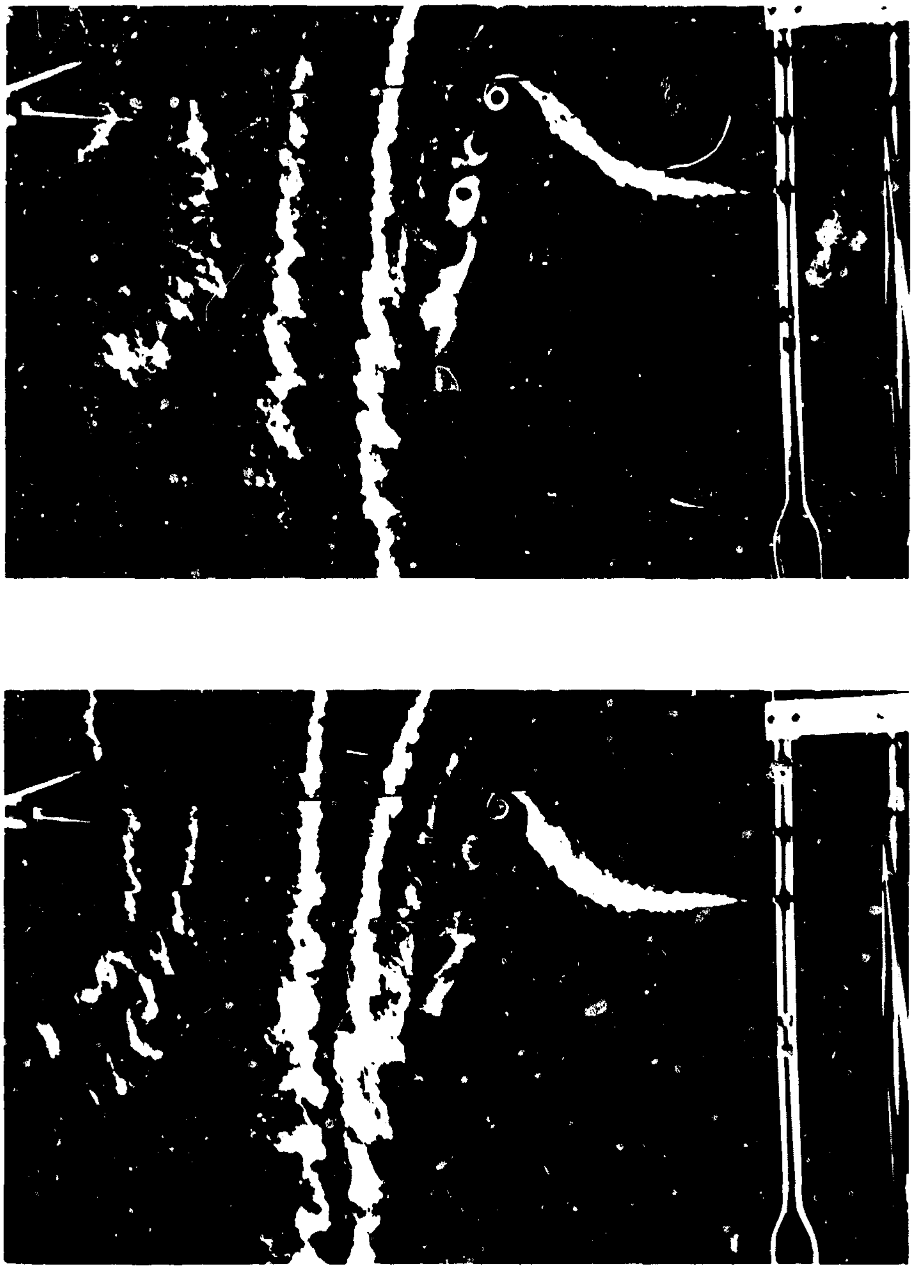

ΩR = 700 FPS
C_T/σ = 0.0690
C_T = 0.00725

ΩR = 600 FPS
C_T/σ = 0.0657
C_T = 0.00689

Figure 37. Photographs Showing Effect of Tip Speed on Wake Geometry -- b = 6.

$\theta_1 = -8°$ AR = 18.2 ΩR = 700 FPS $\theta_{75} \sim 10°$ Z_G/R 1.67 $\psi = 0°$

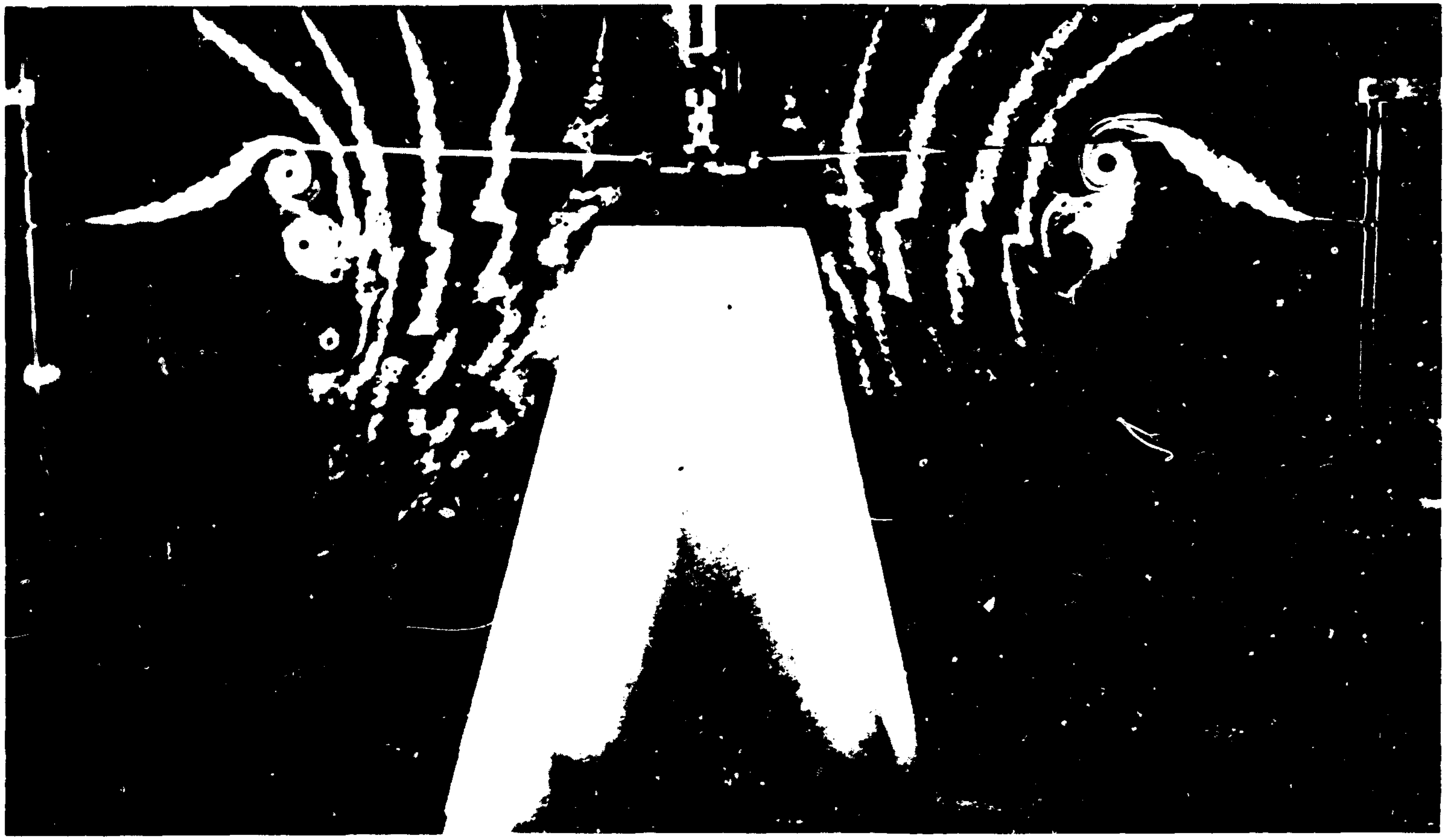

Figure 38. Photograph Showing Effect of Ground and Whirl Stand on Wake Geometry -- b = 2.

θ_1 -8° AR 18.2 ΩR 700 FPS θ_{75} 10° Z_G/R 1.67 ψ 0°

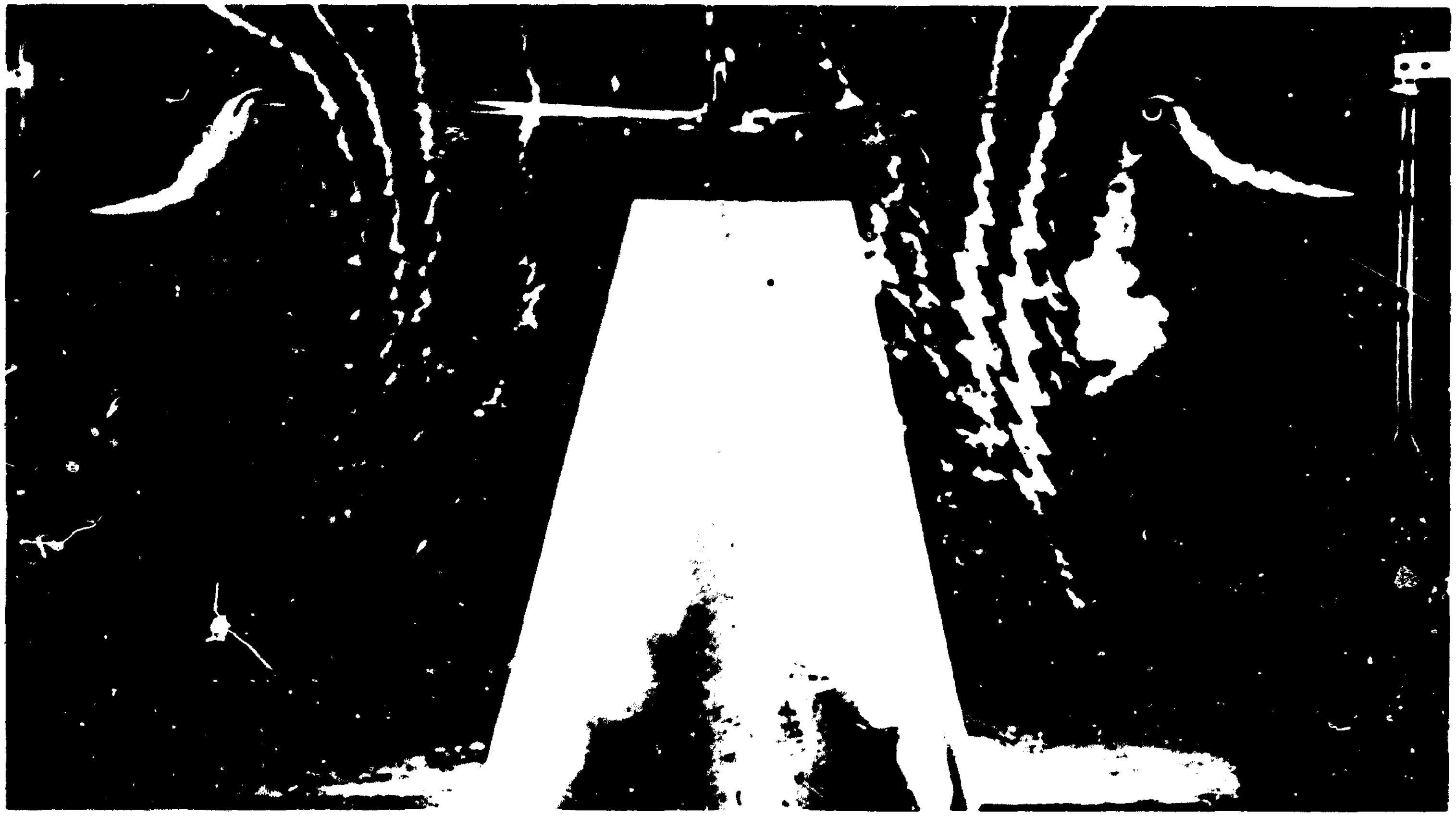

Figure 39. Photograph Showing Effect of Ground and Whirl Stand on Wake Geometry -- b = 6.

$\theta_t = -8°$ AR = 18.2 b = 6 ΩR 700 FPS $\theta_{75} \sim 10°$ $Z_G/R = 1.33$ $\psi = 0°$

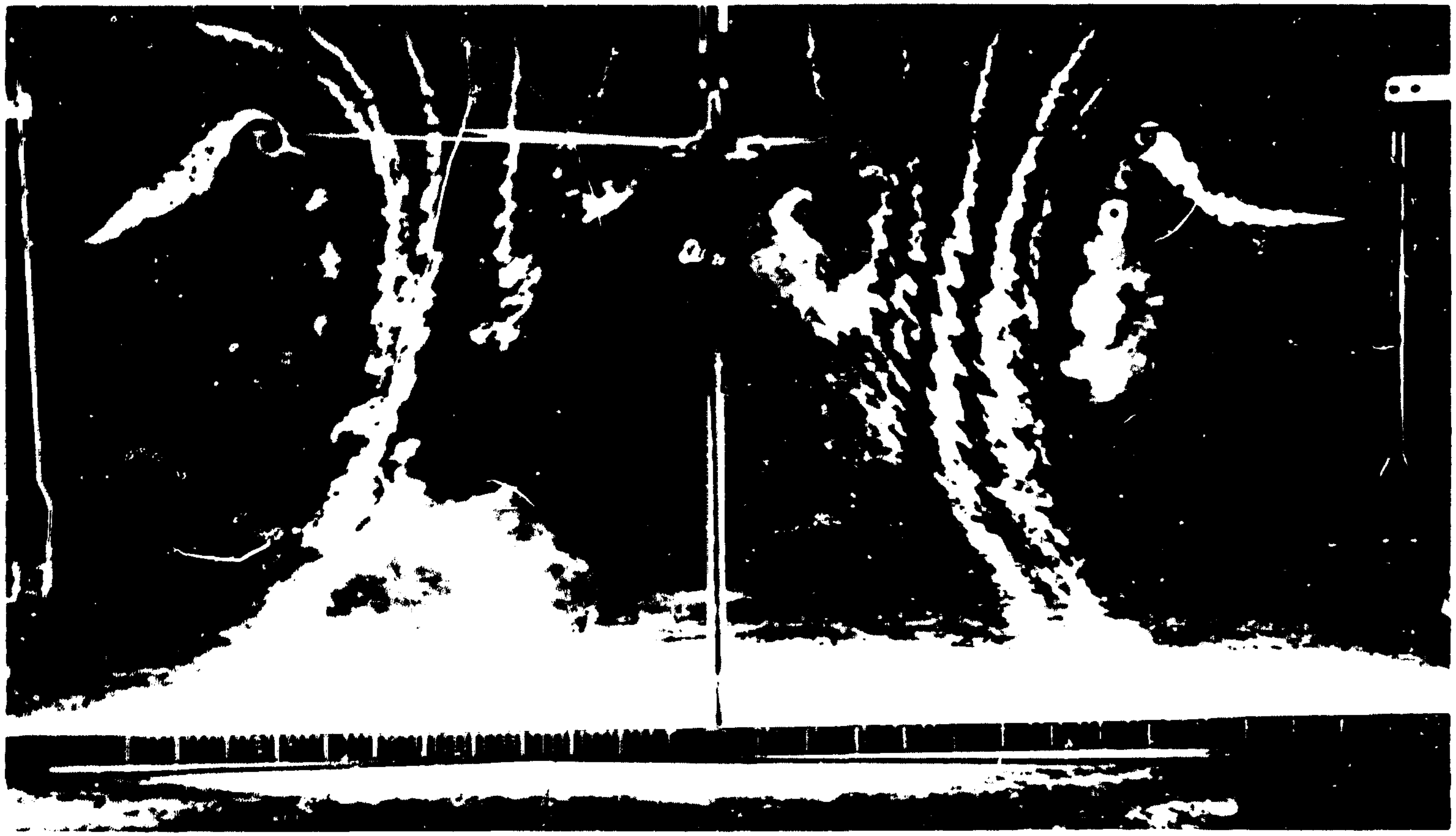

Figure 40. Photograph Showing Effect of Ground on Wake Geometry.

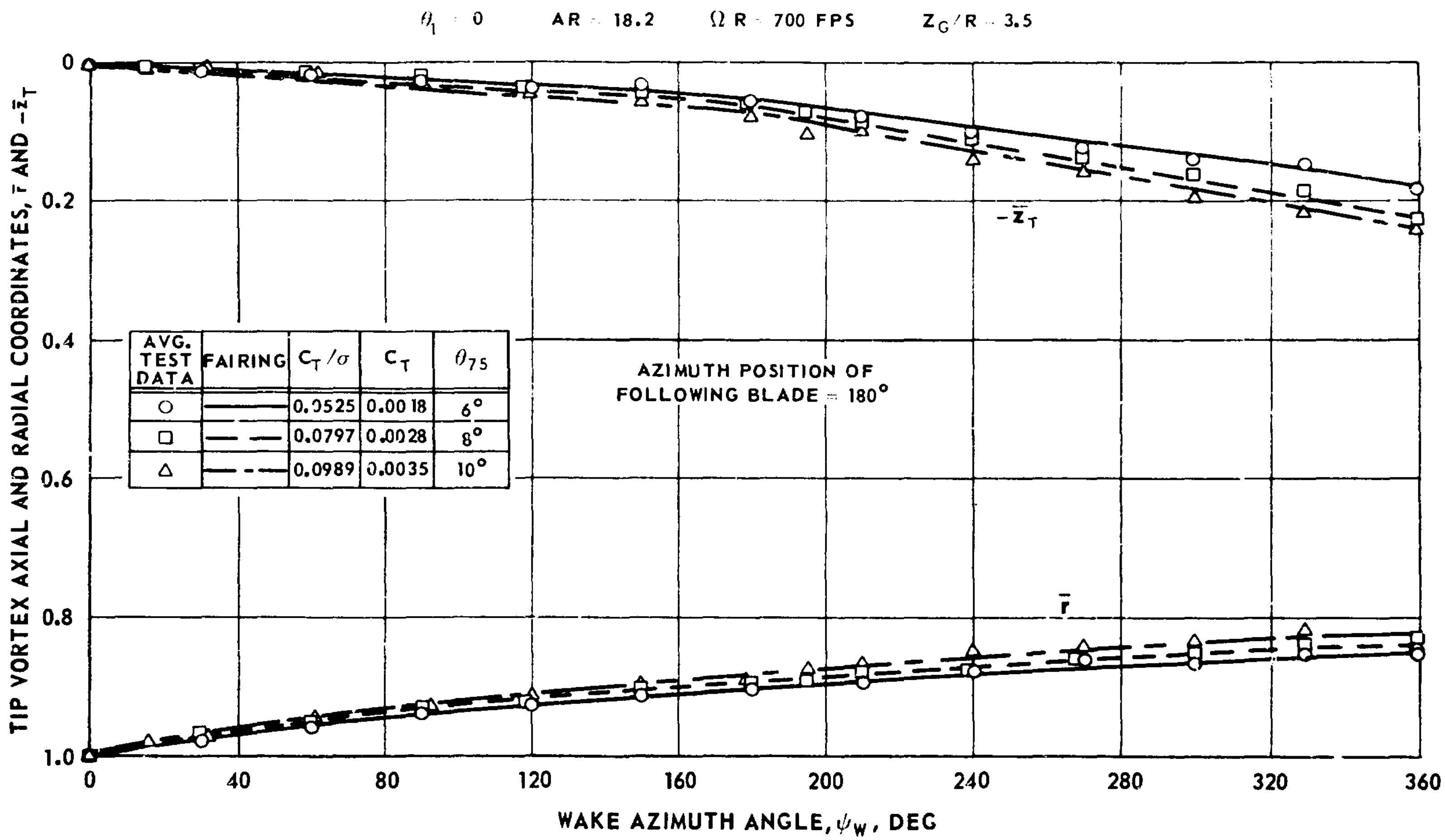

(a) $\psi_w < 360°$

Figure 41. Effect of Thrust on Tip Vortex Coordinates -- b = 2.

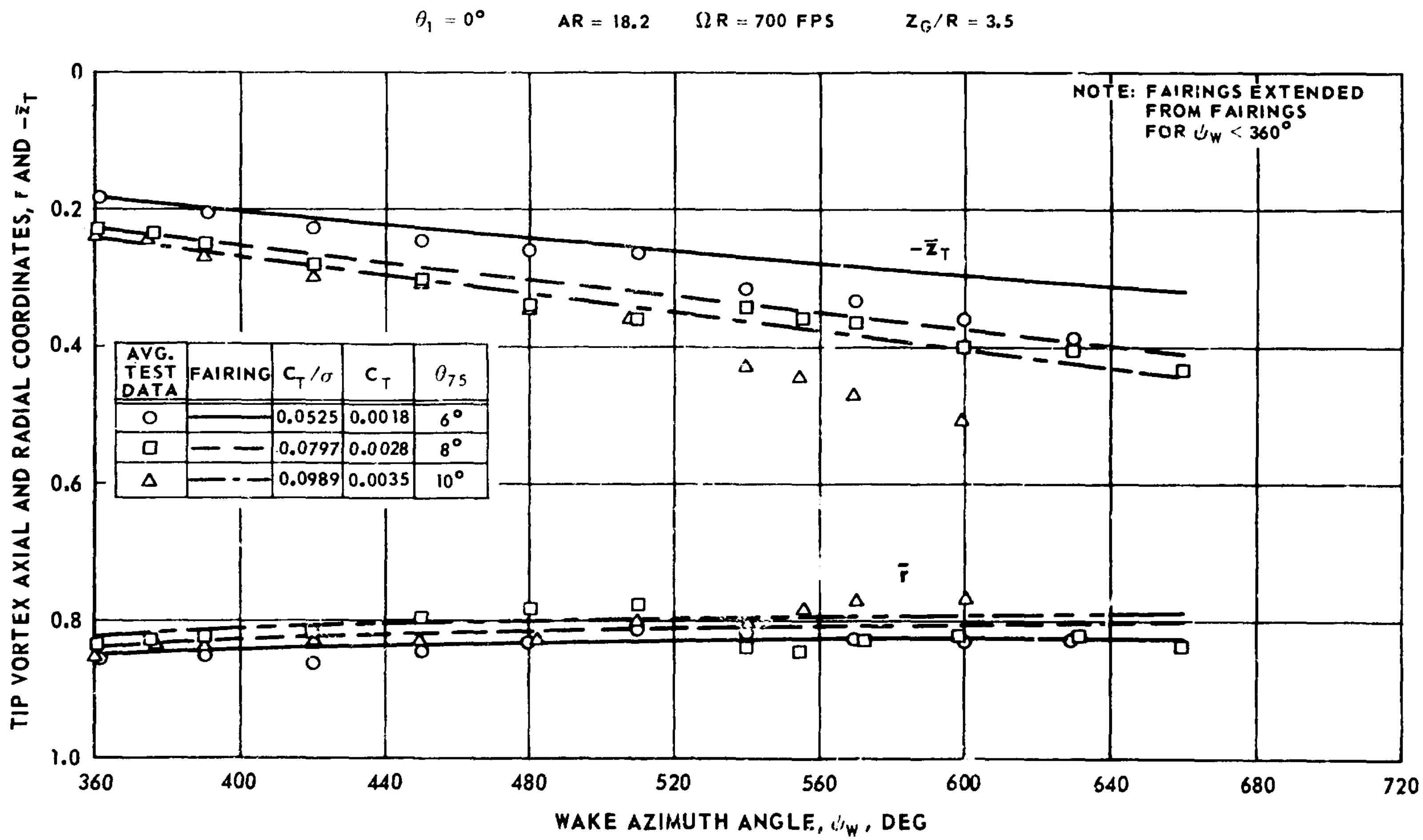

(b) $\psi_w > 360^\circ$
Figure 41. Concluded.

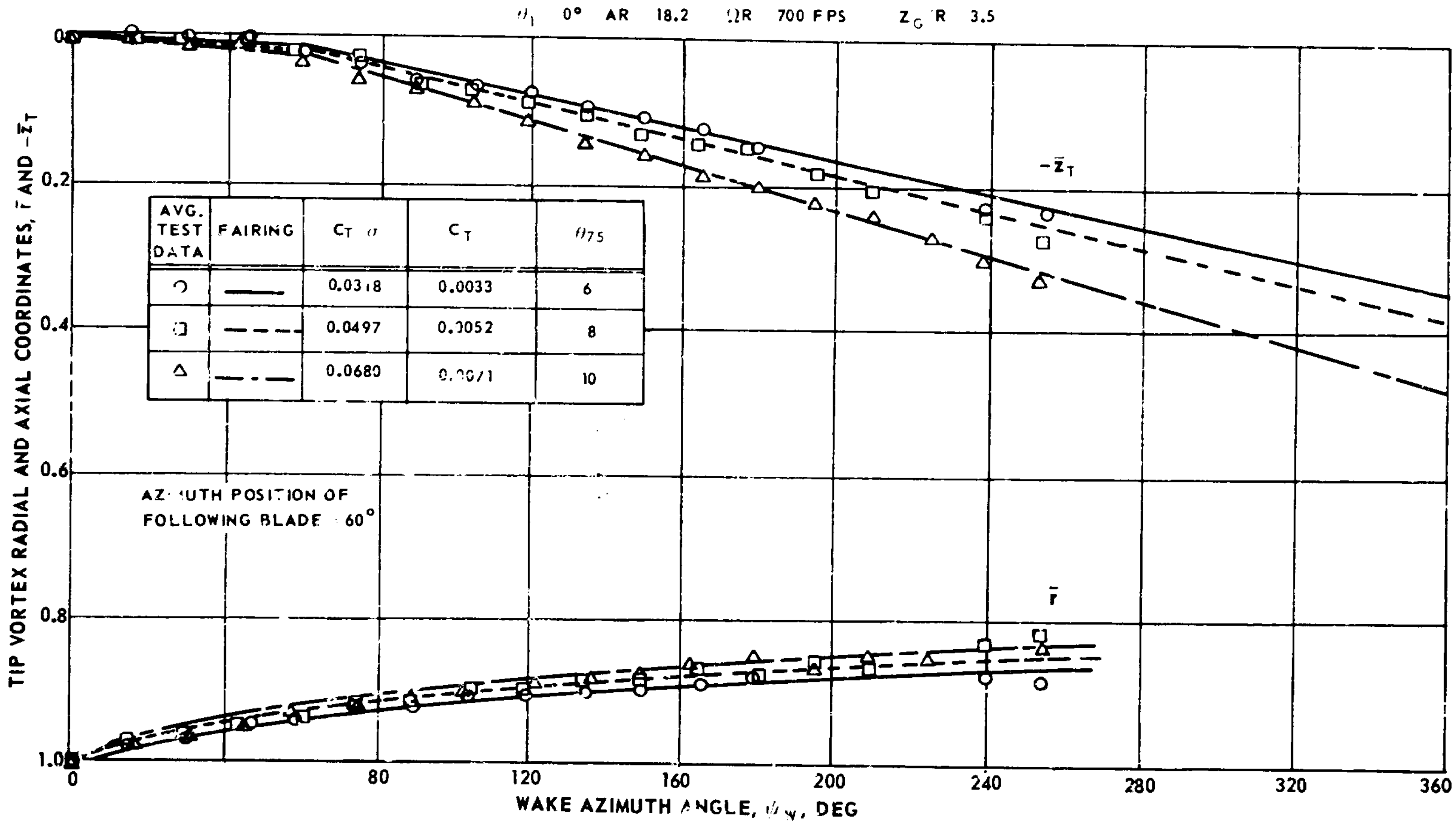

Figure 42. Effect of Thrust on Tip Vortex Coordinates-- b = 6.

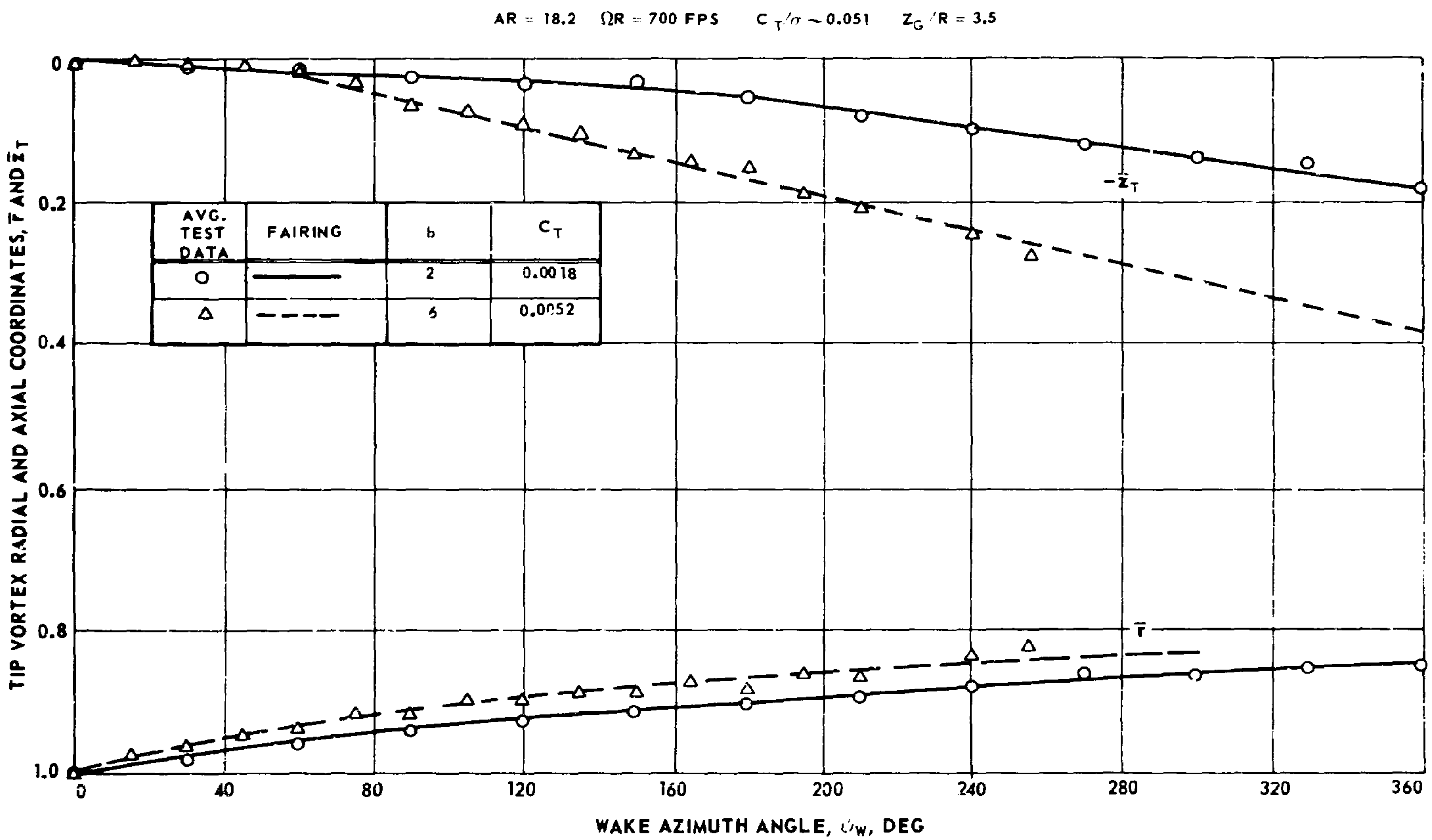

Figure 43. Effect of Number of Blades on Tip Vortex Coordinates for Constant Blade Loading (C_T/σ) -- $\theta_1 = 0^\circ$.

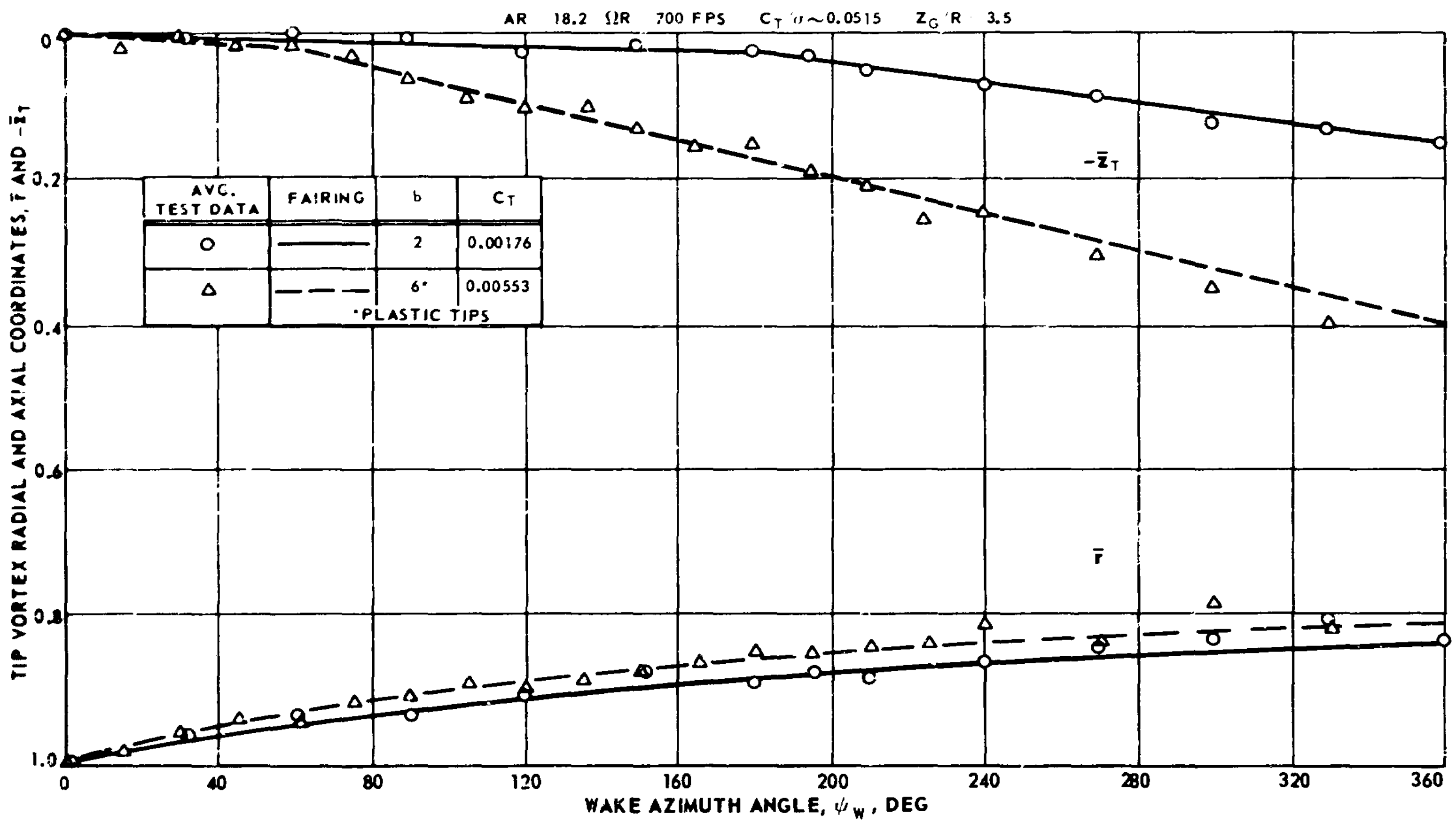

Figure 44. Effect of Number of Blades on Tip Vortex Coordinates for Constant Blade Loading (C_T/σ) -- $\theta_1 = -8^\circ$.

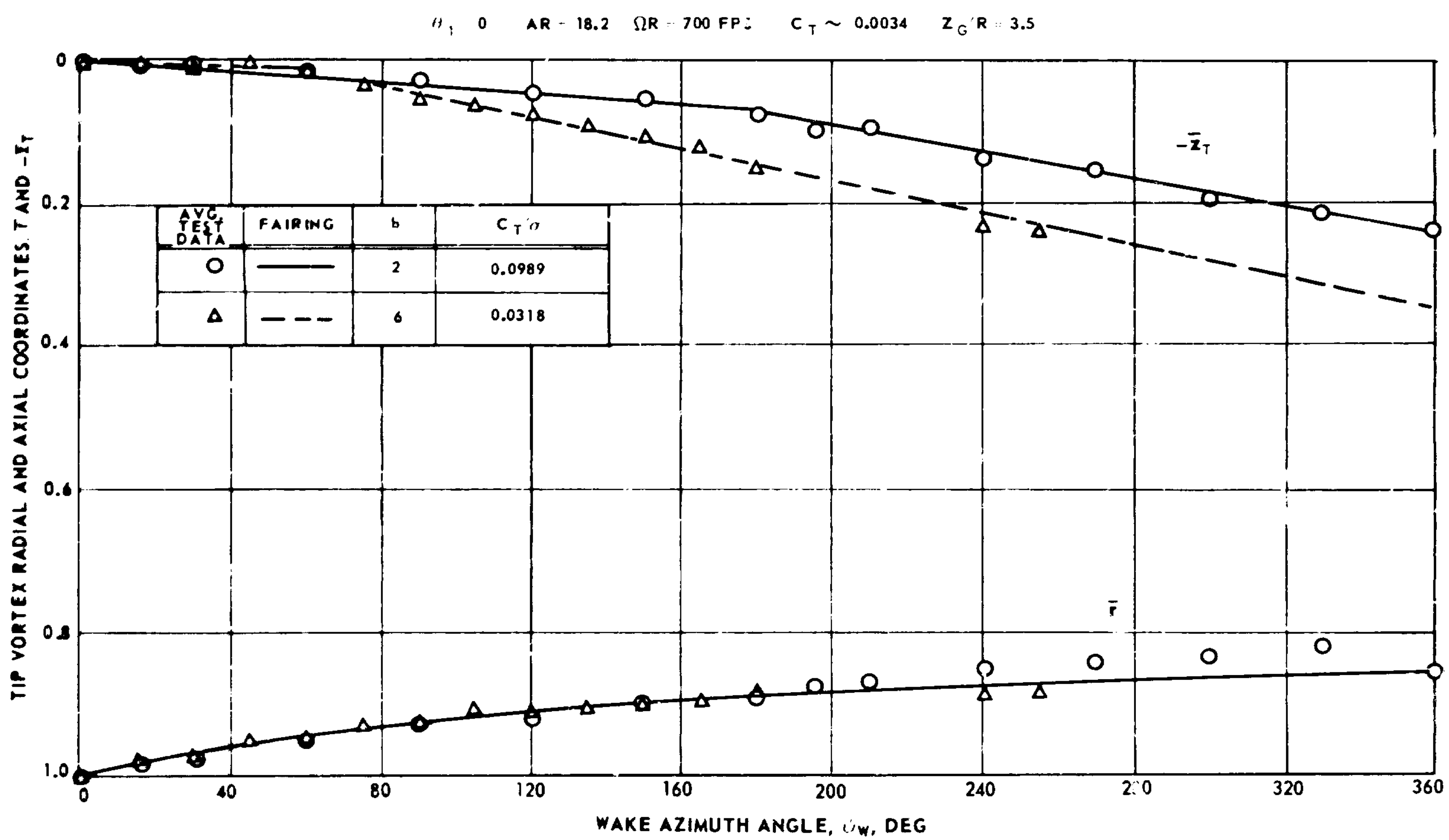

Figure 45. Effect of Number of Blades on Tip Vortex Coordinates for Constant Disc Loading (C_T).

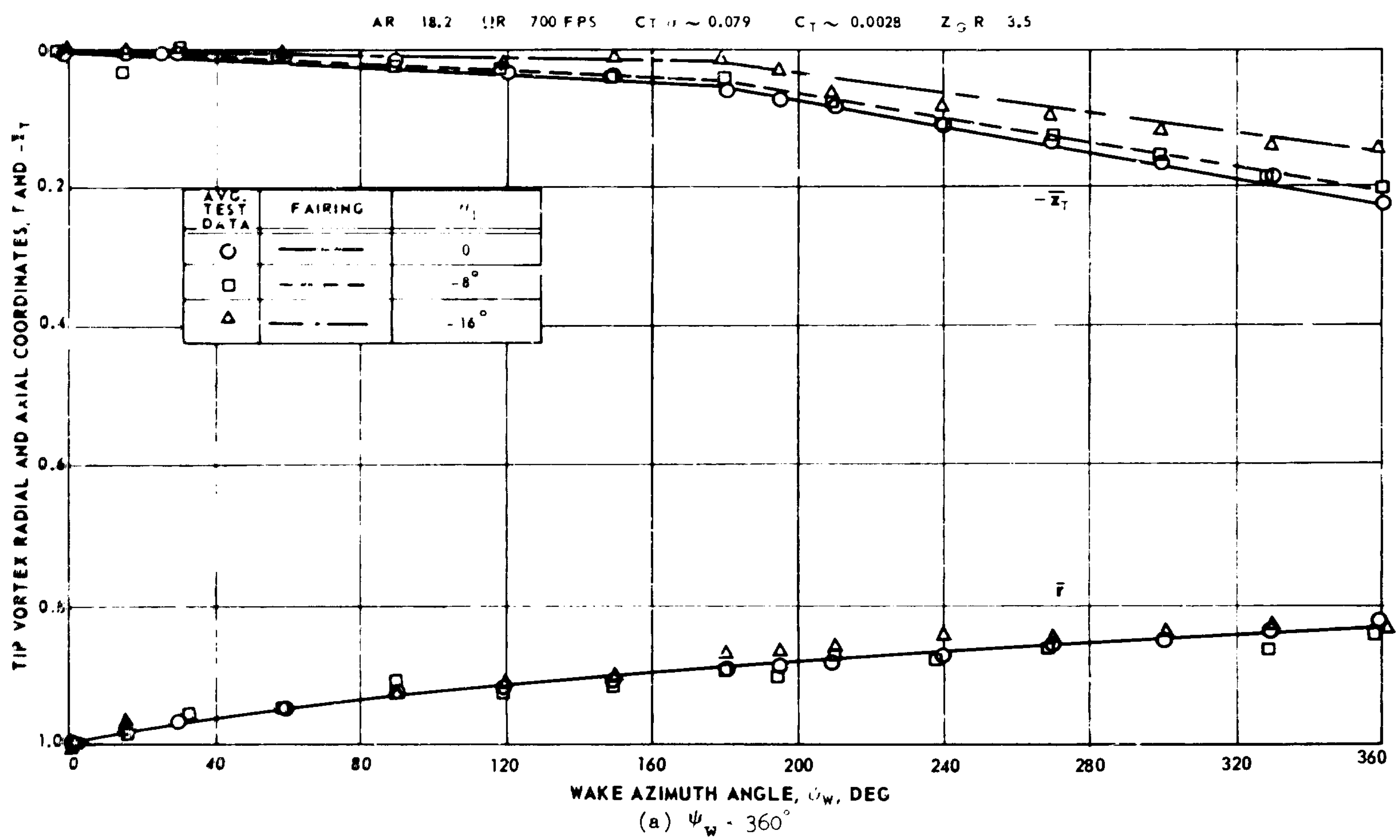

(a) ψ_w - 360°

Figure 46. Effect of Twist on Tip Vortex Coordinates -- b = 2.

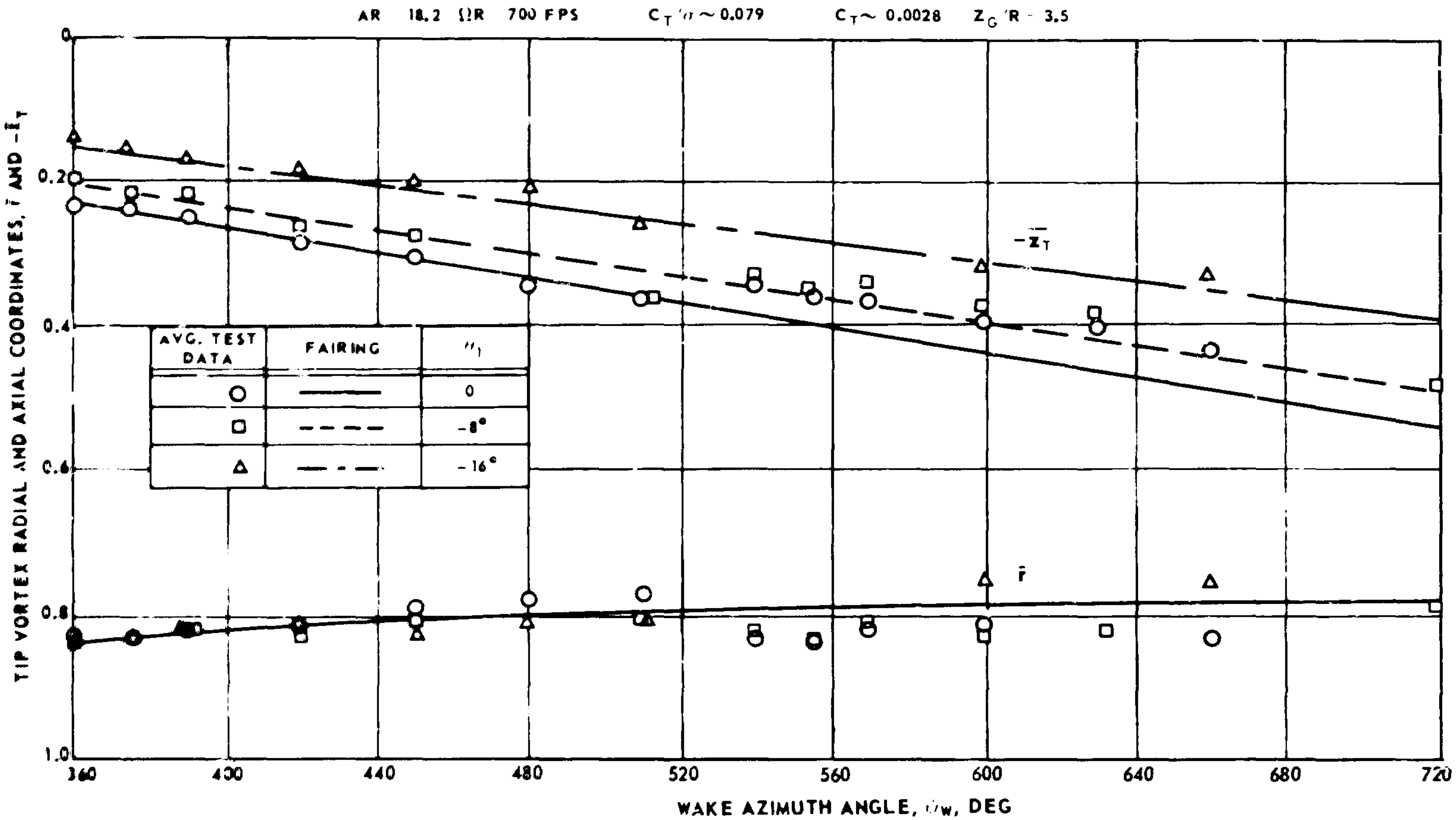

(b) $\psi_w > 360°$

Figure 46. Concluded.

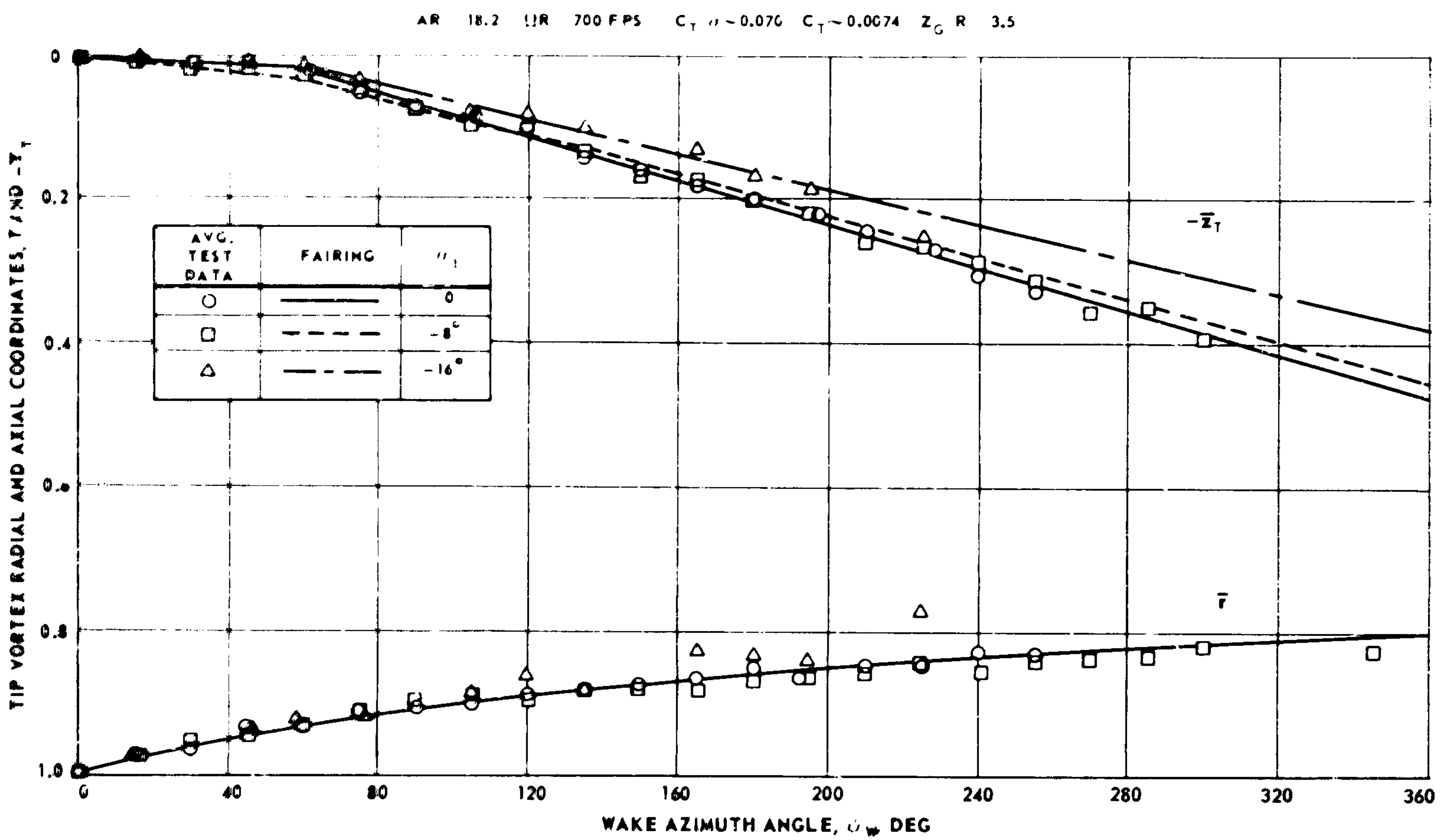

Figure 47. Effect of Twist on Tip Vortex Coordinates -- b = 6.

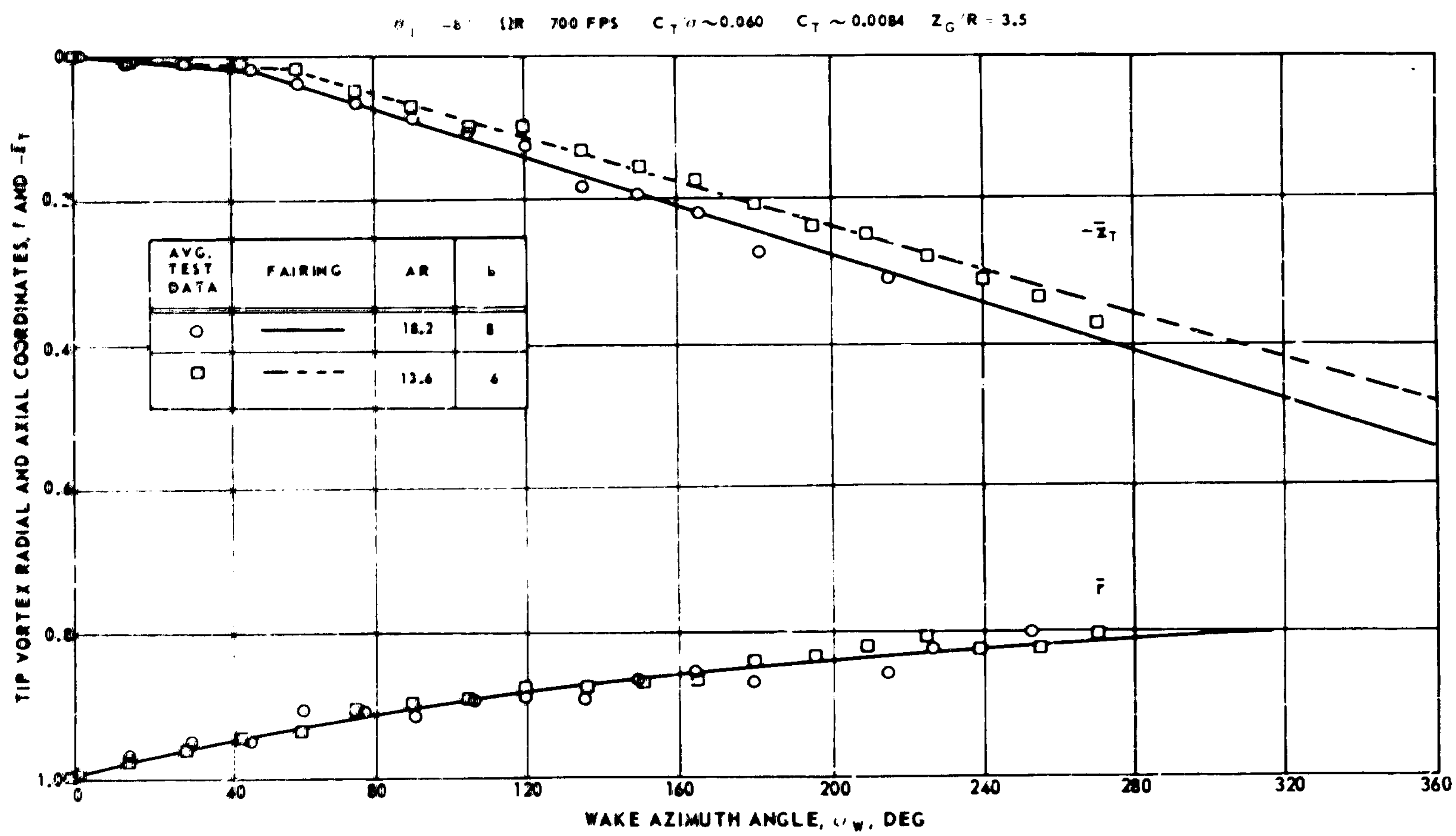

Figure 48. Effect of Aspect Ratio on Tip Vortex Coordinates for Rotor Solidity of 0.140.

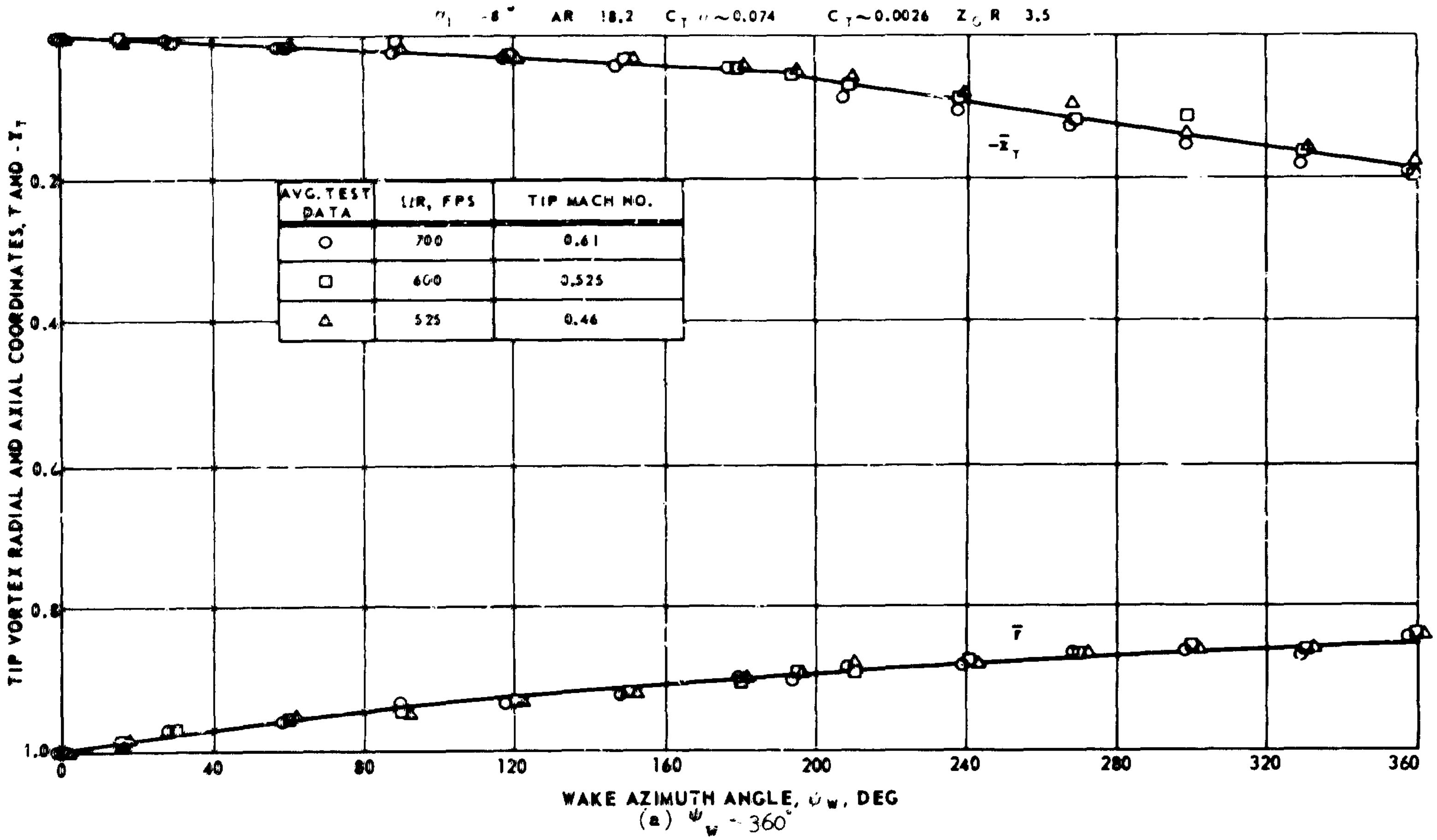

Figure 49. Effect of Tip Speed on Tip Vortex Coordinates -- b = 2.

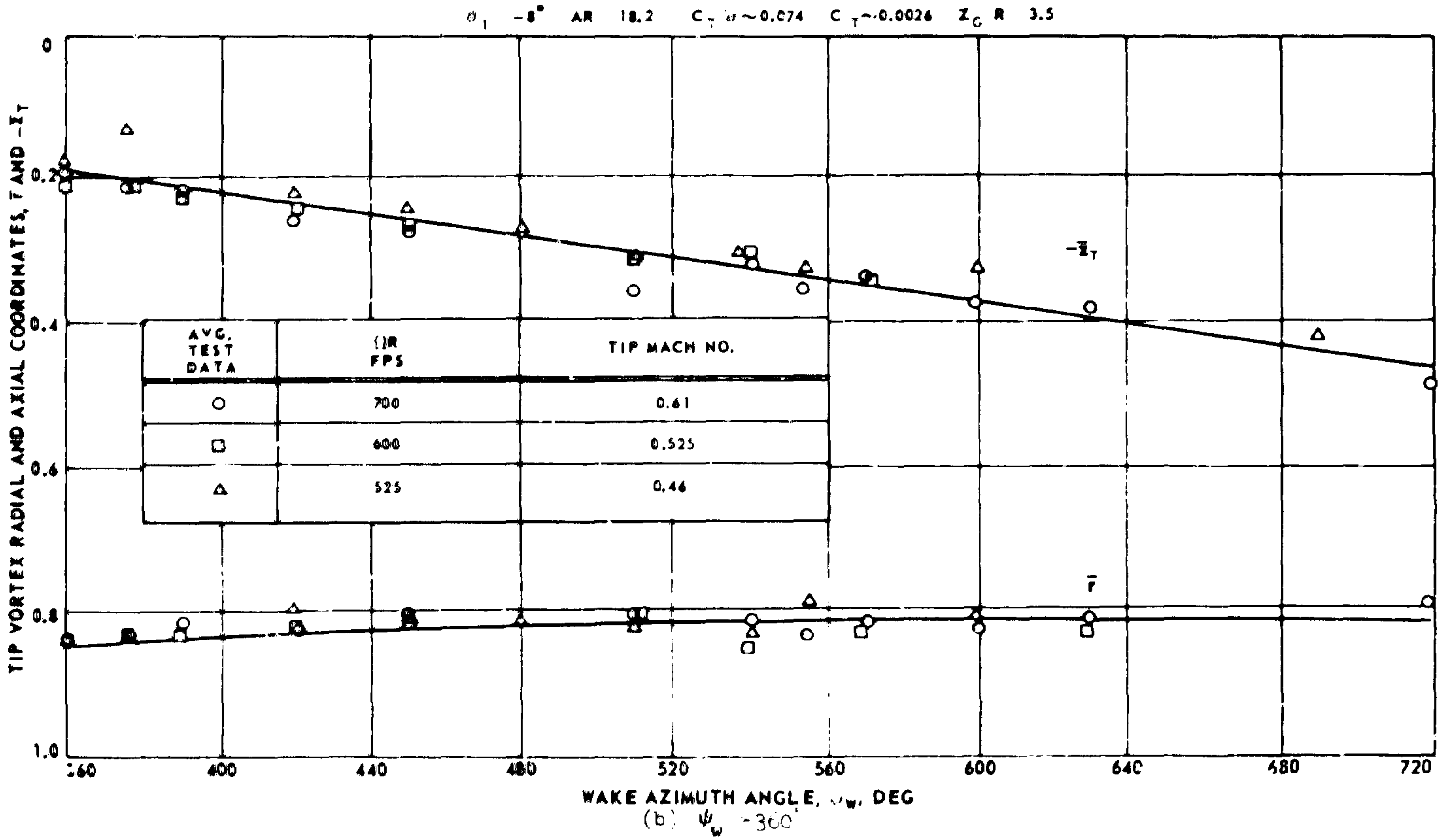

(b) ψ_w -360°

Figure 49. Concluded.

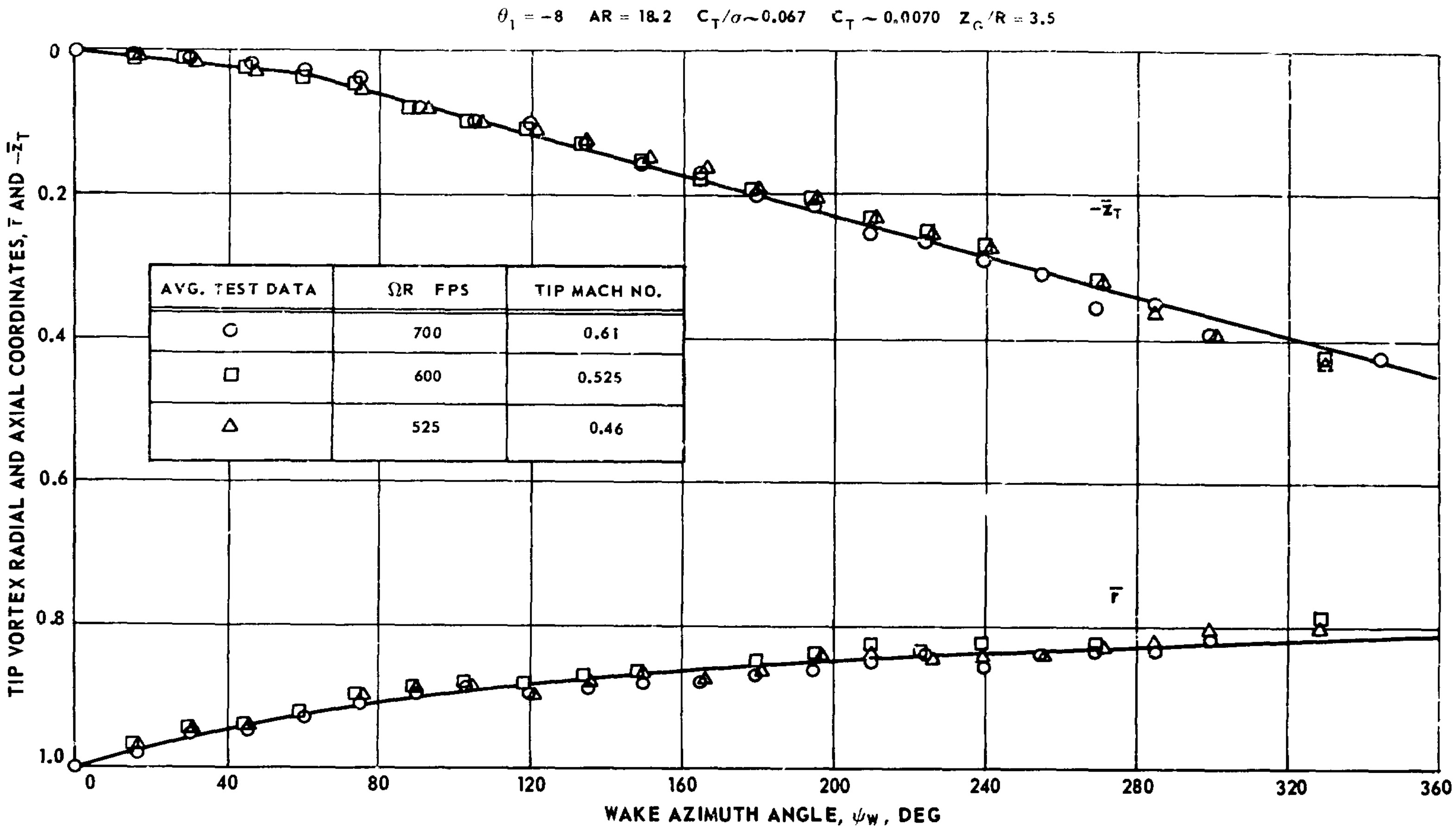

Figure 50. Effect of Tip Speed on Tip Vortex Coordinates -- b = 6.

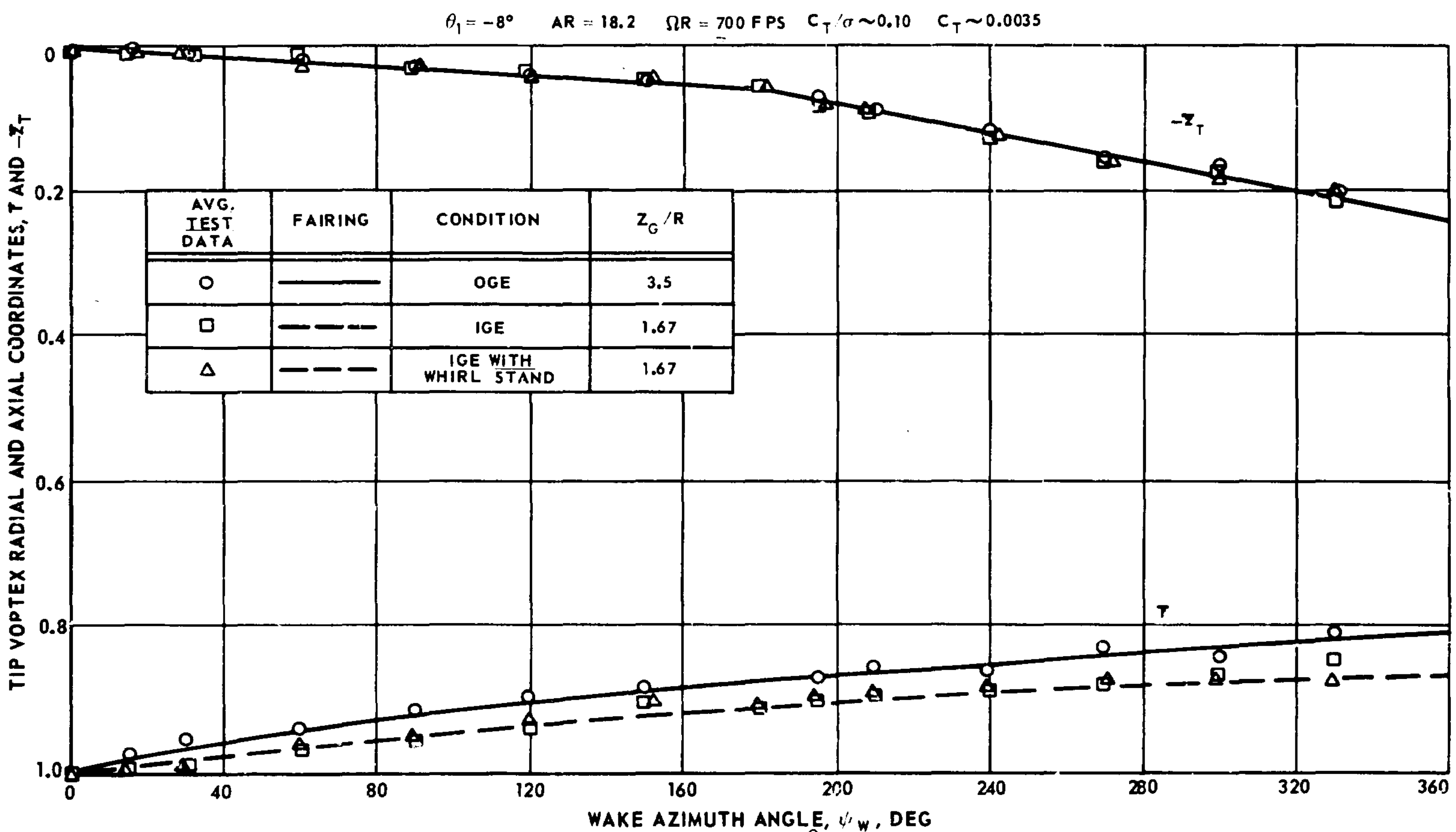

AVG. TEST DATA	FAIRING	CONDITION	Z_G/R
○	———	OGE	3.5
□	— — —	IGE	1.67
△	— — —	IGE WITH WHIRL STAND	1.67

(a) $\psi_w < 360°$

Figure 51. Effect of Whirl Stand Conditions on Tip Vortex Coordinates -- b = 2.

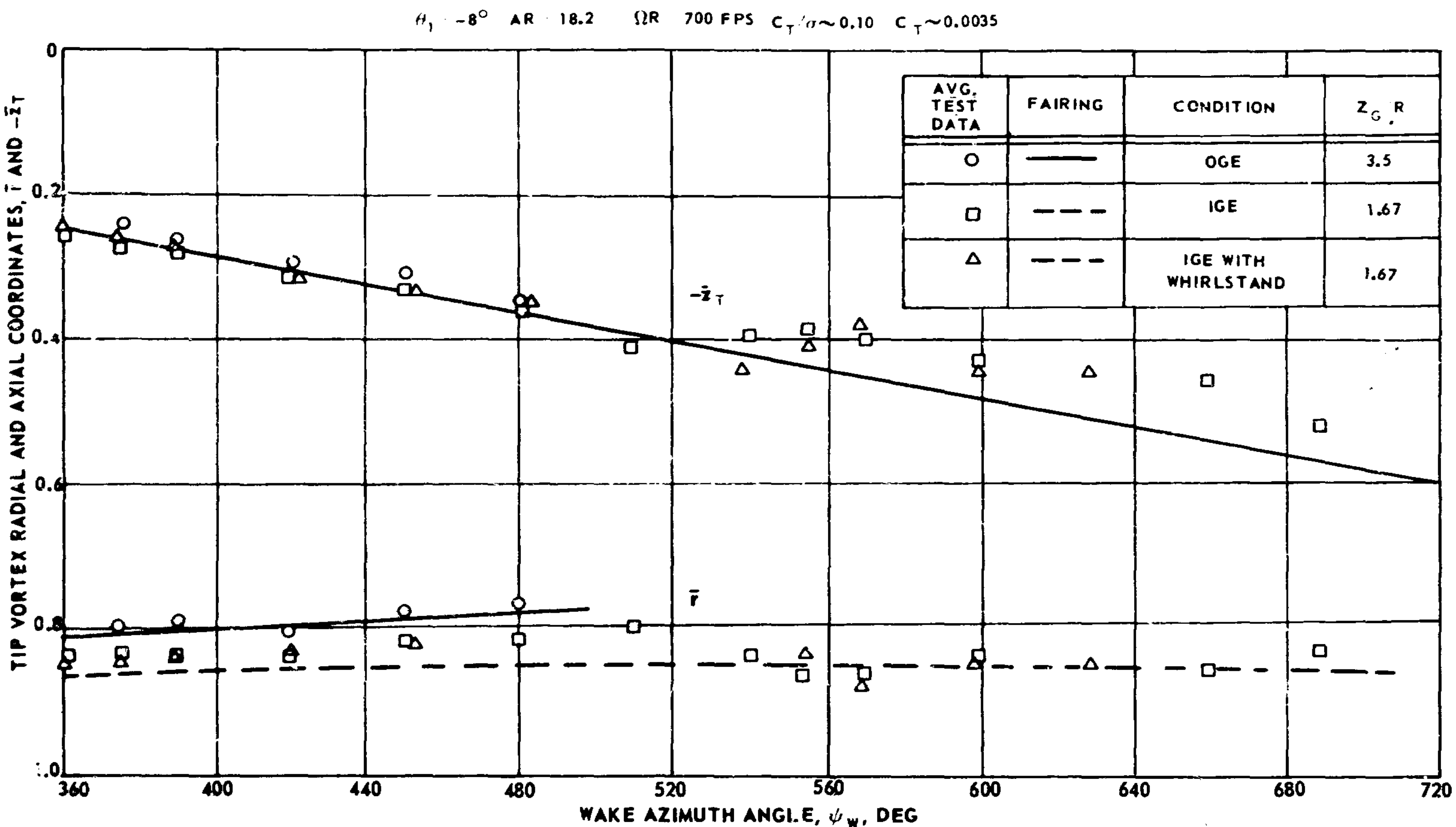

(b) $\psi_w > 360°$

Figure 51. Concluded.

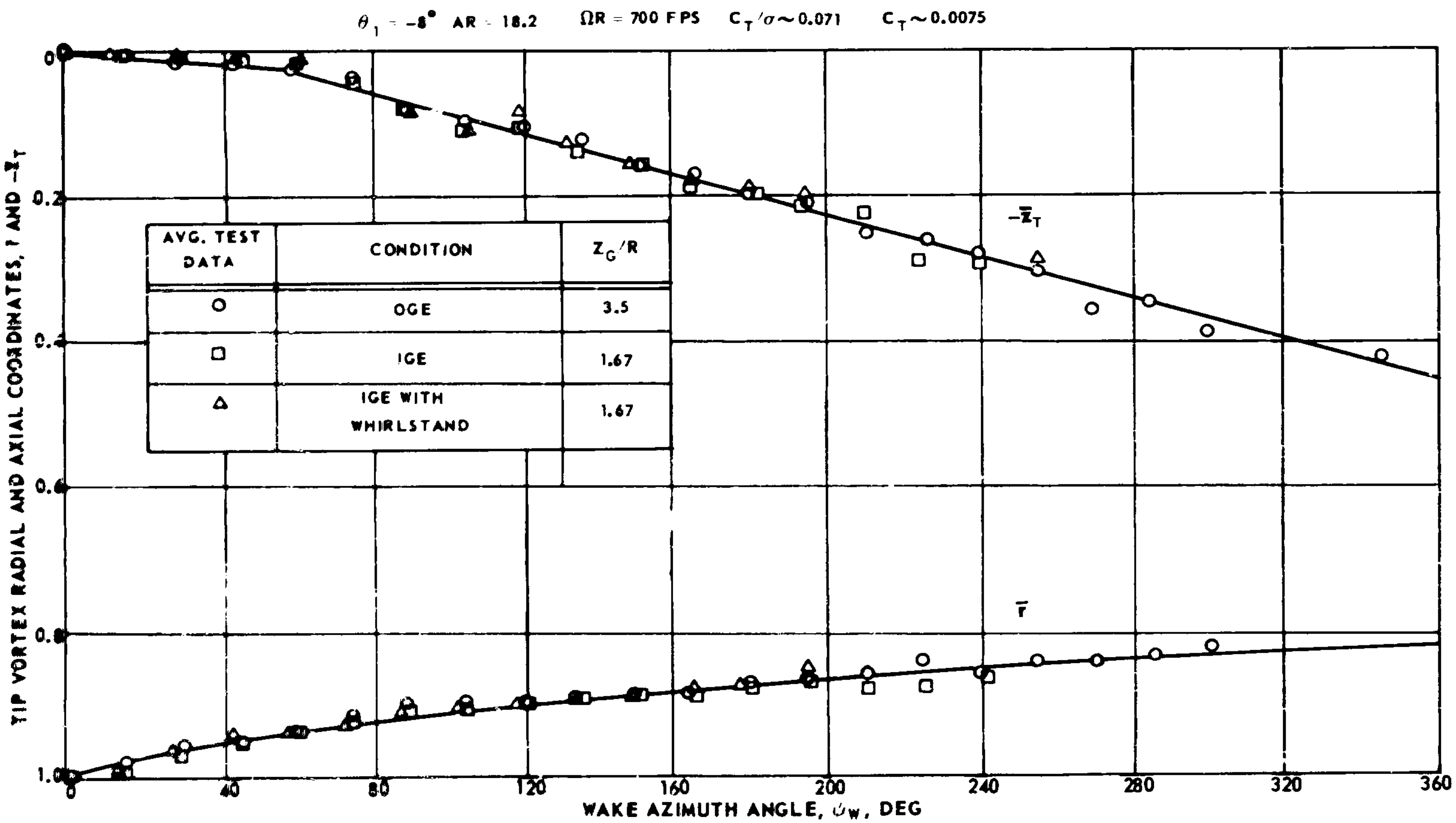

Figure 52. Effect of Whirl Stand Conditions on Tip Vortex Coordinates -- b = 6.

$Z_G/R = 3.5$

DATA	NO. OF BLADES
○	2
□	4
△	6
◇	8

UNFLAGGED SYMBOLS: $\Omega R = 700$ FPS

SINGLE FLAGGED SYMBOLS: $\Omega R = 600$ FPS

DOUBLE FLAGGED SYMBOLS: $\Omega R = 525$ FPS

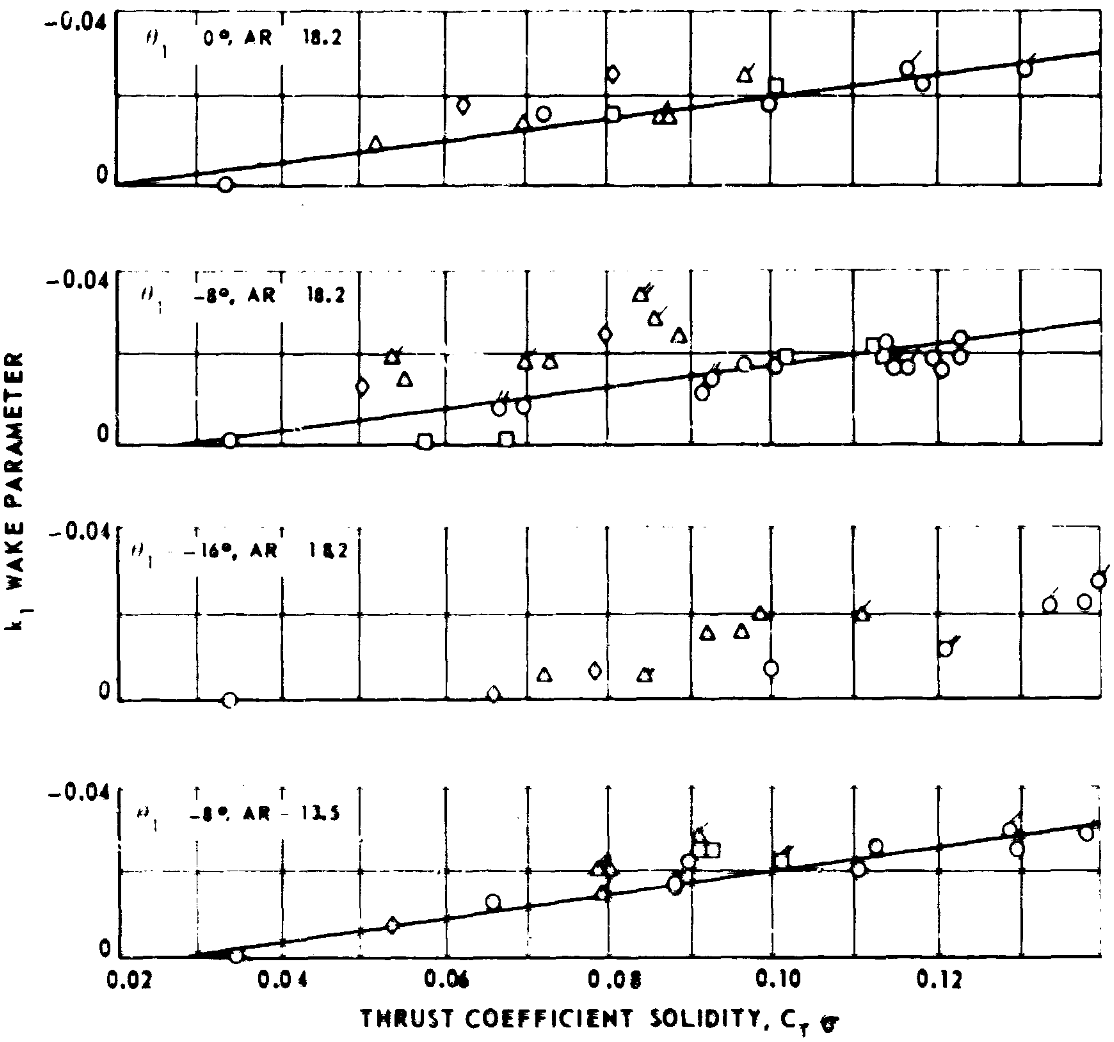

Figure 53. Experimental k_1 Wake Parameter for Model Rotors.

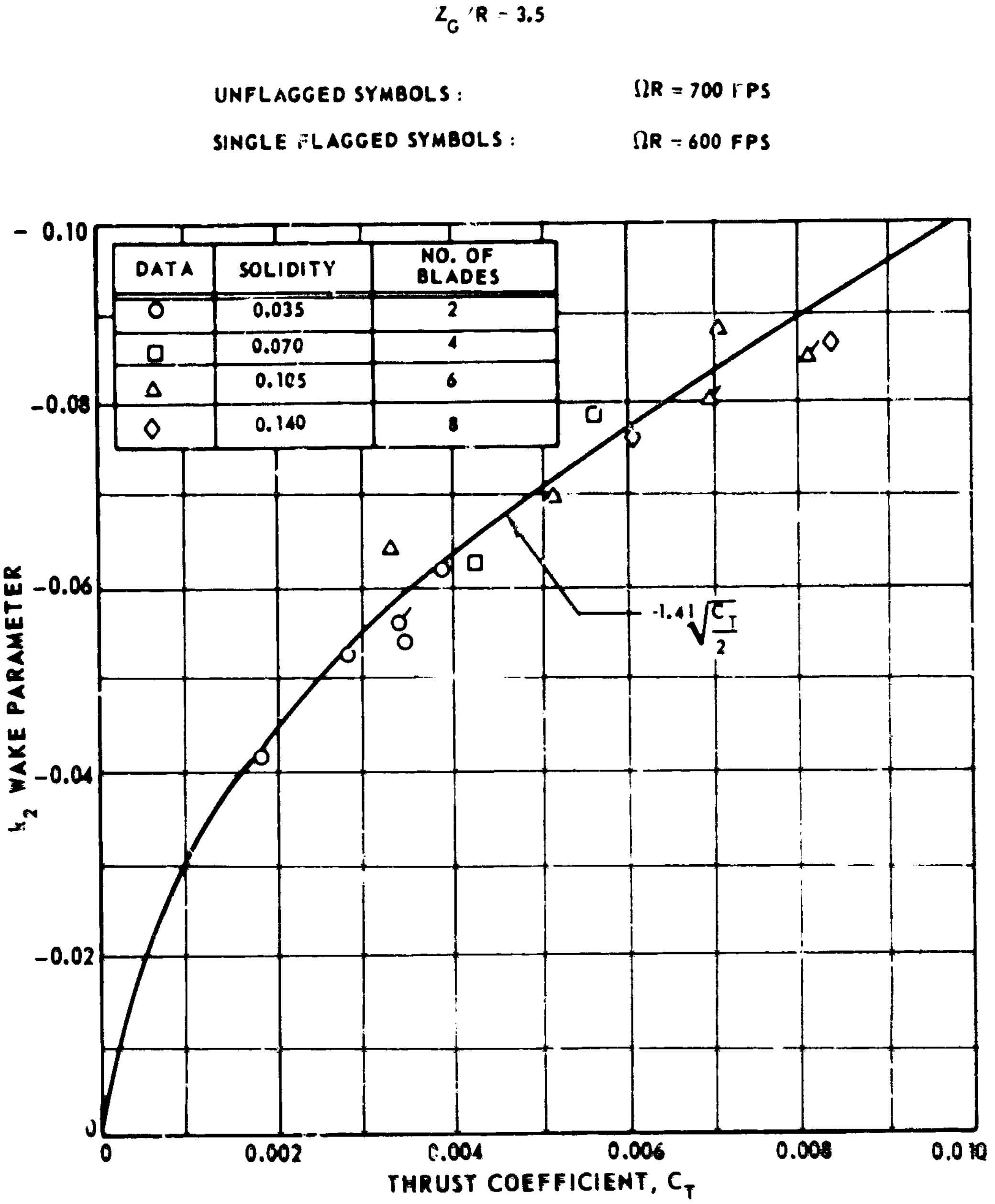

Figure 54. Experimental k_2 Wake Parameter for Model Rotors -- $\theta_1 = 0°$, AR = 18.2.

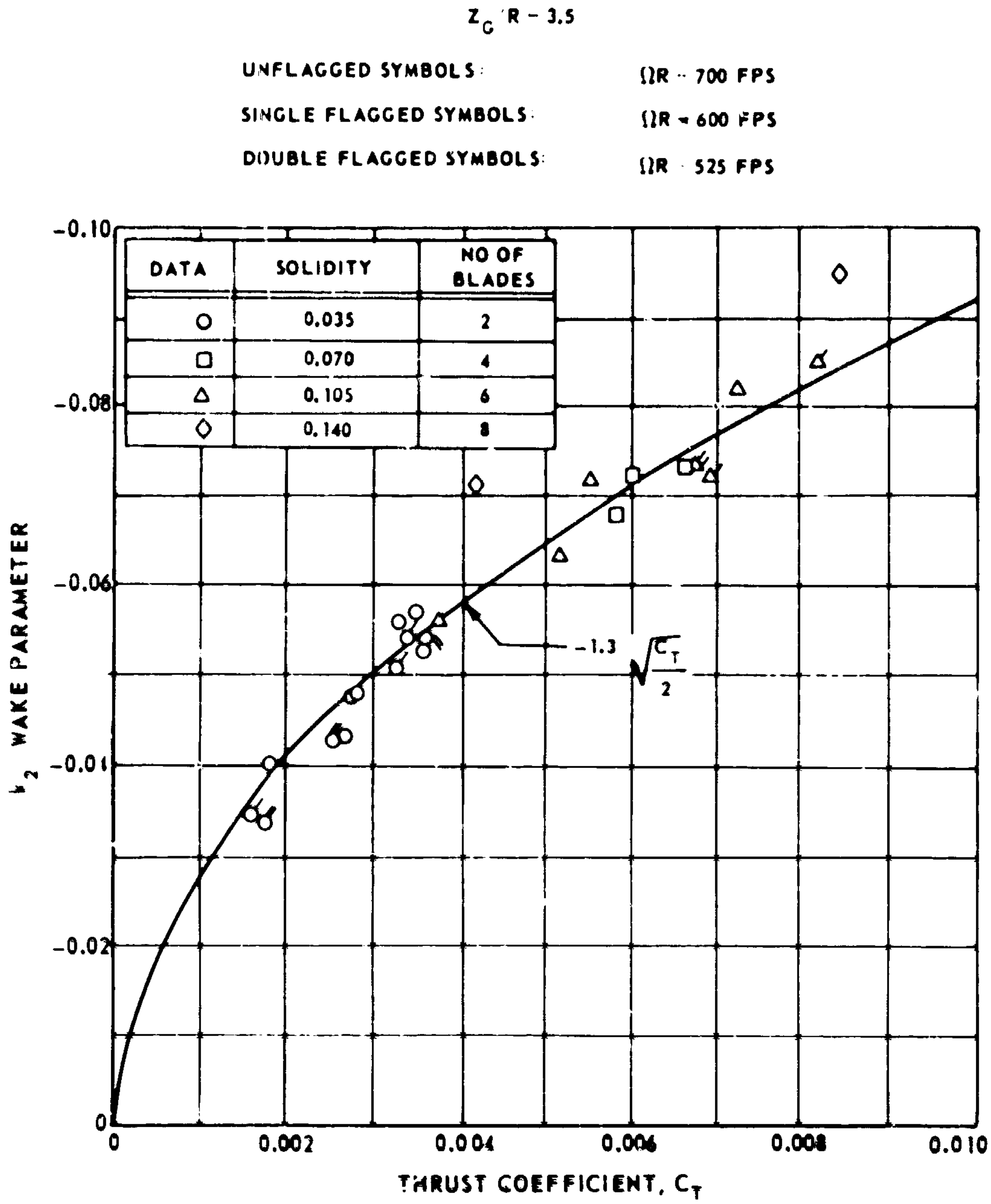

Figure [illegible]. Experimental k_2 Wake Parameter for Model Rotors -- $\theta_1 = -8^\circ$, AR = 18.2.

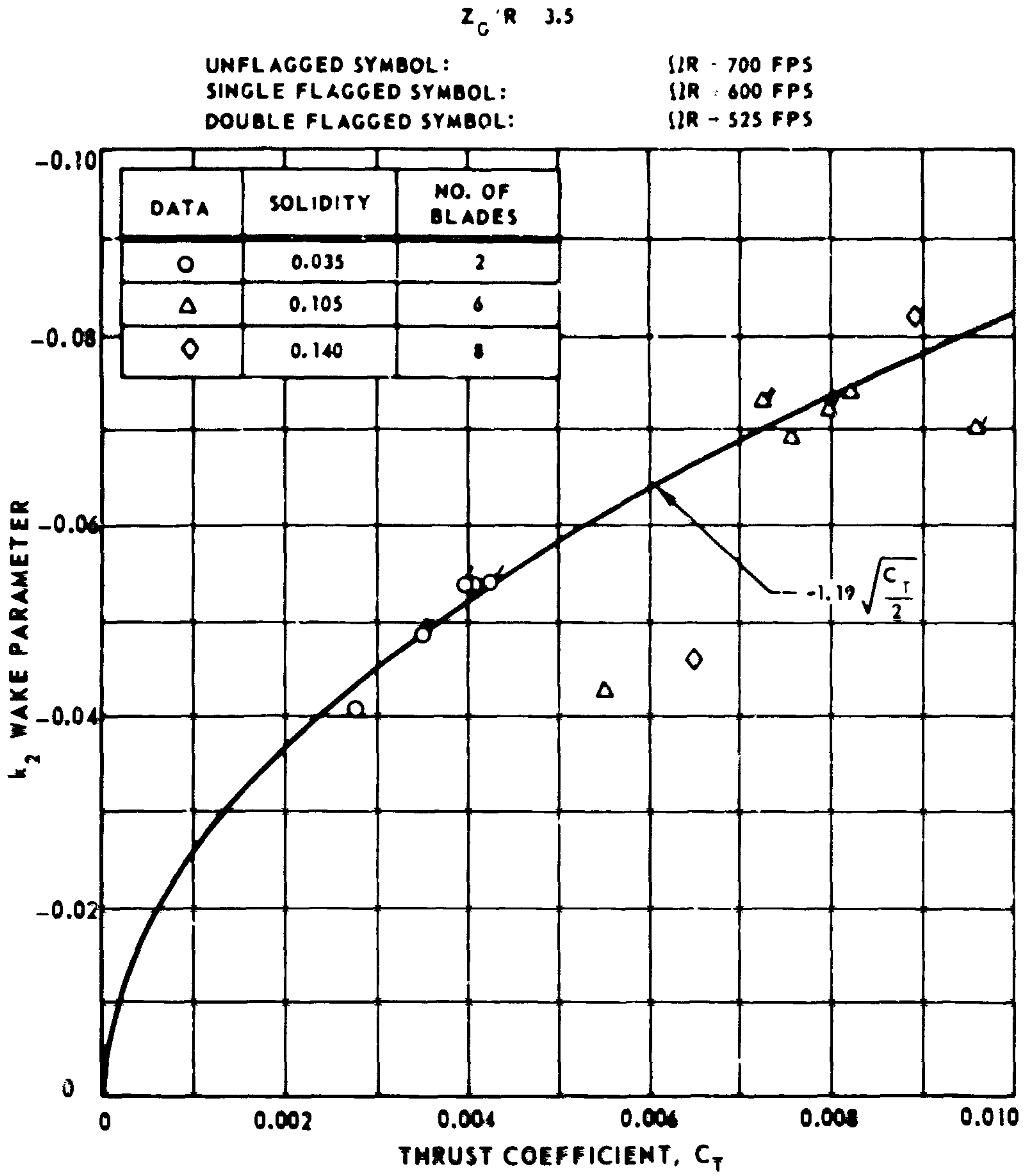

Figure 56. Experimental k_2 Wake Parameter for Model Rotors -- $\theta_1 = -16^\circ$, AR = 18.2.

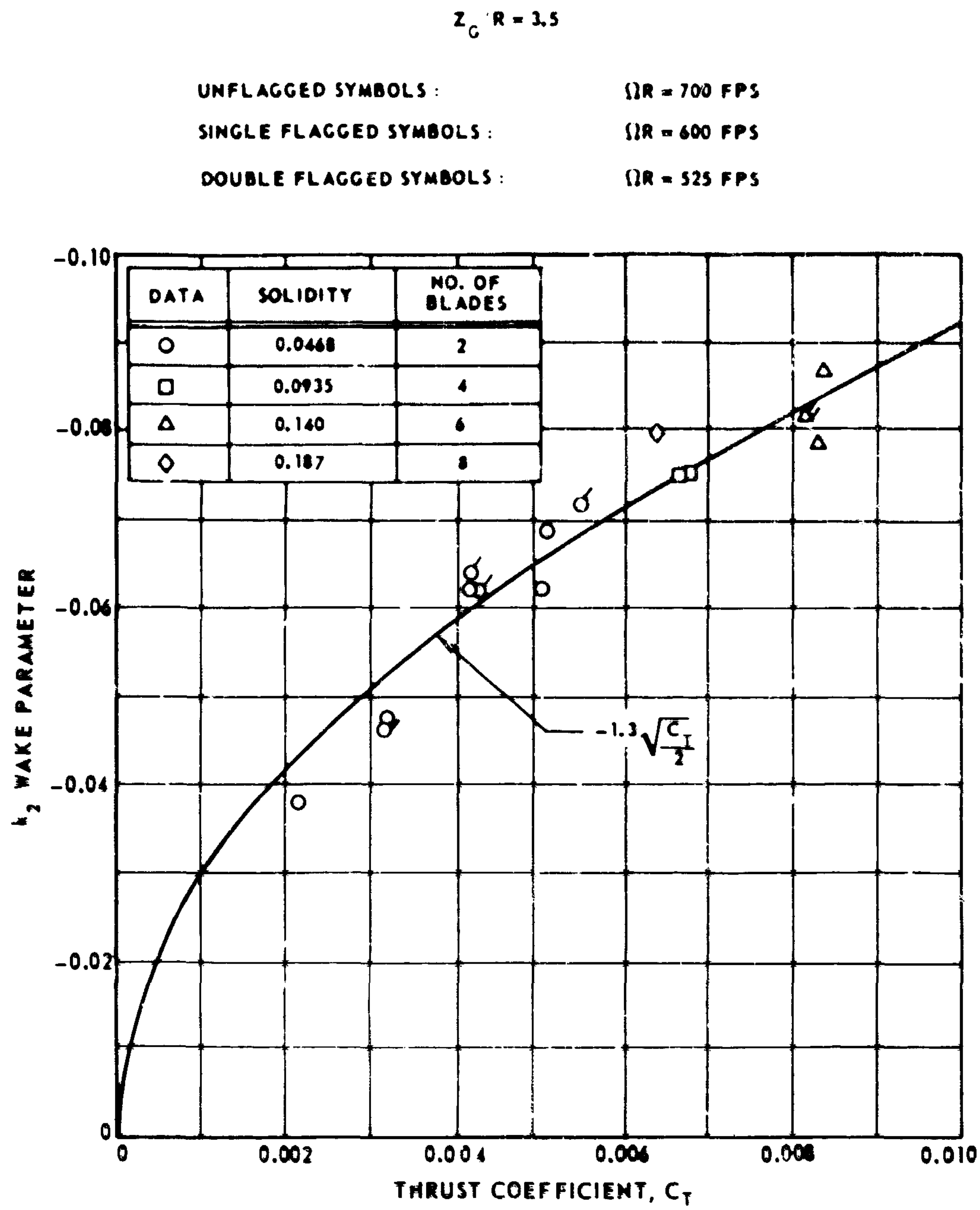

Figure [illegible]. Experimental k_2 Wake Parameter for Model Rotors -- $\theta_1 = -8°$, AR = 13.[illegible].

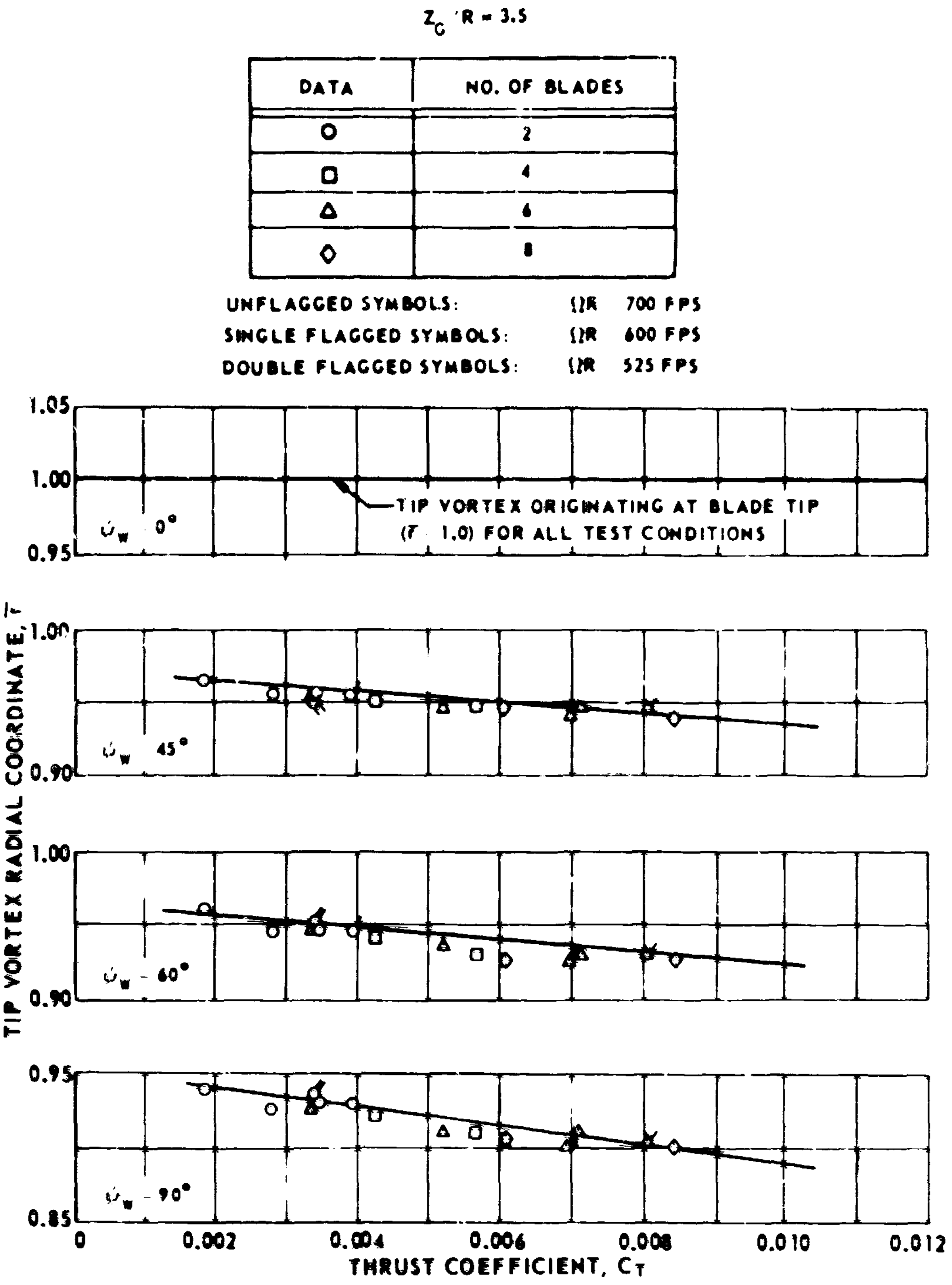

(a) ψ_w = 0°, 45°, 60°, 90°.

Figure 53. Experimental Wake Radial Coordinates for Model Rotors -- θ_1 = 0°, AR = 18.2.

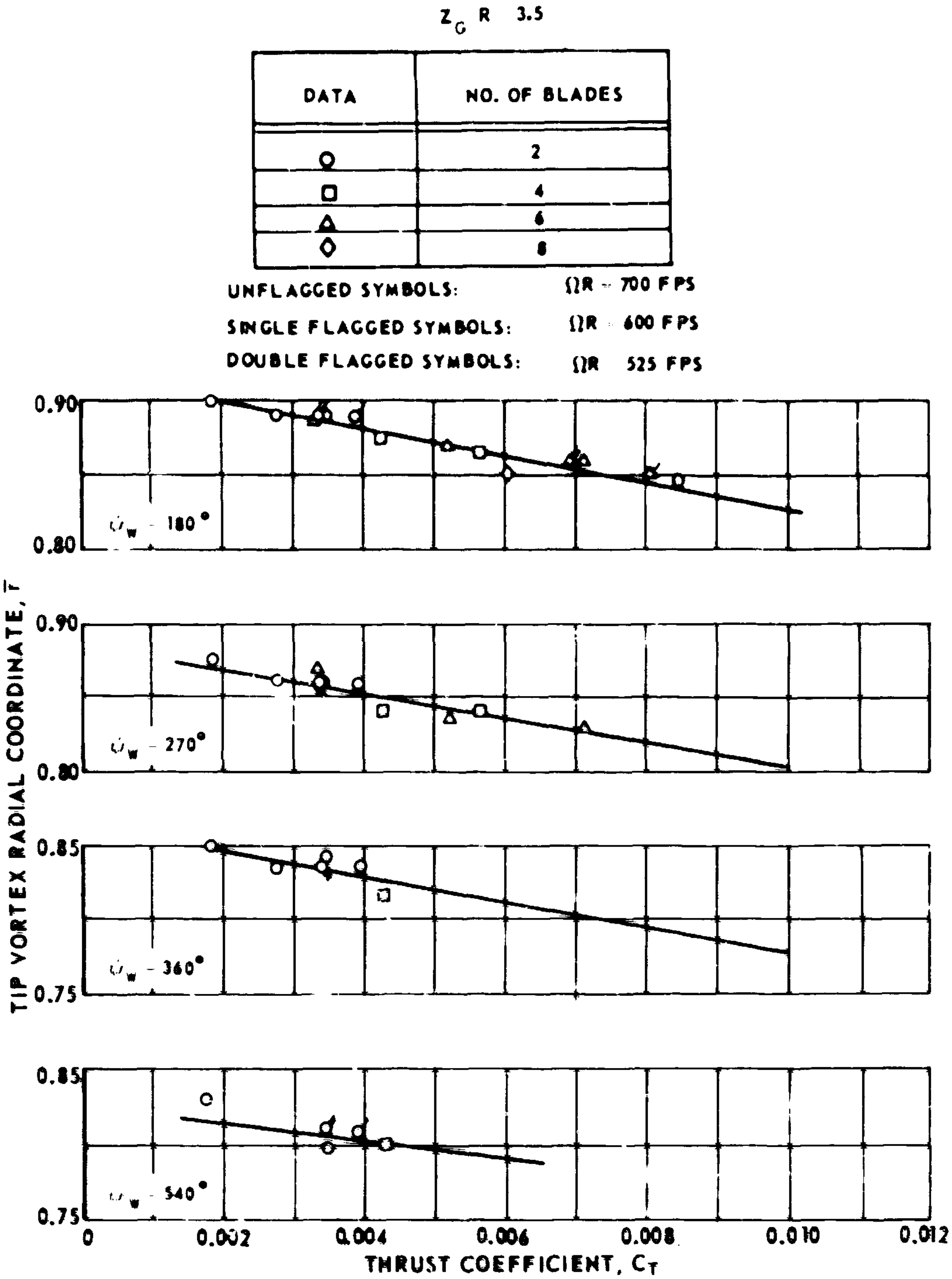

(b) ψ_w = 180°, 270°, 360°, 540°.

Figure 58. Concluded.

$Z_G/R = 3.5$

DATA POINT	NO. OF BLADES
○	2
□	4
△	6
◇	8

UNFLAGGED SYMBOLS: $\Omega R = 700$ FPS
SINGLE FLAGGED SYMBOLS: $\Omega R = 600$ FPS
DOUBLE FLAGGED SYMBOLS: $\Omega R = 525$ FPS

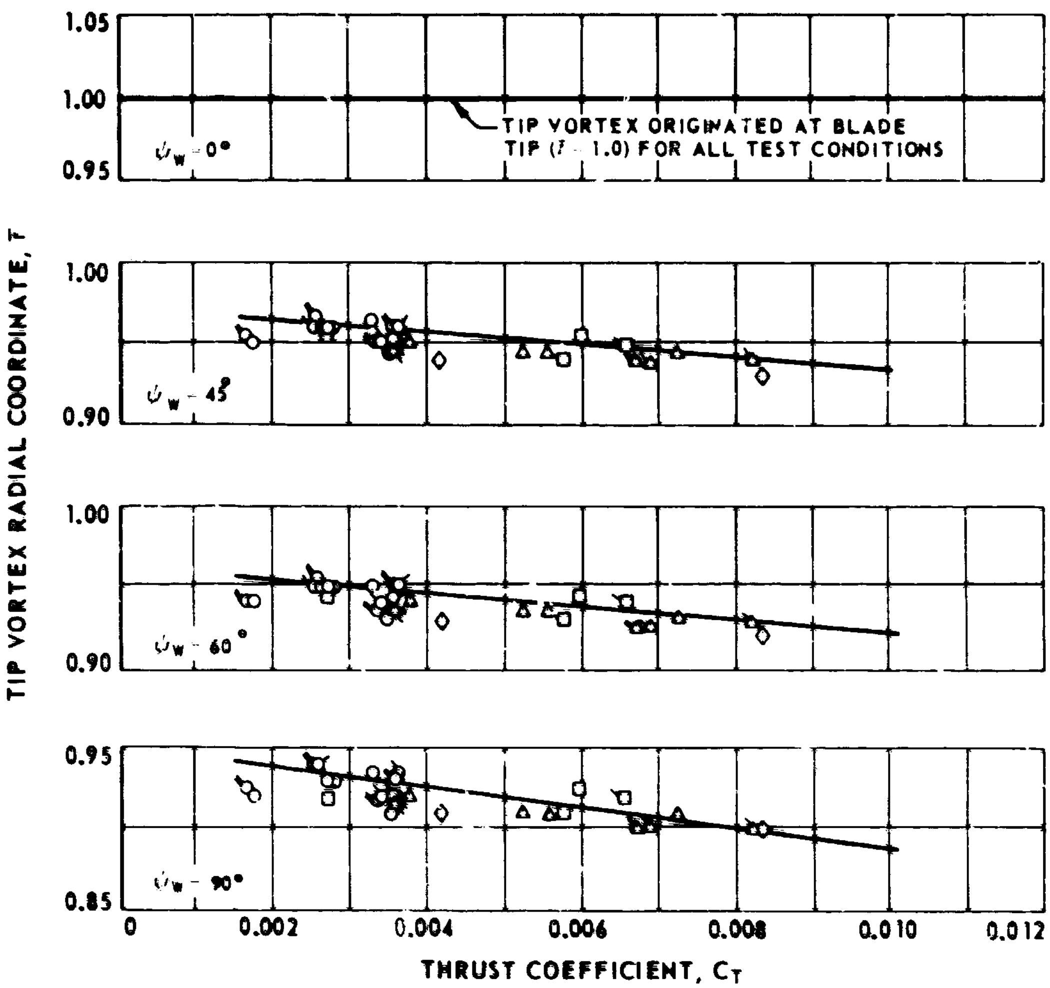

(a) $\psi_w = 0°, 45°, 60°, 90°$.

Figure 59. Experimental Wake Radial Coordinates for Model Rotors -- $\theta_1 = -8°$, AR = 18.2.

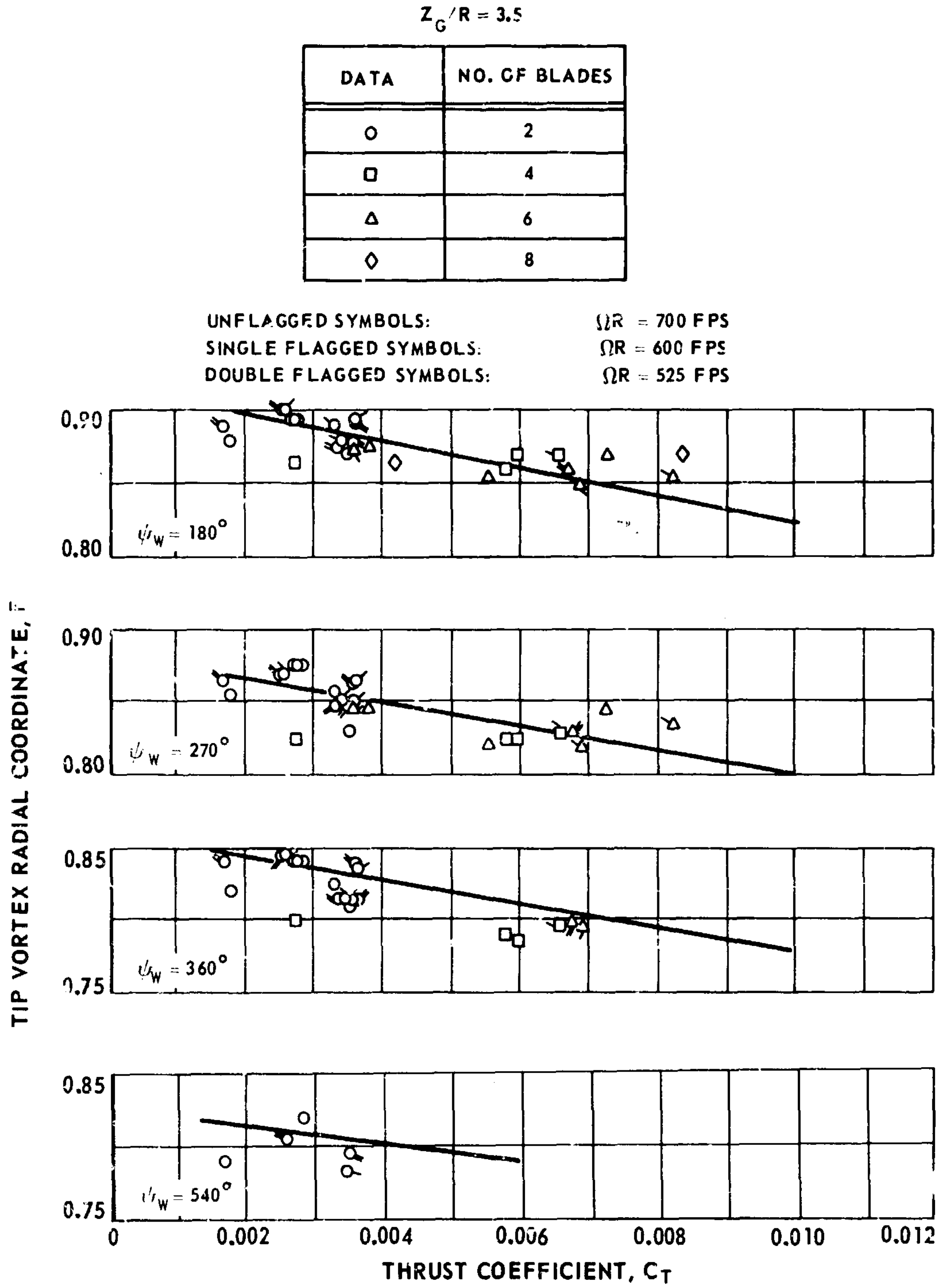

(b) ψ_W = 180°, 270°, 360°, 540°.

Figure 59. Concluded.

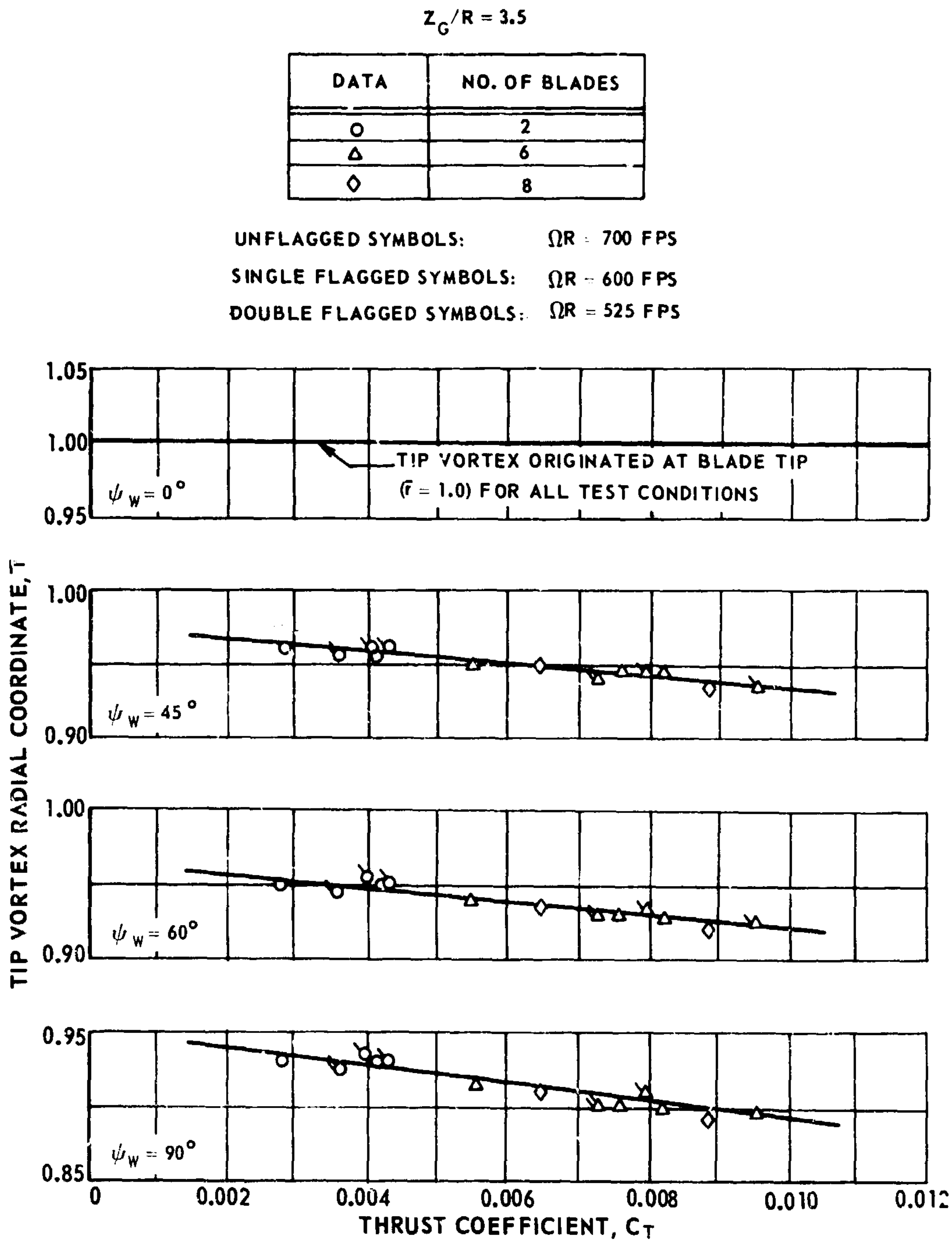

(a) ψ_W = 0°, 45°, 60°, 90°.

Figure 60. Experimental Wake Radial Coordinates for Model Rotors -- θ_1 = -16°, AR = 18.2.

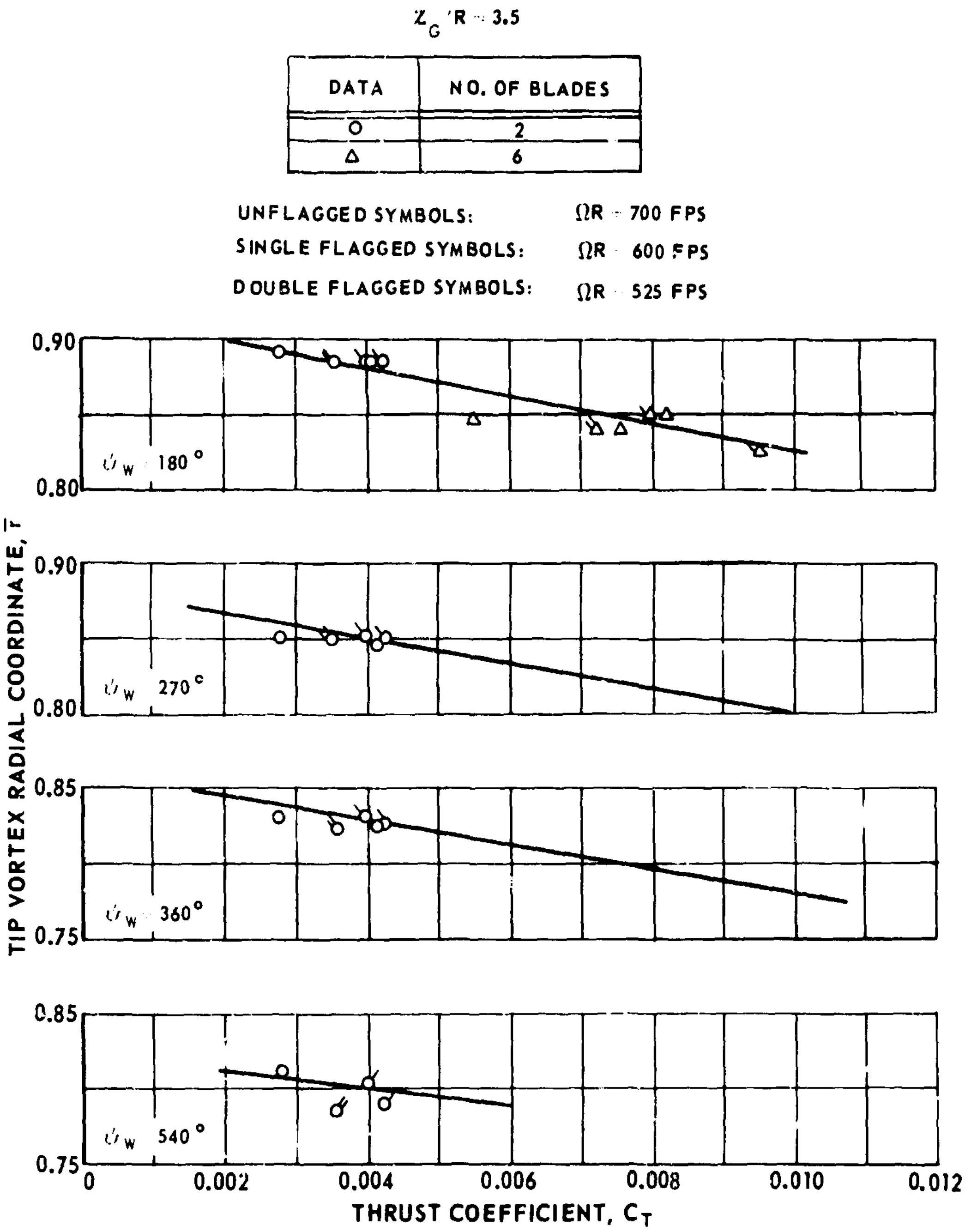

(b) ψ_W = 180°, 270°, 360°, 540°.

Figure 60. Concluded.

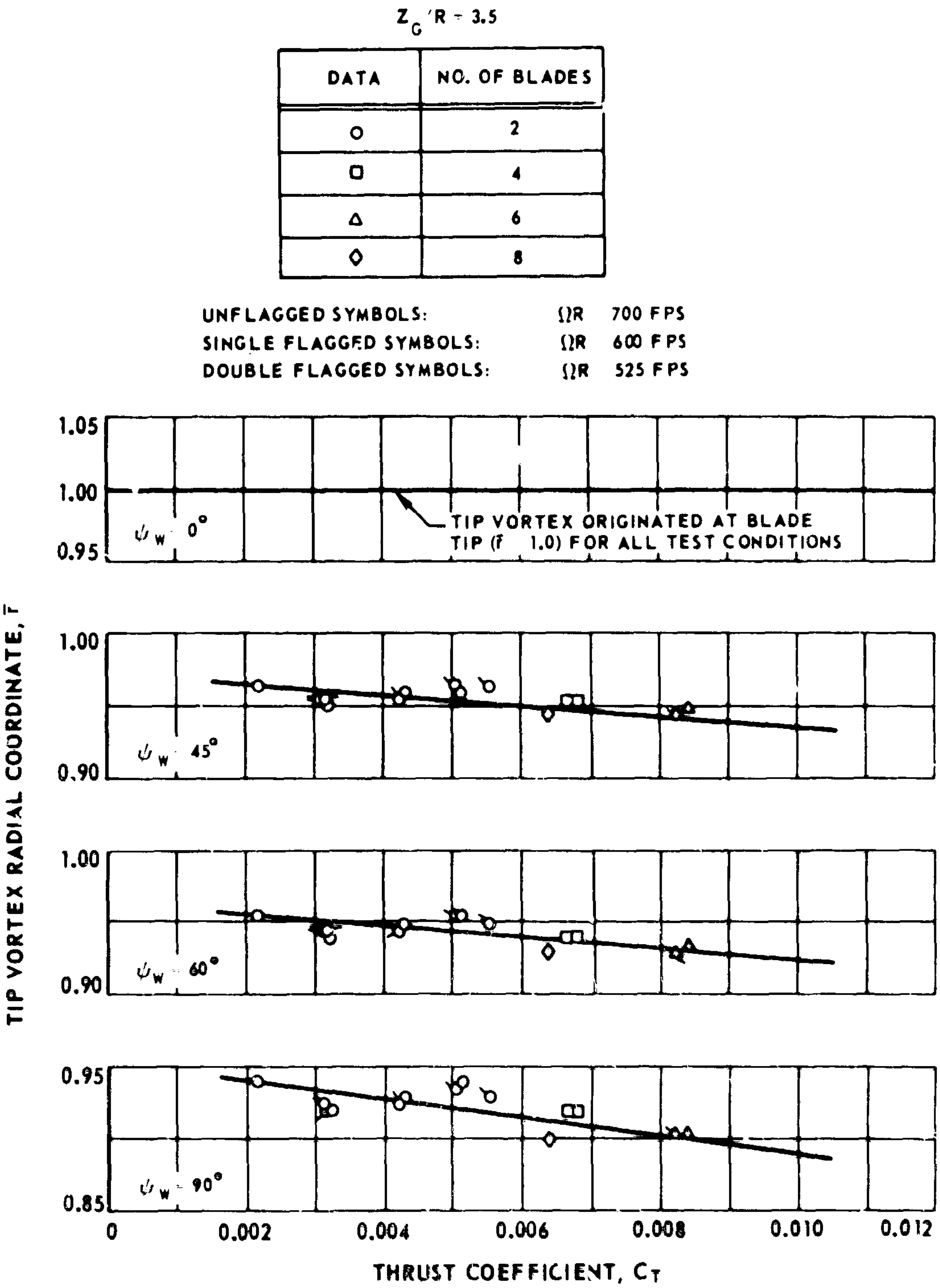

(a) ψ_W = 0°, 45°, 60°, 90°.

Figure 61. Experimental Wake Radial Coordinates for Model Rotors -- θ_1 = -8°, AR = 13.6.

$Z_G/R = 3.5$

DATA	NO. OF BLADES
○	2
□	4
△	6
◇	8

UNFLAGGED SYMBOLS: ΩR 700 FPS
SINGLE FLAGGED SYMBOLS: ΩR 600 FPS
DOUBLE FLAGGED SYMBOLS: ΩR 525 FPS

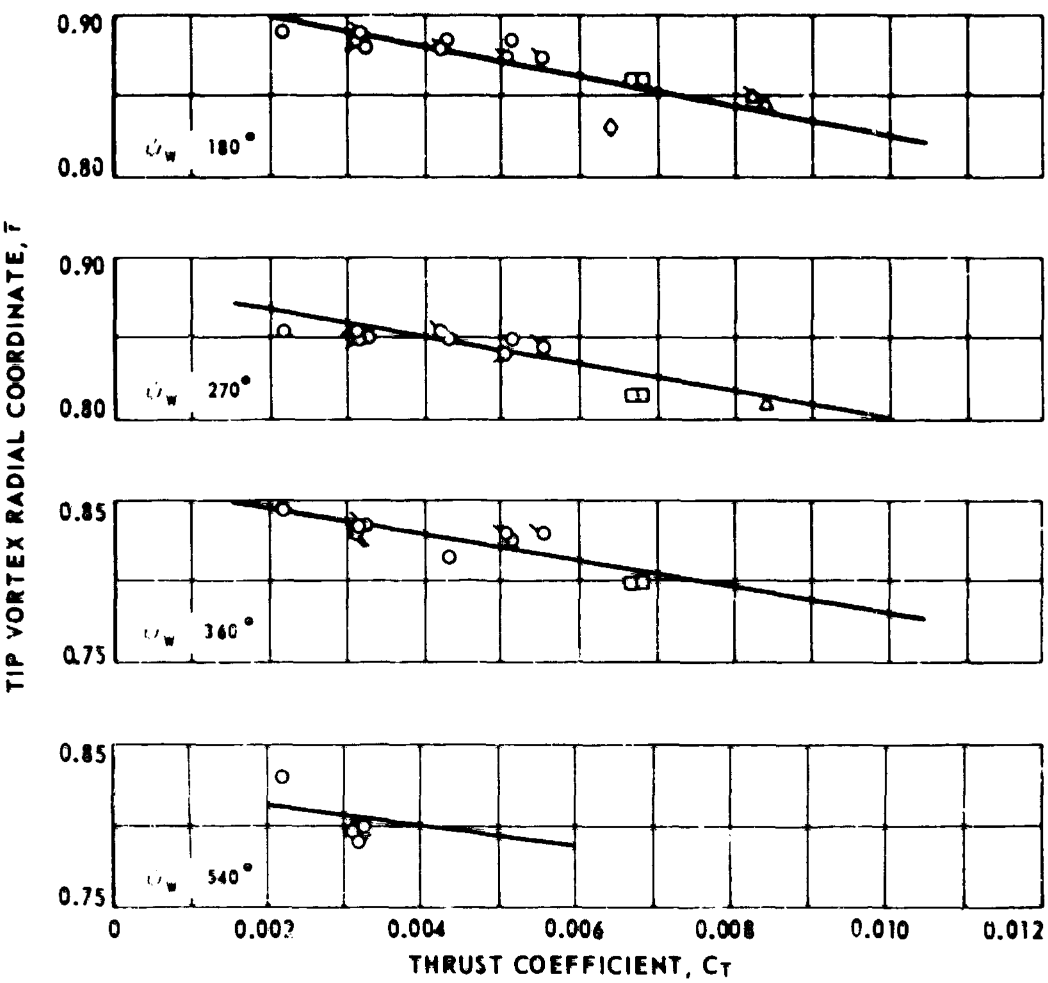

(b) ψ_w = 180°, 270°, 360°, 540°.

Figure 61. Concluded.

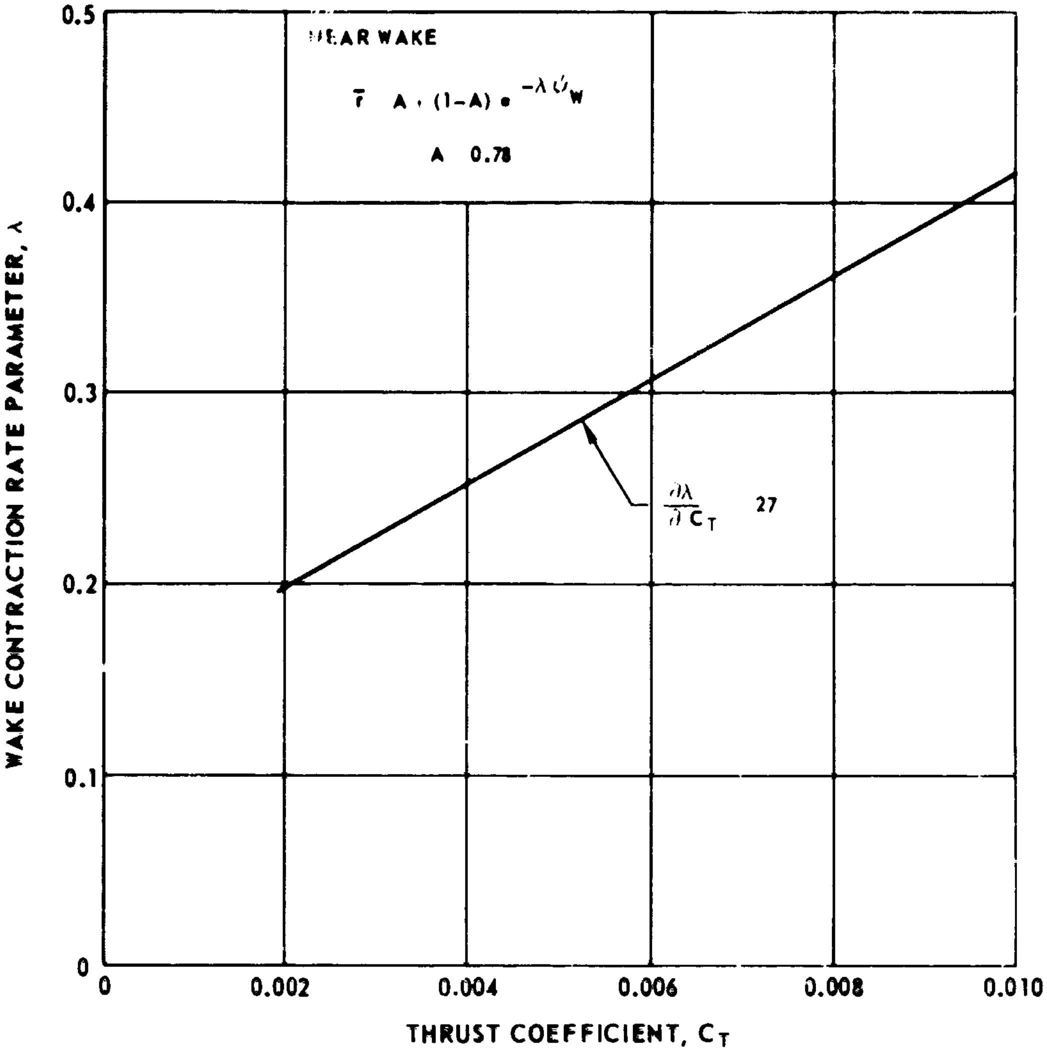

Figure 62. Experimental Wake Contraction Rate Parameter, λ, for Model Rotors.

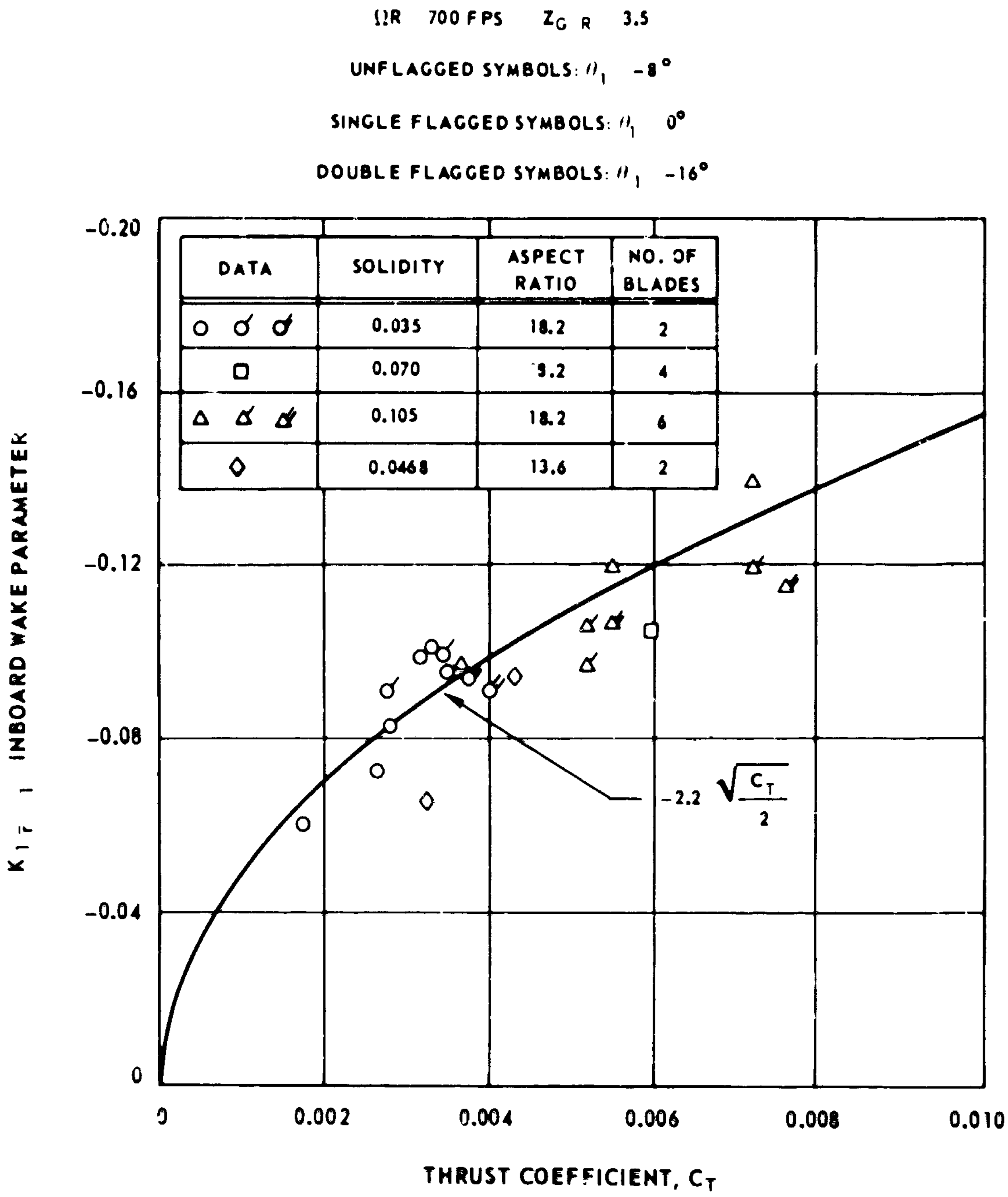

Figure 63. Experimental $K_{1_{\bar{r}=1}}$ Inboard Wake Parameter.

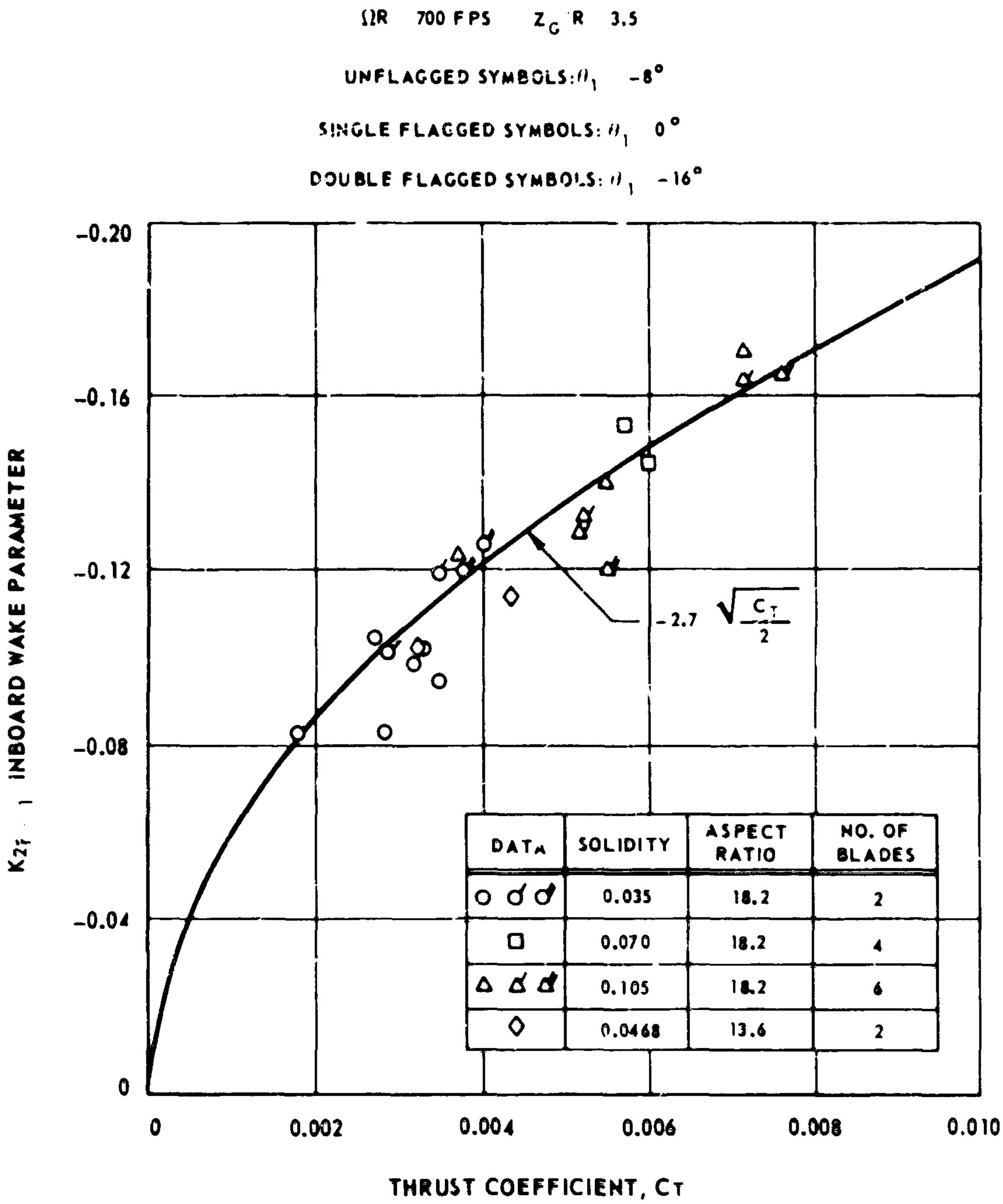

Figure 64. Experimental $K_{2\bar{r}=1}$ Inboard Wake Parameter.

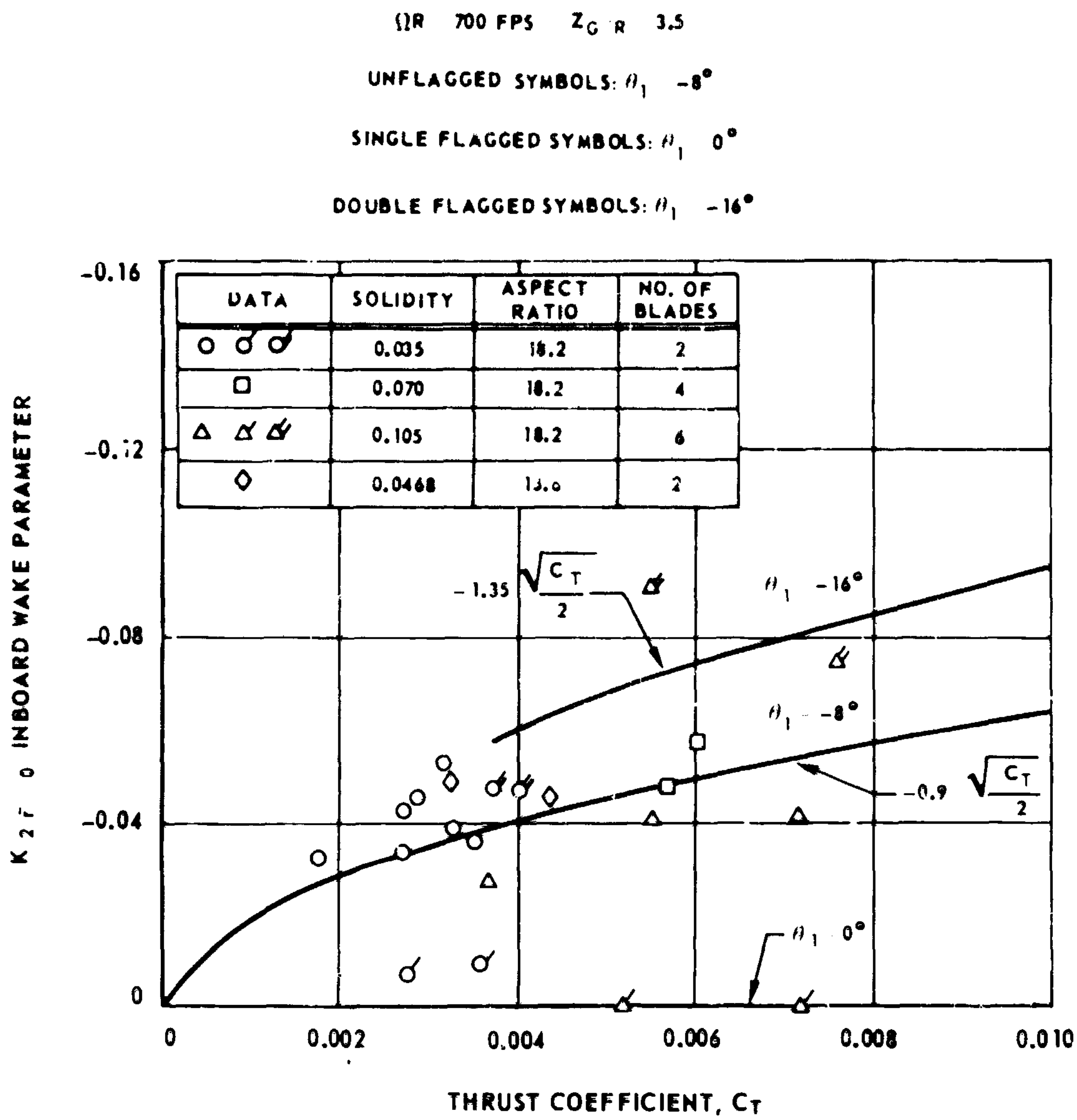

Figure 65. Experimental $K_{2_{\bar{r}=0}}$ Inboard Wake Parameter.

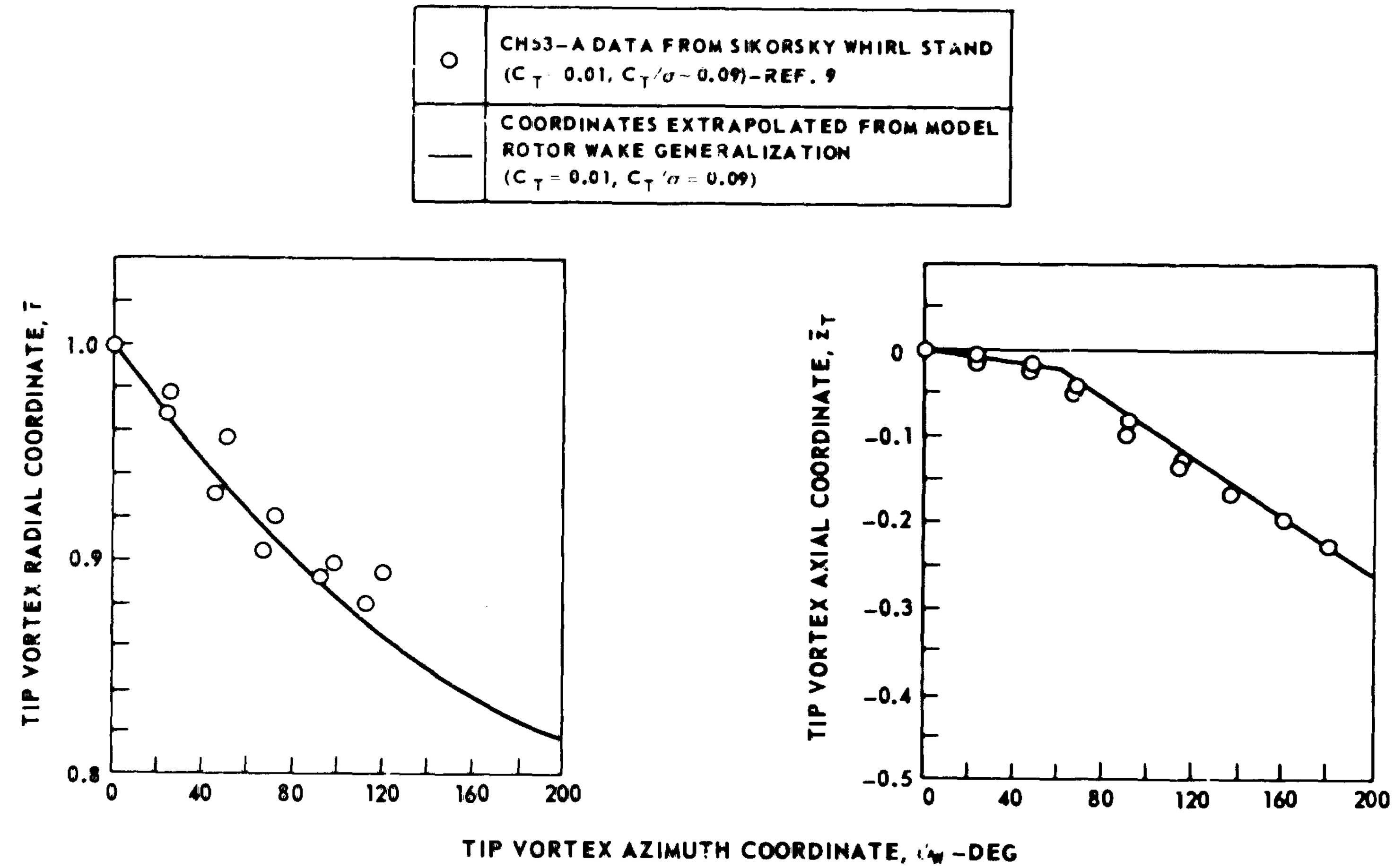

Figure 66. Comparison of Tip Vortex Coordinates From Model and Full-Scale Rotor Tests.

TIP VORTEX

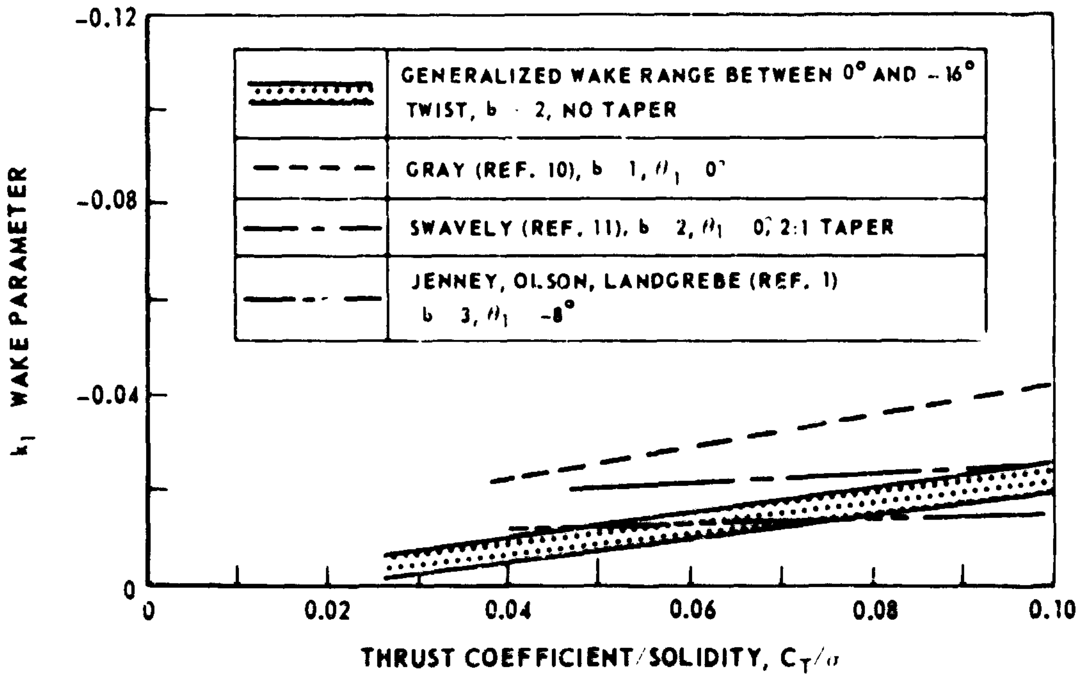

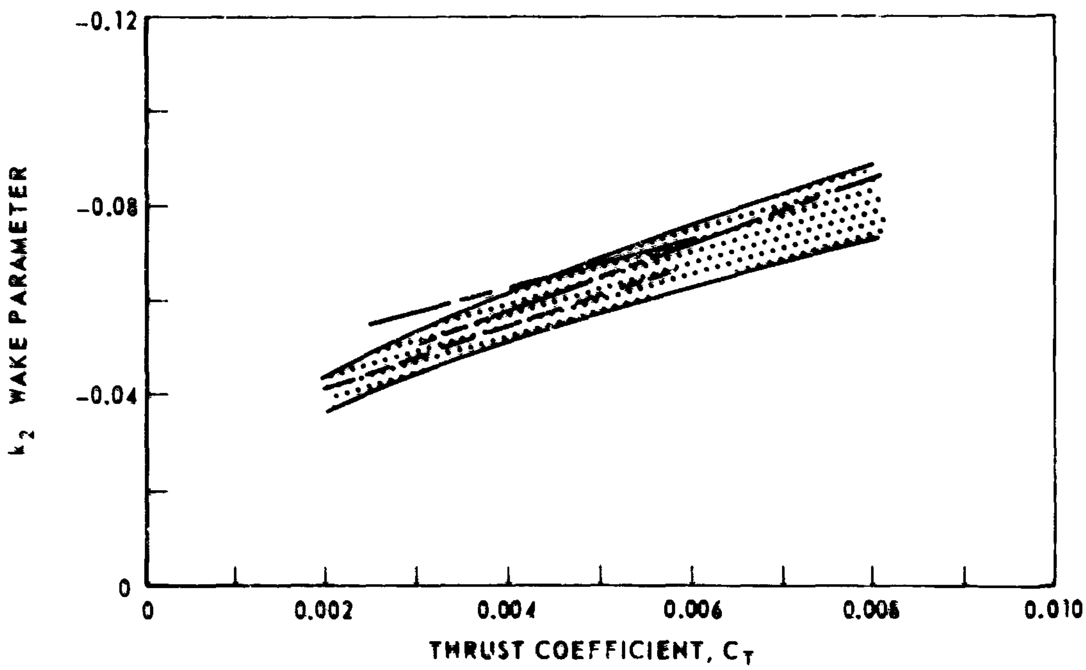

Figure 67. Comparison of Generalized Wake Results With Those of References 1, 10, and 11 -- Axial Coordinates.

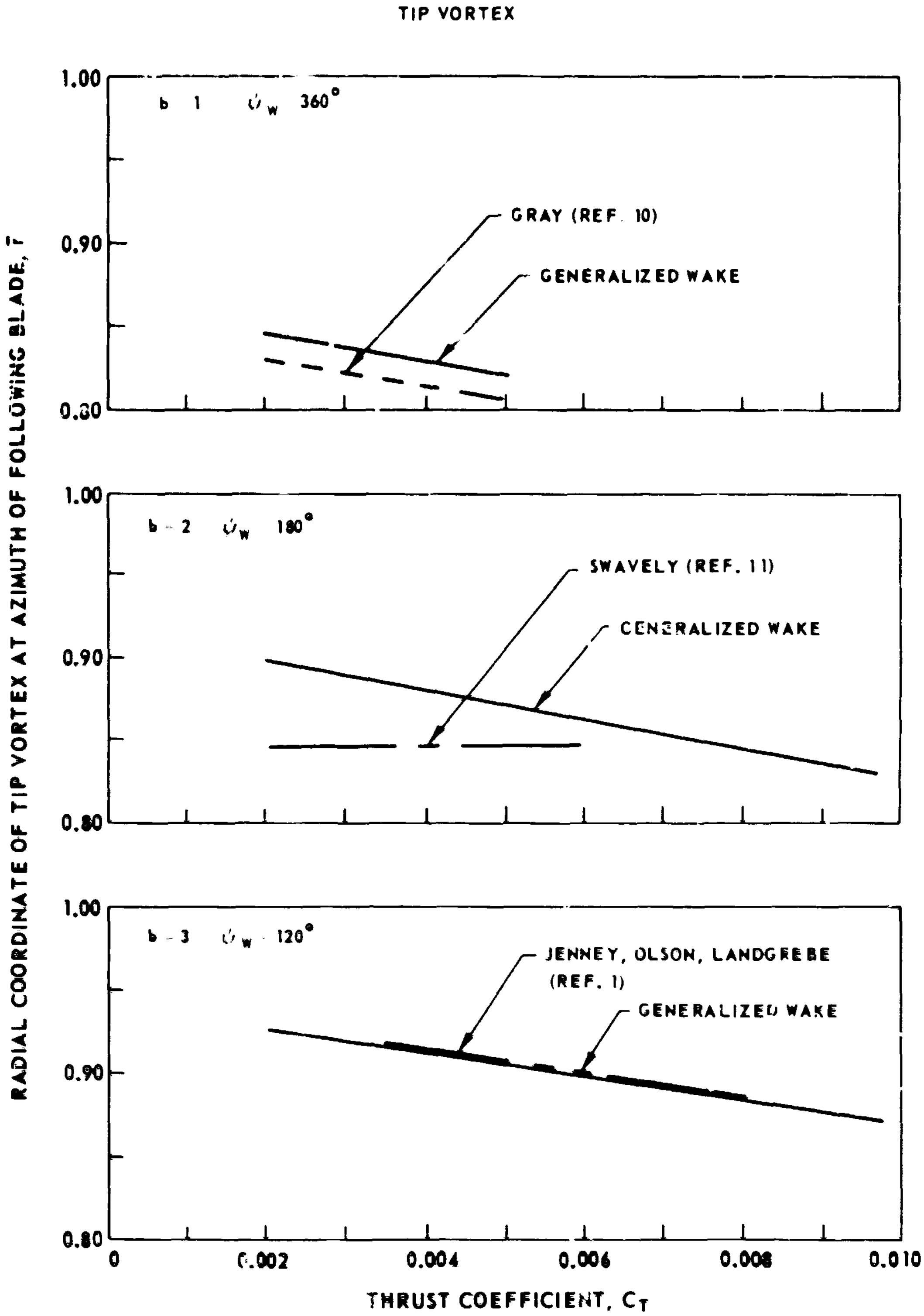

Figure 68. Comparison of Generalized Wake Results With Those of References 1, 10, and 11 -- Radial Coordinates.

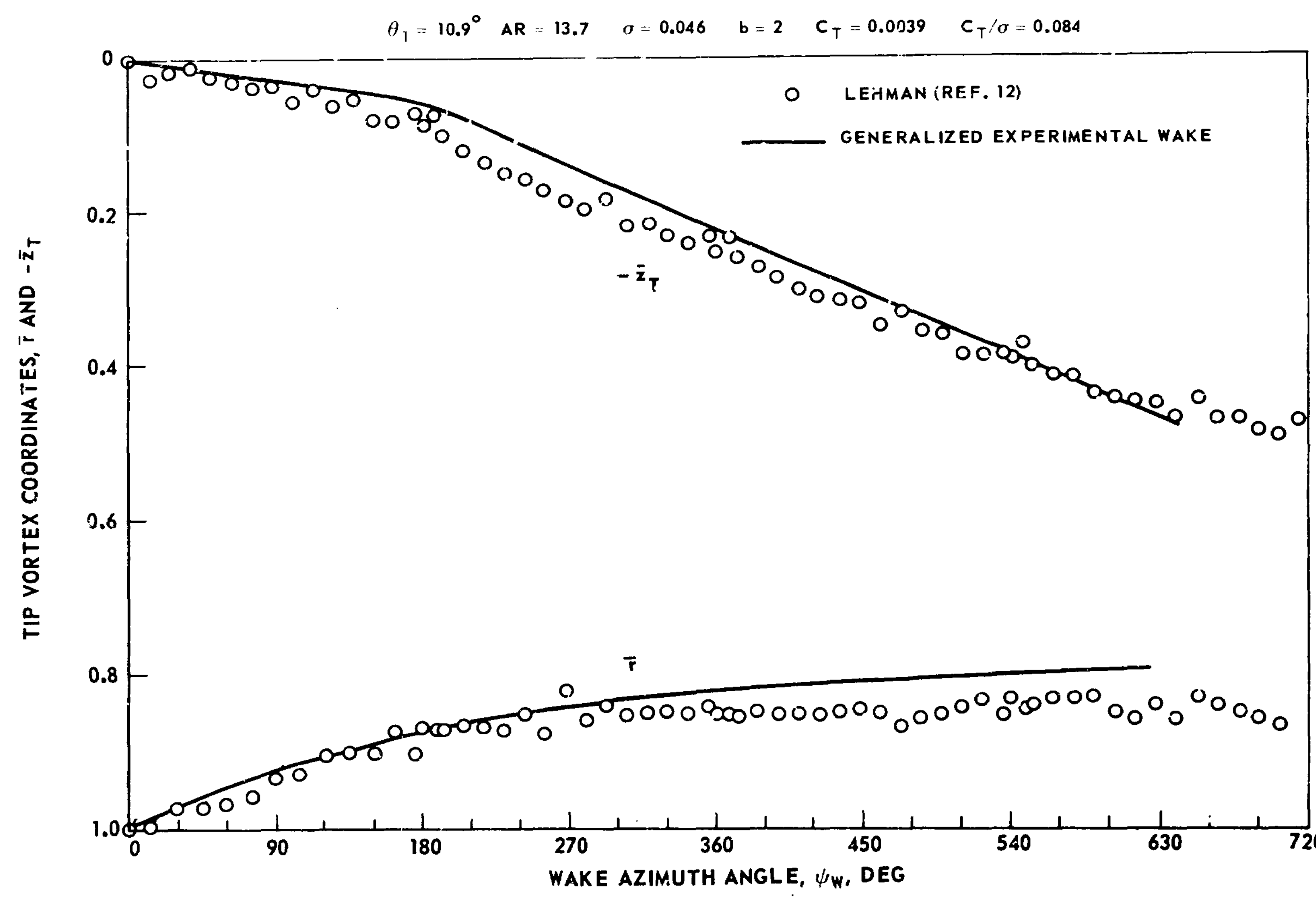

Figure 69. Comparison of Generalized Wake Results With Those of Reference 12.

— — — ACTUATOR DISC THEORY (REFERENCE 14)

GENERALIZED EXPERIMENTAL WAKE BOUNDARIES

$\theta_1 = -8°$, AR = 18.2, ΩR = 700 FPS

CONDITION NO.	b	C_T/σ	C_T
1	2	0.062	0.0022
2	2	0.105	0.0037
3	6	0.034	0.0036
4	6	0.071	0.0075

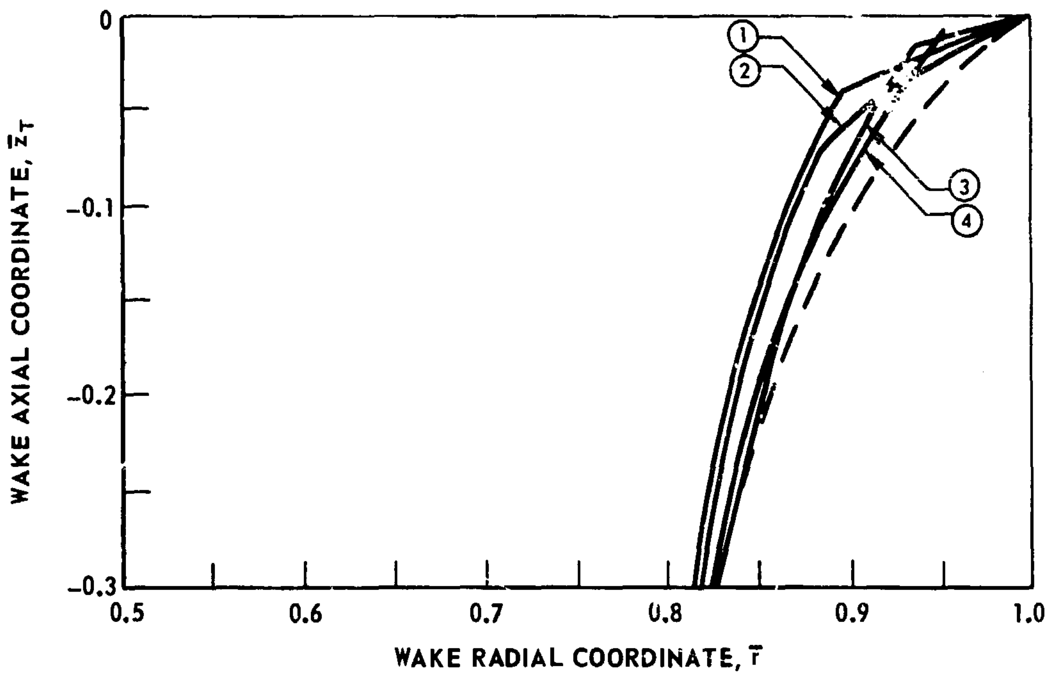

Figure 70. Comparison of Generalized Wake Boundaries With Results of Reference 14.

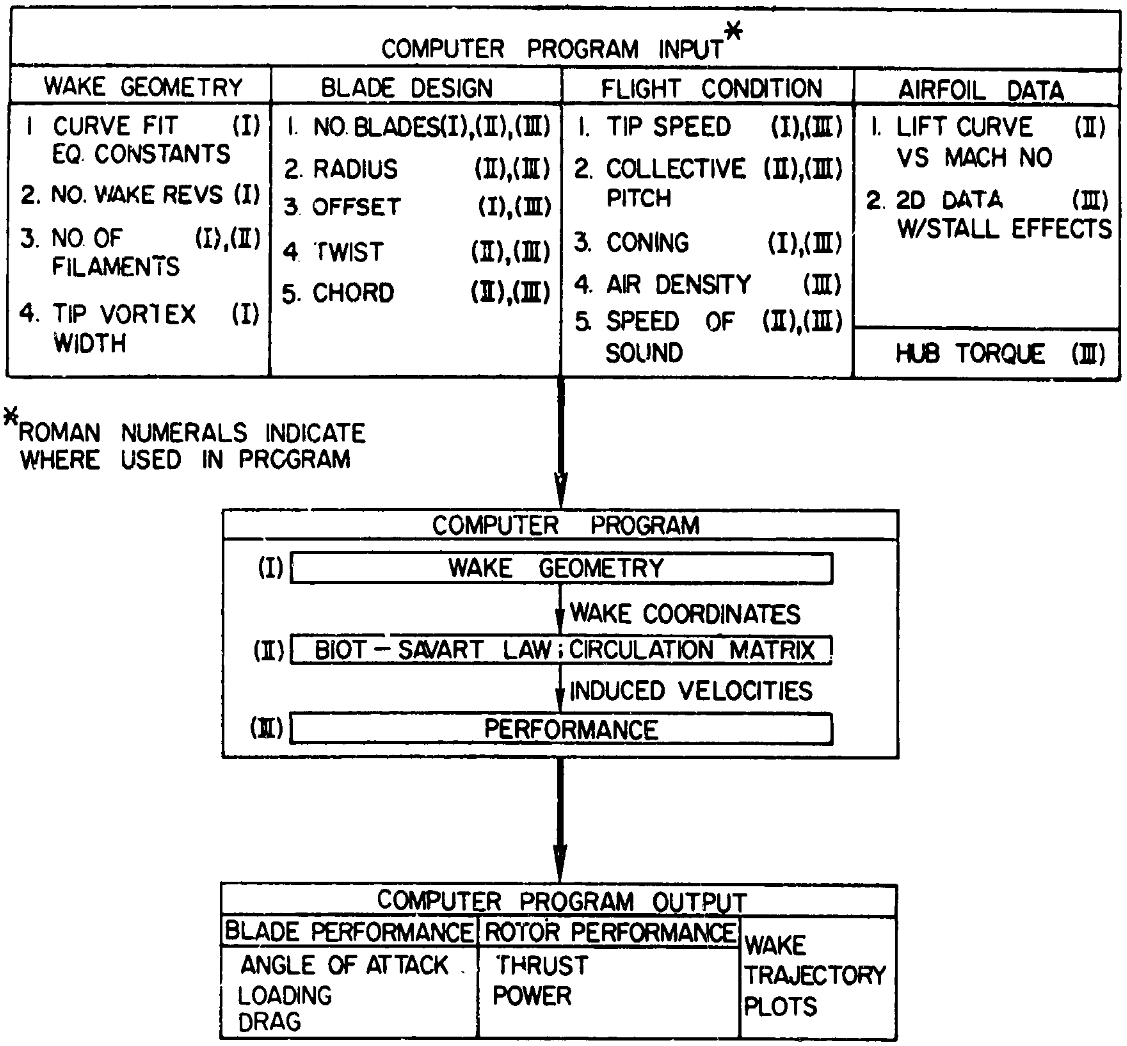

Figure 71. UARL Prescribed Wake Hover Performance Program.

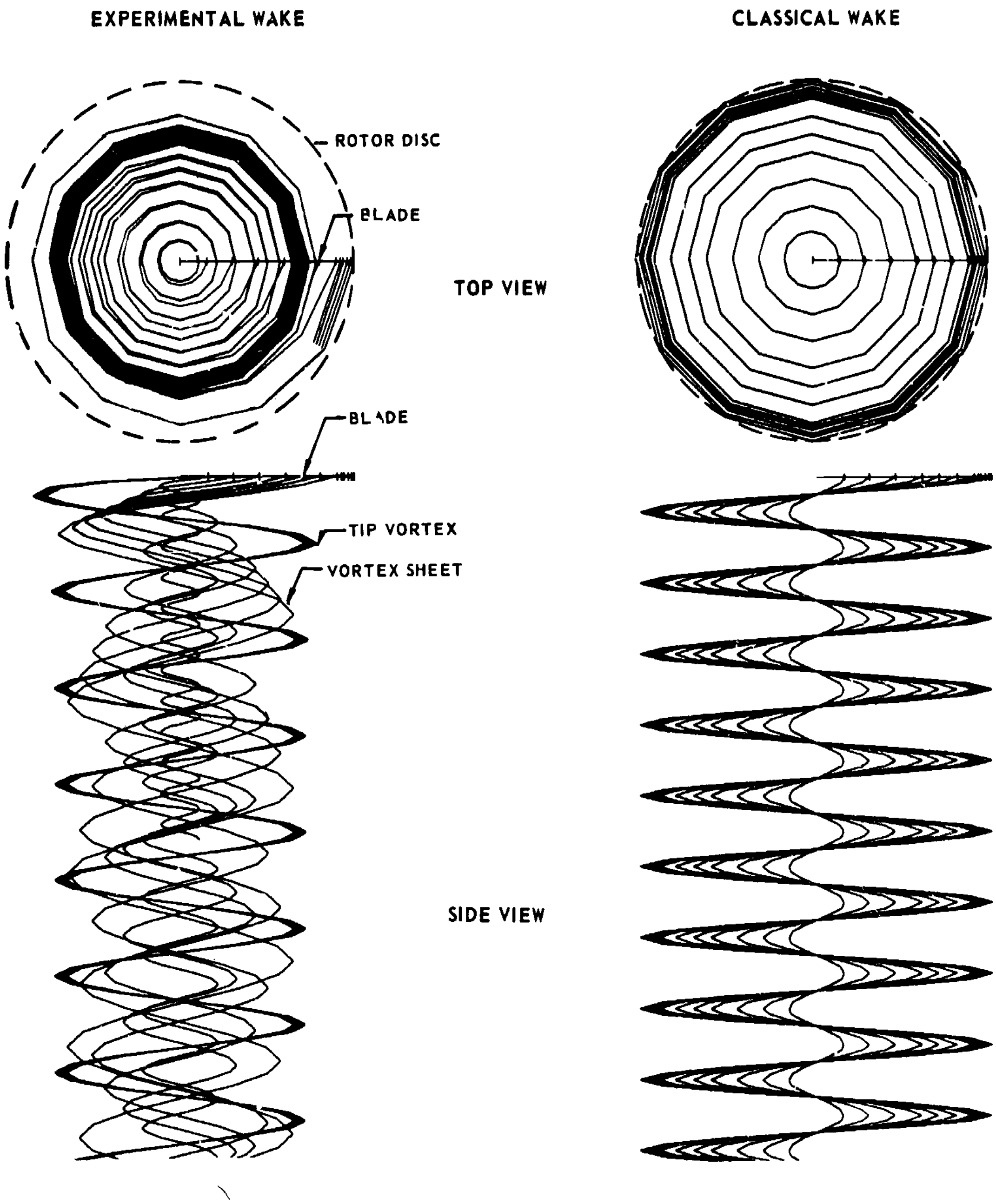

Figure 72. Computer Wake Trajectories for One Blade.

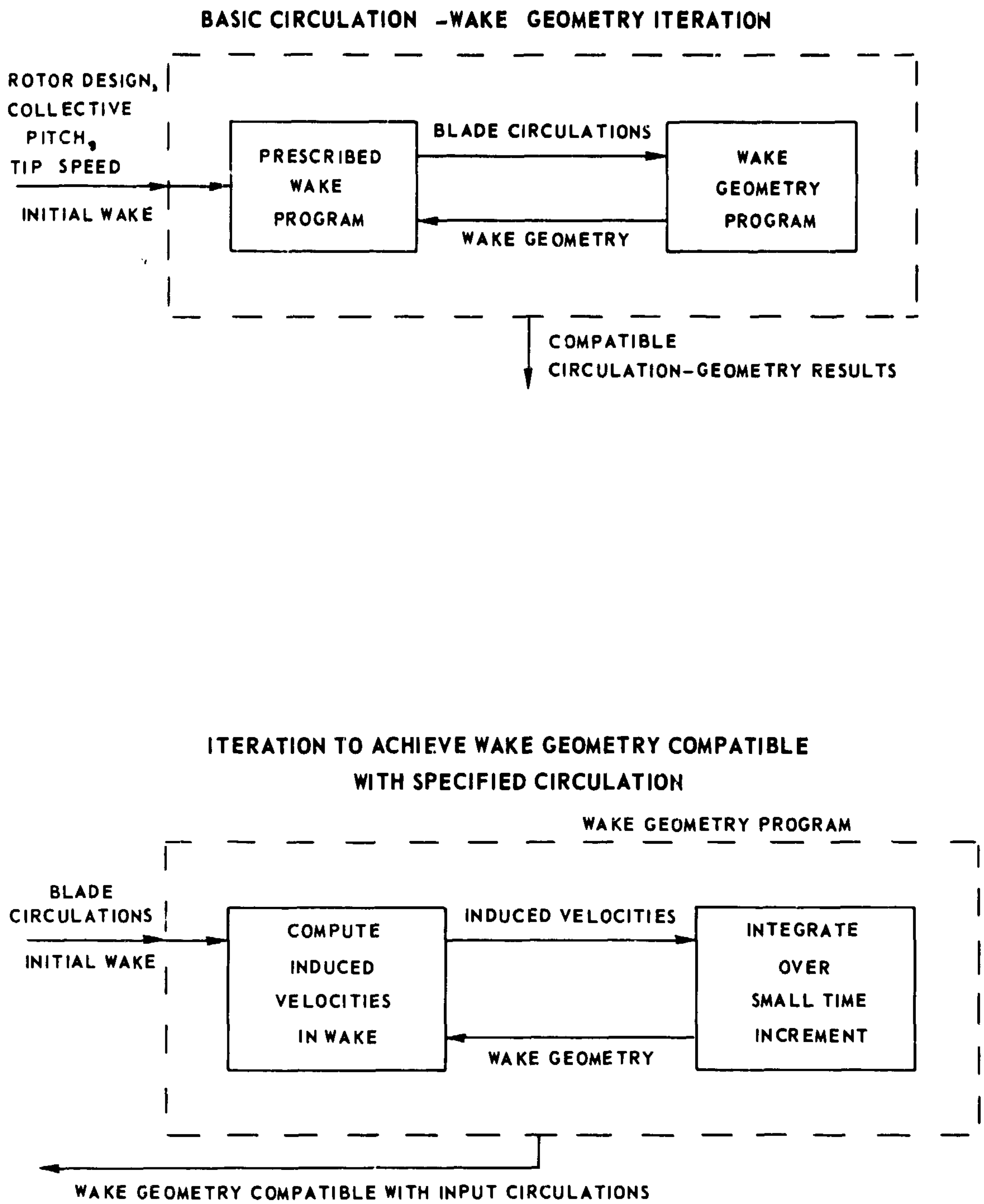

Figure 73. Iteration Procedures for Computing Wake Geometries.

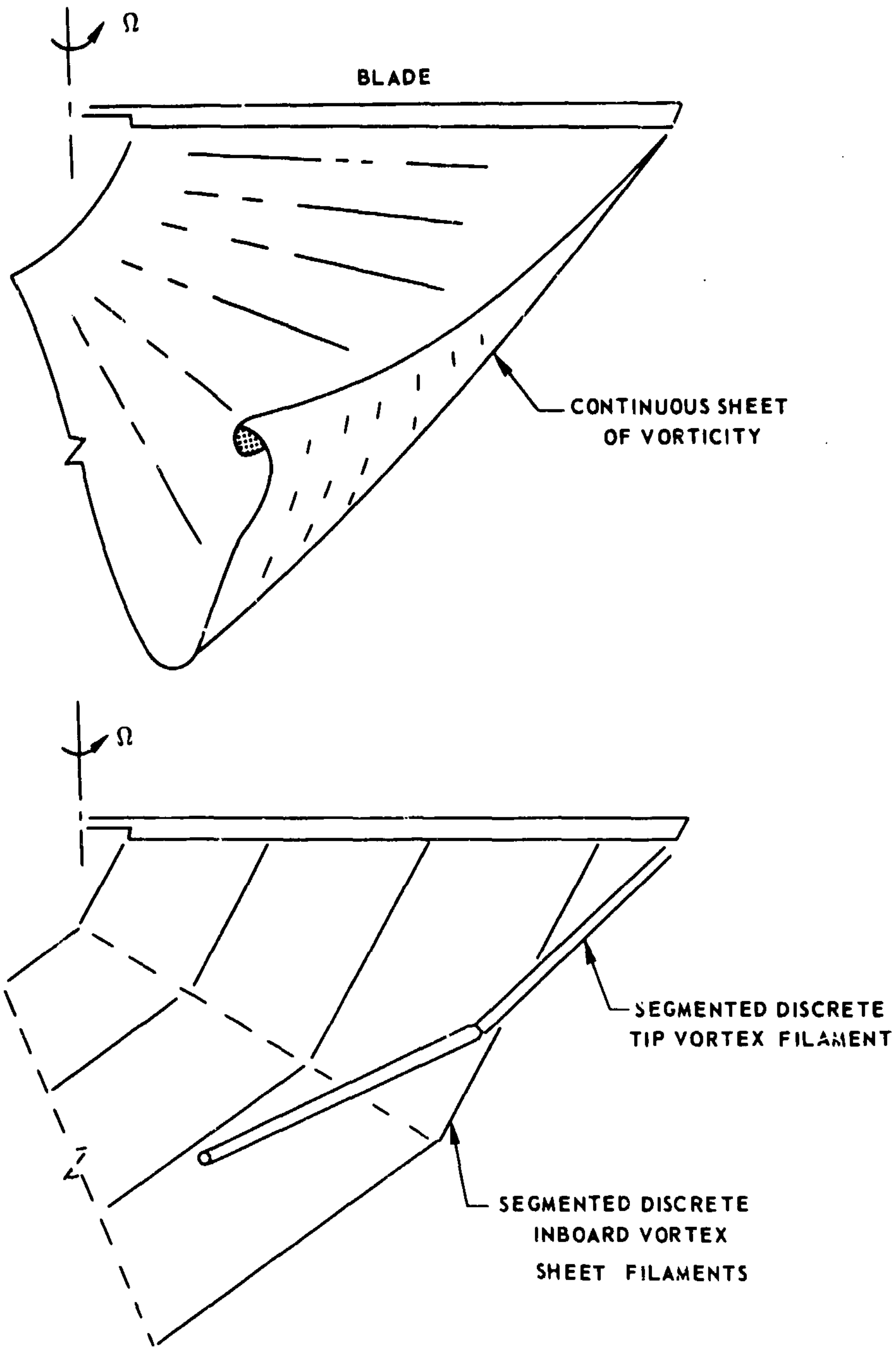

Figure 74. Segmented Discrete Vortex Representation of the Wake.

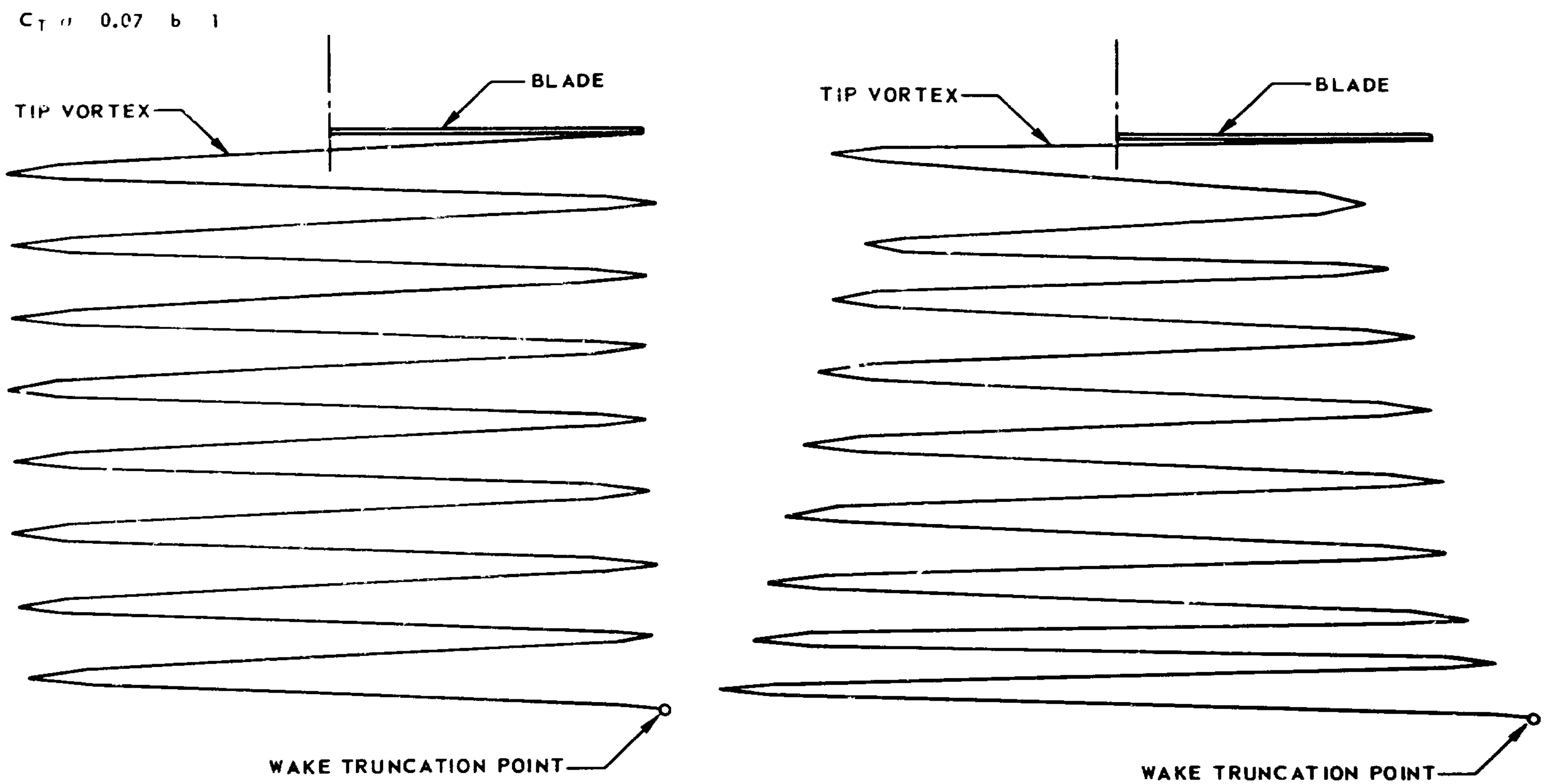

(a) Classical Wake Geometry at Start of Computation (Time Step 0)

(b) Computed Wake Geometry After One Revolution of Rotor (Time Step 12)

Figure 75. Typical Truncated Wake Results.

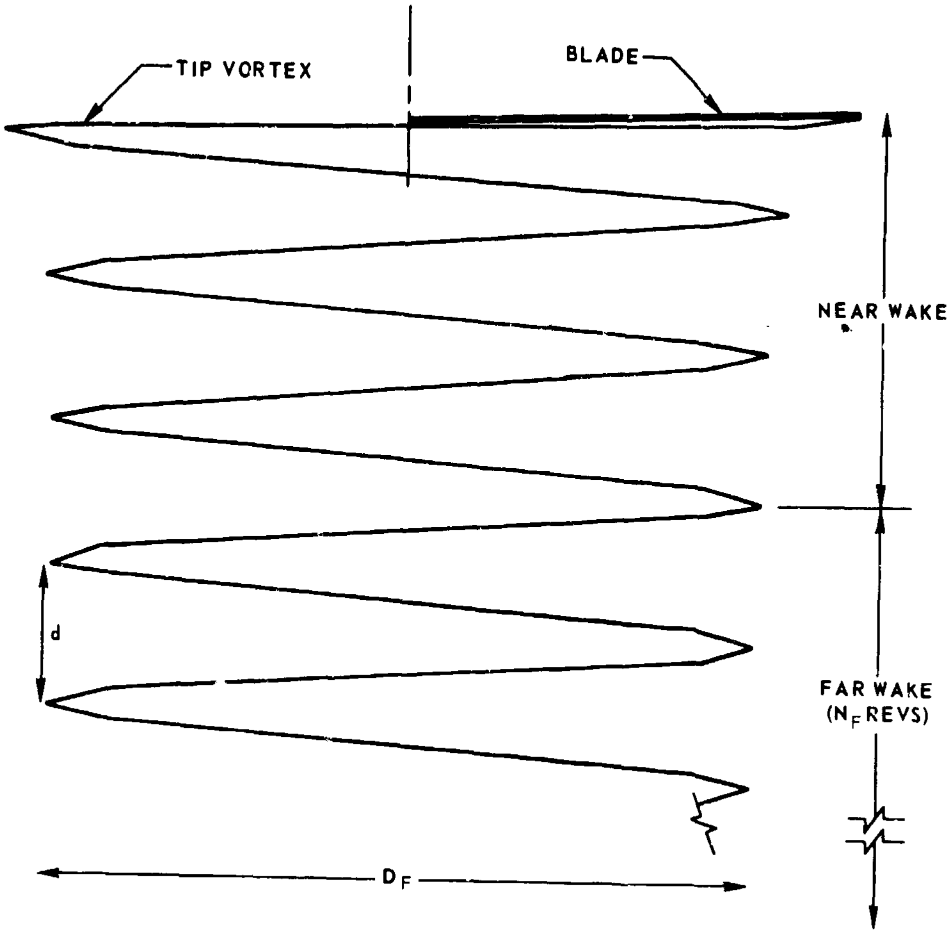

Figure 76. Far-Wake Representation.

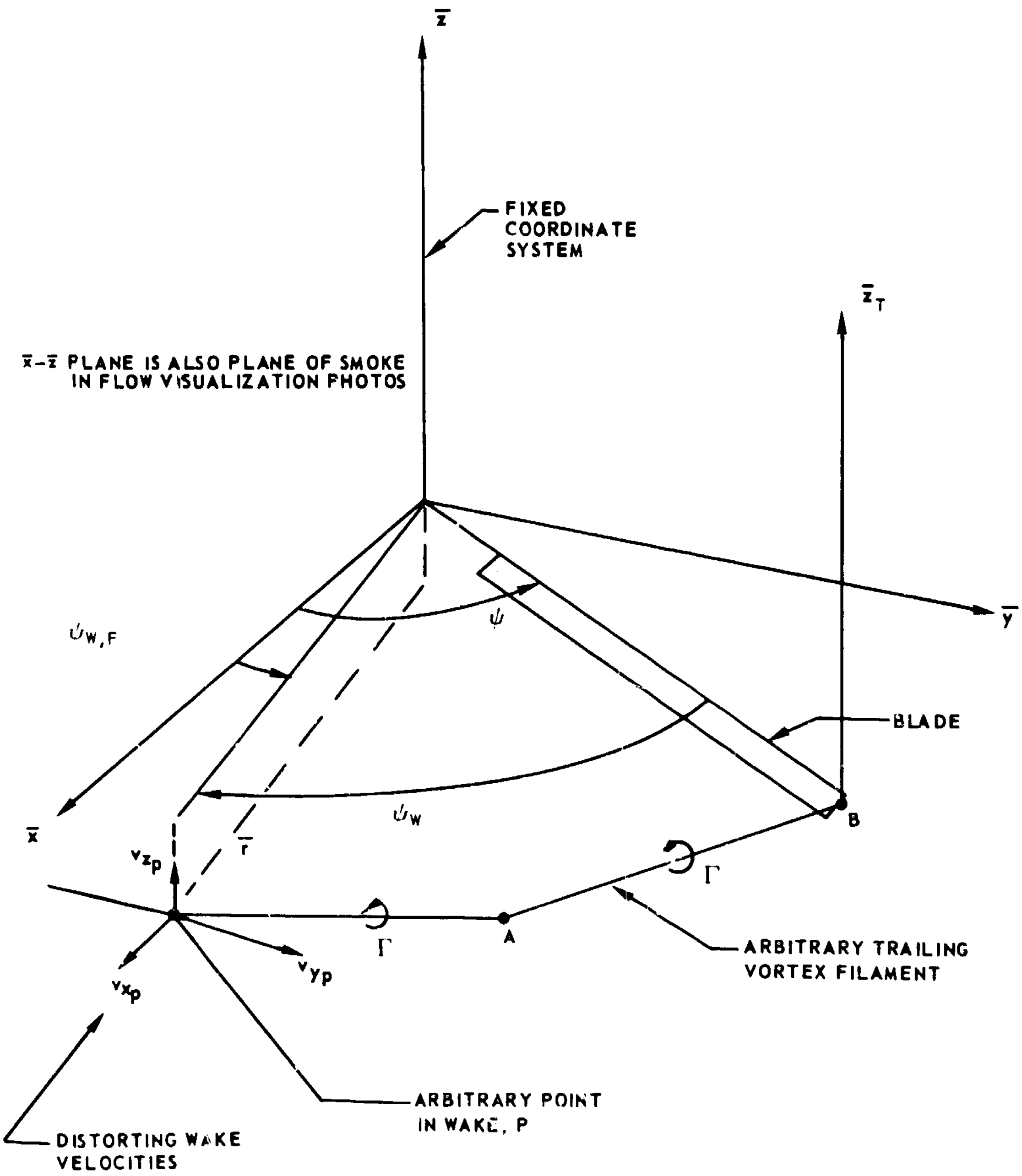

Figure 77. Coordinate Systems and Nomenclature for Theoretical Wake Geometry Computations.

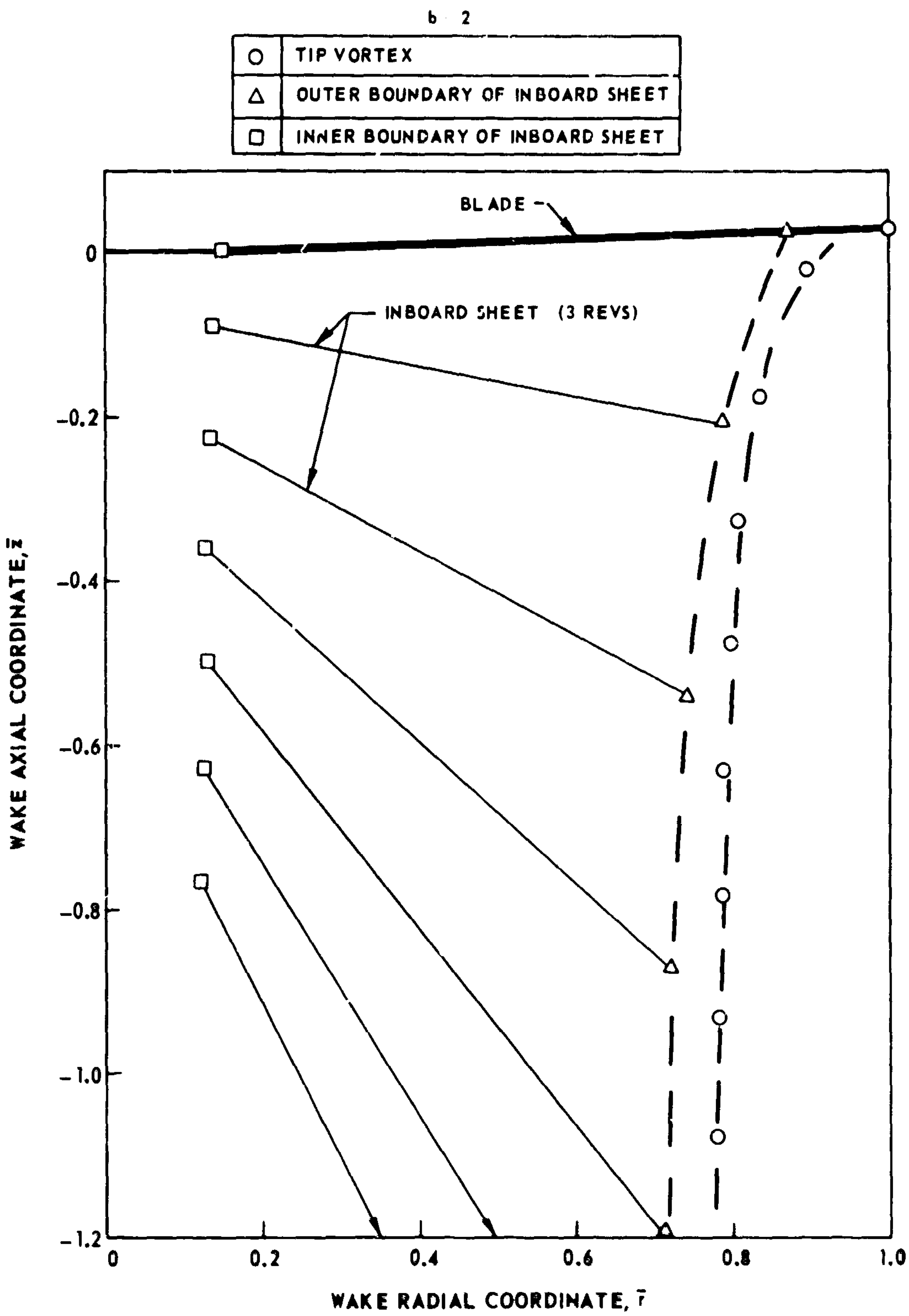

Figure 78. Intersection of Wake With $\bar{r}$-$\bar{z}$ Plane Showing Typical Inboard Vortex Sheet Representation.

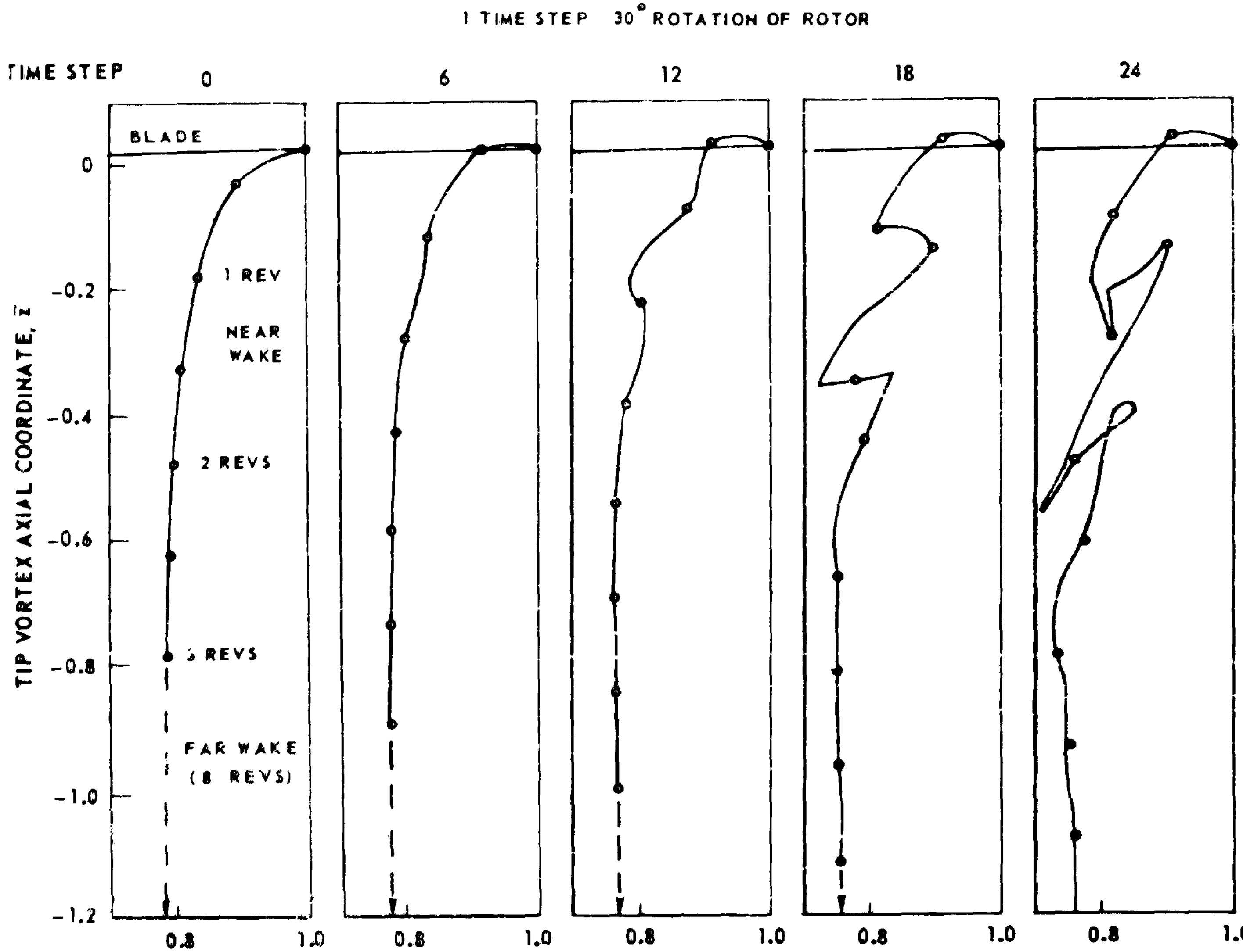

Figure 79. Typical Predicted Rotor Wake Boundaries At Various Time Steps.

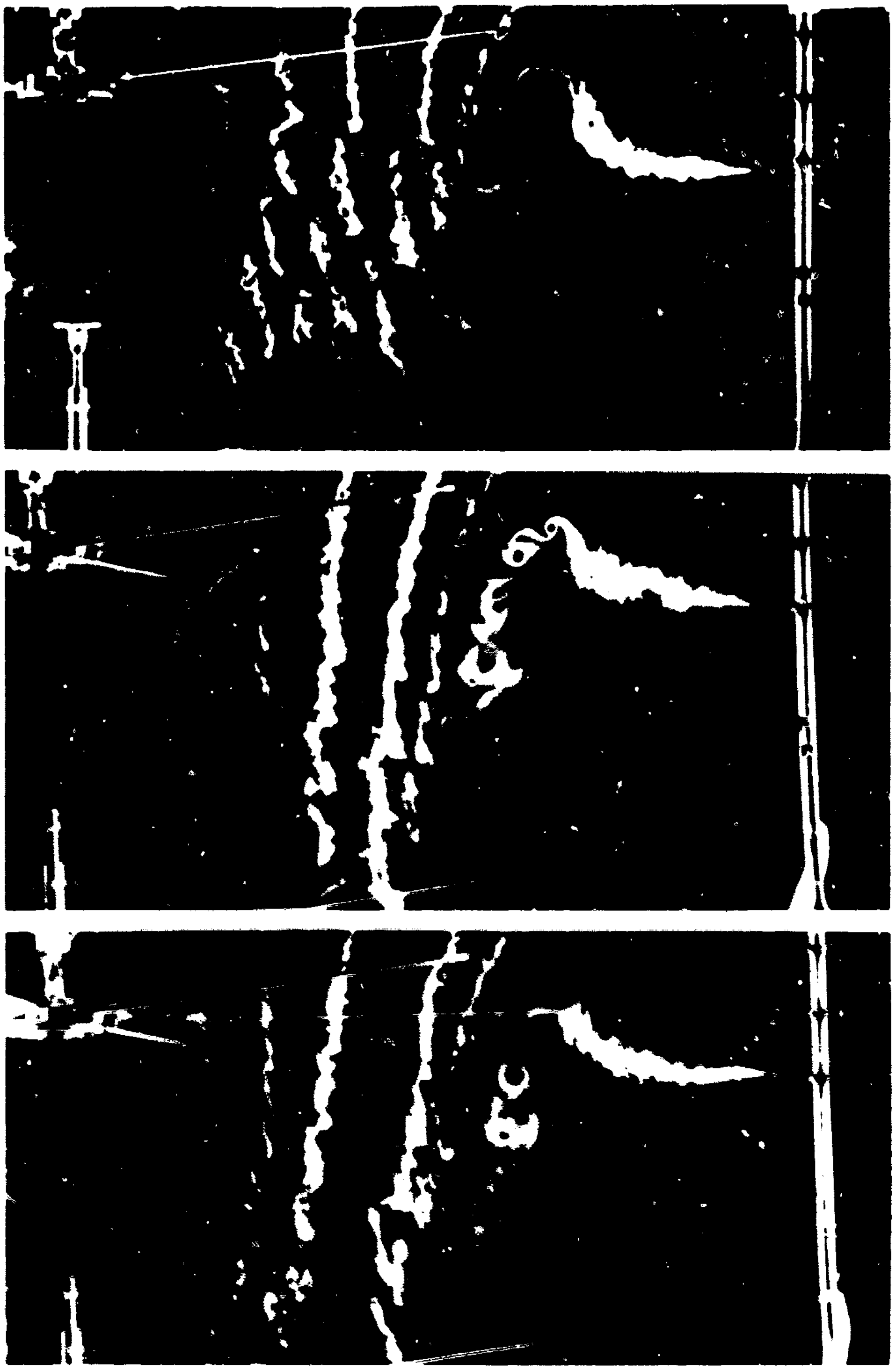

Figure 80. Model Rotor Photographs Showing Typical Local Roll-Up of Tip Vortex.

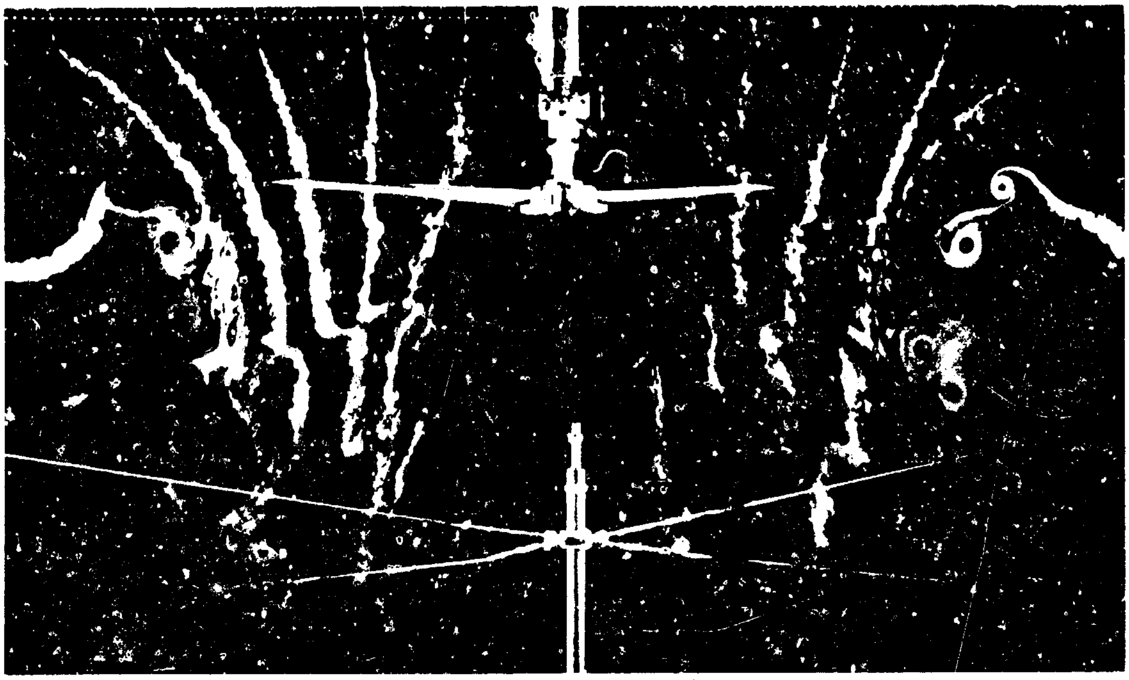

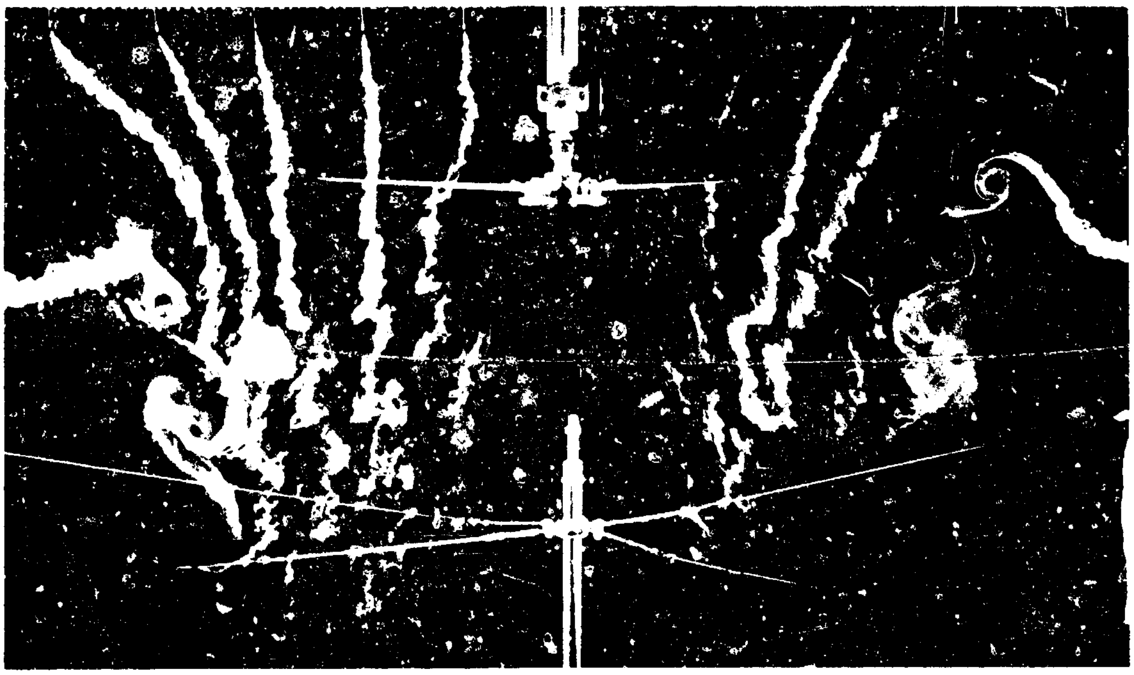

(b)

Figure 80. Continued.

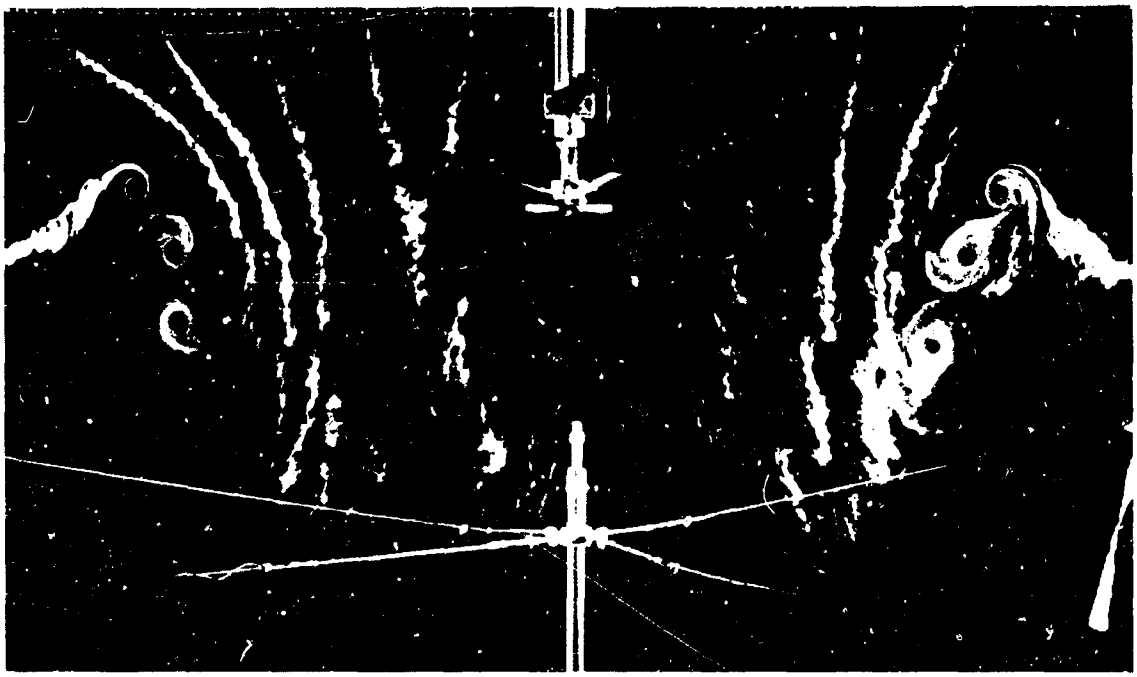

(c)

Figure 80. Concluded.

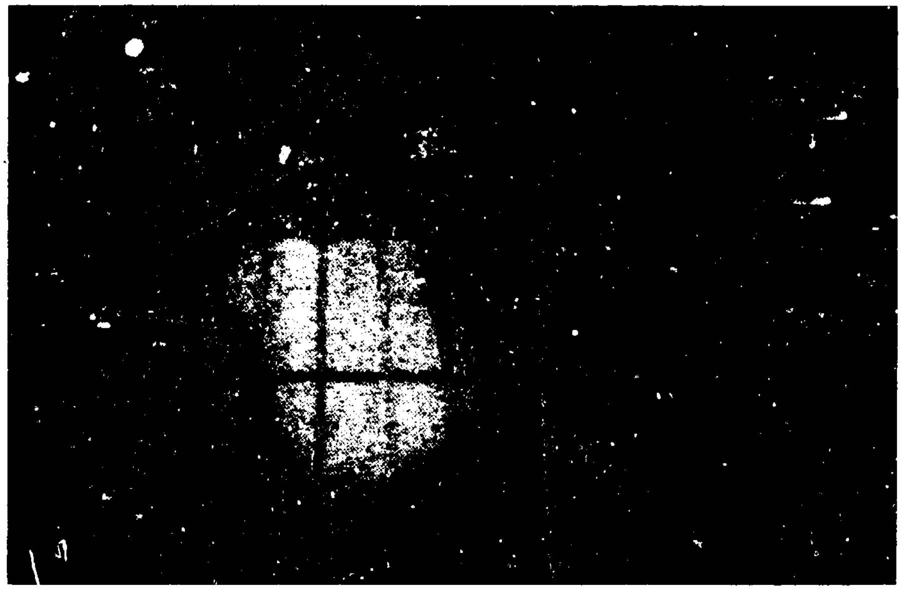

Figure 81. Photograph of Wake for a Full-Scale Rotor Showing Local Roll-Up of the Tip Vortex.

FROM WATER TUNNEL TEST PROGRAM OF REFERENCE 12

Figure 82. Photograph of Wake of Model Rotor Taken in a Water Tunnel Showing Local Roll-Up of the Tip Vortex.

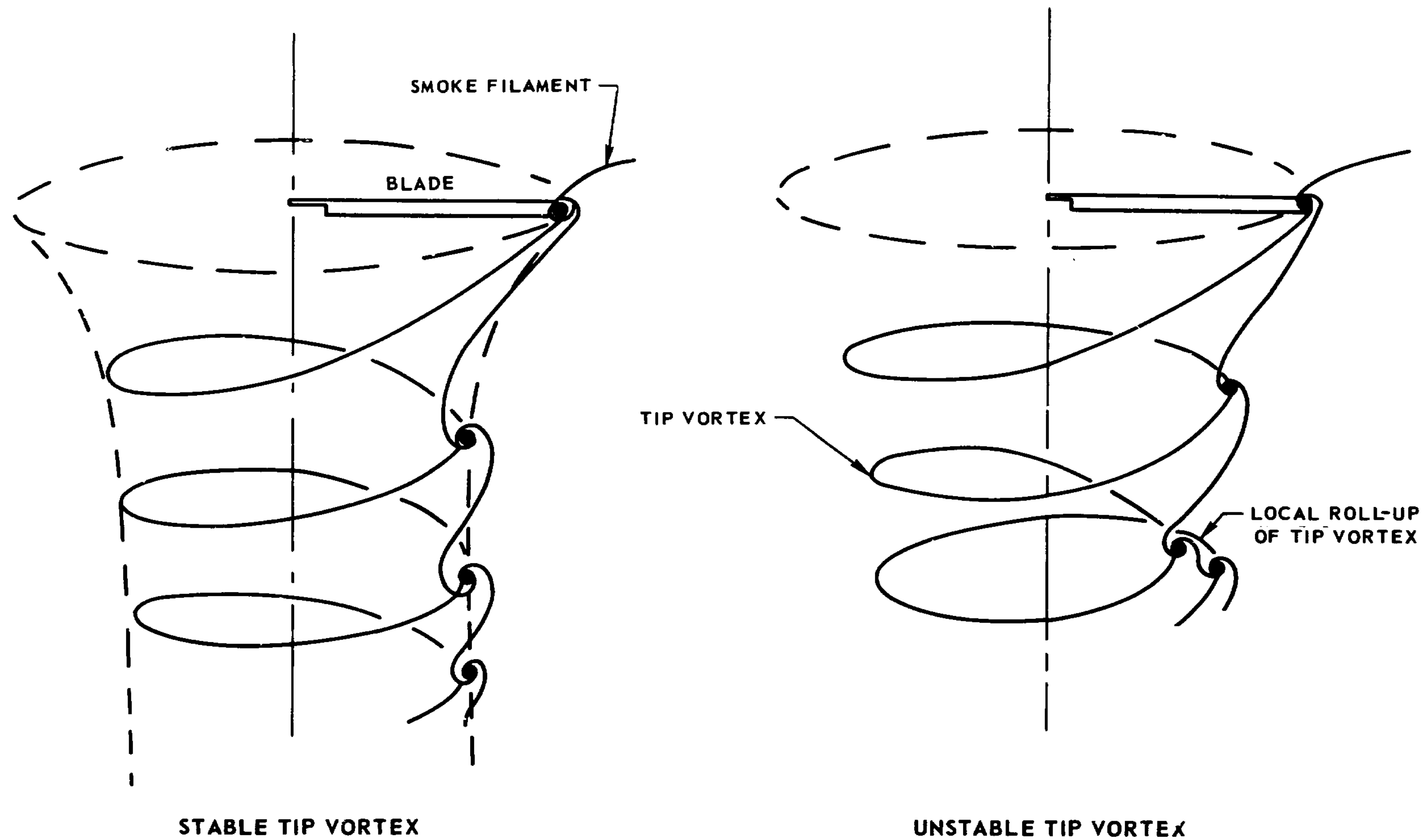

Figure 83. Schematic of Stable and Unstable Tip Vortices.

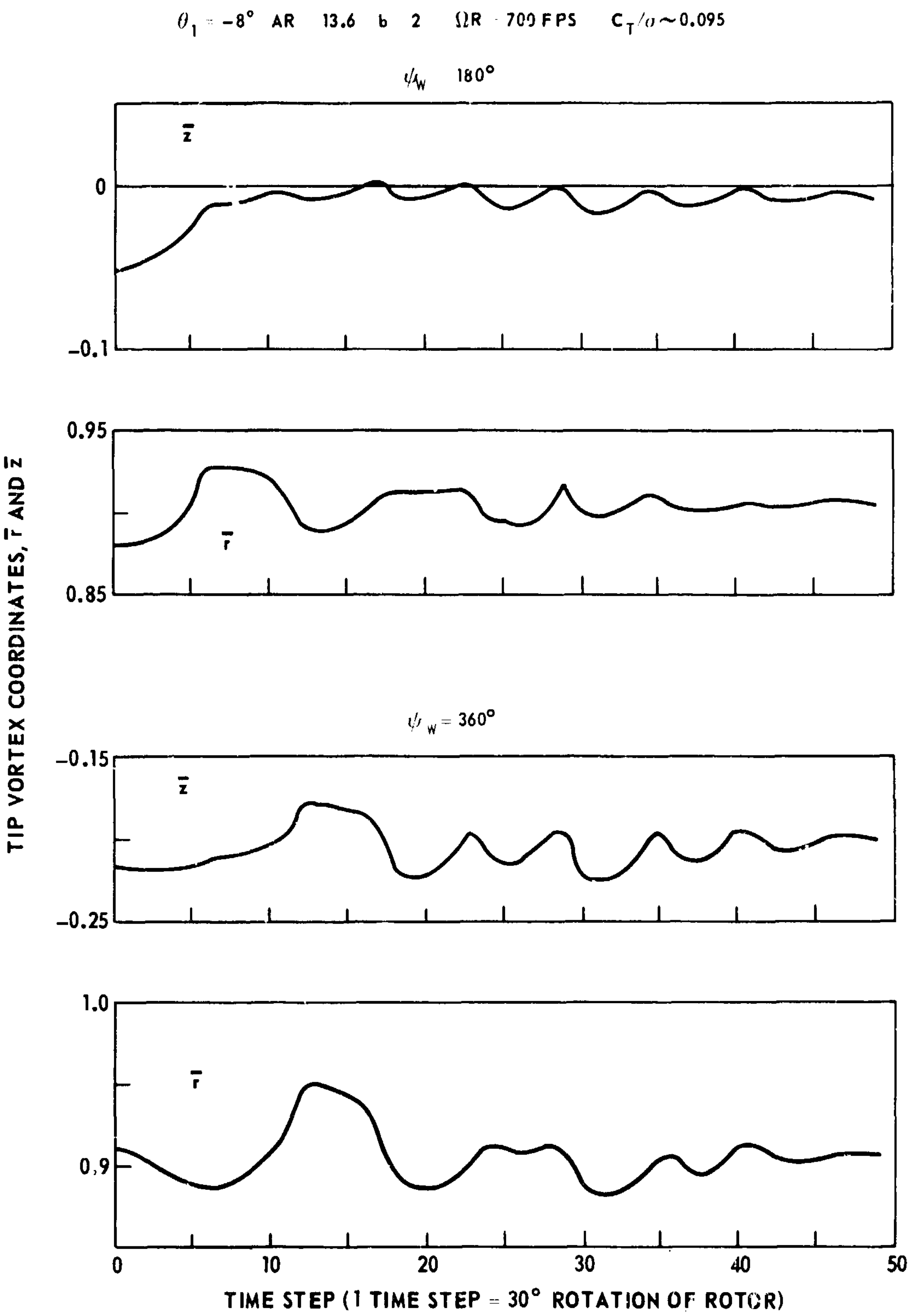

Figure 84. Typical Time Histories of Computed Tip Vortex Coordinates Showing Convergence of Extreme Near-Wake.

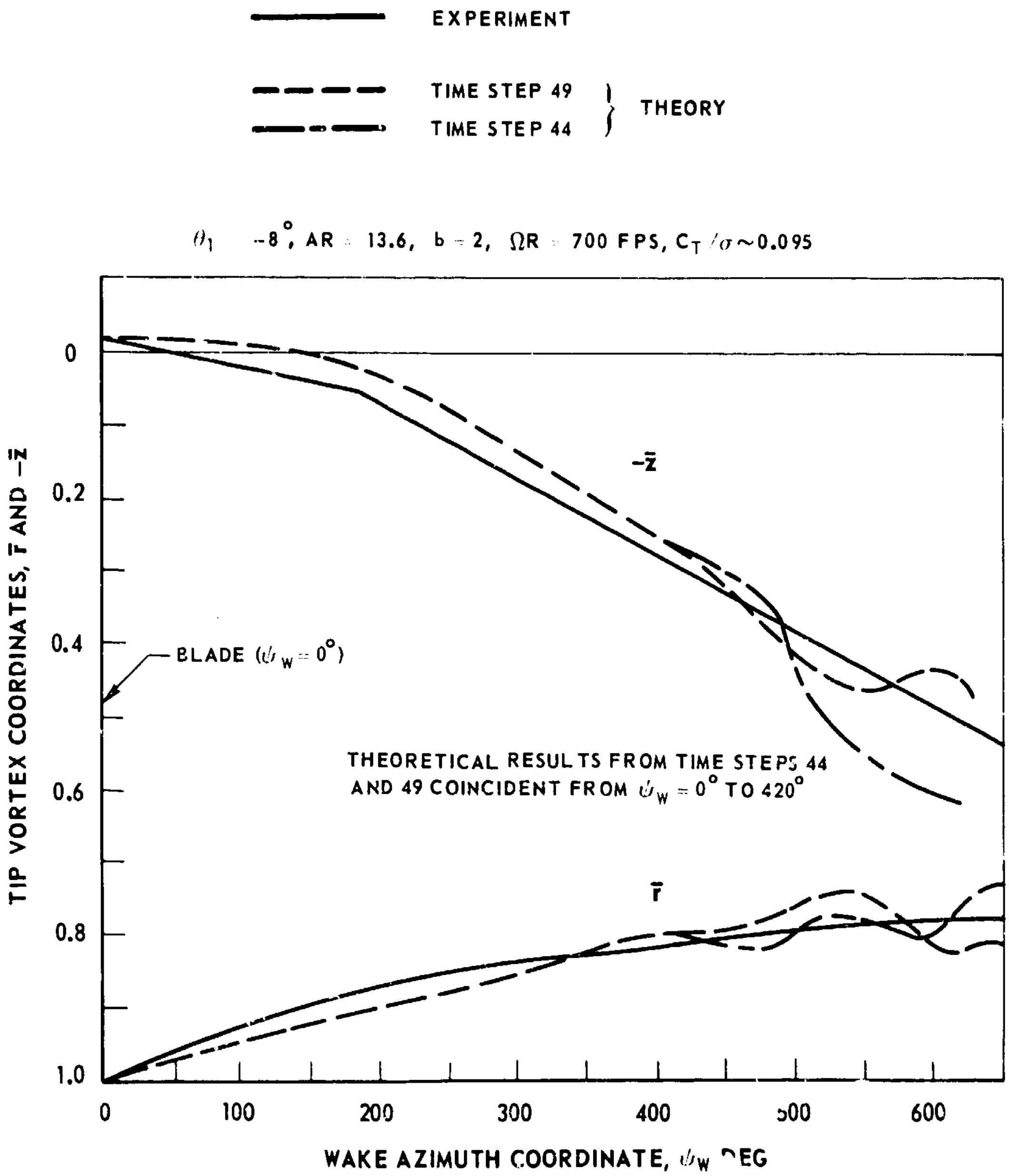

Figure 85. Computed Radial and Axial Coordinates of Tip Vortex for Two Time Steps.

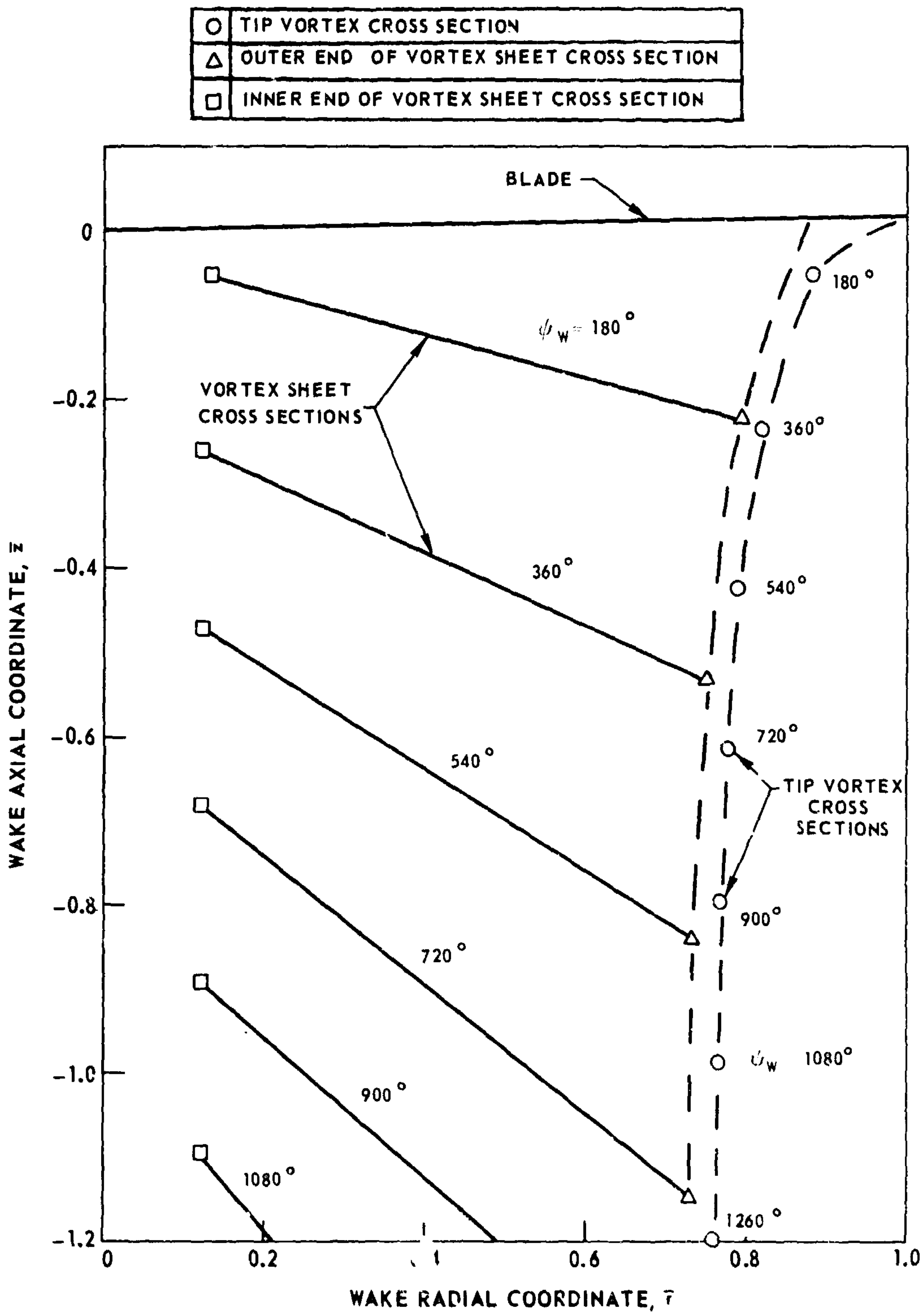

Figure 86. Initial Wake Geometry Used in Sample Computation.

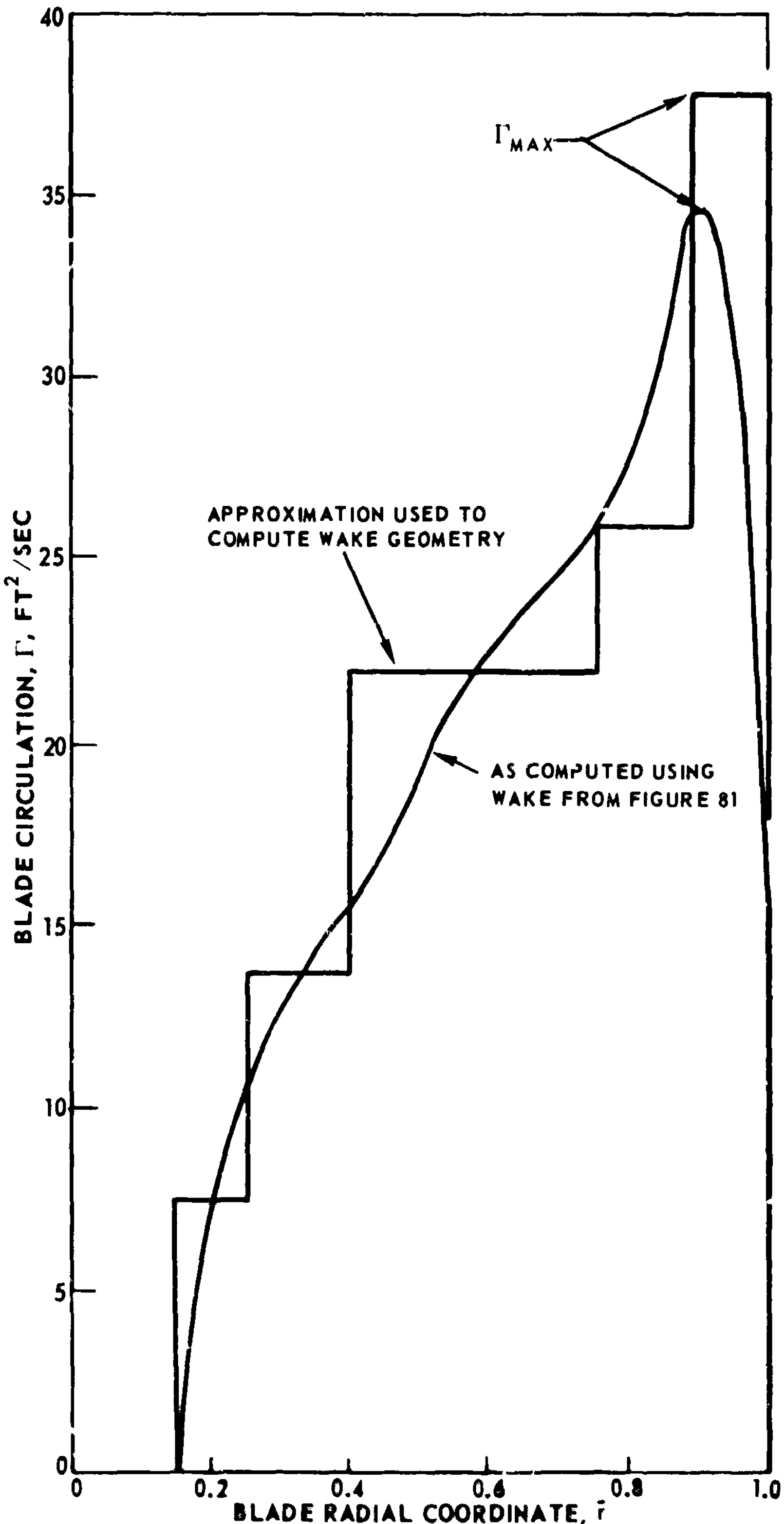

Figure 87. Approximation to Blade Circulation Distribution in Sample Computation.

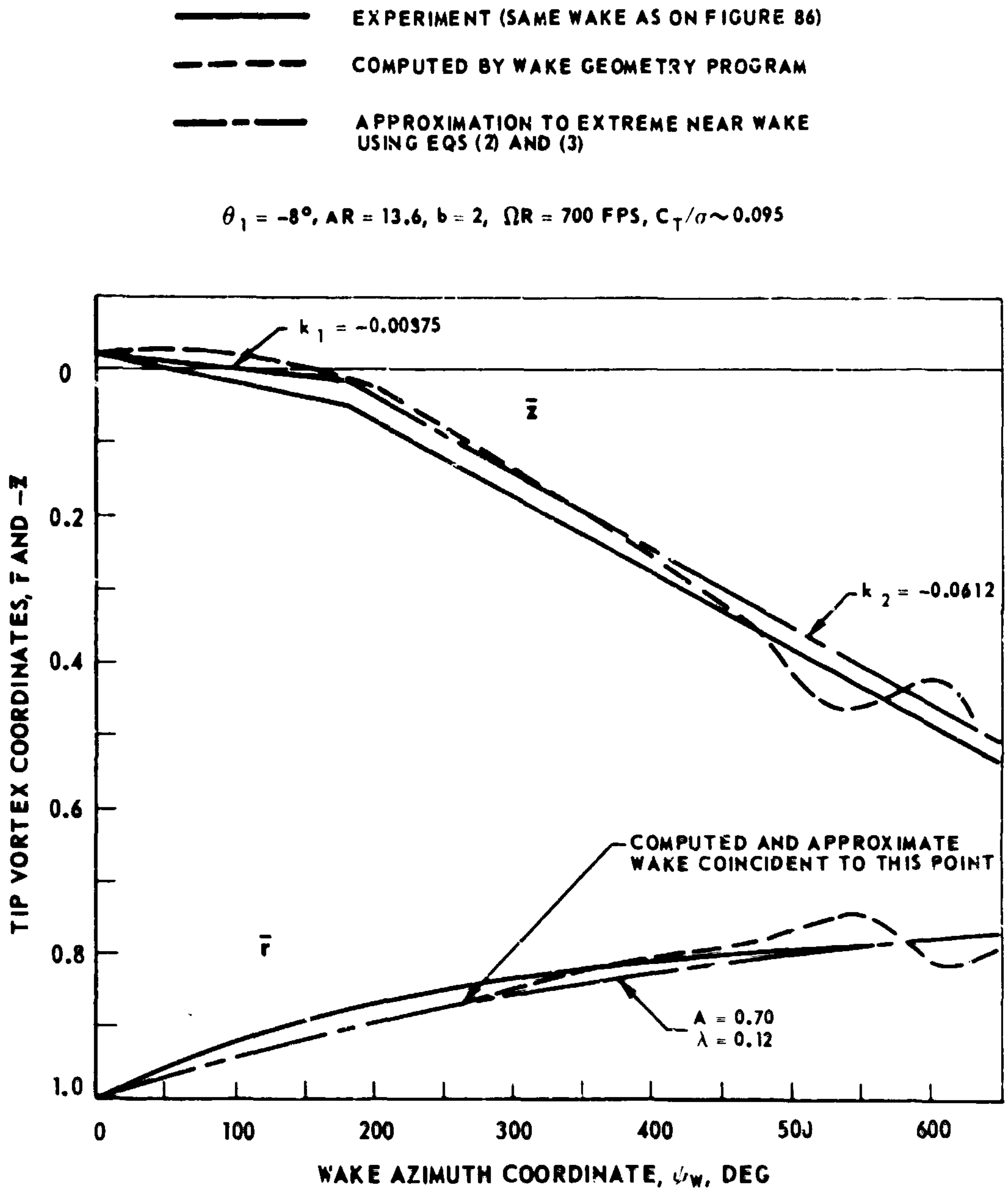

Figure 88. Approximation to Extreme Near-Wake in Sample Computation.

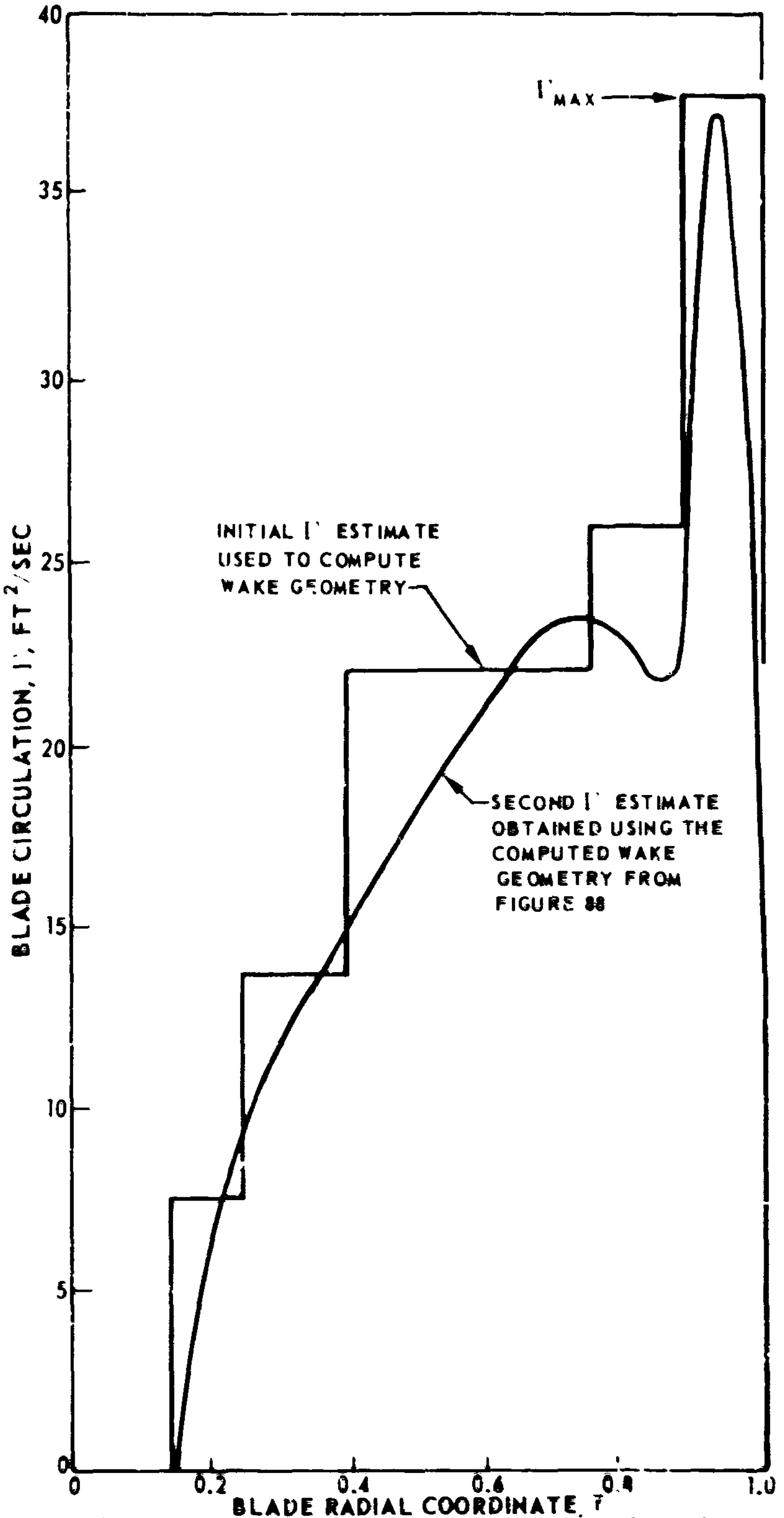

Figure 89. Comparison of Initial and Second Estimates of Blade Circulations in Sample Computation.

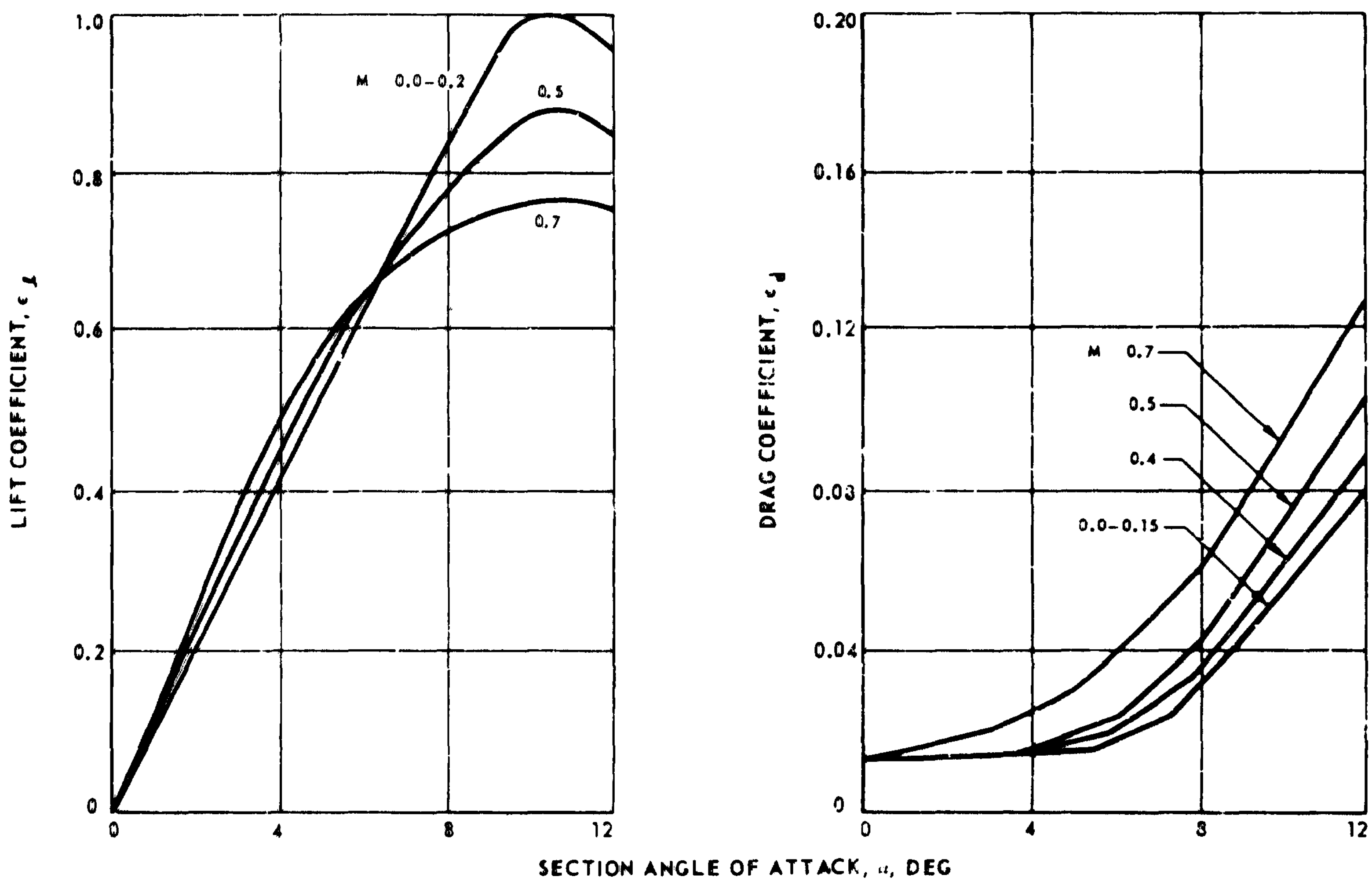

Figure 90. Synthesized Model Rotor Two-Dimensional Airfoil Date.

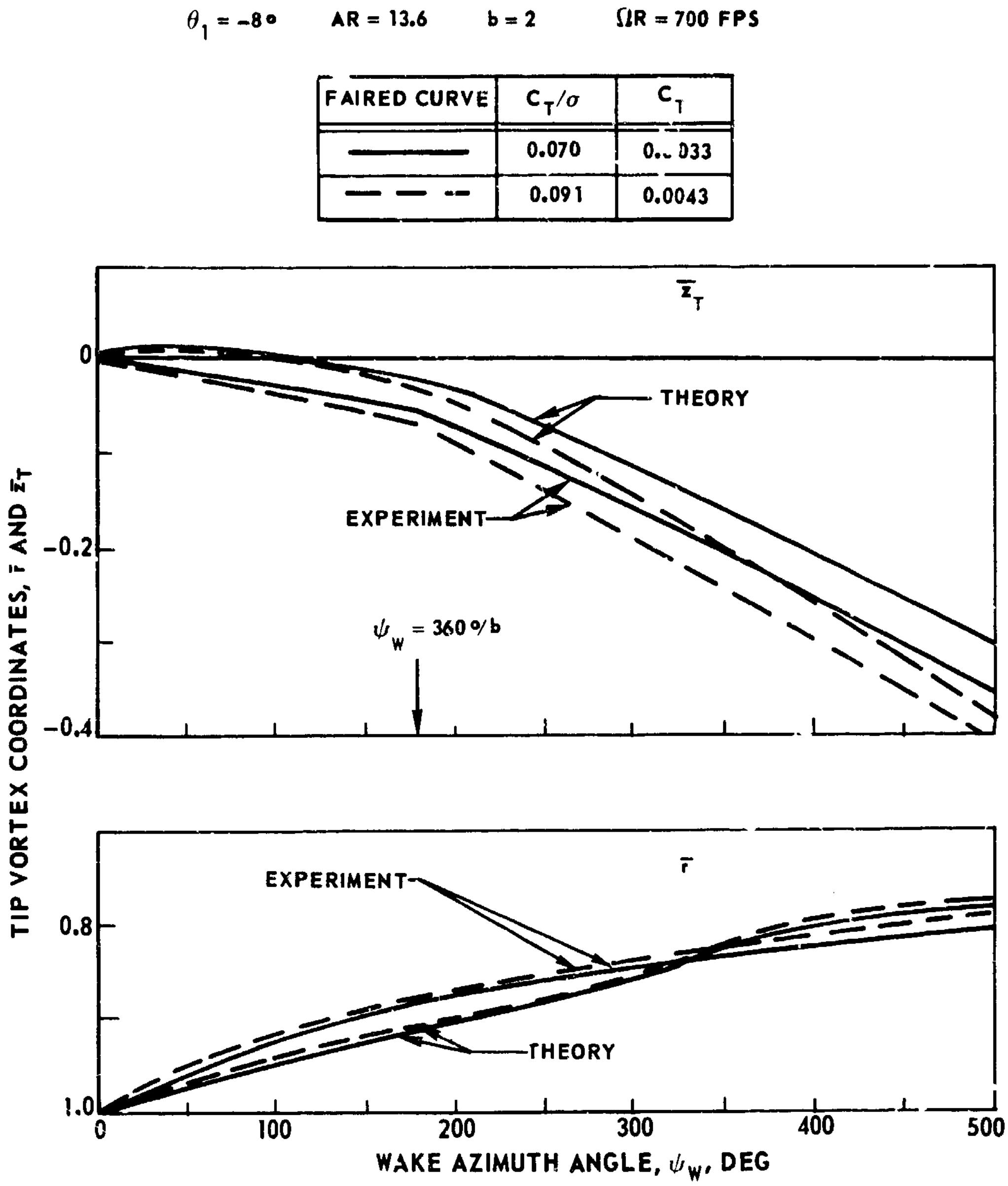

Figure 91. Predicted Effect of Rotor Thrust on Wake Geometry.

AR = 18.2 b = 2 ΩR = 700 FPS

FAIRED CURVE	θ_1	C_T/σ	C_T
——— (solid)	−8°	0.10	0.0035
— — — (dashed)	0	0.10	0.0035

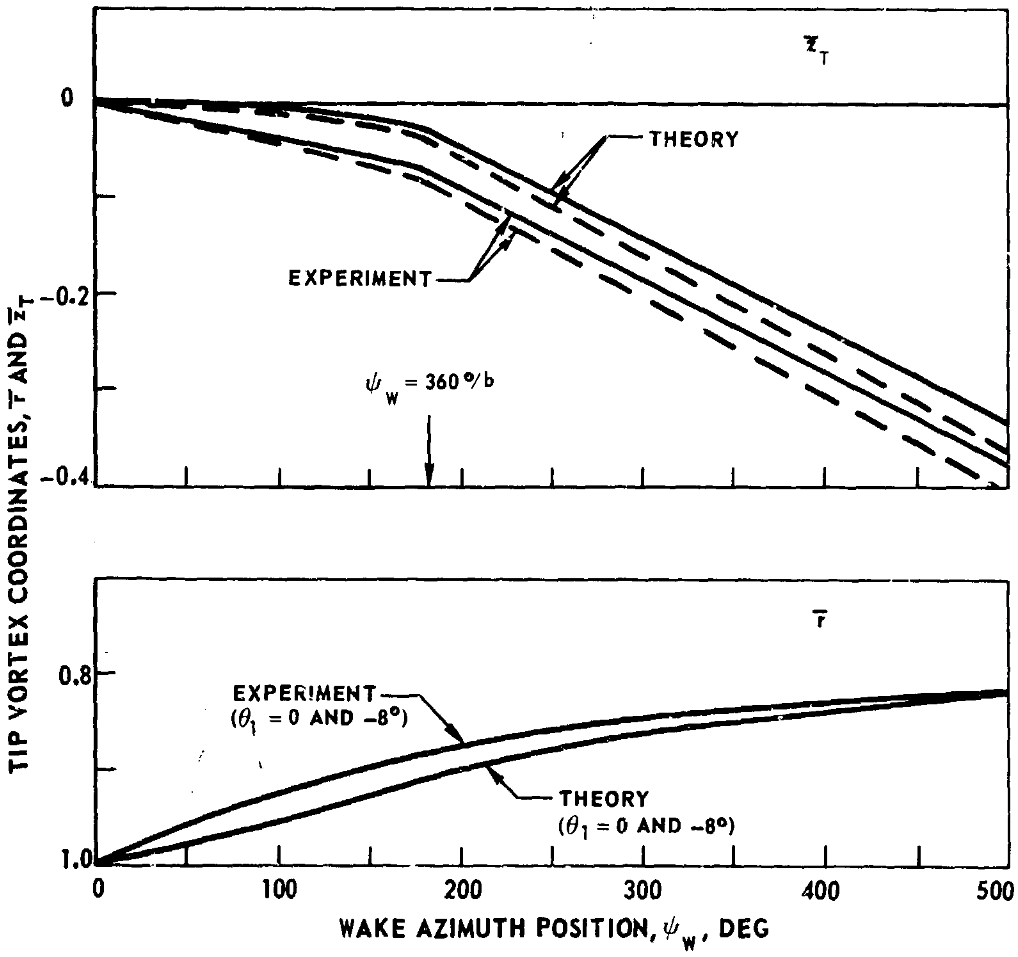

Figure 92. Predicted Effect of Blade Twist on Wake Geometry.

$\theta_1 = -8^\circ$ AR = 18.2 ΩR = 700 FPS

FAIRED CURVE	b	C_T/σ	C_T
———————	2	0.12	0.0042
— — —	6	0.0053	0.0056

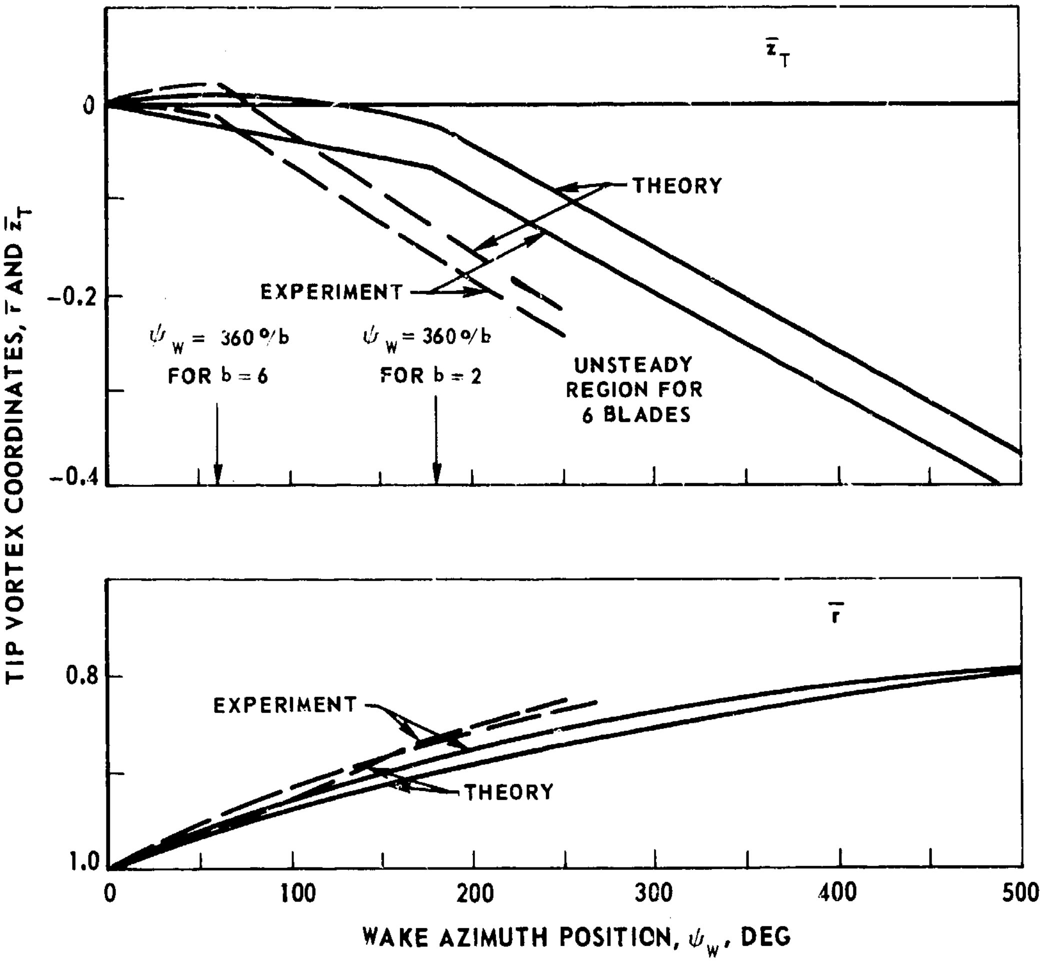

Figure 93. Predicted Effect of Number of Blades and Thrust Level on Wake Geometry.

$\theta_1 = -8^\circ$ $b = 2$ $\Omega R = 700$ FPS

FAIRED CURVE	AR	C_T/σ	C_T
——— (solid)	18.2	0.097	0.0034
— — — (dashed)	13.6	0.073	0.0034

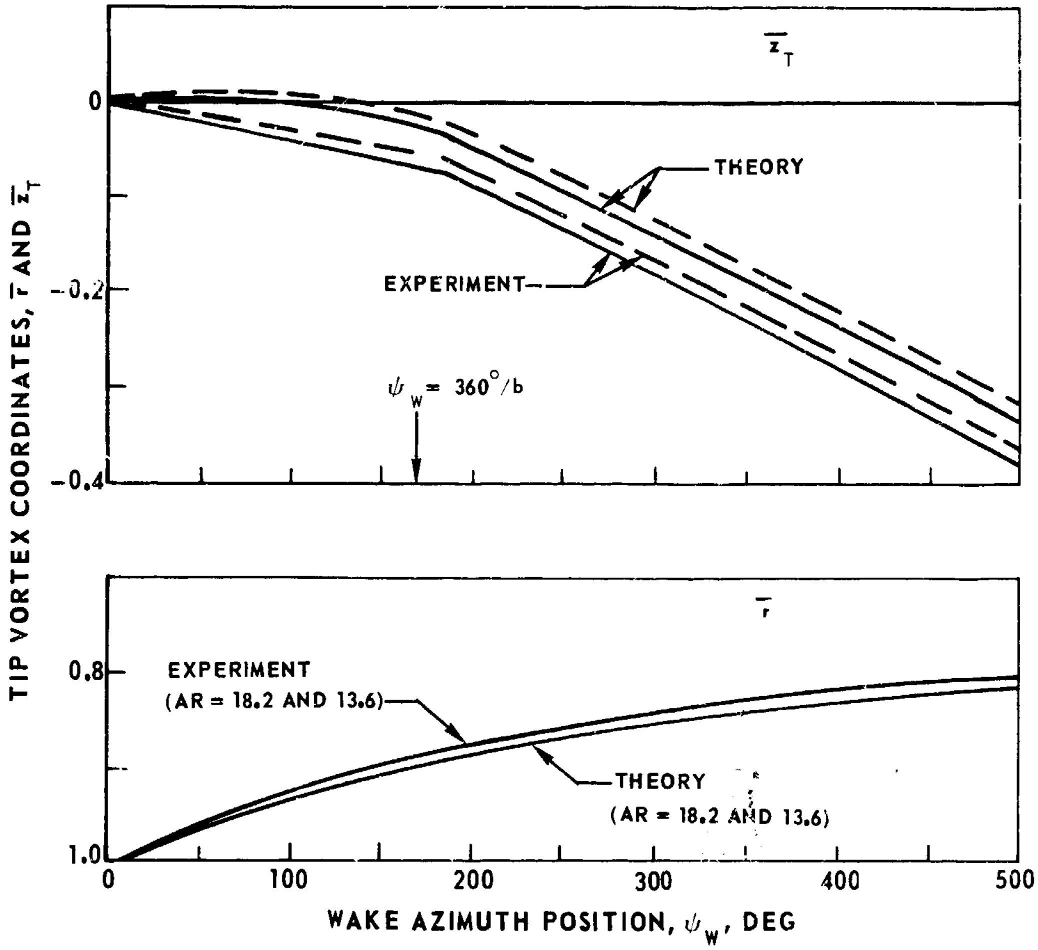

Figure 94. Predicted Effect of Blade Aspect Ratio on Wake Geometry.

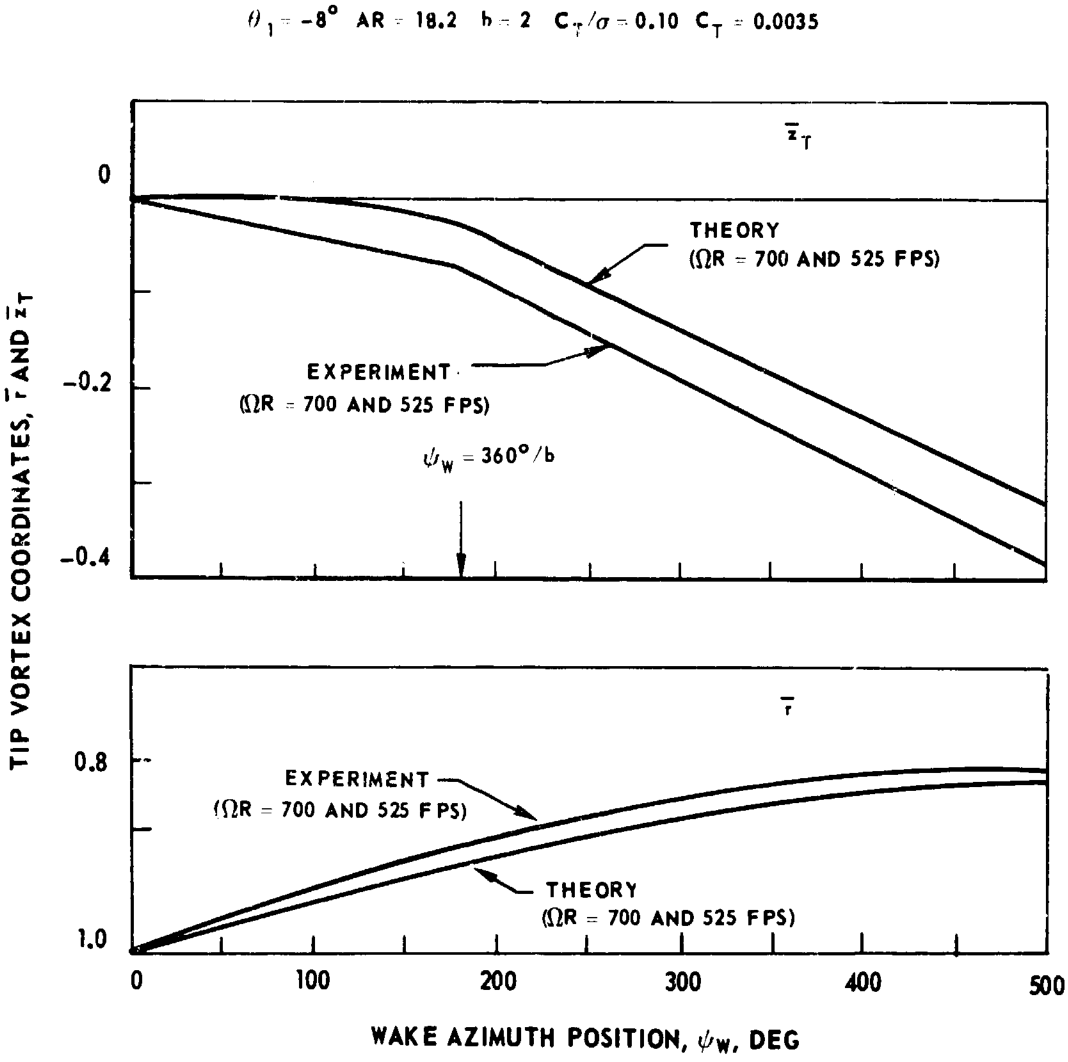

Figure 95. Predicted Effect of Tip Speed on Wake Geometry.

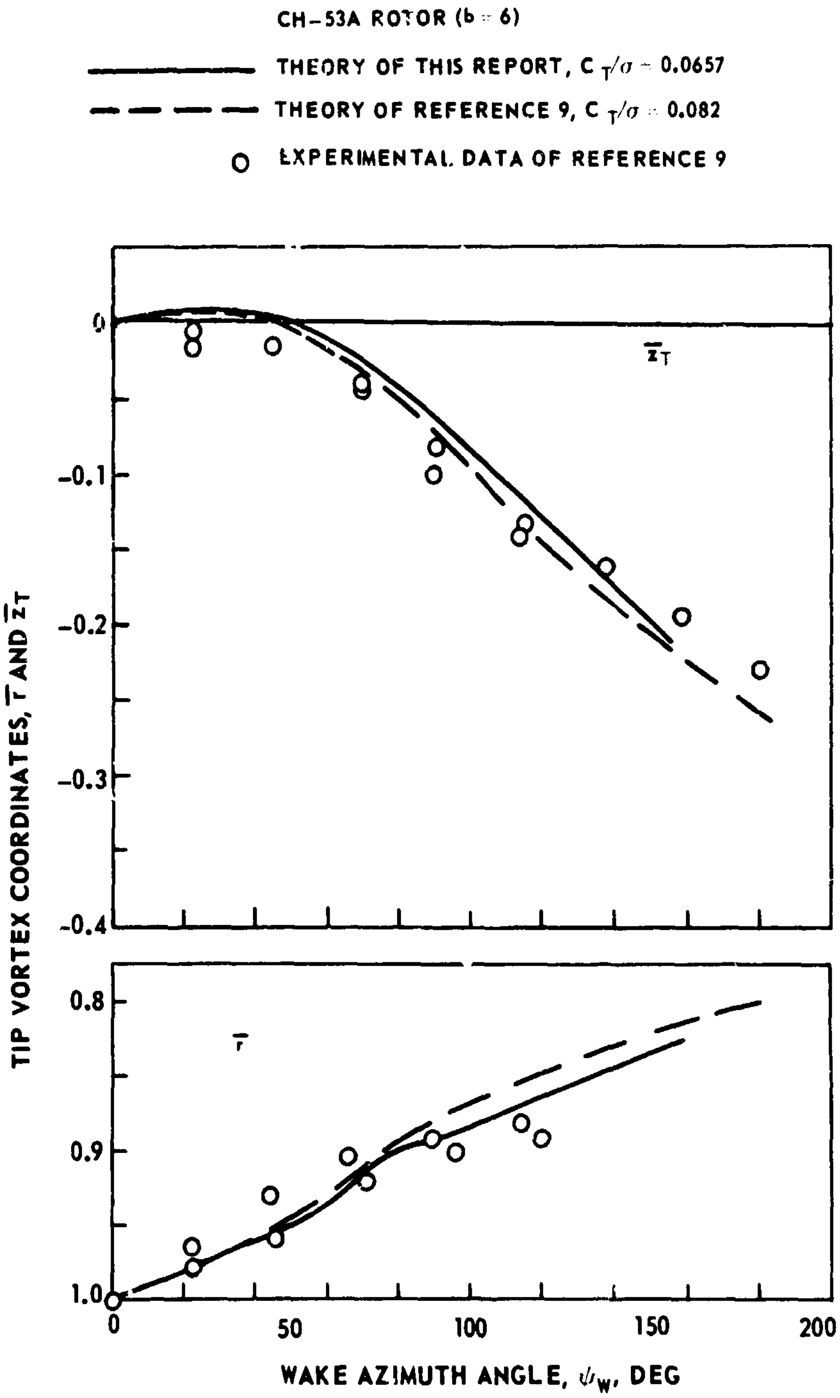

Figure 96. Comparison of Predicted Wake Geometry Results With Results of Reference 9.

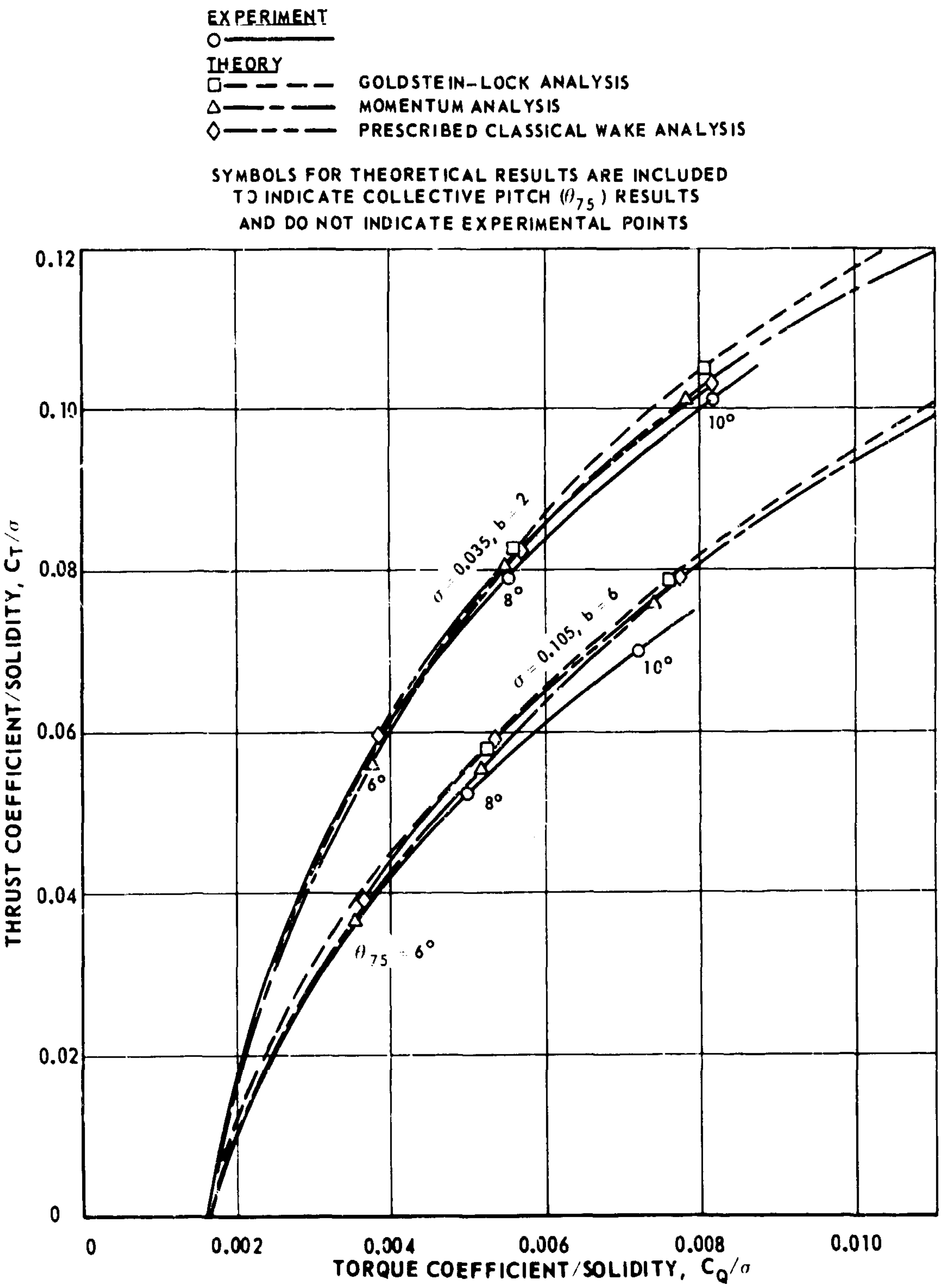

Figure 97. Comparison of Results of Uncontracted Wake Analyses With Experimental Performance Results for Two- and Six-Bladed Rotors -- $\theta_1 = -8°$, AR = 18.2, ΩR = 700 fps.

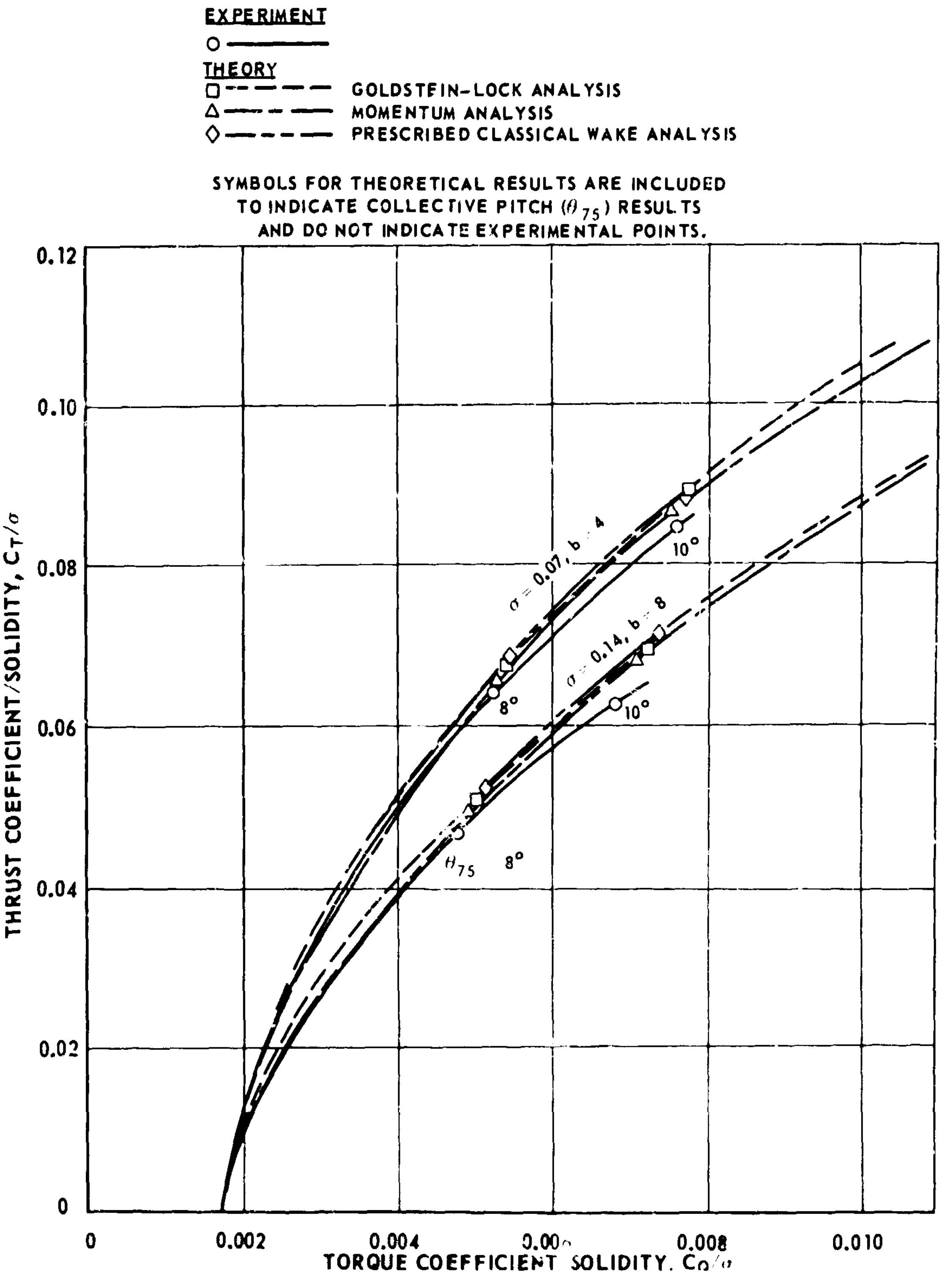

Figure 98. Comparison of Results of Uncontracted Wake Analyses With Experimental Performance Results for Four- and Eight-Bladed Model Rotors -- θ_1 = -8°, AR = .?, ΩR = 700 fps.

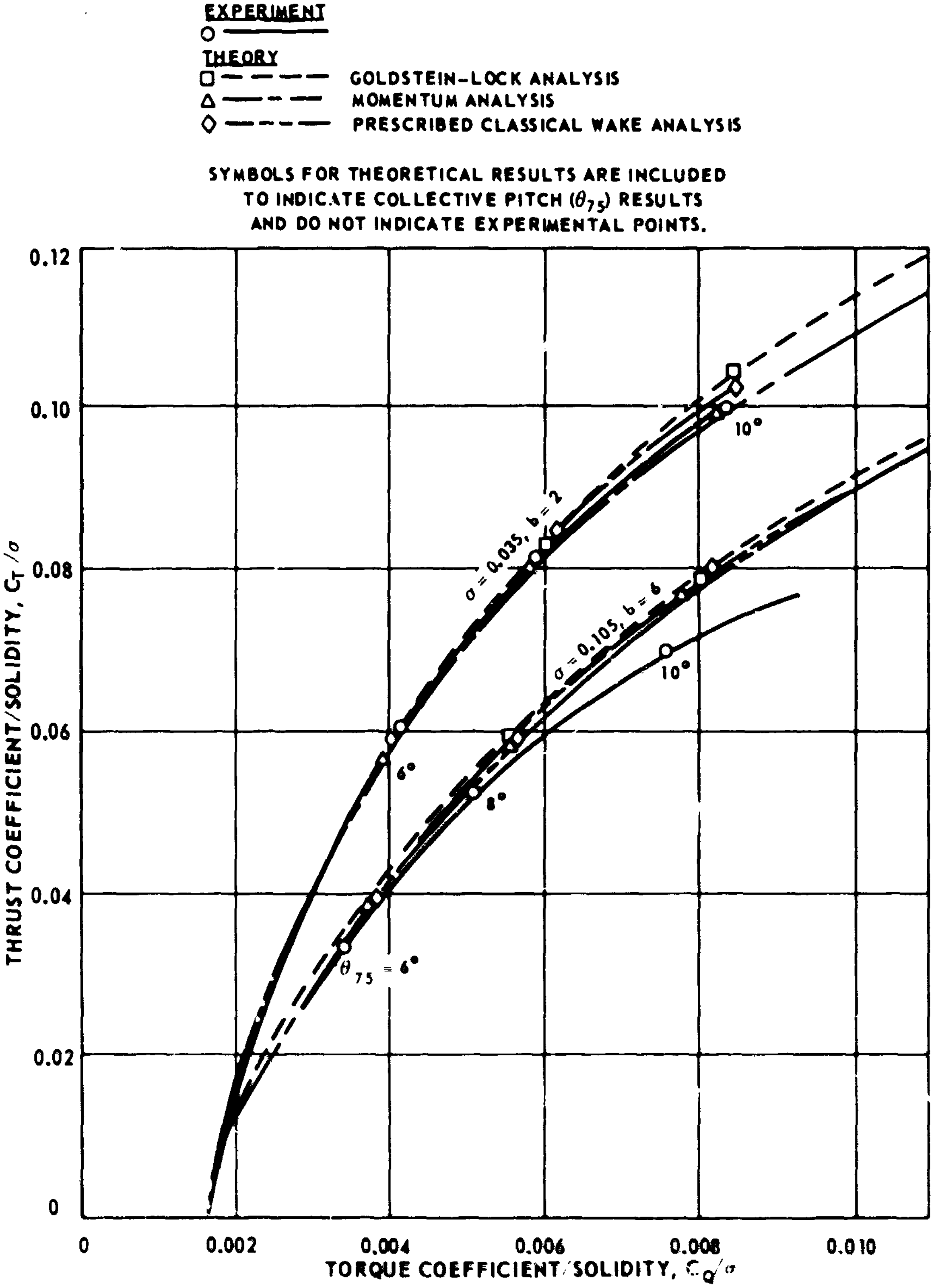

Figure ??. Comparison of Results of Uncontracted Wake Analyses With Experimental Performance Results for Two- and Six-Bladed Model Rotors -- $\theta_1 = 0°$, AR = 18.2, ΩR = 700 fps.

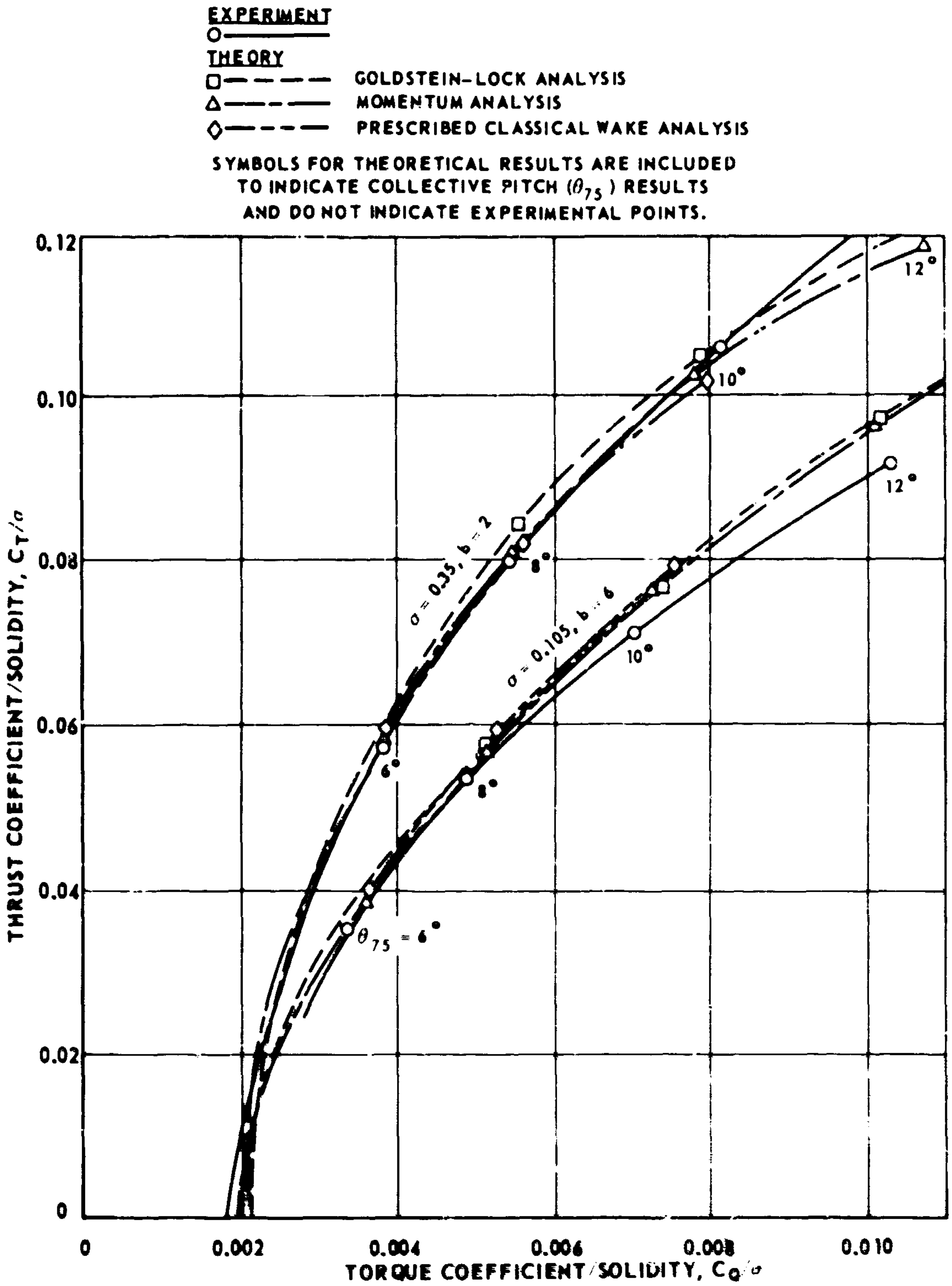

Figure 100. Comparison of Results of Uncontracted Wake Analyses With Experimental Performance Results for Two- and Six-Bladed Model Rotors -- $\theta_1 = -16°$, AR = 18.2, ΩR = 700 fps.

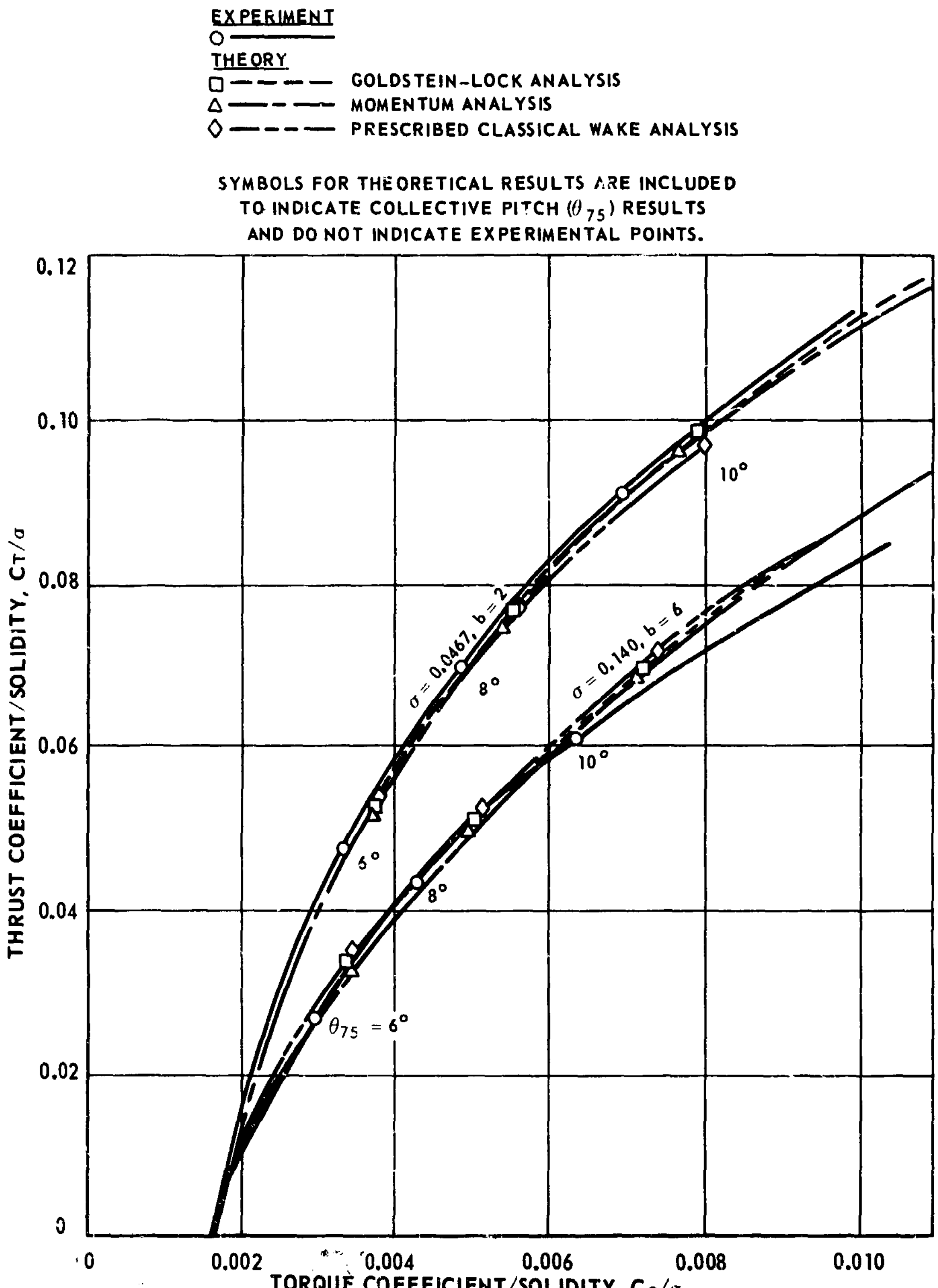

Figure 101. Comparison of Results of Uncontracted Wake Analyses With Experimental Performance Results for Two- and Six-Bladed Model Rotors -- $\theta_1 = -8°$, AR = 13.6, ΩR = 700 fps.

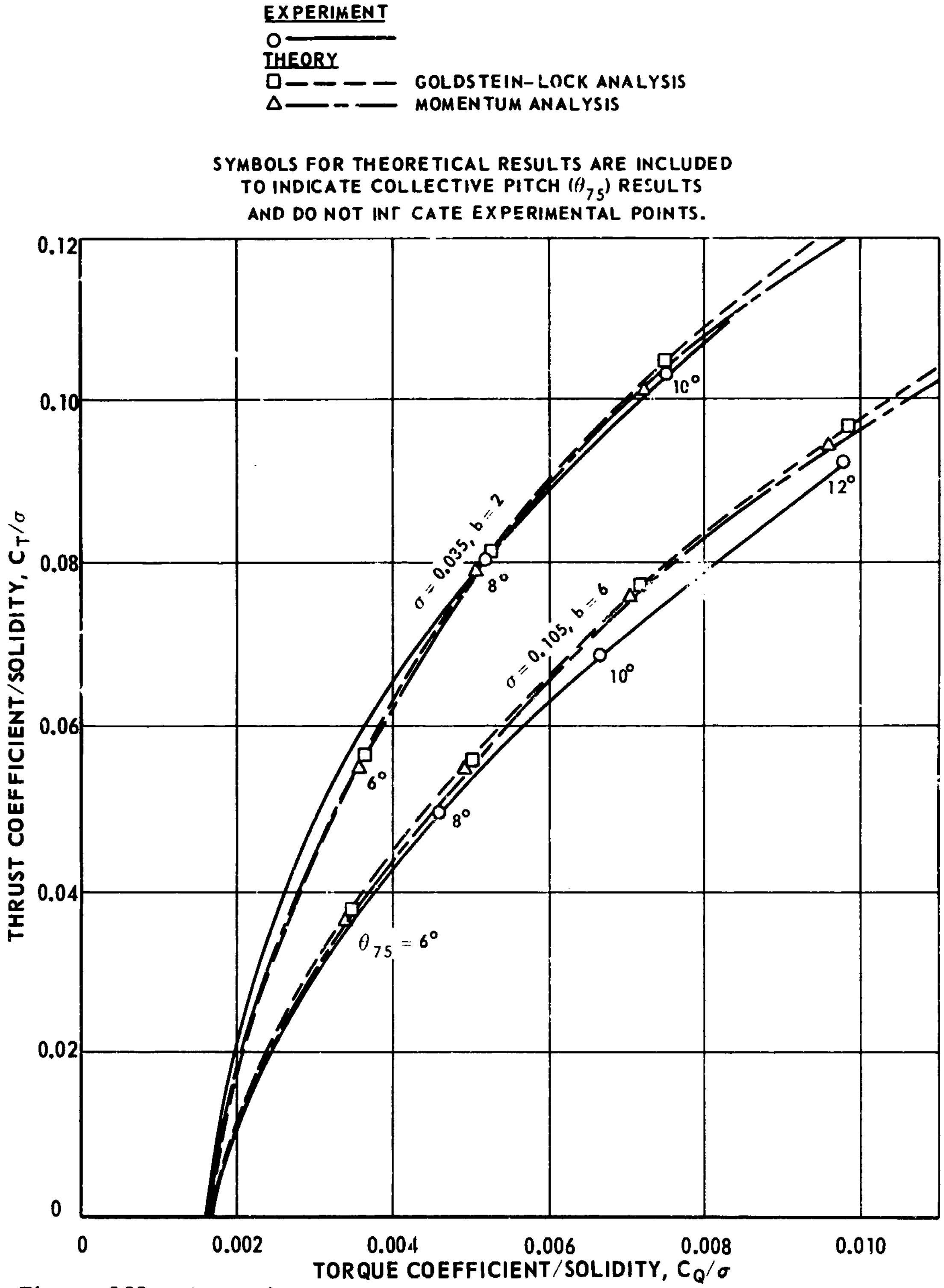

Figure 102. Comparison of Results of Uncontracted Wake Analyses With Experimental Performance Results for Two- and Six-Bladed Model Rotors -- θ_1 = -8°, AR = 18.2, ΩR = 525 fps.

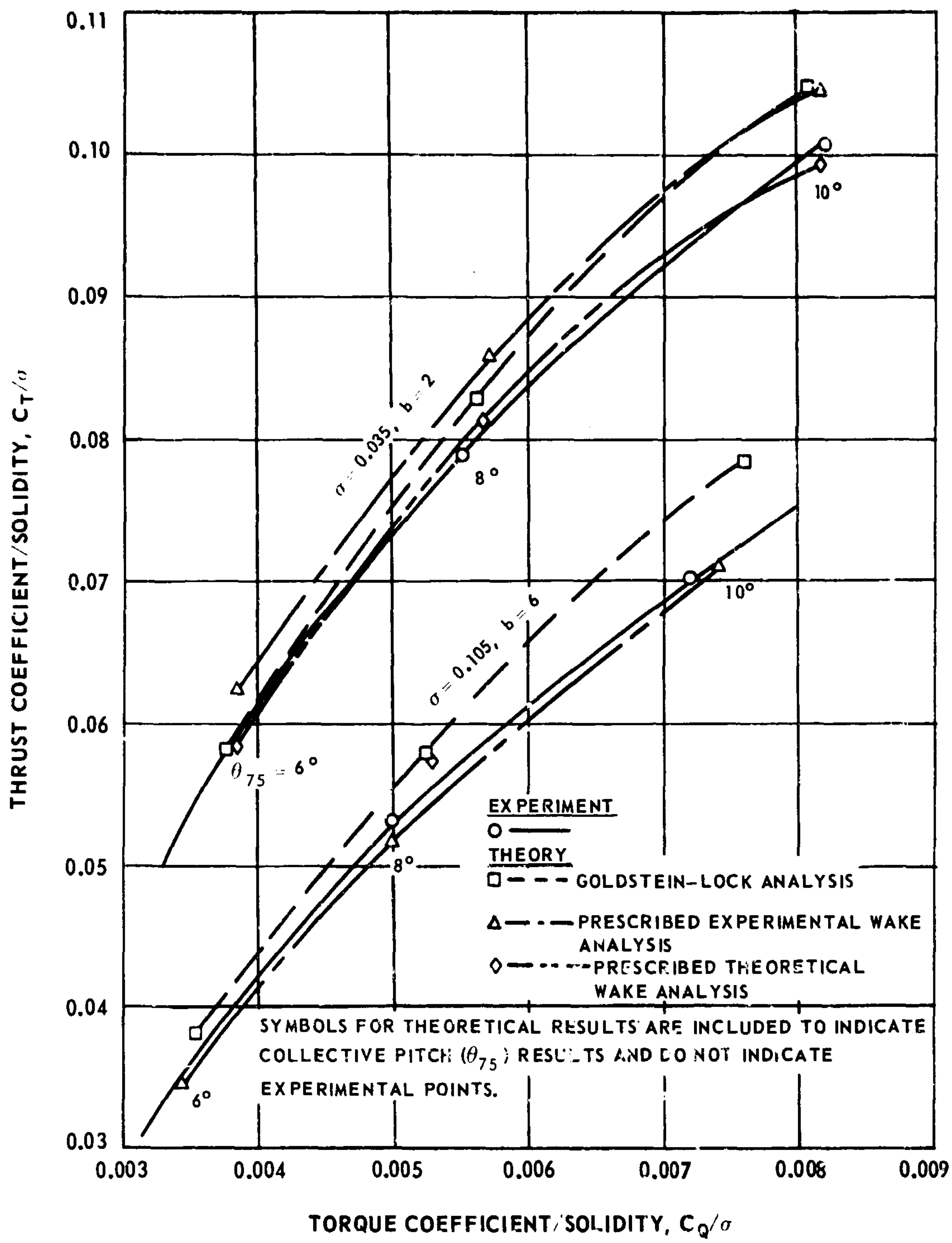

Figure 103. Comparison of Results of Contracted Wake Analyses With Goldstein-Lock Results and Experimental Performance Results for Model Rotors -- $\theta_1 = -8^\circ$, AR = 18.2, ΩR = 700 fps.

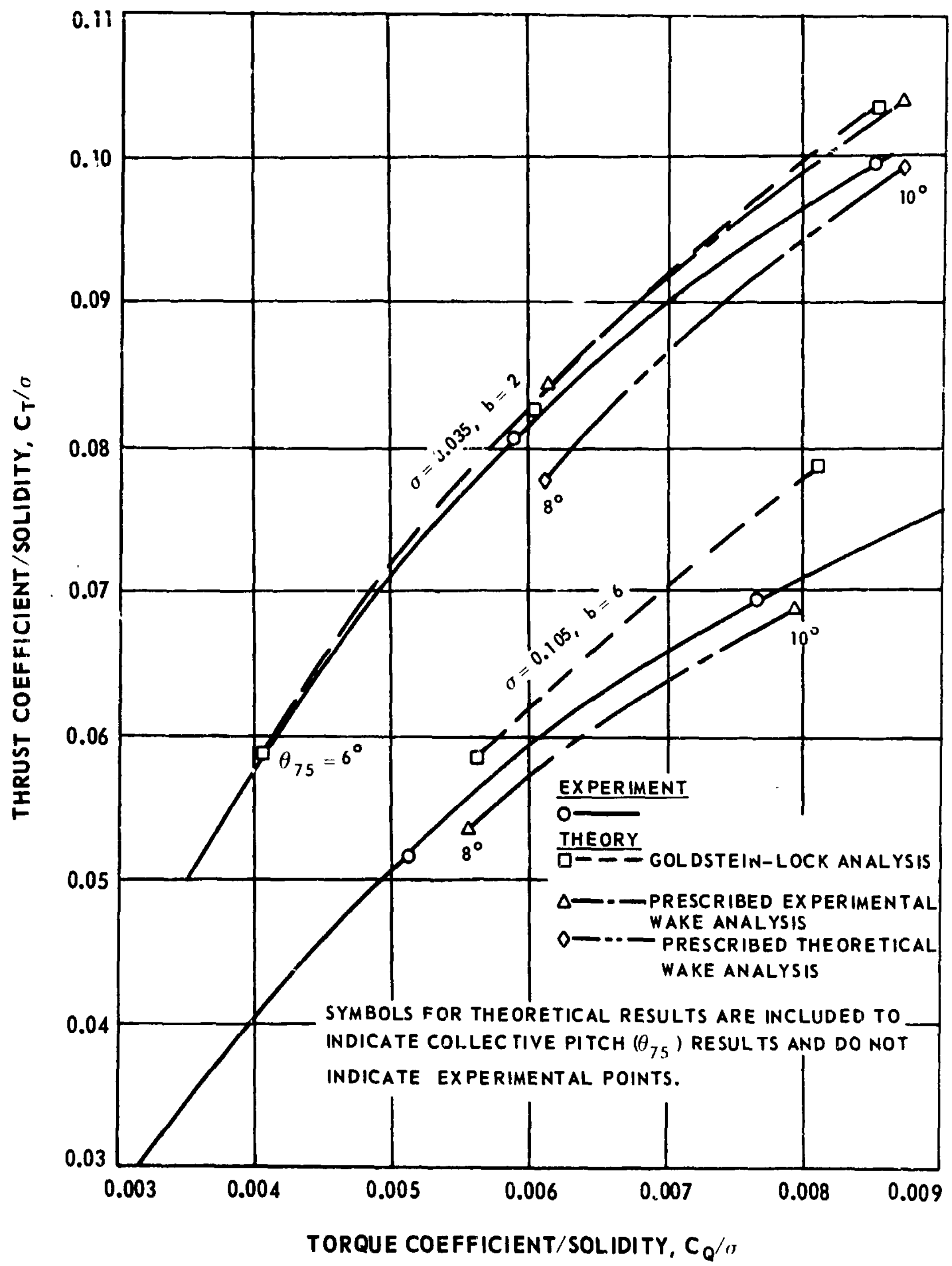

Figure 104. Comparison of Results of Contracted Wake Analyses With Goldstein-Lock Results and Experimental Performance Results for Model Rotors -- θ_1 = 0°, AR = 18.2, ΩR = 700 fps.

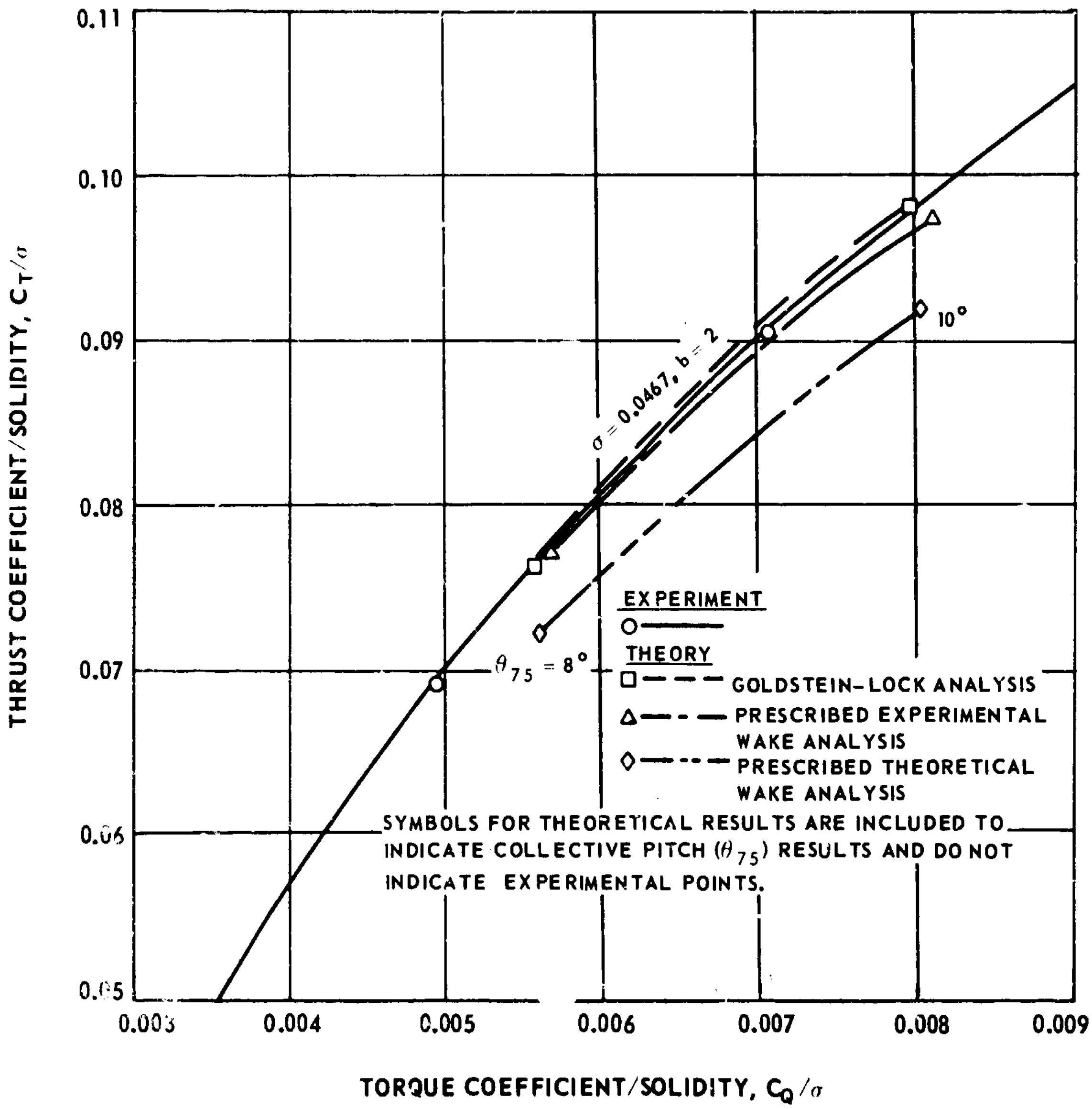

Figure 105. Comparison of Results of Contracted Wake Analyses With Goldstein-Lock Results and Experimental Performance Results for Model Rotors -- $\theta_1 = -8°$, AR = 13.6, ΩR = 700 fps.

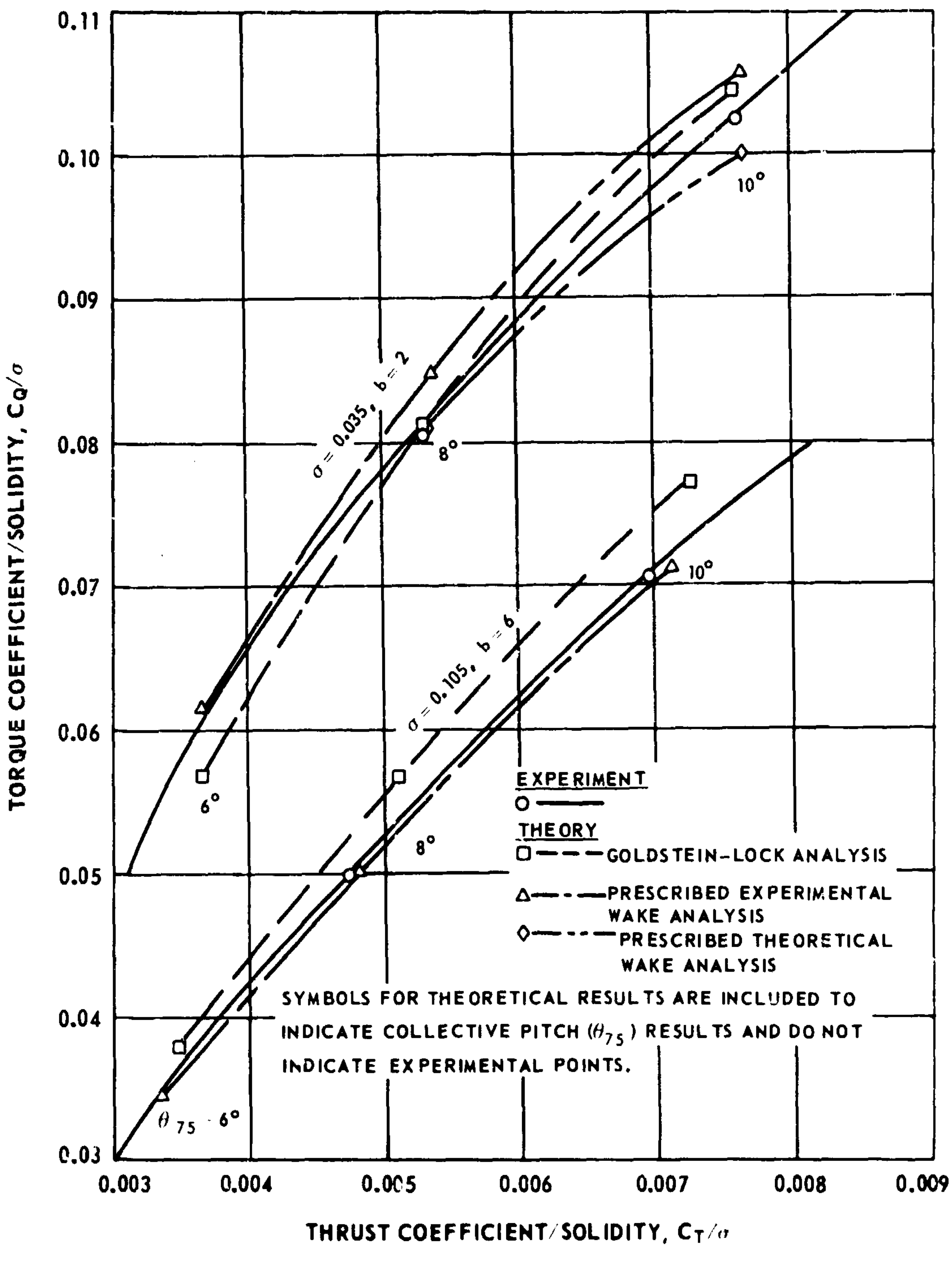

Figure 106. Comparison of Results of Contracted Wake Analyses With Goldstein-Lock Results and Experimental Results for Model Rotors -- $\theta_1 = -8°$, AR = 18.2, ΩR = 525 fps.

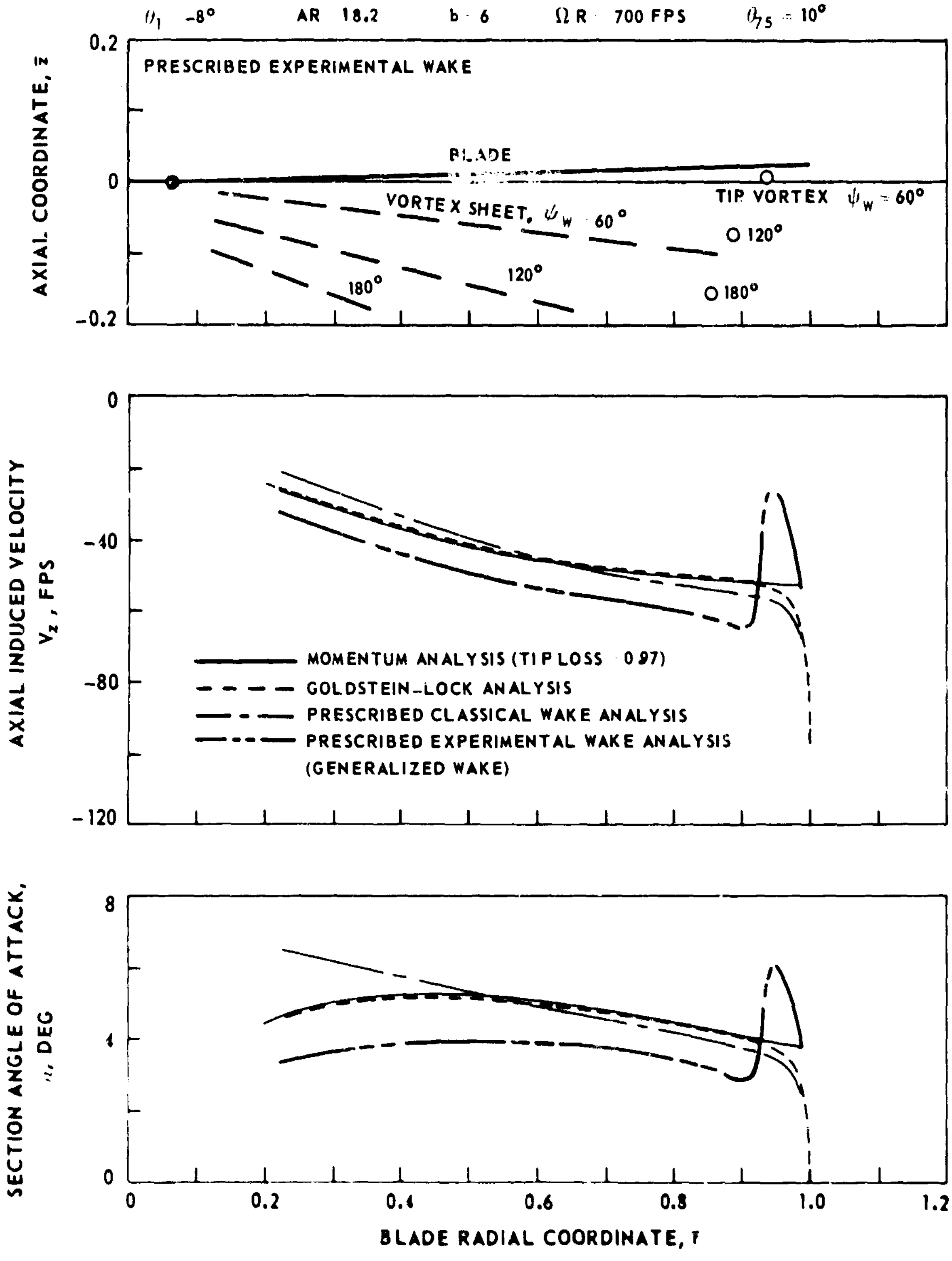

(a)

Figure 107. Comparison of Model Rotor Blade Section Characteristics as Predicted by Various Analyses.

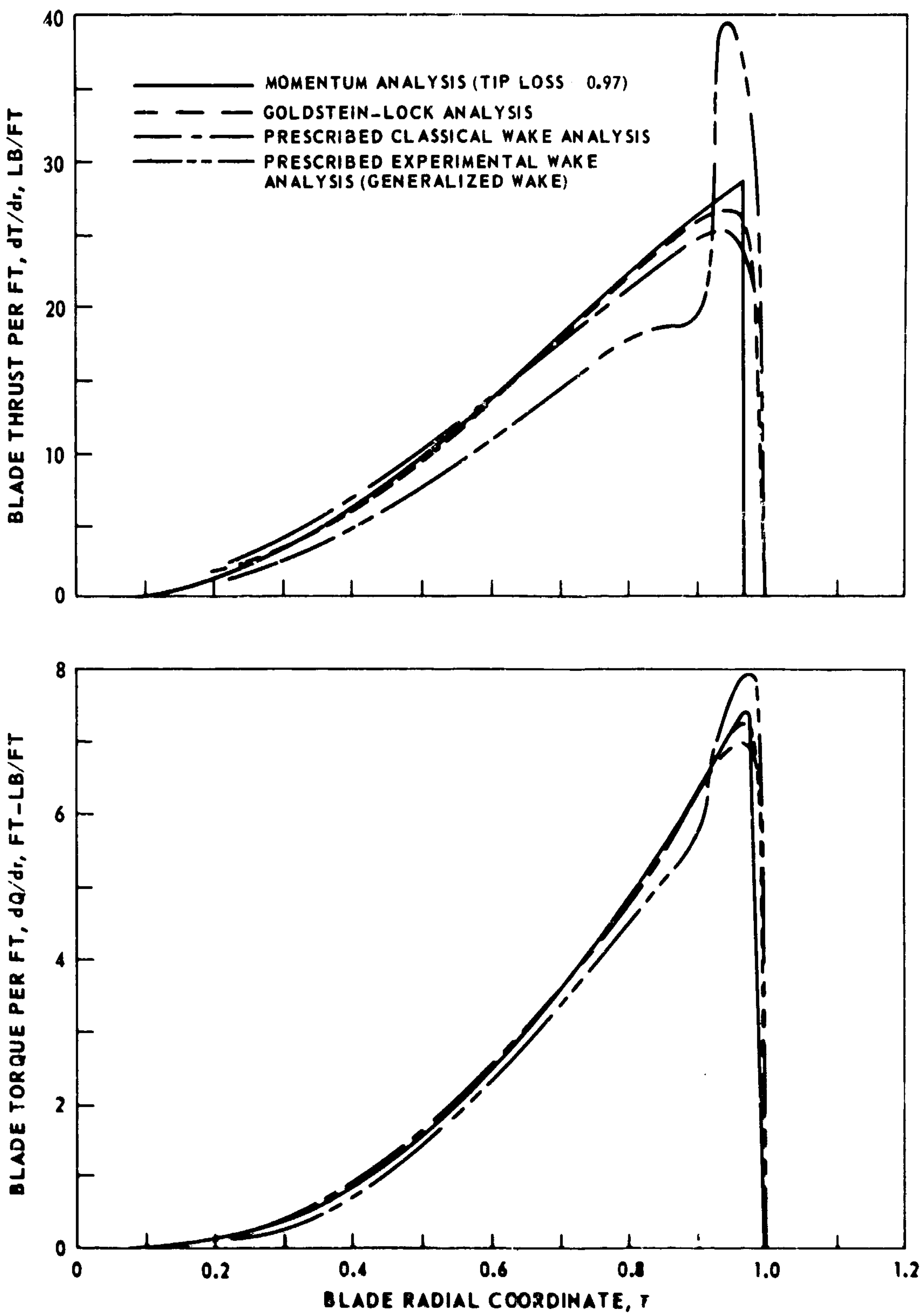

(b)
Figure 107. Continued.

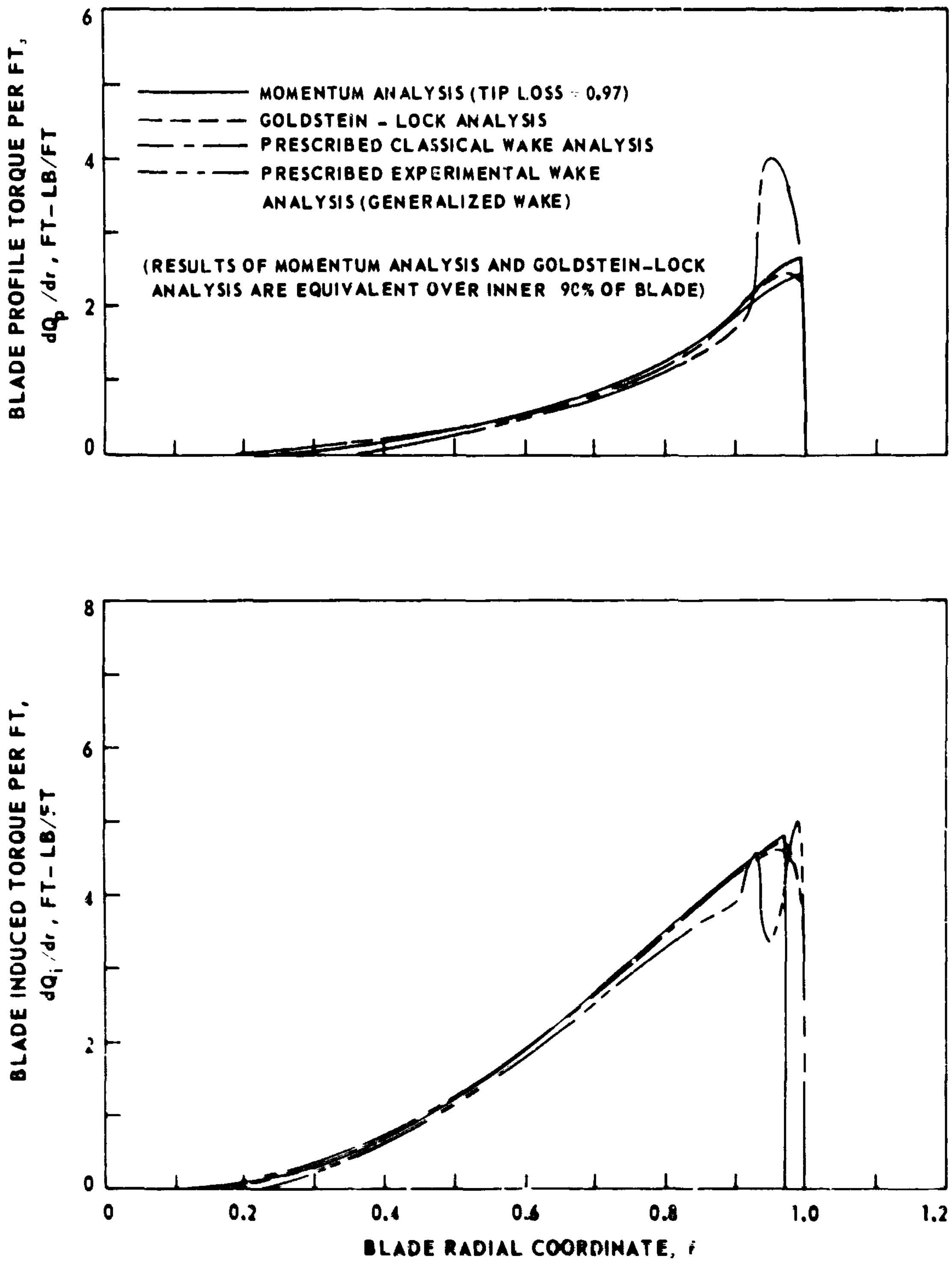

(c)

Figure 107. Concluded.

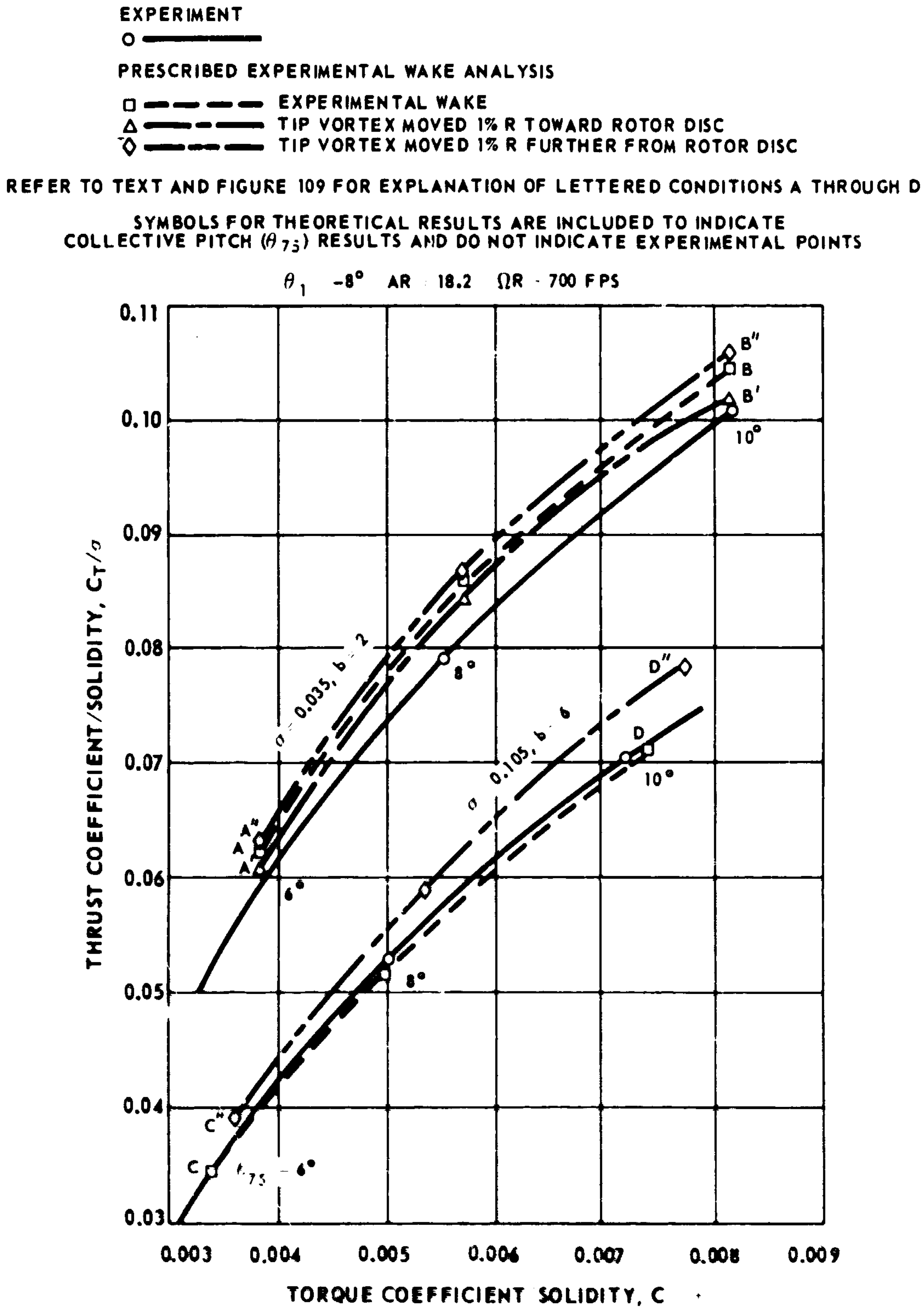

Figure 108. Sensitivity of Predicted Model Rotor Performance to Changes in Tip Vortex Location.

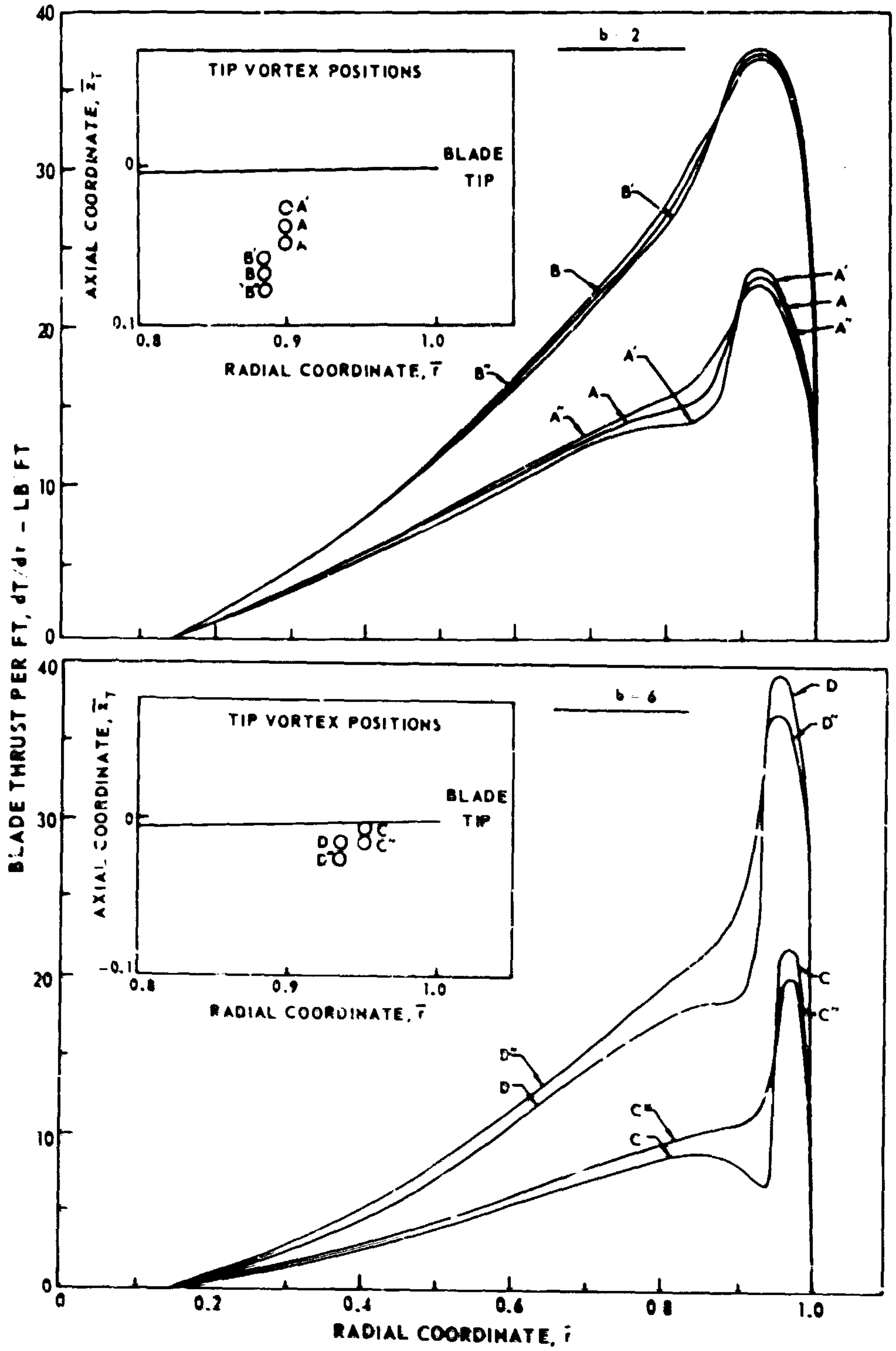

Figure 109. Sensitivity of Model Rotor Blade Section Characteristics to Changes in Tip Vortex Location.

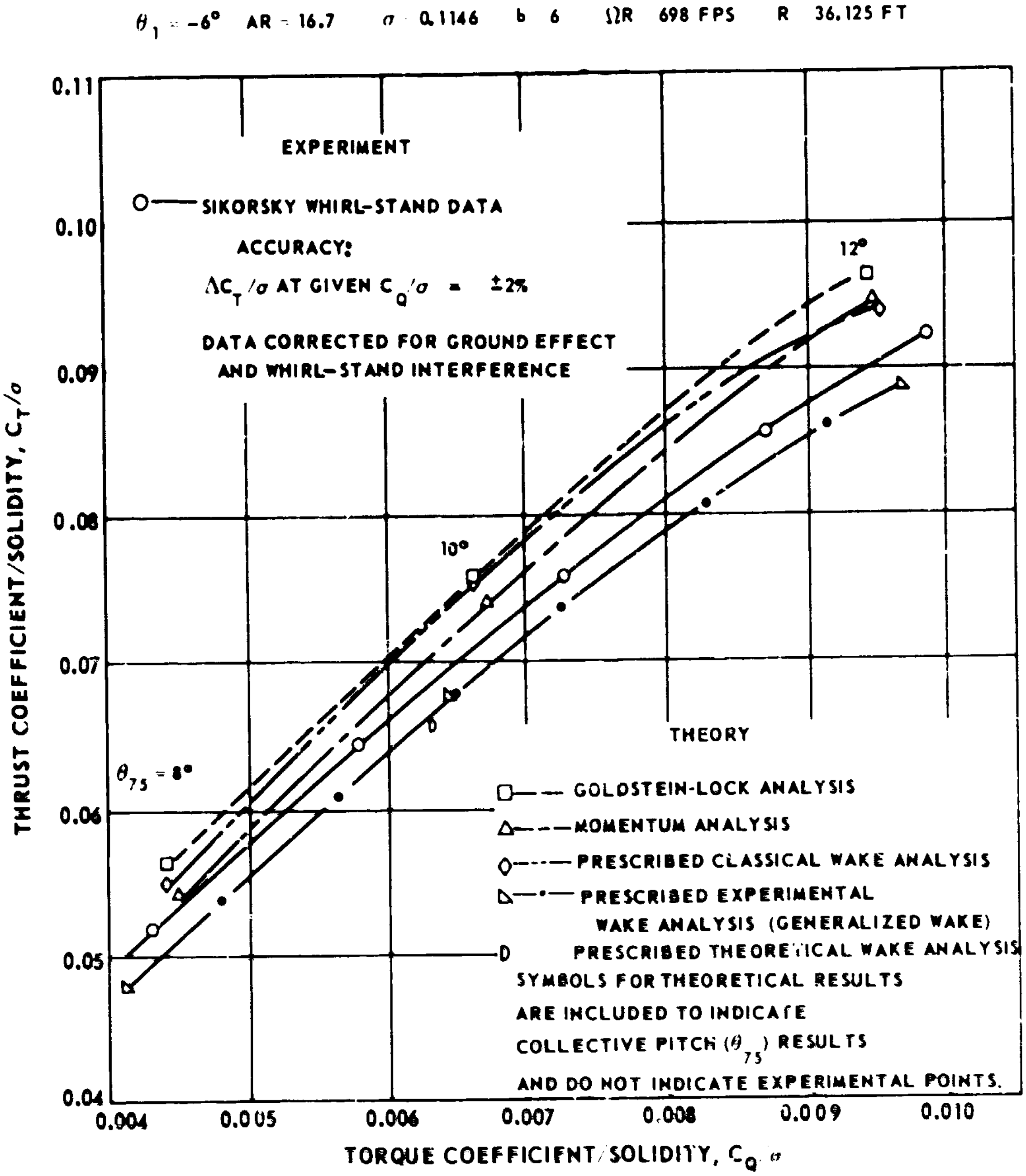

Figure 110. Comparison of Results of Various Analyses With Experimental Performance Results for CH-53A Rotor.

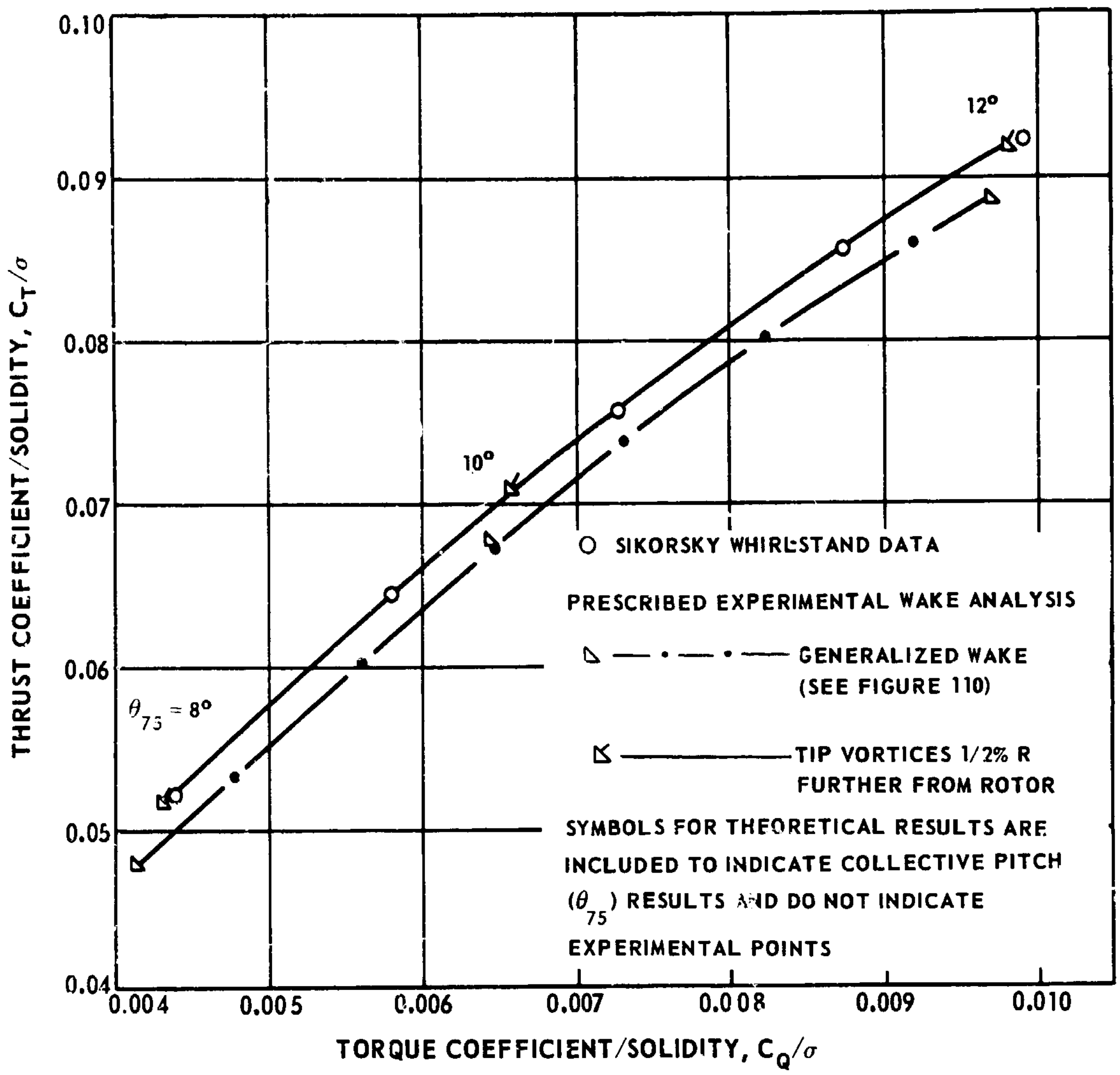

Figure 111. Sensitivity of Predicted CH-53A Rotor Performance to Change in Tip Vortex Location.

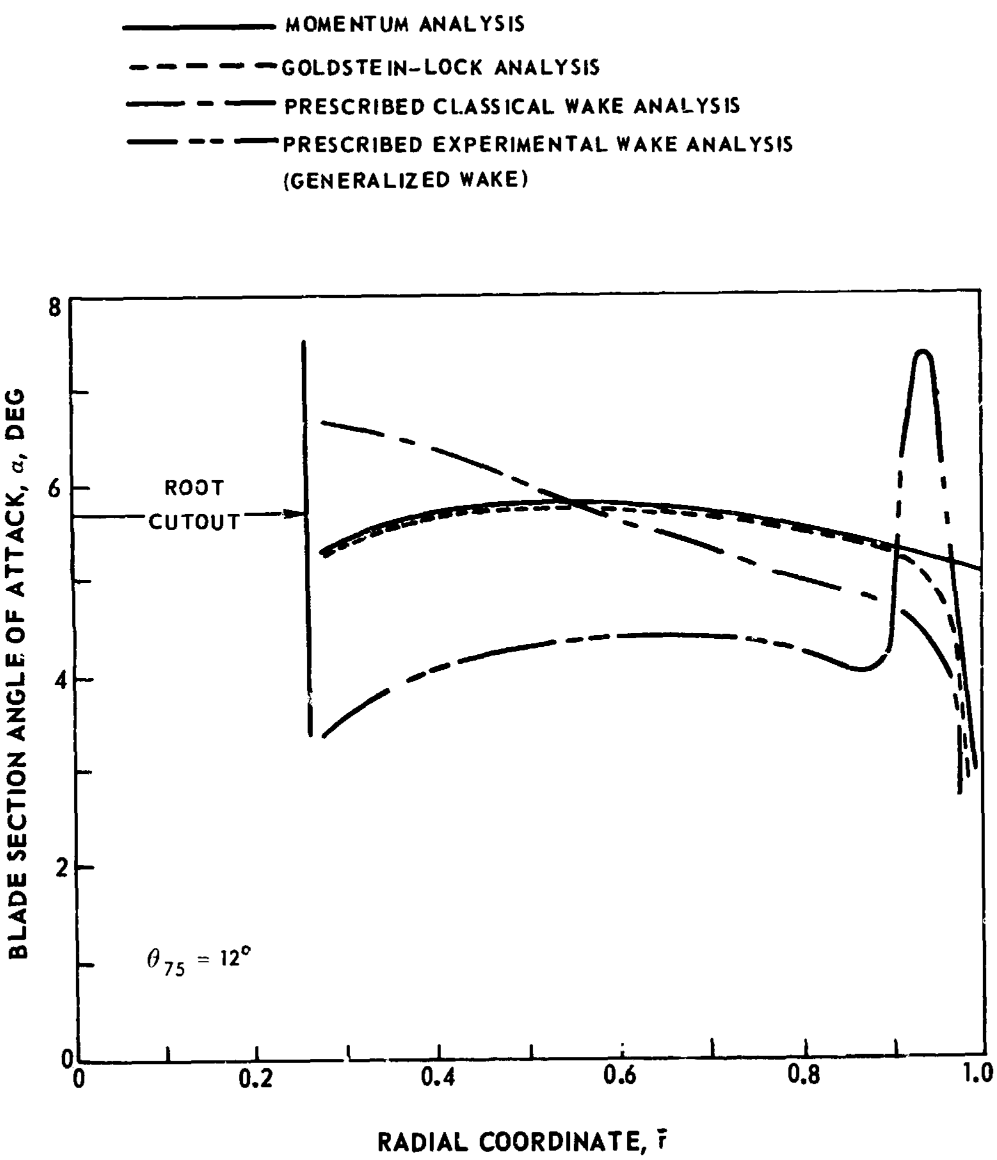

Figure 112. Comparison of CH-53A Blade Angle of Attack Distribution Predicted by Various Analyses.

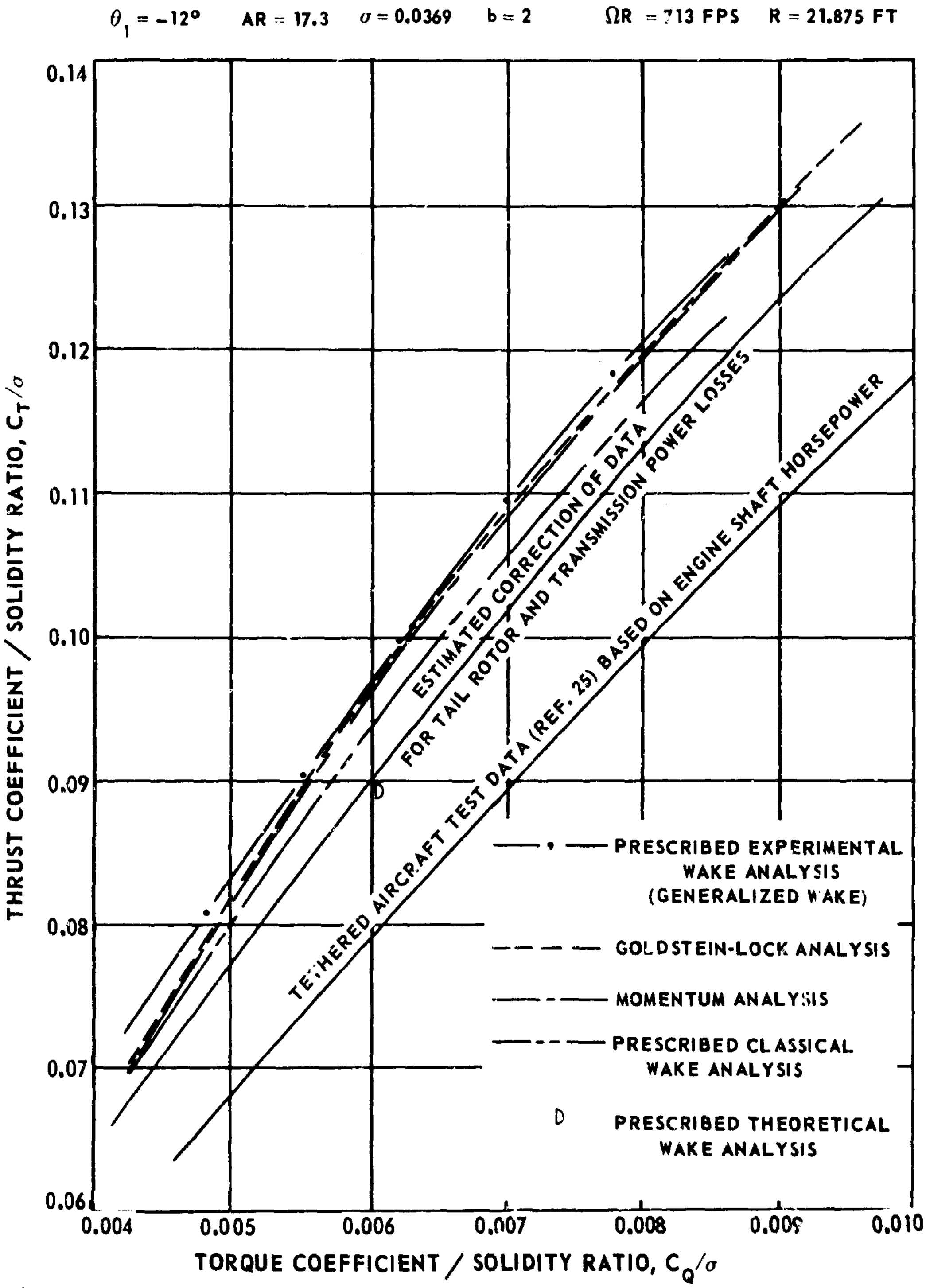

Figure 113. Comparison of Results of Various Analyses With Experimental Performance Results for HU-1A Rotor.

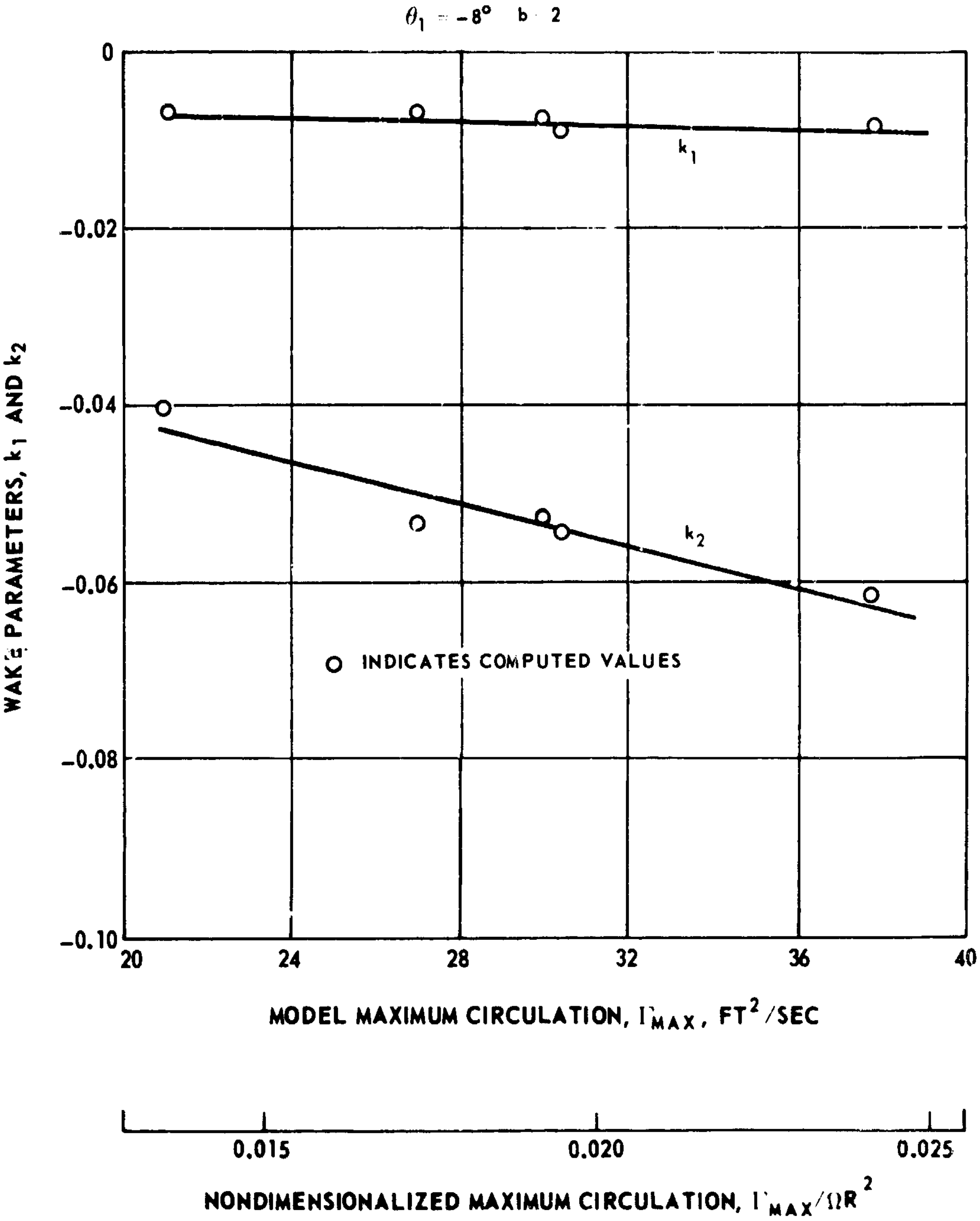

Figure 114. Variation of Computed k_1 and k_2 Wake Parameters With Maximum Blade Circulation.

LITERATURE CITED

1. Jenney, David S., Olson, John R., and Landgrebe, Anton J., A REASSESSMENT OF ROTOR HOVERING PERFORMANCE PREDICTION METHODS, Journal of the American Helicopter Society, Vol. 13, No. 2, April 1968, pp. 1-26.

2. Landgrebe, Anton J., AN ANALYTICAL METHOD FOR PREDICTING ROTOR WAKE GEOMETRY, Journal of the American Helicopter Society, Vol. 14, No. 4, October 1969, pp. 20-32.

3. Gray, Robin B., AN AERODYNAMIC ANALYSIS OF A SINGLE-BLADED ROTOR IN HOVERING AND LOW SPEED FORWARD FLIGHT AS DETERMINED FROM SMOKE STUDIES OF THE VORTICITY DISTRIBUTION IN THE WAKE, Princeton University Aeronautical Engineering Department, Report No. 356, Princeton University, Princeton, New Jersey, September 1956.

4. Hoel, Paul G., INTRODUCTION TO MATHEMATICAL STATISTICS, Second Edition, New York, John Wiley & Sons, Inc., 1958, p. 241.

5. Arcidiacono, P. J., Carta, F. O., Casellini, L. M., and Elman, H. L., INVESTIGATION OF HELICOPTER CONTROL LOADS INDUCED BY STALL FLUTTER, United Aircraft Corporation; USAAVLABS Technical Report 70-2, U. S. Army Aviation Materiel Laboratories, Fort Eustis, Virginia, March 1970, AD 869823.

6. Gilmore, David C., AN EVALUATION OF METHODS FOR PREDICTING THE PERFORMANCE OF PROPELLERS OPERATING AT ZERO ADVANCE RATIO, McGill University Mechanical Engineering Research Laboratories Technical Note 67-2, McGill University, Montreal, Canada, April 1967.

7. SYMPOSIUM ON AIRCRAFT WAKE TURBULENCE, Boeing Scientific Research Laboratories Document D1-82-0993, Boeing Scientific Research Laboratories, Seattle, Washington, September 1970.

8. Rorke, James B., and Wells, Clifford D., THE PRESCRIBED WAKE-MOMENTUM ANALYSIS, United Aircraft Corporation, Sikorsky Aircraft Division; Proceedings of the Third CAL/AVLABS Symposium on Aerodynamics of Rotary Wing and V/STOL Aircraft, Vol. 1, Cornell Aeronautical Laboratory, Inc., Buffalo, New York, June 1969.

9. Clark, David R., and Albert C. Leiper, THE FREE WAKE ANALYSIS - A METHOD FOR THE PREDICTION OF HELICOPTER ROTOR HOVERING PERFORMANCE, United Aircraft Corporation, Sikorsky Aircraft Division; Proceedings of the 25th Annual National Forum of the American Helicopter Society, Paper No. 321, May 1969.

10. Gray, Robin B., ON THE MOTION OF THE HELICAL VORTEX SHED FROM A SINGLE-BLADED HOVERING MODEL HELICOPTER ROTOR AND ITS APPLICATION TO THE CALCULATION OF THE SPANWISE AERODYNAMIC LOADING, Princeton University Aeronautical Engineering Department, Report No. 313, Princeton University, September 1955.

11. Swavely, Craig E., A SMOKE STUDY OF THE MOTION OF THE VORTICES FROM THE TIPS OF A TWO-BLADED MODEL HELICOPTER ROTOR IN HOVERING FLIGHT, Masters Thesis, Georgia Institute of Technology, Atlanta, Georgia, December 1958.

12. Lehman, August F., MODEL STUDIES OF HELICOPTER ROTOR FLOW PATTERNS, Oceanics, Inc.; USAAVLABS Technical Report 68-17, U. S. Army Aviation Materiel Laboratories, Fort Eustis, Virginia, April 1968, AD 671670.

13. Cassarino, Sebastian J., EFFECT OF ROOT CUTOUT ON HOVER PERFORMANCE, United Aircraft Corporation, Sikorsky Aircraft Division; AFFDL Technical Report AFFDL-TR-70-70, Air Force Flight Dynamics Laboratory, Wright-Patterson Air Force Base, Ohio, June 1970.

14. Greenberg, Michael D., and Kaskel, Alvin L., INVISCID FLOW FIELD INDUCED BY A ROTOR IN GROUND EFFECT, Therm Advanced Research, Inc., NASA CR-1027, National Aeronautics and Space Administration, Washington, D.C., May 1968.

15. Heyson, Harry H., A NOTE ON THE MEAN VALUE OF INDUCED VELOCITY FOR A HELICOPTER ROTOR, NASA Langley Research Center; NASA TN D-240, National Aeronautics and Space Administration, Washington, D.C., May 1960.

16. Goldstein, S., ON THE VORTEX THEORY OF SCREW PROPELLERS, Proceedings - Royal Society of London, Vol. A 123, No. A 792, 1929.

17. Betz, A., HANDBUCH DER PHYSIK, Vol. 7, Berlin, J. Springer, 1927, pp. 256-259.

18. Lock, C. N. H., THE APPLICATION OF GOLDSTEIN'S THEORY TO THE PRACTICAL DESIGN OF AIRSCREWS, ARC R&M No. 1377, Aeronautical Research Committee, Great Britain, 1931.

19. Westwater, F. L., ROLLING UP OF THE SURFACE OF DISCONTINUITY BEHIND AN AEROFOIL OF FINITE SPAN, Aeronautical Research Committee; R&M No. 1692, Air-Ministry, Great Britain, August 1935.

20. Squire, H. B., THE GROWTH OF A VORTEX IN TURBULENT FLOW, The Aeronautical Quarterly, August 1965.

21. Brady, W. G., and Crimi, P., REPRESENTATION OF PROPELLER WAKES BY SYSTEMS OF FINITE CORE VORTICES, CAL Report No. BB-1665-S-2, Cornell Aeronautical Laboratory, Inc., Buffalo, New York, February 1965.

22. Levy, M. A., and Forsdyke, A. G., THE STEADY MOTION AND STABILITY OF A HELICAL VORTEX, Royal Society - Proceedings, Vol. 120, No. A786, October 1, 1928, pp. 670-690.

23. Rauscher, Manfred, INTRODUCTION TO AERONAUTICAL DYNAMICS, New York, John Wiley & Sons, 1953.

24. Sopher, Robert, THREE-DIMENSIONAL FLOW PAST THE SURFACE OF A ROTOR BLADE, United Aircraft Corporation, Sikorsky Aircraft Division; Proceedings of the 25th Annual National Forum of the American Helicopter Society, Paper No. 324, May 1969.

25. Macpherson, D. F., and Hodgson, W. J., YH-40 PERFORMANCE EVALUATION, Air Force Flight Test Center, Report AFFTC-TR-59-33, Edwards Air Force Base, California, January 1960.

APPENDIX I
EQUATIONS FOR COMPUTING THE VELOCITIES AND DISPLACEMENTS OF WAKE VORTEX ELEMENTS

The velocities induced at an arbitrary point P by a straight vortex element of strength Γ and bounded by end points A and B (see Figure 77) can be computed using the classical Biot-Savart Law (see Reference 23, p. 373) and are given by the following equations:

$$v_{x_p} = \left(\frac{\Gamma}{4\pi}\right)\bar{k}\left[(y_P - y_A)(z_P - z_B) - (z_P - z_A)(y_P - y_B)\right]$$

$$v_{y_p} = \left(\frac{\Gamma}{4\pi}\right)\bar{k}\left[(z_P - z_A)(x_P - x_B) - (x_P - x_A)(z_P - z_B)\right]$$

$$v_{z_p} = \left(\frac{\Gamma}{4\pi}\right)\bar{k}\left[(x_P - x_A)(y_P - y_B) - (y_P - y_A)(x_P - x_B)\right]$$

where

$$\bar{k} = \frac{1}{R}\,\frac{(AP + BP)/(AP)(BP)}{(AP)(BP) + I + J + K}$$

$$I = (x_P - x_A)(x_P - x_B)$$

$$J = (y_P - y_A)(y_P - y_B)$$

$$K = (z_P - z_A)(z_P - z_B)$$

$$AP = \sqrt{(x_P - x_A)^2 + (y_P - y_A)^2 + (z_P - z_A)^2} \qquad BP = \sqrt{(x_P - x_B)^2 + (y_P - y_B)^2 + (z_P - z_B)^2}$$

The velocities v_{x_p}, v_{y_p}, and v_{z_p} are numerically integrated using the equations below to determine the displacements of the wake which occur during a small time interval, Δt

$$\Delta x_P = \sum v_{x_p}\Delta t$$

$$\Delta y_P = \sum v_{y_p}\Delta t$$

$$\Delta z_P = \sum v_{z_p}\Delta t$$

The summation signs in the immediately preceding equations denote summations of the induced velocities induced at point P by all vortex elements in the wake. The particular integration scheme described above is based on the assumption that the induced velocities remain essentially constant during the time interval, Δt. Also, the length of any vortex element is allowed to vary as its end points move.

Examination of the velocity equations given above discloses that the velocity induced at point P by the straight vortex segments of which P forms an end point is always zero. Actually the vortex filament is curved rather than straight. Some error is thus introduced by the use of straight segments, with the size of the error depending upon the length of the segment and the curvature of the filament involved. To avoid this error, the calculation of the curved vortex element immediately adjacent to the point in question was approximated by a circular segment, and the influence of this circular segment was included in the computational program.

APPENDIX II
CONVERGENCE OF THE WAKE GEOMETRY-BOUND CIRCULATION SOLUTION

As mentioned previously, an iteration is required using the Prescribed Wake Program and Wake Geometry Programs to insure reasonably compatible wake geometries and bound circulation distributions. Because of the computing time required by the Wake Geometry Program, it is obviously desirable to minimize the number of passes through this program. This can be accomplished by (1) adjusting the circulation distributions used as input to the Wake Geometry Program so as to anticipate the final circulation distribution answer as much as possible (using past experience as a guide) and (2) being aware of the sensitivity of the final answer of interest, namely, rotor performance, to possible departures from the ideal, completely compatible, geometry-circulation solution. Both approaches were employed in this study. The paragraphs below present some results which can be used to evaluate the expected sensitivity of rotor performance to departures from the ideally converged solution.

Rotor performance is, of course, given in terms of integrated rotor thrust (C_T/σ) and torque (C_Q/σ). Of these, rotor thrust exhibits the most sensitivity to the k_1 and k_2 wake geometry parameters for the tip vortex. Partial derivatives relating C_T/σ to k_1 and k_2 for two-bladed rotors were estimated by using the Prescribed Wake Program and varying k_1 and k_2 independently. The results indicated the following approximate relation for two-bladed rotors:

$$\Delta C_T/\sigma = -0.44\,\Delta k_1 - 0.5\,\Delta k_2 \qquad (6)$$

Now, if k_1 and k_2 could be related to the bound circulation distribution, one would be able to assess the probable impact of further refinements to the circulation by using Equation (6) to compute an equivalent error in C_T/σ and comparing this with the level of accuracy to which C_T/σ is desired. Assuming that the peak circulation Γ_{max} on the blade is the characteristic quantity determining the flow field and hence k_1 and k_2, one can use the computed wake geometry results that have been obtained under this contract for the various operating conditions to assess the rates of change of k_1 and k_2 with respect to Γ_{max}. Such results are shown in Figure 114 for the -8-degree twist rotor cases. Values are plotted both as functions of the specific Γ_{max} values computed for the model rotor and a nondimensional Γ_{max} to increase the utility of the chart.

If C_T/σ is desired to an accuracy of ±0.001 (typically $\pm1\%$), then from Equation (4) this limits k_1 and k_2 errors to ±0.0023 and ±0.002, respectively. From Figure 114 the corresponding tolerances on Γ_{max} for the model rotor are ±19 and ±1.8 ft^2/sec, respectively. The large tolerance in Γ_{max} associated with the error in k_1 simply reflects the relative insensitivity of k_1 to Γ_{max} (or thrust) as predicted by the Wake Geometry Program. This insensitivity appears to be due to the fact that the general downwash induced by the wake on the tip vortex trailed by a given blade tends to be cancelled by an upwash induced by the contracted vortex trailed by the immediately preceding blade.

All of the geometry-circulation results presented herein have converged to within the smallest tolerance in Γ_{max} quoted above. Thus, the corresponding computed C_T/σ should be accurate to ±0.001.

DISTRIBUTION

Director of Defense Research & Engineering	2
Assistant Secretary of the Army (R&D)	1
Assistant Chief of Staff for Force Development, DA	1
Deputy Chief of Staff for Logistics, DA	1
Third United States Army	2
United States Army, Pacific	1
Chief of Research & Development, DA	2
Army Research Office	1
Army Materiel Command	4
Army Aviation Systems Command	3
Hq, Army Air Mobility Research & Development Laboratory	2
Ames Directorate, Army Air Mobility R&D Laboratory	2
Eustis Directorate, Army Air Mobility R&D Laboratory	20
Langley Directorate, Army Air Mobility R&D Laboratory	2
Lewis Directorate, Army Air Mobility R&D Laboratory	2
Army Aviation Systems Test Activity	2
Army R&D Group (Europe)	2
Army Scientific & Technical Information Team (Europe)	1
Army Advanced Materiel Concepts Agency	1
Army Aeromedical Research Laboratory	2
Harry Diamond Laboratories	1
Army Land Warfare Laboratory	1
Army Human Engineering Laboratories	2
Army Natick Laboratories	1
Army Ballistic Research Laboratory	1
Army Fuels & Lubricants Laboratory	1
Army Research Office - Durham	1
Army Materials & Mechanics Research Center	5
Army Plastics Technical Evaluation Center	1
Army Engineer Waterways Experiment Station	1
Army Test & Evaluation Command	1
Army Materiel Systems Analysis Agency	1
Army Electronics Command	3
Army Missile Command	1
USACDC Aviation Agency	2
USACDC Transportation Agency	1
Army Medical R&D Command	1
Edgewood Arsenal	1
Army Command & General Staff College	1
Army Aviation School	1
Army Aviation Test Board	2
Army Arctic Test Center	1
Army Board for Aviation Accident Research	1
1st Cavalry Division (Airmobile)	1
Air Force Office of Scientific Research	1
Hq, USAF	1
Air Force Flight Test Center	2